Diamond Light Source Ltd Review 2017/18

Mechanical Beamline Technician, Peter Garland, working on the I21 sample station.

Contents

Foreword

Diamond is one of the world's leading synchrotrons, providing its industrial and academic user communities with access to state-of-the-art analytical tools.

The resulting knowledge has wide-ranging impacts - scientific, economic, cultural and societal. The many high-impact peer-review publications we deliver attest to our scientific excellence. Equally important is the breadth and depth of engagement with industry and the resulting translation into economic impact, evidenced by over 125 companies paying for proprietorial access and an increasing number of companies engaging through partnerships with the many university groups who access Diamond. As we look to the future, the key challenge ahead will be to secure the investments in the facility that will ensure our continuing international leadership position. The Diamond Board will continue to use its influence to ensure that we maintain and enhance our leading global reputation.

Professor Sir Adrian Smith
Chairman of the Board of Directors

> **The many high-impact peer-review publications we deliver attest to our scientific excellence.**

Senior Support Scientist, Sarah Day, in the Long Duration Experimental Hutch of I11.

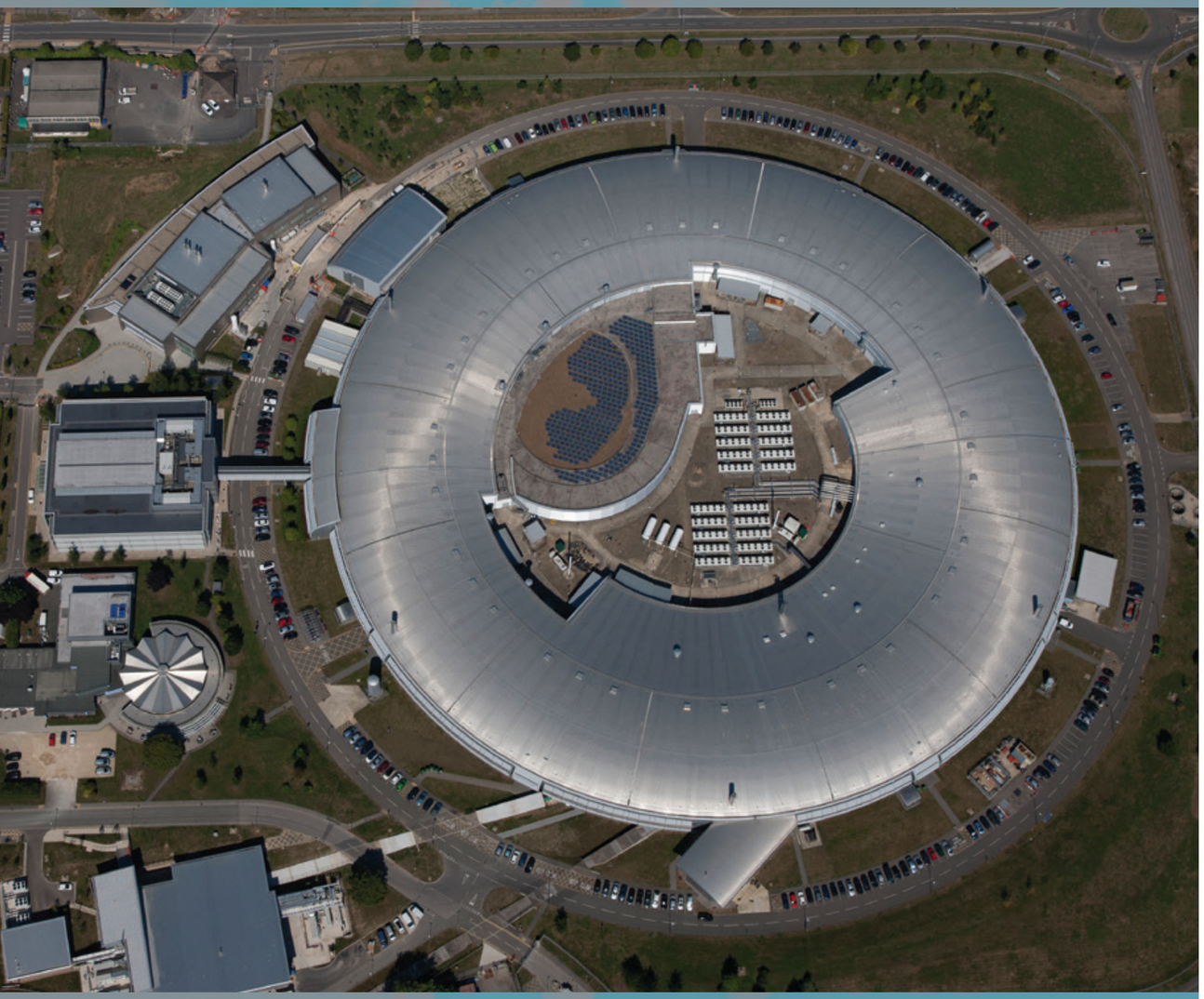

With over 9,000 user visits, a machine up time of 98.2%, and exceptionally dedicated staff supporting every aspect of our activities, our offer to the science community is second to none.

CEO Welcome

2017 marked a double anniversary for Diamond: our 15th anniversary as a company and 10 years of research and innovation. This was marked by the official visit of HRH the Princess Royal last February - a tremendous accolade for everyone involved with Diamond.

Our facility is currently completing its final beamlines, which will see us close Phase III construction in 2019. We now have 31 operational beamlines which are delivering an increasing number of high-impact publications. This review presents some of the highlights of this science, illustrating both new insights we are providing in fundamental science, and the positive impact for the economy and society at large in partnership with our user community.

With over 9,000 user visits, a machine up time of 98.2%, and exceptionally dedicated staff supporting every aspect of our activities, our offer to the science community is second to none. All of this underpins outputs that grow from year to year, most readily illustrated by the number of peer-reviewed publications, numbering 6,825 in 2017 with 41% of the output linked to the life sciences. This is the result of our creating an integrated offer for our structural biology community, which is unique in the world. We now have six microscopes dedicated to the life sciences running seven days a week each delivering 220 days of science per year. We are becoming a one-stop shop to understand the origins of diseases at a molecular or cellular level and to both discover and develop drugs to treat them. The physical sciences are blooming too, from multiprobe and *operando* studies of catalysts to new emerging technologies for ICT such as multiferroics, where electrical and magnetic functionality are coupled, so changing one can switch the other. As you will read in our Materials and Magnetism section, researchers from across the globe have used our I06 beamline to visualise this phenomenon and as the basis for new multifunctional devices that work well at room temperature, are opening up new avenues for creating new electronic storage devices.

Engaging with industry is also an essential part of our mission and the past year has seen a record income from proprietorial access. An increasingly important part of this is the new embedded facilities for electron microscopy for both life and physical sciences at eBIC and ePSIC, respectively. Diamond also provides crucial facilities for metrology, illustrated recently by work performed by FMB Oxford to test the performance of their manufactured components.

As taxpayers essentially fund 86% of the facility, we have kept our commitment to engage with the public. We offer regular open days and work with the media to communicate and create greater awareness of the ground-breaking science achieved here. With 5,635 visitors in the past year alone, of which 3,121 were school students and members of the public, we are continually making sure we present strong and diverse role models across all disciplines. We want to inspire as many youngsters as possible by the work we do and persuade as many of them as possible to choose STEM subjects as the path to their future careers.

If we are to continue to enable world-leading science and innovation, we must ensure that Diamond continues to offer the very best technical facilities, from the machine, through the beamlines to rapid and effective methods of data analysis. In recognition of this, our stakeholders – STFC and the Wellcome Trust – will increase our capital budget from 2019 to support an ambitious programme of rolling upgrades. We prioritised these upgrades in close consultation with our advisory bodies for academia and industry, as well as reflecting on the UK Government's Industrial Strategy, which presented grand challenges to which we can strongly contribute - clean growth, mobility and an ageing society. Our own plans also resonate with wider developments across the Harwell Campus – in particular the Rosalind Franklin Institute to develop enabling technology for medicine and the Faraday Institution for battery research – in which we are to be key partners. In the longer term, we plan a wholesale upgrade of machine itself – Diamond-II – in parallel with machine upgrades at synchrotrons around the world. This will offer an increase in brilliance, coherence and capacity that will offer wholly new scientific opportunities and maintain our competitive edge.

However, such developments should be carried out in partnership with other synchrotrons, which share the same technical challenges and aim to solve similar scientific problems. To this end, Diamond has played an active role in founding the League of Accelerator-based Photon Science (LEAPS), which brings together 16 organisations across Europe representing all 19 European synchrotrons and free electron laser facilities. As Brexit approaches in March 2019, it will be critical to ensure the UK remains a key element of this network and we continue to benefit from the international cooperation and exchange with our strongest international partners that enable us to tackle together some of the key scientific and societal challenges of our time.

Prof Andrew Harrison
CEO Diamond Light Source

Beamline Development and Technical Summary

In its eleventh year of experiments, Diamond is now operating with 31 beamlines and eight high-resolution electron microscopes. The next three years will see the final two Phase III beamlines complete construction and welcome first users. Of the electron microscopes, six are cryo-electron microscopes specialising in life sciences and make up eBIC (Electron Bio-Imaging Centre). The two remaining microscopes dedicated to advanced materials research are supplied by Johnson Matthey and the University of Oxford. These microscopes form ePSIC (Electron Physical Sciences Imaging Centre) and are operated under strategic collaboration agreements to provide for substantial dedicated peer reviewed user access. Both the eBIC and ePSIC centres are next to the Hard X-ray Nanoprobe beamline (I14). For academic research, Diamond instruments (beamlines and microscopes) are free at the point of access through peer-review. For proprietary research, access can be secured through Diamond's industry team.

Following a restructure in 2018, the instruments are organised into eight science groups as described below.

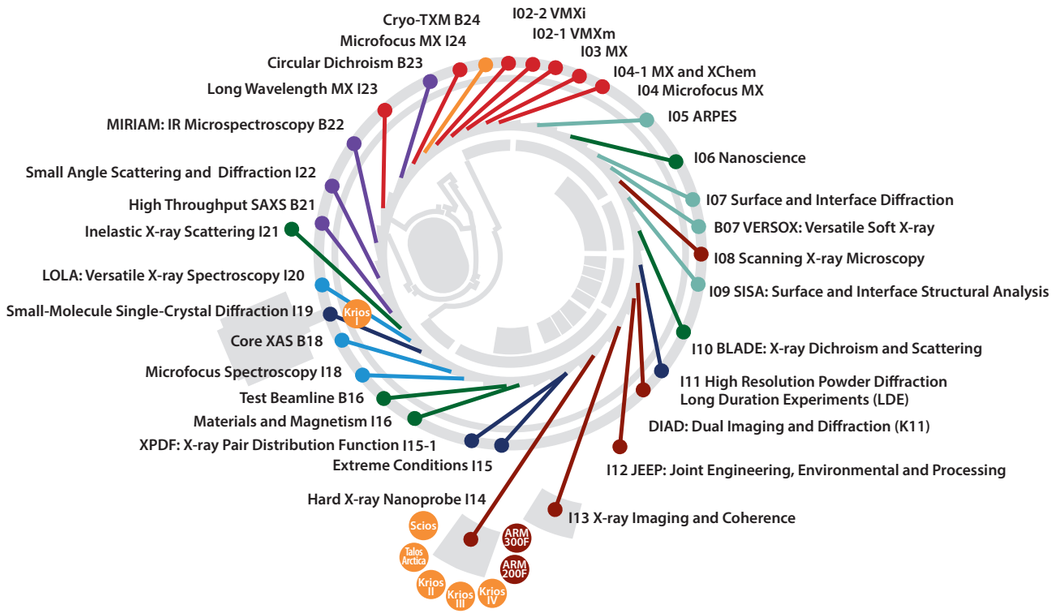

Electron Microscopes

Microscope	Main Capabilities	Accelerating Voltages	Operational Status
Titan Krios I	Cryo-EM, cryo-ET	80, 120, 200, 300 kV	Operational since 2015
Titan Krios II	Cryo-EM, cryo-ET	80, 120, 200, 300 kV	Operational since 2016
Titan Krios III	Cryo-EM, cryo-ET	80, 120, 200, 300 kV	Operational since 2017
Titan Krios IV	Cryo-EM, cryo-ET	80, 120, 200, 300 kV	Operational since 2017
Talos Arctica	Cryo-EM, cryo-ET	200 kV	Operational since 2016
Scios	Cryo-SEM, Cryo-FIB	3 to 30 kV	Operational since 2017
JEOL ARM200F	EDX, EELS, atomic scale STEM imaging, electron diffraction	80, 200 kV	Operational since 2017
JEOL ARM300F	EDX, atomic scale TEM and STEM imaging, electron diffraction	30, 60, 80, 160, 200, 300 kV	Operational since 2017

Diamond's beamlines: current operational status April 2018

Beamline Name and Number	Main Techniques	Energy / Wavelength Range	Status
I02-1 - Versatile MX micro (VMXm)	Versatile macromolecular crystallography (VMX)	10 - 25 keV	**Construction**
I02-2 - Versatile MX *in situ* (VMXi)	VMX	10 - 25 keV	Commissioning
I03 - MX	Macromolecular crystallography (MX), Multiwavelength Anomalous Diffraction (MAD)	5 - 25 keV	Operational
I04 - Microfocus MX	MX, MAD	6 - 18 keV	Operational
I04-1 - Monochromatic MX	MX, XChem fragment screening	13.53 keV (0.9163 Å - fixed wavelength)	Operational
I05 - ARPES	Angle-Resolved PhotoEmission Spectroscopy (ARPES) and nano-ARPES	18 - 240 eV; 500 eV	Operational
I06 - Nanoscience	X-ray Absorption Spectroscopy (XAS), X-ray photoemission microscopy and X-ray magnetic circular and linear dichroism	80eV - 2200eV	Operational
I07 - Surface and Interface Diffraction	Surface X-ray diffraction, Grazing Incidence X-ray Diffraction (GIXD), Grazing Incidence Small Angle X-ray Scattering (GISAXS), X-ray Reflectivity (XRR)	6 - 30 keV	Operational
B07 - VERSOX: Versatile Soft X-ray	Spectroscopic and scanned-probe imaging	50 - 2800 eV	Commissioning
I08 - Scanning X-ray Microscopy	Scanning X-ray microscopy	250 eV - 4.2 keV	Operational
I09 - SISA: Surface and Interface Structural Analysis	XPS (including HAXPES), X-ray Standing Waves (XSW), Near Edge X-ray Absorption Fine Structure (NEXAFS), energy-scanned photoelectron diffraction	Hard X-rays: 2.1 - 18+ keV (currently 2.35 - 18+ keV) Soft X-rays: 0.1 - 2.1 keV (currently 0.1 - 1 keV)	Operational
I10 - BLADE: Beamline for Advanced Dichroism Experiments	Soft X-ray resonant scattering, XAS and X-ray magnetic circular and linear dichroism	Circular: 400-1600eV; Linear Horizontal: 250-1600eV; Linear Vertical: 480-1600eV	Operational
I11 - High Resolution Powder Diffraction	X-ray powder diffraction	6 - 25(30) keV (0.5 - 2.1 Å)	Operational
DIAD: Dual Imaging and Diffraction	Simultaneous imaging and diffraction	7 - 35 keV	**Construction**
I12 - JEEP: Joint Engineering, Environmental and Processing	Imaging and tomography (phase- and attenuation-contrast), single crystal diffraction, powder diffraction, energy dispersive diffraction, high-energy small angle scattering	53 keV - 150 keV monochromatic or continuous white beam	Operational
I13 - X-ray Imaging and Coherence	Phase contrast imaging, tomography, full-field microscopy (under commissioning), coherent diffraction and imaging (CXRD,CDI), ptychography and photocorrelation spectroscopy (XPCS) (under commissioning), innovative microscopy and imaging	Imaging branch: 8 - 30keV Coherence branch: 7 - 20keV	Operational
I14 - Hard X-ray Nanoprobe	Scanning X-ray fluorescence, X-ray spectroscopy, ptychography and transmission diffraction	5 - 25 keV	Optimisation
I15 - Extreme Conditions	Powder diffraction, single crystal diffraction	20 - 80 keV monochromatic focused minimum beam size restrictions for E> 30 keV White beam for special applications	Operational
I15-1 - X-ray Pair Distribution Function (XPDF)	X-ray Pair Distribution Function (XPDF)	40, 65, and 76 keV	Optimisation
I16 - Materials and Magnetism	Resonant and magnetic single crystal diffraction	3 - 15 keV	Operational
B16 - Test beamline	Diffraction, imaging, reflectometry	4 - 20 keV monochromatic focused 4 - 45 keV monochromatic unfocused White beam	Operational
I18 - Microfocus Spectroscopy	Micro XAS, micro Extended X-ray Absorption Fine Structure (EXAFS), micro fluorescence tomography, micro XRD Reflection EXAFS (ReflEXAFS)	2.05 - 20.5 keV	Operational
B18 - Core XAS	X-ray Absorption Spectroscopy (XAS)	2.05 - 35 keV	Operational
I19 - Small-Molecule Single-Crystal Diffraction	Small-molecule single-crystal diffraction	5 to 25 keV / 0.5 to 2.5 Å	Operational
I20 - LOLA: Versatile X-ray Spectroscopy	X-ray Absorption Spectroscopy (XAS), X-ray Emission Spectroscopy (XES) and Energy Dispersive EXAFS (EDE)	Dispersive branch: 6 - 26 keV Scanning branch: 4 - 20 keV	Commissioning Operational
I21 - Inelastic X-ray Scattering	Inelastic X-ray Scattering (IXS)	250 - 3000 eV	Commissioning
B21 - High Throughput SAXS	Solution state small angle X-ray scattering	Currently 11-23 keV but set to 12.4 until variable camera installed	Operational
I22 - Small Angle Scattering and Diffraction	Small angle X-ray scattering and diffraction: SAXS, WAXS, ASAXS, USAXS, GISAXS. Micro-focus.	3.5 - 20 keV	Operational
B22 - MIRIAM: Multimode InfraRed Imaging And Mircrospectroscopy	IR microspectroscopy and imaging, THz spectroscopy	Microscopy (µFTIR): 10,000-100 cm^{-1} (1-100 mm) Imaging (FPA): 5000-900 cm^{-1} (2-11 mm) Spectroscopy (FTIR): 10,000-10 cm^{-1}(1.2 eV-1.2 meV)	Operational
I23 - Long Wavelength MX	Long wavelength macromolecular crystallography	3 - 8 keV (1.5 - 4.1 Å)	Commissioning
B23 - Circular Dichroism	Circular dichroism	Module A: 125 - 500nm (for multiplates and films) Module B: 165 - 650nm (for solutions)	Operational
I24 - Microfocus MX	Macromolecular crystallography, MAD	6.5 - 25.0 keV	Operational
B24 - Cryo Transmission X-ray Microscopy (TXM)	Full field X-ray imaging	200eV - 2600eV	Optimisation

Macromolecular Crystallography Group

Dave Hall, Science Group Leader

Diamond provides a range of techniques for academic and industrial researchers studying the machines of life. As one of those techniques, Macromolecular Crystallography (MX) reveals the shape and arrangement of biological molecules at atomic resolution, knowledge of which provides a highly accurate insight into function. This can be combined with complementary information from many other techniques available at Diamond alongside lab based investigations to reveal the broader picture of molecular interactions and their effects.

MX is a core activity at Diamond with seven beamlines dedicated to the technique alongside the XFEL Hub, Membrane Protein Laboratory and XChem fragment screening facility for the extensive UK structural biology community as well as researchers in Europe and beyond. The staff of the MX group are recognised as innovative world leaders in MX, moving the goalposts of what is feasible for 'conventional' MX as well as developing techniques and beamlines that transform MX to the next level, enabling new experiments and methodologies. The group takes a long term approach to enabling new capabilities at its suite of beamlines to meet the current and future demands of an exacting community of scientists; in 2017 this was no different, as can be seen by the exciting developments here.

In 2017 the Long Wavelength MX beamline (I23) (dedicated to solving the crystallographic phase problem directly from native proteins) entered an exciting phase in its development, with a concerted push to facilitate user access alongside groundbreaking experiments with invited user groups. General user access to this technical *tour de force* was initiated in 2017 by its first call for users via the peer review proposal system for experiments in 2018 with great interest shown by the user community. Ongoing developments will continue on I23 to explore and exploit its potential to the full – we are entering a whole new world of what is possible with *in vacuum* MX and the samples and technology that enable this.

Serial Synchrotron Crystallography (SSX) is another emerging method driven, in part, by the sample requirements imposed by X-ray Free Electron Lasers (XFELs). Serial techniques can also be exploited at synchrotrons, especially at microfocus beamlines, opening up many new opportunities. A number of approaches including fixed targets and extruders have been tried and tested at Diamond's Microfocus MX beamline (I24) and are available for general users. Expertise at I24 is centred on Fixed Target Serial Synchrotron Crystallography (FT-SSX). FT-SSX is attractive as it potentially offers high hit-rates coupled with modest sample consumption. Furthermore, the same approach can be used almost without modification at both synchrotrons and FELs.

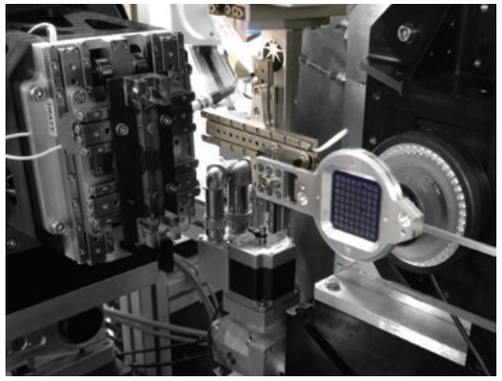

Figure 1: The FT-SSX set-up available at I24.

Our fixed target approach makes use of silicon nitride 'chips' with the current generation of chip capable of holding more than 25,000 crystals. Chips are mounted on a high-speed, high-precision *xyz* stage mounted at the sample position (Fig. 1). This setup allows data collection from all 25,600 positions on a chip in less than 10 minutes.

2017 has seen the final touches to the capabilities of the dedicated *in situ* VMXi beamline being commissioned and new workflows developed. The beamline is now at a state where regular user operation and further hardware/software refinement is continuing in parallel. Input from initial users has been invaluable in progressing the beamline development, and indeed the demand for acting as beta testers from users has illustrated the keen interest amongst the MX community for the new capabilities that the beamline now provides. Alongside the beamline development, the VMXi team has also brought facilities together in a new central crystallisation laboratory located at the Research Complex (RCaH) next to Diamond. This facility is now open to users and can be used to prepare crystallisation experiments for the VMXi beamline – as well as for the Membrane Protein Laboratory and the XChem facility. Furthermore, the beamline team is working with the Diamond-based XFEL Hub to develop serial crystallography functionality which will also become part of the beamlines future offering to the MX community.

The last phase III MX beamline, VMXm, is progressing well. This beamline is designed to address the challenges of data collection from micron and sub-micron sized samples. With commissioning of the VMXm optics hutches essentially complete the end-station is now being assembled ready for commissioning and first experiments. First light into the experimental end-station hutch was seen in early March 2018 when work began on commissioning the microfocus optics. Offline assembly and testing of the sample environment is underway for incorporation into the end-station in April/May ready for first user experiments.

Our more conventional MX beamlines also continue to evolve to provide new functionality as well as increased performance. Through 2017 significant changes were made to the sample positioning systems on beamlines I03 and I04. Both are now equipped with a high precision, fast SmarGon multi-axis goniometer (Fig. 2) coupled to high capacity BART sample robots. The goniometers enable optimised data collection methods on these high throughput beamlines and have brought high speed snaked raster scanning, as developed for FT-SSX on I24, which enables the location of the smallest samples, best regions of samples and in automatic crystal X-ray centering methods. This latter use is part of a set of upgrades to all the MX cryogenic sample beamlines to bring automatic queued data collection to the user programme allowing expert systems to deliver the best data quality. The new goniometry set-up also allows I03 to switch to a fast, large format goniometer for *in situ* crystallisation plates for pathogenic samples or cornea experiments (Fig. 3). Standard MX *in situ* work is available on VMXi and I24.

Finally, fragment screening at the XChem facility attached to beamline I04-1 is now fully integrated into Diamond's user programme. Annually it hosts well over 30 screening experiments from academia and industry. In 2017, the programme contributed 35,000 of the more than 50,000 crystals shot at the beamline, but using less than one third of the total beamtime, illustrating the efficiency of the automated queue mode. With the programme consistently oversubscribed, and demand from industry growing, the facility is expanding its capacity: a dedicated user support team is being assembled, with extra capacity and an increase in dedicated lab space. Additional beamtime has been agreed, given or provided for in the allocation period for 2018

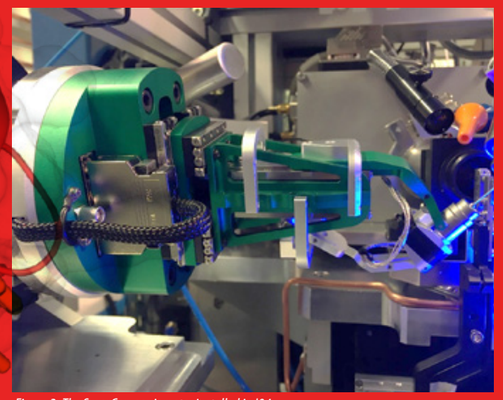

Figure 2: The SmarGon goniometer installed in I04.

The progress made in 2017 for these facilities and their user programmes is underpinned by the dedication and expertise of all staff in the MX group working alongside support group staff from across Diamond as well as collaborations built across the world. The same staff engage in outreach, teaching and training for users, students and the public to build a greater understanding of the capabilities and science of MX in the broader setting of integrated structural biology.

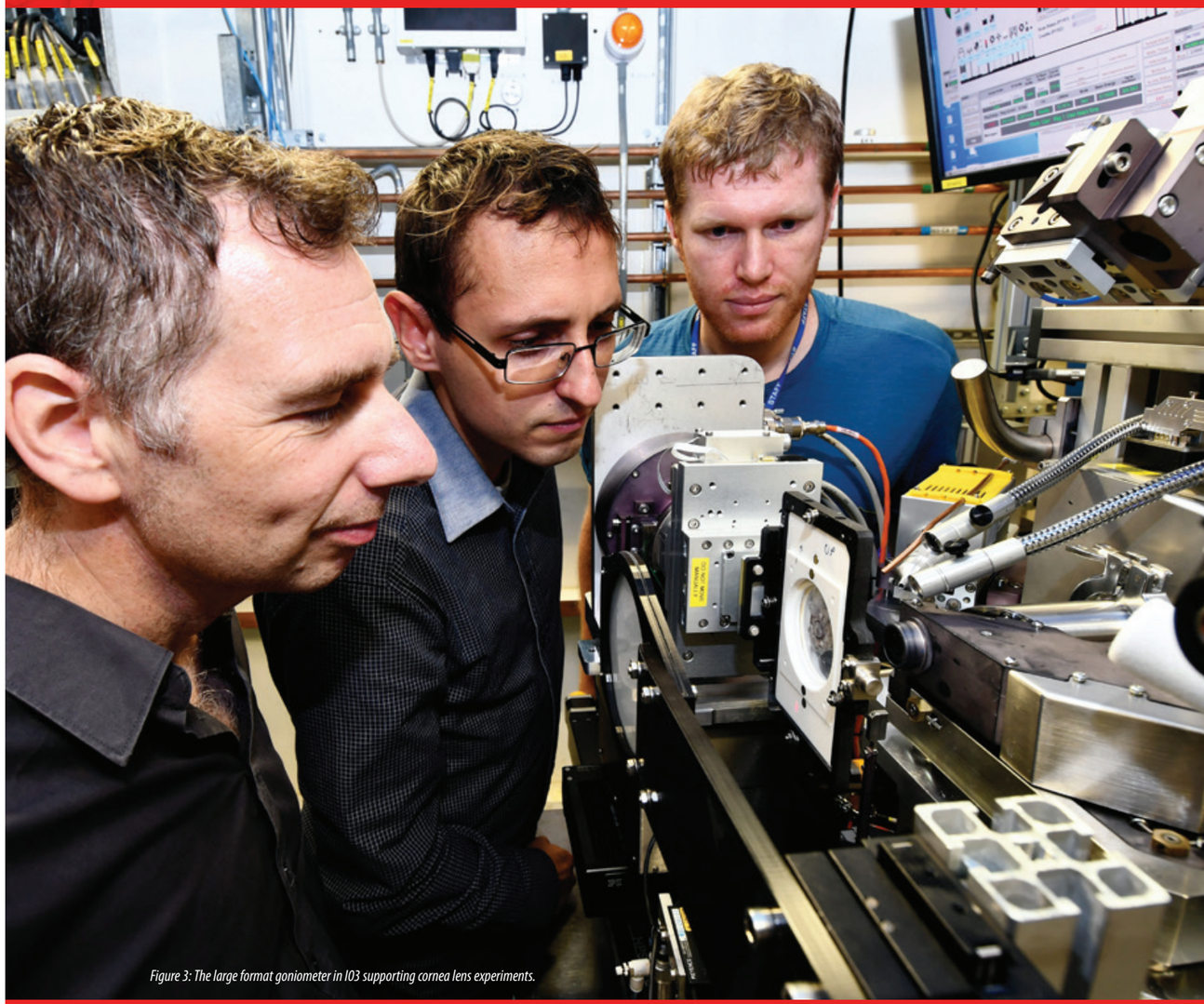

Figure 3: The large format goniometer in I03 supporting cornea lens experiments.

How human endoglin captures its ligand BMP9

Related publication: Saito T, Bokhove M, Croci R, Zamora-Caballero S, Han L, Letarte M, de Sanctis D, Jovine L. Structural Basis of the Human Endoglin-BMP9 Interaction: Insights into BMP Signaling and HHT1. *Cell Reports* **19**, 1917–1928, doi: 10.1016/j.celrep.2017.05.011 (2017).

Publication keywords: TGF-β superfamily; BMP signalling; Cell surface receptors; X-ray crystallography

Endoglin (ENG)/CD105 is a mammalian glycoprotein that is found in the membranes of cells that line blood vessels. It is essential for healthy heart development and blood vessel growth, but conversely it is also involved in preeclampsia and can help tumours establish their blood supply. Additionally, *ENG* gene mutations cause hereditary hemorrhagic telangiectasia type 1 (HHT1), a genetic disorder characterised by complex vascular malformations that affect 1 in 10,000 individuals.

Although ENG plays a crucial role in the vascular system and its inhibition can slow tumour proliferation, no high resolution structural data exist to show how it is organised and how it interacts with its binding partner, bone morphogenetic protein 9 (BMP9).

To gain the much needed structural insights on this protein, several hundred crystals were grown and screened for their diffraction properties. Just one yielded a usable dataset at 4.45 Å resolution using the Macromolecular Crystallography (MX) beamline (I02).

Together with other structures, this showed that the N-terminal orphan region of ENG, which is responsible for its ligand-binding activity, consisted of two duplicated domains. Only the first of these domains recognised BMP9 through a hydrophobic interface. At the other end of the protein, the C-terminal region functioned as a scaffold that optimally positioned the binding site. Overall, ENG cradled BMP9 in such a way to effectively display it to other proteins involved in signalling pathways for blood vessel maintenance.

Endoglin (ENG)/CD105 is an essential endothelial cell co-receptor of the transforming growth factor (TGF)-β superfamily. This consists of extracellular type I and II serine/threonine kinase receptors that, upon interaction with structurally related ligands such as TGF-βs and bone morphogenetic proteins (BMPs), regulate fundamental cellular processes by triggering a signal transduction cascade through cytoplasmic SMAD proteins. Mutations of the human *ENG* gene are linked to hereditary hemorrhagic telangiectasia type 1 (HHT1), an autosomal dominant vascular disorder also known as Osler–Weber–Rendu syndrome; moreover, ENG has been implicated in preeclampsia and - as highlighted by the observation that anti-ENG monoclonals can inhibit tumour angiogenesis - represents a promising target for cancer therapy. Therefore, structural knowledge of human ENG and its complexes constitutes a valuable framework to both understand the molecular basis of BMP-dependent signalling and shed light on its clinical implications.

ENG is a ~180 kDa homodimeric type-I transmembrane protein that consists of an N-terminal orphan region (OR) and a C-terminal zona pellucida module (ZP). Extensive attempts to crystallise the full-length ectodomain of ENG failed, likely because the flexibility of the linker between OR and ZP interferes with crystal packing. Therefore, ENG was divided into two fragments that spanned the ligand-binding OR and the homodimerisation-mediating ZP, respectively. These regions were expressed and crystallised separately using a novel mammalian fusion protein methodology[1]. Furthermore, OR was crystallised in complex with BMP9, a physiological high-affinity ligand for ENG in endothelial cells.

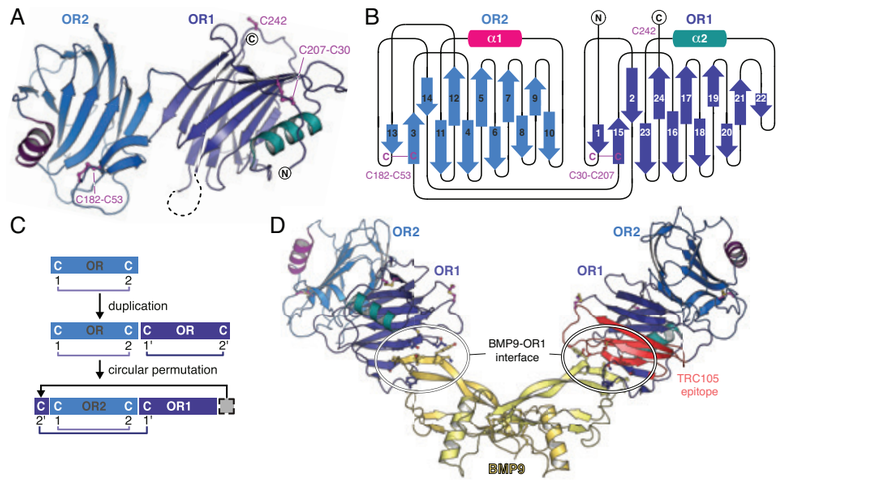

Figure 1: Structure of ENG OR and its complex with BMP9. (a) OR consists of a duplicated β-helical domain (OR1/OR2) whose cysteines are shown in ball-and-stick representation and coloured magenta. (b) The topology of OR highlights its internal domain duplication. (c) Suggested evolutionary origin of ENG OR by duplication and circular permutation of an ancestral β-helical domain. (d) Crystal structure of homodimeric BMP9 bound by two copies of ENG OR. The encircled region indicates the binding interface, which overlaps with a protein fragment containing the epitope of anti-ENG clinical monoclonal TRC105 (red).

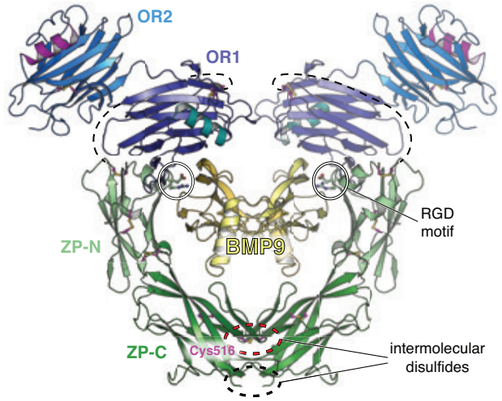

Figure 2: Theoretical model of the full ectodomain of dimeric ENG in complex with BMP9, based on the crystal structures of the individual components and the ENG OR-BMP9 complex.

The structure of OR reveals a monomer consisting of two β-helical-like domains (OR1/OR2) with a common novel fold that also includes an α-helix (Fig. 1a and b). Structure-based sequence alignments show that OR2 is actually inserted after the second β-strand of OR1, suggesting that the OR fold originated by gene duplication and circular permutation (Fig. 1b-c).

To gain mechanistic insights into how ENG modulates BMP signalling by interacting with secreted ligands, the structure of ENG OR in complex with BMP9 was determined. Despite their perfect shape and high reproducibility, the OR-BMP9 crystals diffracted X-rays very poorly, so that efficient screening of hundreds of specimens using the ACTOR sample mounting robot at beamline I02 was essential to obtain a single usable dataset at 4.45 Å resolution. The structure of the complex reveals that the outer tip of the BMP9 β-sheets is recognised by a hydrophobic groove on the OR1 domain of ENG (Fig. 1d). Notably, this binding region involves conserved ENG amino acids Ser278 and Phe282, mutations of which are found in patients suffering from HHT1[3]; on the other hand, the structural data suggests that many other pathological mutations act indirectly, by interfering with proper folding of ENG. Remarkably, the BMP9-binding region of OR1 overlaps with the epitope of TRC105/SN6j (Fig. 1d), a monoclonal antibody against ENG that is being clinically investigated for the treatment of solid tumours together with vascular endothelial growth factor inhibitors[4].

How does co-receptor ENG present the BMP9 ligand to other members of the signalling pathway, such as type I receptors activin receptor-like kinase 1 (ALK1)? As mentioned above, the C-terminal half of the ENG ectodomain corresponds to a ZP module. This is a bipartite element that consists of a ZP-N and a ZP-C domain and mediates protein-protein interactions in many other extracellular matrix components with unrelated biological functions. While it contains characteristic ZP-N domain features such as an immunoglobulin-like fold and two conserved disulphides, ENG ZP-N is unique in that it includes an additional disulphide bridging two α-helices and exposes to the solvent a loop carrying an RGD motif associated with cell surface adhesion (Fig. 2). Interestingly, the immunoglobulin-like ZP-C domain is quite different from other ZP-Cs. This is because the absence of an extended cysteine-carrying loop results in a minimal fold that is stabilised by one disulphide rather than the conventional three or four, leaving a single cysteine residue unpaired.

ENG lacks a conserved ZP-N tyrosine that is implicated in ZP module-mediated polymerisation, as well as a consensus cleavage site in ZP-C whose processing is also associated with extracellular assembly; together with a short interdomain linker and an occluded ZP-N homodimerisation interface, these features explain why ENG is a non-polymerising ZP-module-containing protein[2]. Consistent with mutagenesis studies, the structure shows that solvent exposure of unpaired Cys516 within a membrane-proximal ZP-C loop allows it to covalently cross-link two molecules of ENG by forming an intermolecular disulphide with another copy of itself. Furthermore, it suggests that Cys582 - an additional cysteine not present in the ENG ZP expression construct - would be located in the vicinity of Cys516, where it could form a second intermolecular disulphide. These observations result in a model wherein two disulphide-bonded copies of the ENG ZP module would position the respective OR regions so that, together, they can embrace a BMP9 homodimer (Fig. 2).

The abundance of ENG, together with its nanomolar affinity for BMP9 and avidity-conferring antibody-like structure, allows the co-receptor to efficiently capture its ligand and retain it on the surface of endothelial cells. However, in order for the signalling cascade to initiate, ENG must deliver its cargo to the type I and type II receptors. Notably, the ENG-BMP9 interface is compatible with BMP9 recognition by ALK1[5], resulting in a model of the ternary ENG-BMP9-ALK1 complex (Fig. 3). However, the same interface overlaps with the BMP9 binding site for type II receptor activin receptor type-2B (ActR2B)[5], suggesting that signalling requires handing over of the ALK1-BMP9 complex from ENG to ActR2B (or alternatively bone morphogenic protein receptor type II (BMPRII), another type II receptor). Collectively, these observations bring detailed insights into the mechanism of BMP signalling and inform ongoing efforts to therapeutically target this essential cellular pathway.

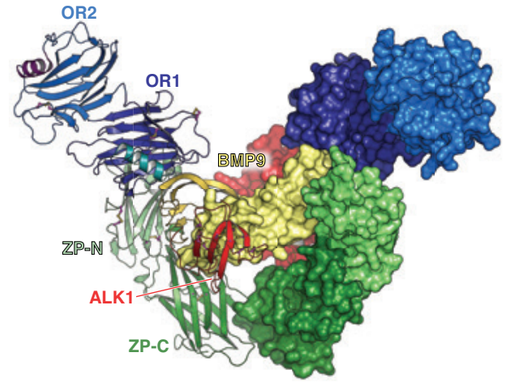

Figure 3: Theoretical model of the ternary ENG-BMP9-ALK1 complex, generated by merging the model of the binary ENG-BMP9 complex (Fig. 2) with crystallographic information on the BMP9-ALK1 interaction[5].

References:

1. Bokhove, M. *et al*. Easy mammalian expression and crystallography of maltose-binding protein-fused human proteins. *J Struct Biol.* **194(1)**, 1-7, doi: 10.1016/j.jsb.2016.01.016 (2016).
2. Bokhove, M. *et al.* A structured interdomain linker directs self-polymerization of human uromodulin. Proc Natl Acad Sci U S A. **113(6)**, 1552-7, doi: 10.1073/pnas.1519803113 (2016).
3. Mallet, C. *et al*. Functional analysis of endoglin mutations from hereditary hemorrhagic telangiectasia type 1 patients reveals different mechanisms for endoglin loss of function. *Hum Mol Genet*. **24(4)**, 1142-54, doi: 10.1093/hmg/ddu531 (2015).
4. Rosen, L. S. *et al.* Endoglin for Targeted Cancer Treatment. *Curr Oncol Rep* **16(2)**, 365, doi: 10.1007/s11912-013-0365-x (2014).
5. Townson, S. A. *et al*. Specificity and Structure of a High Affinity Activin Receptor-like Kinase 1 (ALK1) Signaling Complex. *The Journal of Biological Chemistry* **287(33)**, 27313-27325, doi: 10.1074/jbc.M112.377960 (2012).

Corresponding author: Professor Luca Jovine, Karolinska Institutet, luca.jovine@ki.se

Insights into the mechanism of colistin resistance from crystal structures of MCR-1

Related publication: Hinchliffe P, Yang QE, Portal E, Young T, Li H, Tooke C, Carvalho MJ., Paterson NG., Brem J, Niumsup PR., Tansawai U, Lei L, Li M, Shen Z, Wang Y, Schofield CJ, Mulholland AJ, Shen J, Fey N, Walsh TR, Spencer J. Insights into the Mechanistic Basis of Plasmid-Mediated Colistin Resistance from Crystal Structures of the Catalytic Domain of MCR-1. *Scientific Reports* **7**, 39392, doi:10.1038/srep39392 (2017).

Publication keywords: Antibiotic resistance; Polymyxin; Lipid A

Gram-negative bacteria that are extensively resistant to multiple antibiotics are an ever-increasing global threat. Colistin is an antibiotic used as the last line of defence against highly resistant Gram-negative bacteria. However, in recent years bacteria have emerged with resistance to this crucial antibiotic.

Resistance to colistin is determined by an enzyme called 'mobilised colistin resistance' (MCR-1), which has rapidly disseminated worldwide and is found in clinical strains of *E. coli* and *Klebsiella pneumoniae.* MCR-1 modifies the outer membrane of Gram-negative bacteria, preventing it from interacting with colistin, but despite its huge importance, the mechanism by which this happens remains to be established.

To shed some light on the workings of MCR-1, the crystal structure was solved using the Macromolecular Crystallography (MX) beamlines I04-1, I03 and I02. MCR-1 was found to be a zinc metalloprotein, with an alkaline phosphatase fold containing three disulphide bonds. These high-resolution data provided a detailed view of the active site, identifying areas of the enzyme that were critical for function. Moreover, these results allowed a computational prediction of the mechanism of action, and determined that a single zinc ion may be sufficient for MCR-1 to function. Knowing these important details could enable the rational development of novel antimicrobials to effectively combat colistin-resistant bacteria in the future.

Bacterial diseases, particularly those caused by Gram-negative bacteria (GNB), are a serious and increasing clinical threat worldwide. Treatment of GNB infections is complicated by their intrinsic resistance to many antibiotic classes and ready acquisition of resistance to additional agents. There are now some bacteria for which there are few treatment options remaining, with only a handful of antibiotics that are considered reliable for therapy. The polymyxin colistin is one such key `last-resort' antibiotic, used to treat infections by multidrug-resistant GNB pathogens. Colistin is a positively-charged polycationic peptide that binds to and disrupts the outer membrane of GNB by interacting with the negatively-charged lipid A headgroup. Until recently, resistance to colistin was considered rare, limited to changes in expression of chromosomal proteins that collectively modify the lipopolysaccharide, the component of GNB outer membranes. However, in November 2015 our team described colistin resistance mediated by MCR-1, a plasmid-encoded phosphoethanolamine (PEA) transferase[1]. Since this initial report, it has now been reported in over 40 countries, and is found in numerous bacterial strains, mainly *E. coli* and *Klebsiella pneumoniae*. In addition, a number of homologues have been further identified, including MCR-2[2]. MCR-1 has now been reported in bacteria producing other resistance determinants, such as carbapenemases, which can result in essentially untreatable bacterial infections. However, expression of *MCR-1* in *E. coli* comes at significant cost to the host, highly attenuating virulence and resulting in decreased growth rate, cell viability, and degradation of the cell membrane[3].

MCR-1 is an integral inner-membrane enzyme that catalyses the transfer of positively-charged PEA onto a phosphate of the glucosamine headgroup of lipid A, which is subsequently incorporated into the outer membrane. This confers resistance to colistin by reducing the net negative charge and preventing colistin from binding to, and subsequently inserting into, the outer membrane. The catalytic mechanism of MCR-1 (and other bacterial PEA-transferases) remains to be established.

To understand this mechanism, crystal structures of the catalytic domain of MCR-1 were obtained using beamlines I02, I03 and I04-1. To facilitate crystallography the protein was purified lacking the trans-membrane domain, so the soluble, periplasmic domain containing the predicted active site (i.e. the

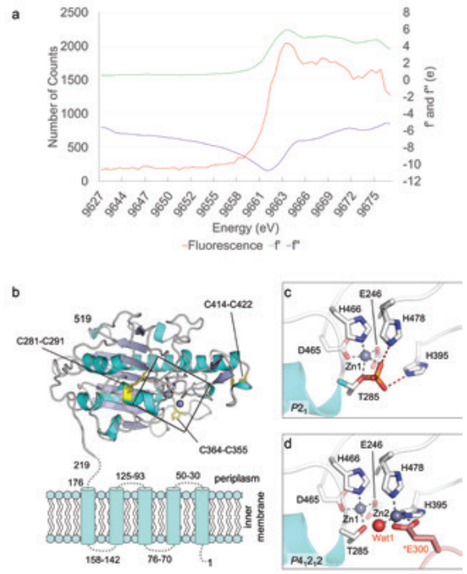

Figure 1: Crystal structure of MCR-1 (a) X-ray fluorescence scan of MCR-1 crystal. The peak was measured at 9664.04 eV (f': 5.92 / f": -8.15 e), consistent with a zinc signal. (b) Organisation of MCR-1 showing 5 predicted membrane-spanning α-helices and the periplasmic domain (residues 219–541). Intramolecular disulphide bonds are labeled and active site is boxed. (c) Active site of P21 crystal form showing a single bound zinc ion (grey sphere) and Thr285 phosphorylation. (d) Active site of P41212 crystal form showing a dinuclear zinc centre and coordination of Zn2 by residue Glu300 (pink) from an adjacent molecule in the crystal lattice.

MCR-1 catalytic domain; residues 219 onwards) of the protein was crystallised. A fluorescence scan on beamline I03 of these crystals revealed a strong peak at the Zn-edge, indicating the presence of zinc ions (Fig. 1a). Using this information, the crystallographic phases were determined using four single-wavelength anomalous dispersion (SAD) datasets collected on I03 at 2.50 Å resolution. These

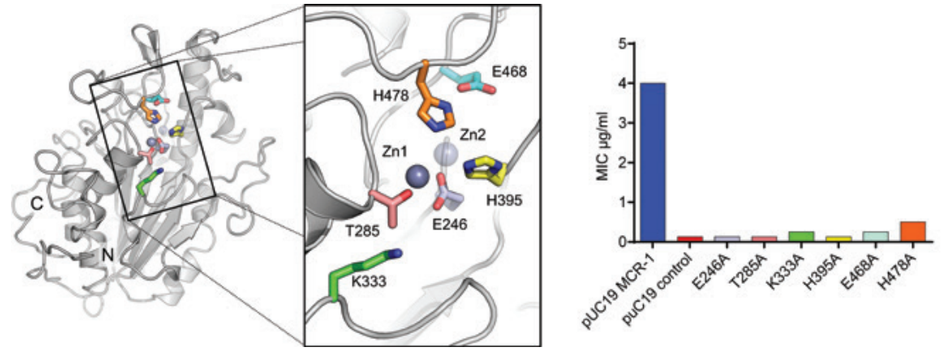

Figure 2: Effect of mutation upon MCR-1 Activity. (Left) MCR-1 active site (P21 crystal form) with colours identifying positions of alanine substitutions. (Right) Colistin MICs (determined by agar dilution; data shown are modes for two independent experiments, each performed in duplicate) for alanine substitutions at positions shown to the left.

phases were used to solve the crystal structure of two higher resolution native datasets that were collected on I04-1 and I02 on two different crystal forms in the space groups $P4_12_12$ (1.75 Å resolution) and $P2_1$ (1.55 Å resolution). The two structures are essentially identical (RMSD 0.37 Å), revealing the MCR-1 catalytic domain to have an overall α-β-α fold, containing three intramolecular disulphide bonds, typical of alkaline phosphatase or sulphatase enzymes, with the N-terminus indicating the likely position of the five transmembrane helices (Fig. 1b). However, the two structures differ in zinc content, with the $P2_1$ structure containing one zinc ion (Zn1), coordinated by Asp465, His466, Glu246 and Thr285 in a tetrahedral geometry (Fig. 1c), while the $P4_12_12$ structure contains density for an additional, also tetrahedral, zinc site (Zn2) coordinated by His395, His478, a water molecule (Wat1) and Glu300 from a symmetry related molecule (Fig. 1d). Furthermore, the active site of the $P2_1$ structure contains electron density corresponding to the presence of a phosphate group attached to Thr285, the conserved residue believed to act as the acceptor for the PEA group during the transfer reaction.

The presence of zinc in the active site is required for activity as MCR-1-positive strains were more susceptible to colistin on EDTA treatment. In addition, mutation of the Zn1 ligand Glu246 or the acceptor Thr285 reduces the colistin Minimal Inhibitory Concentration (MIC) of recombinant *E. coli* to that of vector-only control (Fig. 2). The effects of mutations at other active site residues are however more variable. Whilst replacement of the conserved His395, part of the Zn2 site ($P4_12_12$ structure), reduces colistin MIC to basal levels, substitutions

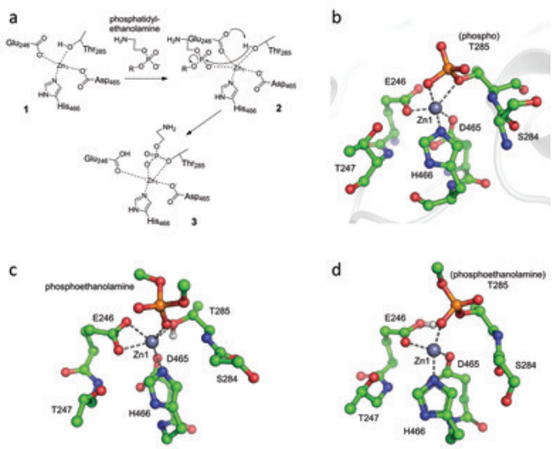

Figure 3: Density Functional Theory (DFT) Modelling of the MCR-1 Active Site (Mono-zinc form). (a) Possible mechanism for phosphoethanolamine addition (2) to MCR-1 Thr285 of mono-zinc MCR-1 (1) to form the Thr285 adduct (3). (b) MCR-1 active site crystal structure (P21 form) showing residues used in cluster model. (c) DFT-optimised geometry of phosphoethanolamine non-covalently bound to MCR-1 active site (2 in panel (a) above). (d) DFT-optimised geometry of MCR-1 active site in the phosphoethanolamine-bound form (3 in panel (a) above).

of the adjacent His478, or its hydrogen-bonding partner Glu468, give smaller reductions (3 to 4 dilutions). Similarly, the alanine mutation of Lys333 substantially reduces colistin MIC, but not to basal levels. Thus, at positions other than His395, alanine mutants away from the Zn1 site retain some ability to protect expressing strains from colistin action. Hence, while important, these residues are not absolutely essential to MCR-1 function. To further investigate the roles of the zinc sites (particularly Zn2, which is present in only one structure) computational density functional theory models of intermediates in the putative reaction mechanism were calculated for both a mono- and a di-zinc mechanism (Fig. 3). These data indicated that small structural changes required by the reaction are achievable within the constraints of the active site and that, in contrast to alkaline phosphatase enzymes, a single zinc ion may be sufficient to support at least the first stage of the MCR-1 catalysed reaction.

As *mcr-1* continues to spread, and more homologues are identified and disseminated, it is more crucial than ever to understand MCR-1 mechanism. These data, alongside our recently determined 1.12 Å resolution structure of MCR-2 from I04[2], will provide a starting point for more extensive investigations of MCR-1 mechanism that can in turn be used for structure-based design of inhibitors for use in potential colistin-based combination therapies.

References:

1. Liu, Y-Y. *et al.* Emergence of plasmid-mediated colistin resistance mechanism MCR-1 in animals and human beings in China: a microbiological and molecular biological study. *Infectious Diseases* **16 (2)**, 161-168, doi:10.1016/S1473-3099(15)00424-7 (2016).
2. Coates, K. *et al.* 1.12 A resolution crystal structure of the catalytic domain of the plasmid-mediated colistin resistance determinant MCR-2. *Acta Crystallogr. F* **73 (Pt8)**, 443-449, doi:10.1107/S2053230X17009669 (2017).
3. Yang, Q. *et al.* Balancing mcr-1 expression and bacterial survival is a delicate equilibrium between essential cellular defence mechanisms. *Nature Communications* **8**, 2054, doi:10.1038/s41467-017-02149-0 (2017).

Funding acknowledgement: This study was supported by the UK Medical Research Council (MR/P007295/1, TRW, PH and JaS; and MR/N002679/1, JB and CJS); the National Natural Science Foundation of China (grant nos 8661138002, 31530076 and 31422055, HL, LL, ML, ZS, YW and JiS); the Thailand Research Fund (PHD/0054/2555, PN and UT; Royal Golden Jubilee Ph.D Program and Rajamangala University of Technology, Lanna, UT); the U.K. Engineering and Physical Science Research Council (Catalysis Hub EP/M013219/1, AJM and NF; and BristolBridge EP/M027546/1, AJM and JaS); the UK Biotechnology and Biological Sciences Research Council (BB/L018756/1, AJM and NF) and the Royal Society of Chemistry (Undergraduate Research Bursary, TY).

Corresponding author: Dr James Spencer, University of Bristol, jim.spencer@bristol.ac.uk

How does an inspector call: structures of UGGT, the eukaryotic glycoprotein quality control checkpoint.

Related publication: Roversi P, Marti L, Caputo AT, Alonzi DS, Hill JC, Dent KC, Kumar A, Levasseur MD, Lia A, Waksman T, Basu S, Soto Albrecht Y, Qian K, McIvor JP, Lipp CB, Siliqi D, Vasiljevic S, Mohammed S, Lukacik P, Walsh MA, Santino A, Zitzmann N. Interdomain conformational flexibility underpins the activity of UGGT, the eukaryotic glycoprotein secretion checkpoint. *Proceedings of the National Academy of Sciences* **114(32),** 8544-8549, doi:10.1073/pnas.1703682114 (2017).

Publication keywords: UGGT; Endoplasmic reticulum; Glycoprotein folding; UDP-glucose:glycoprotein glucosyltransferase; Eukaryotic secretion

In all cells derived from animals, plants, fungi and protozoa a single protein called UGGT acts as a quality control checkpoint that inspects secreted glycoproteins. UGGT has fascinated scientists for many years as it has the capacity to check the quality of a huge array of glycoproteins, which come in many different shapes and sizes and folds. The way in which it screens such a diverse group of proteins is poorly understood, and no structures exist of UGGT. Furthermore, UGGT is implicated in human diseases as it can ensure that glycoproteins from viruses (such as influenza, hepatitis C, HIV and Zika) are folded correctly. By fully characterising UGGT, it is hoped that an inhibitor could be developed that may act as a broad-spectrum anti-viral drug.

Using the Macromolecular Crystallography (MX) beamlines (I02, I03, I04 and I04-1) and cryo-electron microscopy (cryo-EM) at the Electron Bio-Imaging Centre (eBIC), the structure of UGGT was solved. Four distinct crystal structures of a full-length UGGT revealed a novel seven domain fold, with four thioredoxin-like domains arranged in a long arc, which terminates in two β–sandwich domains that tightly clasp the catalytic domain. Together, the cryo-EM map, the crystal structures and the biochemical data suggested that UGGT is highly flexible, a feature which enables it to check such a wide variety of glycoproteins.

A wonderfully efficient protein folding machinery in the Endoplasmic Reticulum (ER) of eukaryotic cells ensures that only correctly folded glycoproteins can exit the ER and proceed to the Golgi, and from the Golgi continue along the secretory pathway towards their individual cellular or extracellular destinations.

The stringency of ER Quality Control (ERQC) – while of great advantage to healthy cells – can lead to severe disease in patients carrying certain mutant glycoproteins: the latter are detected as incorrectly folded, and either retained in the ER or degraded by ER-associated degradation (ERAD). The zeal of the otherwise excellent ERQC machinery bears particularly unfortunate consequences when the mutation affecting the glycoprotein is mild, i.e. it impairs but does not abrogate its function ('responsive mutant'). In these cases, ERQC blocks mutated competent glycoprotein secretion - and disease ensues.

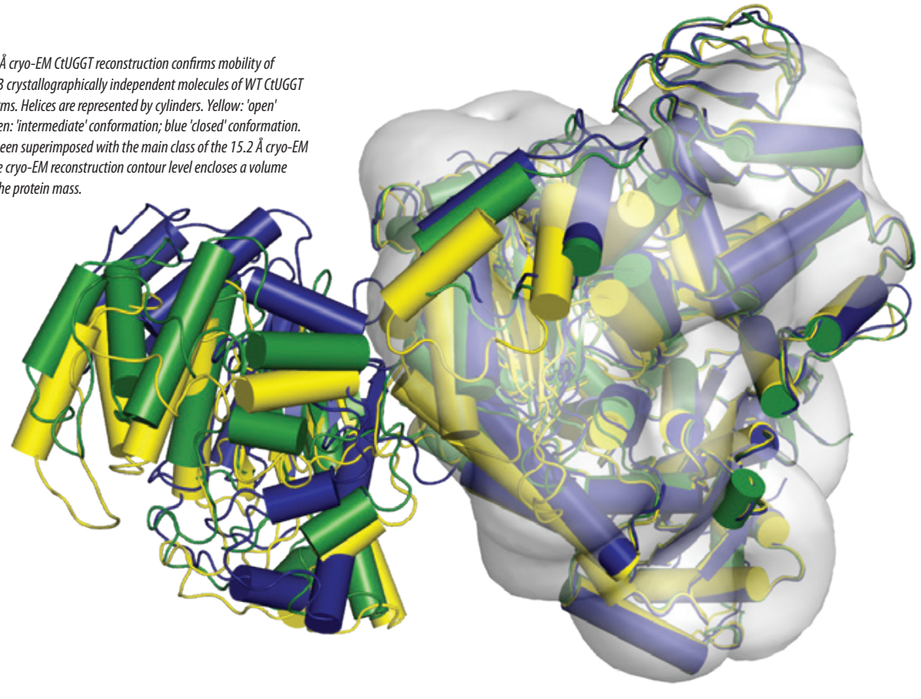

Figure 1: The 15.2 Å cryo-EM CtUGGT reconstruction confirms mobility of TRXL2. Overlay of 3 crystallographically independent molecules of WT CtUGGT across 3 crystal forms. Helices are represented by cylinders. Yellow: 'open' conformation; green: 'intermediate' conformation; blue 'closed' conformation. The models have been superimposed with the main class of the 15.2 Å cryo-EM reconstruction. The cryo-EM reconstruction contour level encloses a volume corresponding to the protein mass.

Figure 2: The 3D-printer generated CtUGGT model with its seven domains coloured TRXL1 (purple), TRXL2 (blue), TRXL3 (cyan), TRXL4 (green), βS1 (yellow), βS2 (orange) and GT (red). (a) a large, white LEGO glycoprotein; (b) a medium-size magenta LEGO glycoprotein; (c) a small, purple LEGO glycoprotein. Jelly babies at the end of a piece of string symbolise the Man9GlcNAc2 N-linked glycans on the glycoproteins. Disclaimer: the relative size of glycan to protein is not to scale.

In rare disease patients carrying responsive glycoprotein mutants, it is postulated that small molecule modulators of ERQC would rescue the secretion and residual activity of slightly misfolded and yet still active glycoproteins, thus alleviating pathogenic symptoms[1]. The fraction of responsive patients who could derive therapeutic benefit from ERQC modulation therapy depends on the disease, and varies between 70% in cystic fibrosis patients to 15-50% in lysosomal storage diseases[2].

A second important field of medicine in which ERQC modulation may be of therapeutic value is virology, with many enveloped viruses (e.g. flu, Hepatitis C, HIV, and a number of tropical viruses such as Zika and dengue) needing the help of ERQC in order for their glycoproteins to fold correctly, and for infectious viruses to be successfully secreted from an infected cell.

At the heart of ERQC is the glycoprotein folding quality control checkpoint, the enzyme UDP-glucose:glycoprotein glucosyltransferase (aka UGGT). The enzyme selectively re-glucosylates misfolded glycoproteins, promotes their association with ER lectins and associated chaperones and prevents premature secretion from the ER[3]. UGGT has long resisted structural determination and sequence-based domain boundary predictions. It is currently still a big mystery how the many UGGT substrate glycoproteins, each of which has a different size, shape and fold, can all be surveyed by UGGT alone.

Before our study, no full-length UGGT structures were known[4]; nor to this date are UGGT inhibitors known (other than its product UDP). The protein sequence of UGGT does not resemble any other in the eukaryotic genome, so any structural details about the enzyme could shed light on UGGT function and inform ongoing efforts to develop UGGT inhibitors. We set out to characterise UGGT both structurally (X-ray crystallography, SAXS, cryo-EM) and biochemically.

Our crystal structures of a full-length UGGT revealed a novel seven domain fold, with four thioredoxin-like (TRXL) domains arranged in a long arc, which terminates in two β–sandwiches tightly clasping the glucosyltransferase domain. The presence of TRXL domains in the N-terminal part of UGGT brings to mind bacterial periplasmic disulphide isomerases and eukaryotic ER luminal chaperones binding misfolded proteins and/or peptides[5].

Together with the 15 Å cryo-EM map, the same UGGT crystal structures reveal pronounced inter-domain flexibility (Fig. 1). Structure-based double cysteine point mutants that engineer extra inter-domain disulfide bridges, rigidify the UGGT structure and exhibit impaired activity. Thus, UGGT enzymatic activity depends on inter-domain conformational mobility, suggesting UGGT's intrinsic flexibility as a key requirement for the enzyme to be able to recognise and react with its many different misfolded substrates, flagging them for retention. By changing the relative orientations between its four TRXL domains, the enzyme could adapt its conformation to fit the particular glycoprotein it has bound and needs to re-glucosylate.

Structures of complexes of a UGGT with substrate misfolded glycoproteins would help verify these ideas, and we have started work towards biochemical purification and structural elucidation of such UGGT:misfolded glycoprotein complexes. In the meantime, in order to illustrate and communicate the novel hypothesis that the enzyme's flexibility may be necessary to enable substrate promiscuity, we have generated a 3D –printed molecular representation of CtUGGT, and assembled three distinct LEGO generic glycoproteins models, each of different size and shape, and bearing one jelly-baby 'glycan'. Figures 2a-c show the 3D-printer UGGT model in three arbitrary conformations, with the TRXL domains (coloured purple, blue, cyan and green) grabbing hold of the LEGO glycoproteins. The latter are oriented in such a way that the jelly-baby "glycan" is presented to the UGGT catalytic glucosyltransferase domain, coloured in red.

References:

1. Amara, J. F. *et al*. Intracellular protein trafficking defects in human disease. *Trends in Cell Biology* **2(5),** 145-149, doi:10.1016/0962-8924(92)90101-R (1992).
2. Parenti, G. *et al*. Pharmacological Chaperone Therapy: Preclinical Development, Clinical Translation, and Prospects for the Treatment of Lysosomal Storage Disorders. *Molecular Therapy* **23(7),** 1138-1148, doi: 10.1038/mt.2015.62 (2015).
3. Parodi, A. J. *et al*. UDP-Glucose: Glycoprotein Glucosyltransferase 1,2 (UGGT1,2). *Handbook of Glycosyltransferases and Related Genes, Springer* 15–30, doi:10.1007/978-4-431-54240-7_107 (2014).
4. Zhu, T. *et al*. Structural insight into substrate recognition by the endoplasmic reticulum folding-sensor enzyme: crystal structure of third thioredoxin-like domain of UDP-glucose:glycoprotein glucosyltransferase. *Scientific Reports* **4(7322)** doi: 10.1038/srep07322 (2014).
5. Kozlov, G. *et al*. A structural overview of the PDI family of proteins. *The FEBS Journal* **277**, 3924-3936, doi: 10.1111/j.1742-4658.2010.07793.x (2010).

Funding acknowledgement:

This work was supported by the Oxford Glycobiology Endowment. JH and ATC were supported by Wellcome Trust Structural Biology Studentships (numbers ?). Italian funding?

Corresponding authors: Dr Pietro Roversi and Prof Nicole Zitzmann, Oxford Glycobiology Institute, University of Oxford, pietro.roversi@bioch.ox.ac.uk, nicole.zitzmann@bioch.ox.ac.uk.

Structure of the surface layer surrounding *Caulobacter crescentus* bacteria

Related publication: Bharat TAM, Kureisaite-Ciziene D, Hardy GG, Yu EW, Devant JM, Hagen WJH, Brun YV, Briggs JAG, Löwe J. Structure of the hexagonal surface layer on Caulobacter crescentus cells. *Nature Microbiology* **2**, 17059, doi:10.1038/nmicrobiol.2017.59 (2017).

Publication keywords: Cryo-EM; X-ray crystallography; Tomography; Sub-tomogram averaging; Bacteria; S-layer

Many types of single-celled microorganisms such as bacteria are covered with a protective outer layer of proteins known as the S-layer. The S-layer defends the cell from the external environment and acts as a supportive scaffold. In fact for some species, the S-layer is the only component of the cell wall so its strong structure is paramount for protection.

The S-layer proteins are repeating units that fit together like chain mail to form the essential armour for the cells. Although these proteins have been previously imaged, their high resolution details have so far eluded scientists.

Two of the Macromolecular Crystallography beamlines (I03 and I04) were used to solve the crystal structure of the S-layer protein, RsaA, in a bacterium called *Caulobacter crescentus*. The X-ray structure was then combined with an electron cryotomography (cryo-ET) map garnered from living cells to determine the exact pattern of S-layer proteins on the surface of the bacterium.

The innovative combination of crystallography and cryo-ET in this study showed how the RsaA proteins coated and protected the bacteria, and also highlighted the small pores within the arrangement. This study demonstrates the merit in combining two techniques to explore a structure in living cells.

S-layer proteins (SLPs) are a diverse class of molecules found on many prokaryotes including Gram-positive and Gram-negative bacteria and the majority of archaea[1]. SLPs assemble to form planar sheets called S-layers on the surface of cells, where they are anchored, usually through non-covalent interactions with other surface molecules such as lipopolysaccharide [2]. The propensity of SLPs to form sheets in solution and their absence from early model organisms such as *Escherichia coli* have hampered high-resolution structural biological analysis of this abundant and important class of molecules[3]. We turned to *Caulobacter crescentus*, a well-studied Gram-negative alphaproteobacterium with a characteristic ultrastructure. The cells are completely covered with an S-layer that is continuous between the cell body and the stalk (Fig. 1a). Cryo-ET imaging showed that the density corresponding to the S-layer of *C. crescentus* CB15 is almost perfectly hexameric (Fig 1a, inset) with a ~220 Å repeat distance. Two discrete densities were observed in the S-layer, the outer highly connected S-layer lattice and the discrete inner domains located around the centres of the hexamers (Fig. 1b-c).

We purified the sole component of the *C. crescentus* CB15N (NA1000) S-layer, the ~98 kDa RsaA protein (Fig. 2a) directly from cells using a previously described [4] S-layer extraction procedure that employs low pH. It was confirmed that the purified protein retained its characteristic polymerisation function by reconstituting S-layers in solution at physiological pH (Fig. 2b). Using the purified material, the crystals of RsaA with Ca^{2+} or Sr^{2+} were obtained and determined a 2.7 Å X-ray structure (Figure 2C-D) using single anomalous diffraction (SAD) data collected at Diamond. RsaA amino acid residues 249-1026 were resolved in the resulting electron density map.

$RsaA_{249-1026}$ adopts a predominantly β-helical fold with ~30 right-handed turns (Figure 2C-D), forming an overall L-shape (Fig. 2c). In the crystals, the L-shaped monomers were arranged into hexamers that have a central pore with a size of ~20 Å (Fig. 2d). The N-termini of all six RsaA monomers point towards the central pore, while the C-termini are located on the outside of the hexamer. Although the space group of the crystal was $P2_1$, the unit cell is almost hexameric with an inter-hexameric spacing of ~215 Å. Intriguingly, this pseudo-hexameric repeat is close to the repeat observed in cellular S-layers in tomograms (Fig. 1).

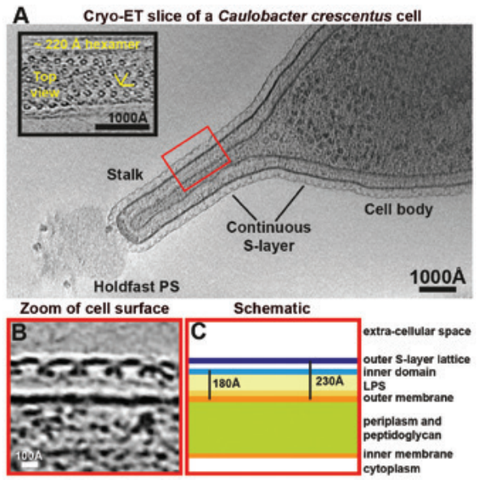

Figure 1: (a) A tomographic slice of a CB15 C. crescentus cell. The S-layer is continuous between the cell body and the stalk. Inset – a magnified tomographic slice of a top view of a stalk. A hexameric lattice with a ~220 Å spacing is seen. (b) A magnified tomographic slice of a side view of the cell surface. The S-layer is arranged in two layers and is seen ~180 Å away from the outer membrane of the cell. The outer S-layer lattice is highly inter-connected while the inner domains are ~220 Å apart. (c) A schematic representation of the cell surface.

All residues in the RsaA X-ray structure were well ordered, reflecting a requirement that the S-layer lattice and the RsaA protein must avoid flexible loops, as they would be easy targets for extra-cellular proteases (Fig 2c). Amino acid side chains buried inside the β-helix domain of RsaA are either hydrophobic, or are negatively charged and co-ordinated tightly to structural Ca^{2+} ions (Fig. 2c-d, grey spheres), with very few exceptions. Some Ca^{2+} ions are in close proximity to the central pore of the hexamer (Fig. 2d), where they appear to stabilise the hexameric interface.

To relate the RsaA X-ray structure to actual S-layers found on the surface of cells, the structure of the *C. crescentus* S-layer using electron cryotomography (cryo-ET) of cells was resolved and subsequent sub-tomogram averaging also. The final refined 7.4 Å structure allowed us to locate different domains of the S-layer in the map and identify secondary structure elements (Fig. 3a). The outer S-layer lattice is highly inter-connected and consists mainly of β-sheets while the inner domain is discrete.

We then docked the hexamer from the $RsaA_{249-1026}$ X-ray structure into the cryo-ET density map of the outer S-layer lattice as a rigid body. The docked atomic model shows that the lattices formed in the crystals through crystal packing and on cells are extremely similar and allows us to describe the arrangement of the S-layer lattice on cells at the atomic level (Fig. 3b-e). In the X-ray lattice, the hexameric interface contains amino acids bound to Ca^{2+} ions. We propose that Ca^{2+} ions bound near this interface are essential for the assembly of the RsaA hexamer. There is a strong dimeric interface and a less extensive trimeric contact is also observed in the lattice. Ca^{2+} ions are located near both the dimeric and trimeric interfaces in the lattice, possibly increasing the Ca^{2+} dependency of S-layer assembly.

The structures explain the modular architecture and function of RsaA, the permeability barrier and sieve function created by the S-layer and the strong Ca^{2+}-dependence of RsaA polymerisation since Ca^{2+} ions are tightly co-ordinated within the RsaA fold or bound near the hexameric, trimeric, and dimeric interfaces.

Guided by the S-layer structure reported above, *C. crescentus* cells carrying mutated versions of the *rsaA* gene may be used for surface display of molecules for nanotechnological or antigen display applications and it will be possible to investigate S-layer biogenesis and its morphological changes during the cell's life cycle at the molecular and atomic levels.

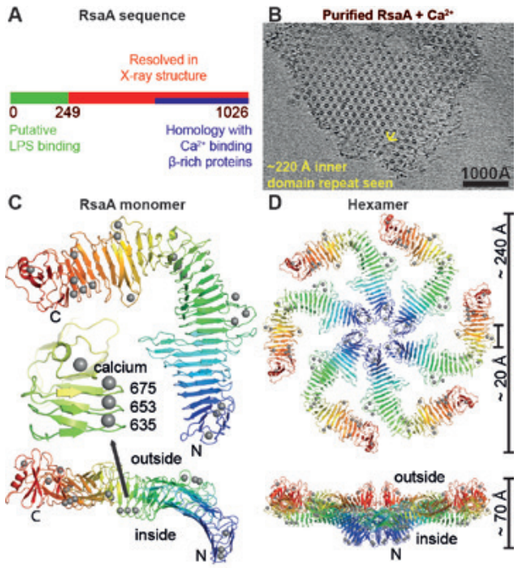

Figure 2: (a) Schematic diagram of the RsaA protein sequence. (b) On addition of Ca2+ ions to RsaA, 2D sheets were obtained with the same appearance and repeat as S-layers on cells. A cryo-ET slice through a reconstituted sheet. (c) One monomer of RsaA shown as a ribbon diagram, coloured as a rainbow, N- to C-terminus from blue to red. Ca2+ ions are shown as grey spheres. The inset shows a region around amino acid 653 where three tightly bound structural Ca2+ ions stabilise the fold. (d) Non-crystallographic hexamer of RsaA resolved in the X-ray structure, shown in two orthogonal orientations.

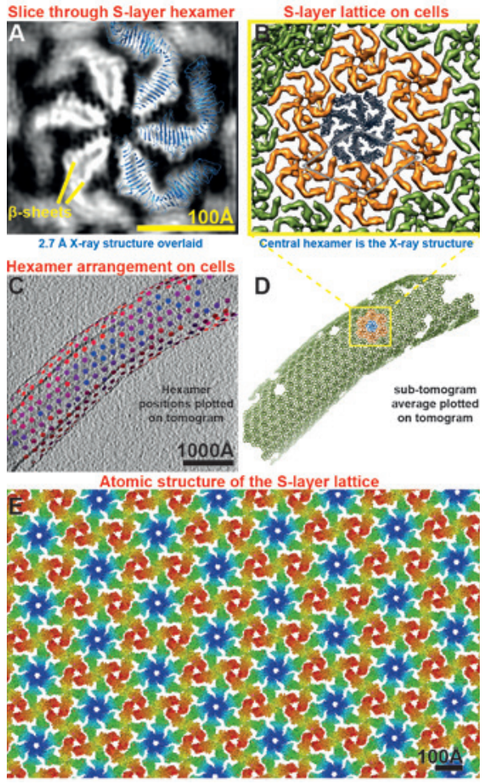

Figure 3: (a) A slice through the cryo-ET averaged density corresponding to the S-layer lattice. Three of the fitted RsaA proteins from the X-ray hexamer are overlaid (blue). (b) The S-layer lattice as seen on cell stalks. (c) Positions of all S-layer hexamers plotted on a cryo-ET tomogram of a cell stalk. (d) The sub-tomogram averages plotted on the same tomogram. (e) Atomic structure of the S-layer lattice from X-ray crystallography. The lattice seen in crystals and on cells from two completely orthogonal methods was the same. Each RsaA protein is coloured from blue to red from the N- to the C-terminus.

References:

1. Margit, S. *et al.* S-Layer proteins. *J Bacteriol* **182**, 859-868, (2000).
2. Fagan, R. P. *et al.* Biogenesis and functions of bacterial S-layers. *Nat Rev Microbiol*. **12**, 211-222, doi:10.1038/nrmicro3213 (2014).
3. Sleytr, U. B. *et al.* Bacterial S-layers. *Trends Microbiol* **7**, 253-260 (1999).
4. Nomellini, J. F. *et al.* Factors controlling in vitro recrystallization of the Caulobacter crescentus paracrystalline S-layer. *J Bacteriol* **179**, 6349-6354 (1997).

Funding acknowledgement:

Part of this work was funded by the European Molecular Biology Organization (aALTF 778-2015 to TAMB), the Medical Research Council (U105184326 to JL), the Wellcome Trust (095514/Z/11/Z) to JL. This work has been supported by iNEXT, project number 1482, funded by the Horizon 2020 program of the European Union.

Corresponding authors: Dr Jan Löwe, MRC Laboratory of Molecular Biology, jyl@mrc-lmb.cam.ac.uk

Dr Tanmay Bharat, University of Oxford, tanmay.bharat@path.ox.ac.uk

Structural insights into the mechanism of bacterial ABC transporters

Related publication: Bountra K, Hagelueken G, Choudhury HG, Corradi V, El Omari K, Wagner A, Mathavan I, Zirah S, Wahlgren WY, Tieleman DP, Schiemann O, Rebuffat S, Beis K. Structural basis for antibacterial peptide self-immunity by the bacterial ABC transporter McjD. *The EMBO Journal* **36**, 3062-3079, doi: 10.15252/embj.201797278 (2017).

Publication keywords: ABC transporter; Antibacterial peptide export; ATP-vanadate; Long-wavelength; Anomalous difference

Bacteria utilise ATP-binding cassette (ABC) transporters to import nutrients and detoxify themselves. These transporters have been shown to exist in wide open conformations that permit the access of many substrates in the binding pocket. They alternate between an inward-open to an outward-open conformation much like a gate. One such ABC transporter, McjD, was previously characterised and it was found to adopt a novel conformation that was distinct from others of its class.

In this study, McjD was trapped in two different conformations to provide further insights into its mechanism of action. Two of Diamond's Macromolecular Crystallography (MX) beamlines, I23 and I04-1, were used to solve the structure of it both in the absence of a substrate or ATP and with just ADP-vanadate, where I23 is the Long Wavelength MX beamline. Biochemical and biophysical measurements were also collected to complete the picture.

The structures showed that the transporter remained in an occluded conformation in the absence or presence of ATP/ADP. Additionally, the biochemical data showed that the transporter opened transiently to allow the release of its substrates from the binding pocket. This is the first time such a mechanism has been proposed for ABC transporters and it is thought to be the root of its substrate specificity. By understanding how McjD works, it might be possible to understand how other ABC transporters acquire multi-drug resistance in bacteria.

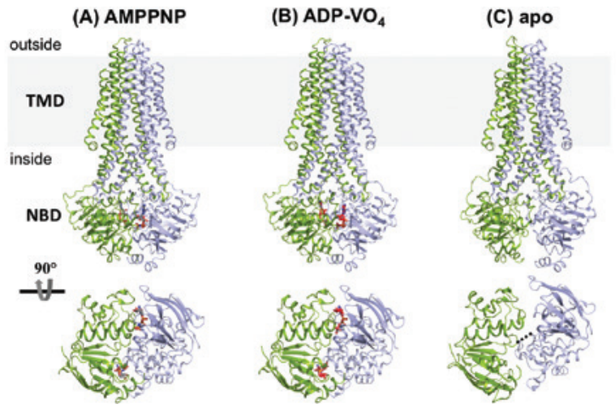

Figure 1: Crystal structures of McjD in distinct conformations. McjD is shown in cartoon and nucleotides in red sticks. Each half transporter is coloured in blue and green. Top panel is a view along the plane of the membrane and bottom panel shows the NBDs for each state. The membrane is depicted in grey. (a) AMPPNP bound outward-occluded conformation, (b) high-energy transition outward-occluded conformation (ADP-VO4) and (c) apo inward-occluded.

Bacteria, under nutrient starvation, produce and release antibacterial peptides, microcins, which can kill microcin-sensitive cells and therefore provide more nutrients for the surviving bacteria. These microcins are also toxic and lethal to the producing organism that utilise dedicated ATP-binding cassette (ABC) transporters (exporters) to provide them with self-immunity. ABC transporters are one of the largest superfamilies of membrane transporters and are found in both bacteria and eukaryotes. Many ABC exporters can confer multidrug resistance in bacteria and eukaryotic cells. ABC transporters require the binding and hydrolysis of ATP for energisation. ABC exporters exist either as homodimers or heterodimers; their core architecture is composed of a dimeric transmembrane domain (TMD) of twelve transmembrane (TM) helices, which forms the translocation pathway across the membrane bilayer and contains the ligand binding site, and a dimeric nucleotide binding domain (NBD) where ATP binds and is hydrolysed[1]. ABC exporters use the alternating access mechanism switching between inward- and outward-facing states, which exposes the ligand binding site alternatively to the inside or outside of the membrane, coupled to ATP binding and hydrolysis[1].

Previously functionally characterised and the high-resolution structure of the antibacterial peptide McjD from *E. coli* [2] that exports the lasso peptide Microcin J25 (MccJ25) (Fig. 1) was determined. The previous structure of McjD was determined in a nucleotide-bound (in the form of adenosine 5′-(β,γ-imido) triphosphate (AMPPNP), a non-hydrolysable ATP analogue) outward-occluded conformation (occluded at both sides of the membrane), representing an intermediate state between the outward- and the inward-facing conformations[2]. In order to understand the detailed mechanism of antibacterial peptide export by bacterial cells, it is important to trap the transporter in different conformations. In this study, the structure of McjD in a novel conformation, apo inward-occluded, and an additional nucleotide-bound state, high-energy outward-occluded intermediate with bound ATP-vanadate (ADP-VO_4) was determined.

The structure of McjD in the absence of nucleotides, apo form, 4.7 Å resolution

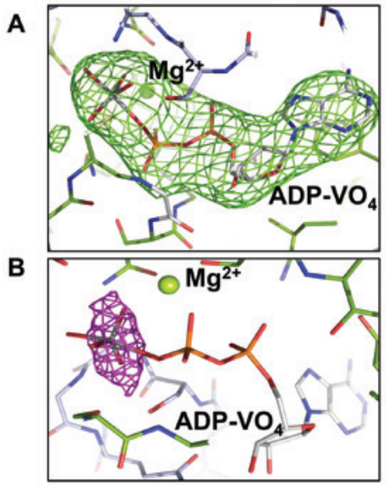

Figure 2: Electron density maps. (A) Clear |Fo|-|Fc| electron density map (green mesh contoured at 3 s) could be observed around the ADV-VO_4 molecule after molecular replacement. ADV-VO_4 is only shown for clarity but it was not included in the refinement. (B) Anomalous difference electron density map (pink mesh) around the vanadate, from data collected close to the vanadium edge, 2.26 Å. The map is contoured at 10α. McjD and ADV-VO_4 are shown as sticks. The magnesium ion is shown as green sphere. The ADV-VO_4 carbons are coloured grey, oxygens red, phosphate orange and vanadate dark grey.

(Diamond Light Source, beamline I04-1) (Fig. 1)[3] was determined. In the absence of nucleotides, ABC transporters adopt an inward conformation with their TMDs separated and NBDs disengaged[4] (Fig. 2b). Comparison between McjD-apo and other apo ABC exporters, such as MsbA[4], revealed that its TMD is in an occluded conformation, similar to the McjD-AMPPNP structure, whereas the NBDs have disengaged in the absence of nucleotides. This conformation is called here apo inward-occluded. Inward-facing ABC exporters display domain intertwining of TMs 1-3 and 6 from one subunit and TMs 4-5 from the opposite subunit, which results in opening of the TMD to the cytoplasmic side of the inner membrane. In the inward-occluded McjD, TMs 3-5 from one subunit have moved towards the equivalent TMs of the opposite subunit, resulting in the loss of intertwining and occlusion of the cytoplasmic opening. In the absence of nucleotides, the NBDs of ABC exporters disengage[4]. The NBDs of the McjD-apo have separated by 7.9 Å relative to the McjD-AMPPNP structure, a distance much shorter compared to MsbA-apo with a distance of 35 Å[4]. The NBDs have moved in a 'scissors-like' motion.

Its structure in the presence of the transition state analogue ADP-VO_4 (mimic of ATP hydrolysis) at 3.4 Å resolution (Diamond Light Source, beamline I23) (Fig. 1)[3] was also determined. Clear electron density was observed for ADP-VO_4 and Mg^{2+}. Since the ADP-vanadate crystals were prepared by reacting ATP with vanadate and then setting up crystal trials, we wanted to confirm the presence of vanadate in the structure, especially of the medium resolution of the data. In order to verify the presence of vanadate, data were collected close to the vanadium K-edge, 2.26 Å wavelength using the long wavelength beamline I23. The anomalous difference electron density maps (Fig. 2) were calculated. At both NBDs, two strong electron density peaks of 14 and 20 σ, respectively, confirmed the presence of two VO_4 groups. Due to the medium resolution of the data, the anomalous difference maps were used to place the VO_4. McjD-ADP-VO_4 is almost identical to the McjD-AMPPNP, as the two structures can be superimposed with a root-mean-square deviation (rmsd) of 0.7 Å over 560 Cα atoms. In contrast to the MsbA-ADP-VO_4 structure that adopts an outward-open conformation as a result of domain intertwining[4], the McjD-ADP-VO_4 structure is outward-occluded without domain intertwining (Fig. 2a). We call it here high-energy intermediate outward-occluded. The TMD dimer interface in McjD-ADP-VO_4 is formed between TM2 and TM5/TM6 from one subunit with the equivalent TMs from the opposite

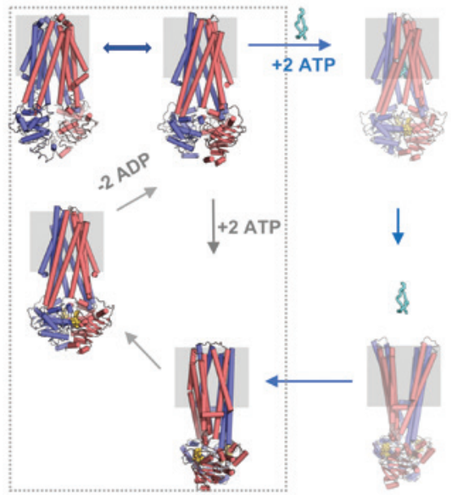

Figure 3: Mechanism of antibacterial peptide export by McjD. McjD is shown in red and blue cartoons. The membrane is depicted in grey box. The nucleotides are shown as yellow spheres and MccJ25 as cyan ribbon. The transient states are shown in light colour. The inward- and outward-open conformations of McjD are based on MsbA and Sav1866 structures.

subunit similar to the McjD-AMPPNP structure. In the presence of ADP-VO_4 the NBDs are dimerised. The McjD-ADP-VO_4 structure represents the transition state of a water molecule making a nucleophilic attack on the γ-phosphate of ATP.

In light of the new structures, biochemical and biophysical measurements, we are able to provide a detailed mechanism for antibacterial peptide export by ABC transporters [3]. In the absence of nucleotides and substrate, McjD adopts an inward-occluded conformation that is sealed at both ends of the membrane and with the NBDs disengaged. Binding of ATP alone results in the dimerisation of the NBDs and formation of the nucleotide bound outward-occluded conformation that does not induce conformational changes along the TMD. Futile ATP hydrolysis (in the absence of substrate) results in the restoration of the inward occluded conformation that progresses via a high-energy transition state. While cells produce MccJ25, McjD is capable to sample an inward-open conformation for MccJ25 to enter the cavity. Binding of ATP results in a transient outward-occluded conformation that is quickly followed by a transient/short-lived outward-open conformation that allows the release of the MccJ25 from the cavity. Release of the substrate results in the outward-occluded conformation. Finally, ATP hydrolysis resets the transporter to an inward conformation to transport another MccJ25 molecule (Fig. 3).

References:

1. Beis, K. Structural basis for the mechanism of ABC transporters. *Biochemical Society Transactions* **43(5),** 889-893, doi:10.1042/BST20150047 (2015).
2. Choudhury, H. G. *et al.* Structure of an antibacterial peptide ATP-binding cassette transporter in a novel outward occluded state. *PNAS* **111(25)**, 9145-9150, doi:10.1073/pnas.1320506111 (2014).
3. Bountra, K. *et al*. Structural basis for antibacterial peptide self-immunity by the bacterial ABC transporter McjD. *The EMBO Journal* **36**, 3062-3079, doi:10.15252/embj.201797278 (2017).
4. Ward A. *et al*. Flexibility in the ABC transporter MsbA: Alternating access with a twist. *PNAS* **104(48)**, 19005-19010, doi:10.1073/pnas.0709388104 (2007).

Funding acknowledgement:

This work was supported by the Medical Research Council (MR/N020103/1 to K.B.)

Corresponding author: Dr Konstantinos Beis, Imperial College London, kbeis@imperial.ac.uk

Sweet Success: Crystal structure of the full-length GLP-1 receptor bound to a peptide agonist

Related publication: Jazayeri A, Rappas M, Brown AJH, Kean J, Errey JC, Robertson NJ, Fiez-Vandal C, Andrews SP, Congreve M, Bortolato A, Mason JS, Baig AH, Teobald I, Doré AS, Weir M, Cooke RM, Marshall FH. Crystal structure of the GLP-1 receptor bound to a peptide agonist. *Nature* **546**, 254-258, doi: 10.1038/nature22800 (2017).

Publication keywords: X-ray crystallography; G protein-coupled receptors

Glucagon-like peptide 1 (GLP-1) is an important hormone released from the gastrointestinal tract in response to food intake. Through its interaction with its binding partner, the glucagon-like peptide 1 receptor (GLP1R), GLP-1 promotes the release of insulin from the pancreas to regulate blood sugar. As a consequence, the stimulation of GLP1R is considered an attractive means of treating type 2 diabetes.

GLP-1 peptide analogues are effective in treating type 2 diabetes, but despite there being several medically approved variants on the market, they are expensive to produce and are administered by injection. Alternatives, such as small molecules or smaller peptides that could be taken orally would significantly simplify the treatment regimen for people with type 2 diabetes.

To design such small molecules, a detailed map of the interactions between GLP-1 and its receptor was needed. To obtain that information, the crystal structure of a truncated stabilised GLP-1 analogue bound to the receptor was solved using the Macromolecular Crystallography (MX) Microfocus beamline (I24). The structure revealed that the GLP-1 analogue adopted a very specific conformation and reached deep into the receptor's binding pocket. It made numerous interactions with the receptor, the details of which enabled the design of a new GLP-1 analogues that were active in a mouse model of diabetes. These new smaller analogues could be the precursors of future diabetes treatments.

G protein-coupled receptors (GPCRs) are cell surface transmembrane receptors that transmit extracellular signals into intracellular signalling cascades. They are delicate molecular rheostats adopting multiple conformational states in response to specific hormonal and metabolic stimuli. One subfamily of GPCRs is the multi-domain class B secretin-like family, members of which are characterised by an extracellular domain (ECD) that binds peptide hormones juxtaposed to a transmembrane domain (TMD), and are validated drug targets for numerous diseases including osteoporosis, depression and anxiety and type 2 diabetes.

GPCRs' inherent flexibility, which is integral to their function, is the cause of their extreme instability when they are extracted from their native cell membrane environment. To obtain an X-ray structure of GLP1R the receptor had to first be thermostabilised using a radiolabelled truncated and modified version of the GLP-1 agonist peptide. The final thermostabilised (StaR) GLP1R contains eleven thermostabilising amino-acid mutations, which facilitated expression and purification of the receptor and trapped it in an active conformation. Peptide 5 was designed in-house and despite being just a third of the size of native GLP-1, activates the receptor with comparable efficiency.

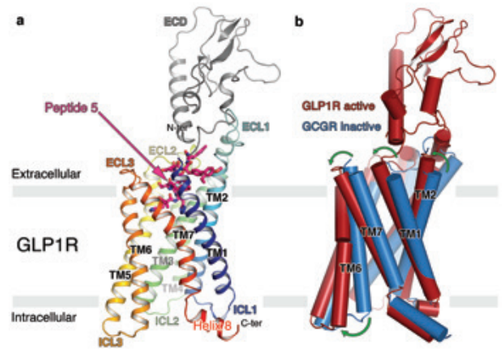

Figure 1: Structure of GLP1R in complex with Peptide 5 and conformational changes occurring upon peptide binding; (a) ribbon representation of GLP1R (TMD rainbow coloured from N- to C-terminus; ECD coloured grey), as viewed from a plane parallel to the membrane. Peptide 5 is shown in stick representation with carbon, nitrogen and oxygen atoms coloured purple, blue and red respectively; (b) superposition of Peptide 5-bound GLP1R (red) onto antagonist bound GCGR (blue; PDB ID: 5EE7). Green arrows depict the changes in TM positions.

Co-crystals of GLP1R in complex with a high affinity truncated peptide agonist (Peptide 5) were grown using the vapour diffusion method. The 100 x 40 x 20 μm rod shape crystals were cryo-cooled in liquid nitrogen and mounted for data collection. Using the raster scanning capabilities at Diamond's Microfocus Macromolecular Crystallography beamline (I24) together with an attenuated X-ray beam, the best diffracting parts in single crystals could be rapidly located without damaging them and then collected approximately 12° of diffraction images at each of these locations with higher transmission. The 96-well crystallisation plate mounting facilities at I24 were also used to diffract crystals *in situ* and so efficiently tested crystals grown in the presence of various additives in search of better diffraction. Due to the onset of radiation damage from the high intensity X-ray beam on the inherently fragile membrane protein crystals, data from eight crystals were merged together to obtain a complete dataset to 3.7 Å resolution. The structure was solved by molecular replacement using the glucagon receptor[1] (PDB ID: 5EE7) and GLP1R ECD[2] (PDB ID: 3IOL) as independent search models. GLP1R adopts an elongated conformation with the ECD extending away from the TMD (Fig. 1a). The TMD exhibits the canonical seven transmembrane helices (TM1-TM7) in a similar arrangement to previously published structures of class B GPCRs[1,3] (Fig. 1 and Fig. 2). All intra- and extracellular loops (ICLs and ECLs) were resolved in the electron density map and could therefore be modelled. ECL1 adopts an alpha helical conformation and ECL2 is tethered to TM3 through a disulphide bond. Additional electron density for an α-helix was observed in the intra-helical cavity of GLP1R and Peptide 5 was modelled into it with its N-terminus buried in the TMD and its C-terminus directed towards the ECD (Fig. 2 and Fig. 3).

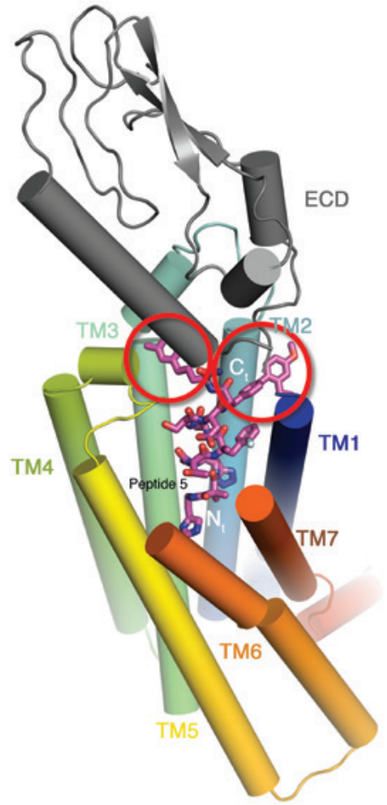

Figure 2: Peptide 5 interactions with GLP1R. Cylindrical representation of GLP1R (TMD rainbow coloured from N- to C-terminus; ECD coloured grey), as viewed from the extracellular space. Peptide 5 is shown in stick representation with carbon, nitrogen and oxygen atoms coloured purple, blue and red respectively. The N- and C-terminal extremities of Peptide 5 are highlighted in white and the C-terminal unnatural residues are circled in red.

The structure reveals which residues in GLP1R are key in Peptide 5 binding and agrees with a wealth of previously published mutagenesis data characterising the binding of GLP-1 to GLP1R[4]. The interaction surface between Peptide 5 and GLP1-R is extensive with the N-terminal natural and unnatural residues of Peptide 5 interacting mainly with residues in TMs 1, 2, 3 and 7 and the C-terminal unnatural residues lying in hydrophobic pockets formed between TM1 and TM2 and ECL1 and the ECD (Fig. 2). Despite being shorter than GLP-1 and interacting less extensively with the ECD, Peptide 5 still binds with very high affinity to GLP1R. The reason for retaining such high binding affinity is likely due to the hydrophobic interactions involving the C-terminus of the peptide. These Peptide 5-specific interactions are also responsible for orienting the ECD differently than when bound to GLP-1[4] (Fig. 2).

Comparison of the Peptide 5-bound GLP1R structure to that of another class B GPCR, GCGR, bound to an antagonist molecule (Fig. 1b; PDB ID: 5EE7) reveals changes in the positions of the extracellular portions of TM1, TM2, TM3 and TM7 and the entirety of TM6 which swings away from the central axis of the TMD. Similar changes have been observed when comparing agonist- (active) and antagonist- (inactive) bound structures of class A GPCRs suggesting that the Peptide 5-bound GLP1R structure is more akin to an active conformation. This observation also indicates a common activation mechanism across class A and B GPCRs where specific and concerted movements of TMs lead to a substantial repositioning of TM6 and the consequent opening up of the intracellular surface of the receptor permitting docking of the G-protein trimer.

Diabetes and obesity are serious public health concerns which put great pressure on healthcare systems across the globe. Developing effective and affordable drugs to treat these conditions remains a pressing need. With the GLP1R structure in hand, the perceived historical lack of success in developing small molecules that adequately target and activate GLP1R can now be explained by the extent and complexity of interactions between hormone and receptor (Fig. 2). Guided by the structure, we have rationally designed a series of truncated peptide agonists (Fig. 3) with improved pharmacokinetic properties and important insulinotropic activity, as demonstrated through *in vivo* diabetic mouse models. Reducing the size of these peptides drops the manufacturing costs, making them more affordable and easier to administer. Increasing their half-life and bioavailability prolongs their activity and consequently reduces the frequency with which they need to be delivered. To conclude, this landmark structure not only aided the development of new peptide agonists against GLP1R but also concomitantly increased our understanding of the general mechanism of activation of the class B secretin group of GPCRs which includes many other important drug targets.

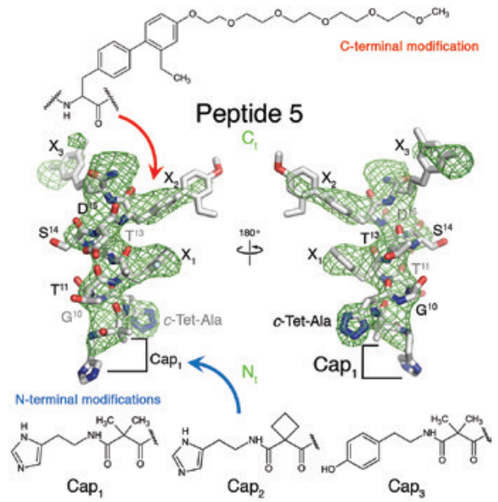

Figure 3: Details of Peptide 5 and its modifications. Peptide 5 is shown in stick representation with carbon, nitrogen and oxygen atoms coloured white, blue and red respectively. FoFc omit electron density map of Peptide 5 contoured at 2.5σ (green mesh). The N- and C-terminal structure-guided modifications are shown in two dimensional chemical representations and their positions highlighted by blue and red arrows respectively.

References:

1. Jazayeri, A. *et al.* Extra-helical binding site of a glucagon receptor antagonist. *Nature*, **533**, 274-277, doi:10.1038/nature17414 (2016).
2. Runge, S. *et al.* Crystal structure of the ligand-bound glucagon-like peptide-1 receptor extracellular domain. *J. Biol Chem.* **283**, 11340-7, doi:10.1074/jbc.M708740200 (2008).
3. Hollenstein, K. *et al.* Structure of class B GPCR corticotropin-releasing factor receptor 1. *Nature* **499**, 438-443, doi:10.1038/nature12357 (2013).
4. Wootten, D. *et al*. A Hydrogen-Bonded Polar Network in the Core of the Glucagon-Like Peptide-1 Receptor Is a Fulcrum for Biased Agonism: Lessons from Class B Crystal Structures. *Mol Pharmacol* **89**, 335-347, doi:10.1124/mol.115 (2015).

Funding acknowledgement: Funded solely by Heptares Therapeutics Ltd.

Corresponding authors: Dr Mathieu Rappas, Heptares Therapeutics Ltd., mathieu.rappas@heptares.com, Dr Andrew S Doré, Heptares Therapeutics Ltd., andy.dore@heptares.com

Membrane Protein Laboratory (MPL)

Andrew Quigley, MPL Facilities Coordinator

The Membrane Protein Laboratory (MPL) is a well-established, state-of-the-art facility that provides a pipeline from protein production to high throughput protein crystallisation. The MPL was the world's first membrane protein laboratory to be based inside a synchrotron, and its close proximity to the beamlines allows MPL staff and users to collaborate closely with beamline staff, creating a highly productive working environment.

The MPL was established to assist researchers investigating proteins that are embedded in the membranes that coat thousands of cells in the body. These proteins make up around 30% of the human genome. We have over 7,000 membrane proteins in our bodies and many of these are important drug targets; over 50% of current commercially available drugs target membrane proteins.

Crystallising membrane proteins is an essential, and extremely difficult step towards solving their structure. Having a dedicated laboratory with cutting edge equipment, close to the experimental stations where membrane protein structures can be solved, greatly enhances scientists' ability to successfully crystallise membrane proteins and further our understanding of these important drug targets.

The MPL is open to user applications from anywhere in the world, and proteins crystallised here have been used in experiments in other facilities. A forthcoming paper will describe the successful XFEL data collection at SACLA-Japan from the MPL team, Diamond (I24 and XFEL team) and Oxford collaborators (Department of Biochemistry).

Recently published work[1] details a collaboration between Brazilian scientists and the MPL, which investigated the role that two mitochondrial pyruvate carrier subunits, MPC1 and MPC2, play in the active transport of glycolytic pyruvate across the inner mitochondrial membrane. Diseases such as cancer, Alzheimer's disease, and diabetes are known to be pyruvate-related, and a greater understanding of these membrane proteins will aid in the development of treatments for these diseases.

Research conducted elsewhere has proposed that MPC1 and MPC2 function together via the formation of an oligomeric structure. However, in this new work researchers provided an unprecedented *in vitro* demonstration that human MPC2 functions independently of MPC1 to induce pyruvate transport. They used synchrotron radiation circular dichroism (SRCD) analysis, on beamline B23, to investigate the secondary structure composition of human MPC2, and to gauge the conformational changes due to binding of substrate and inhibitor. The significant changes in the secondary structure content of MPC2 that they detected support the interaction between the protein and ligands.

These results are the first successful, large-scale, recombinant production and functional reconstitution of this family of solute carriers in an artificial lipid bilayer. It opens up a discussion concerning pyruvate import regulation by at least two different molecular entities in human mitochondria: heterotypic MPC1:MPC2 and homotypic MPC2:MPC2, and has immediate implications for the development of small-molecule-oriented therapeutics that specifically target MPC2 in pyruvate-related diseases.

Over the last decade, data collection and data processing landscape in X-ray crystallography for biomolecules has changed significantly. Improvements include faster readouts from silicon pixel detectors, ubiquitous presence of robotic arms and related cryogenics, new types of set-up for single and multiple crystal mounting, fast data transfer and larger capacity for data storage, new processing software and continued introduction and update of process pipelines. One consequence of these changes is the ability to create complete datasets from several crystals, rather than a single crystal.

Also in collaboration with the MPL research published in the journal *Crystals*[2], discusses how the use of multiple crystals has become an accepted methodology in structural biology, with synchrotrons installing technology, hardware and software to make the technique routinely accessible to users. Diamond's automated VMXi beamline is a prime example; handling large numbers of crystals for data collection is also the standard mode of operation for free-electrons laser sources. The article describes how to use the computer program *BLEND* to help assemble complete datasets for the solution of macromolecular structures derived from data collection from multiple crystals.

1. Nagampalli RSK *et al*. doi:10.1038/s41598-018-21740-z

2. Mylona A *et al.* doi:10.3390/cryst7080242

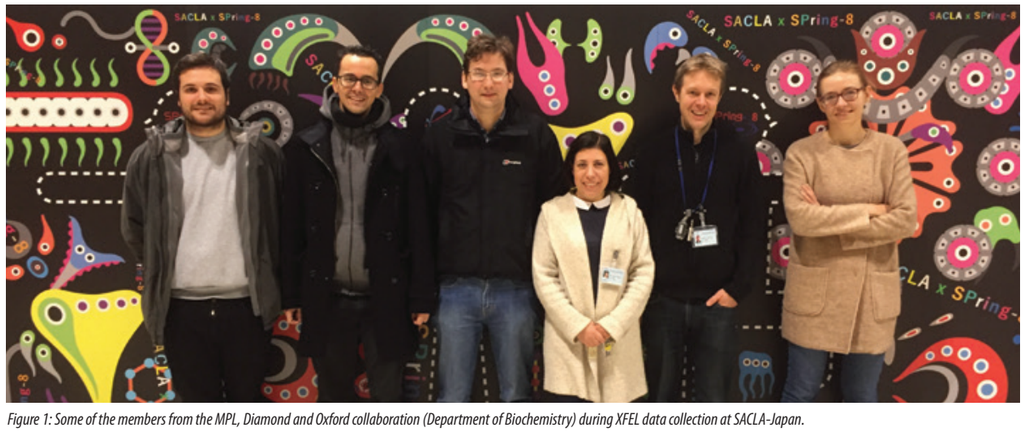

Figure 1: Some of the members from the MPL, Diamond and Oxford collaboration (Department of Biochemistry) during XFEL data collection at SACLA-Japan.

XFEL Hub at Diamond

Allen Orville, XFEL Hub Group Leader

The XFEL Hub at Diamond is funded by the Wellcome Trust and the Biotechnology and Biological Research council (BBSRC) to provide expertise and support to the UK community engaged in XFEL-related research in the life sciences. This includes all aspects of various XFEL experiments from conception to beamtime proposals through sample preparations and testing, to XFEL data collection, analysis and publication.

Over the past year, members of the XFEL Hub have visited and/or conducted serial femtosecond crystallographic (SFX) and time-resolved SFX (tr-SFX) experiments at all five XFEL facilities: i) the Linac Coherent Light Source (LCLS) at SLAC National Accelerator Laboratory in Menlo Park, California, USA; ii) SPring-8 Angstrom Compact free electron LAser, (SACLA) in Hyogo, Japan; iii) the European XFEL in Schenefeld Germany; iv) The Pohang Accelerator Laboratory XFEL (PAL-XFEL) in Pohang Korea; and v) The Swiss FEL at the Paul Scherrer Institute in Villigen PSI Switzerland. Six out of eight, and eight out of 11 experiments conducted at either LCLS, SACLA or the European XFEL included UK research groups in 2017 and the first half of 2018, respectively. The XFEL Hub also provided travel awards to several UK research groups that were granted XFEL beamtime at these three facilities.

The XFEL Hub continues methods R&D to support on-demand acoustic sample delivery methods for SFX and tr-SFX. These complement fixed target strategies developed by the I24 and I23 teams at Diamond. We have also formed a new Beamtime Access Group (BAG) at Diamond titled, 'Dynamic Structural Biology at Diamond & XFELs', which emphasises serial data collection strategies at ambient temperature and pressure using slurries of microcrystals. The new BAG uses some of Diamond's MX beamlines I24, I04, and VMXi.

In autumn 2017, Dr Allen M. Orville, group leader of the XFEL Hub, participated in the first, and directed the third, set of user-assisted SFX commissioning experiments at the SPB/SFX instrument at the European XFEL. Following the wishes of the facility, both peer-reviewed proposals were open to the whole community, highly collaborative, and attracted more than one hundred interested scientists from around the world. The distribution lists for these early experiments span 18 time zones.

The European XFEL delivers X-ray pulses in a discontinuous train structure that repeats at 10 Hz and with a 'dark period' or 'idle time' between each train. For example, a 600 ms pulse train is followed by a 99.4 ms gap. The maximum intra-train repetition rate is 4.5 MHz with 2700 X-ray pulses per train, but it can also operate slower by integer divisions. During the user-assisted commissioning studies, the facility delivered 60 ms pulse trains at 10 Hz with an intra-train frequency of 1.1 MHz.

These characteristics require sample delivery methods that replenish samples very quickly and clear the debris from the interaction region. To this end, the teams used flow-focusing gas dynamic virtual nozzles operating at approximately 30 – 100 ms. These first results demonstrated that ground-state SFX structures collected in the MHz regime can produce high quality atomic structures of macromolecules. This suggests that when the European XFEL, detector speed, sample delivery, and data analysis is fully optimised for maximum rates, then one might expect complete SFX data sets to high resolution in approximately one minute.

During the 19 March 2018 ceremony at the UK embassy in Berlin, representatives for the UK government, the German federal government, and the European XFEL signed documents to bring the UK into the European XFEL Convention. The agreement stipulates that the UK will contribute about 2% annually to the operations budget as well as €26M to the construction costs of the facility. The Science and Technology Facilities Council (STFC) is a shareholder and will represent the interests of UK scientists and citizens in the European XFEL.

The XFEL Hub, through its membership in the SFX Consortium, is working to supply an on-demand droplet sample injector for the downstream interaction region of the SPB/SFX instrument. One of our goals is to support SFX and tr-SFX by delivering ~30 picolitre droplets of microcrystal slurries directly into and synchronized with the XFEL beam pulses. At the end of this year or early next year, we anticipate testing sample delivery at 10 kHz within each pulse train to yield a 60 Hz overall data collection rate. Longer-term goals include 100 kHz sample delivery within a pulse train, which will produce SFX data at 600 Hz overall. Although MHz sample delivery rates are likely to require fast jets, an advantage of on-demand acoustic methods is that they are more efficient with samples since none is wasted in the gap between the X-ray trains.

Structures and Surfaces Group

Chris Nicklin, Science Group Leader

The recent Science Division reorganisation has resulted in a rationalisation of the beamlines that were originally members of the Surfaces & Interfaces village. The new Structures and Surfaces Group consists of four beamlines, I05 (Angle Resolved Photoelectron Spectroscopy – ARPES), I07 (Surface and Interface X-ray Diffraction), B07 (Versatile Soft X-ray Scattering – VERSOX) and I09 (Surface and Interface Structural Analysis – SISA). There will be a much closer working relationship within this new structure, including more extensive internal collaborative research and improved offline facilities to serve the user community. The alignment has extended beyond just the science division and we are now able to work much more closely with engineering colleagues and software developers that are aligned with the new groups, leading to common solutions across the beamlines. Obvious overlap in the science programmes will be developed, such as Angle Resolved PhotoElectron Spectroscopy (ARPES) on I05, B07 and I09, who have also been offering hard X-ray Photoelectron Spectroscopy (HAXPES) for studying bulk electronic structures. Beamlines I07 and B07 will strengthen the programme in areas of non-ultrahigh vacuum (non-UHV) studies including catalysis and electrochemistry. The new structure will also encourage cross group developments and we expect strong interactions with the Magnetic Materials Group, Spectroscopy beamlines and the Soft Condensed Matter Group in a number of science areas such as energy materials or catalysis. The grouping will enhance our ability to work more closely with user groups, offering a comprehensive range of techniques to non-specialists that will aid understanding of their science problems.

The beamlines within the group continue to develop through a number of upgrade projects, both major and minor. VERSOX (B07) is in the process of bringing its second branch online, which will enable high throughput X-ray Photoelectron Spectroscopy (XPS) measurements on multiple samples and Near-edge Extended X-ray Absorption Fine Structure (NEXAFS) in a non-UHV environment. Together with the Near Ambient Pressure XPS experiments on the existing branch, this provides excellent opportunities to study the electronic and structural properties of different samples of relevance to a range of science areas including atmospheric chemistry, pharmaceuticals, catalysts or cultural heritage amongst others. Beamline I09 is adding new capabilities to its end station provision; a HAXPES system to enable studies of the electronic states of buried interfaces and a momentum microscope to produce images of the electron band structure directly in momentum space. Beamline I05 has two branches, one of which is the high resolution facility that has proven to be a very successful addition to the suite of beamlines, since it became operational in 2014. Many experiments make use of the *in situ* cleaving techniques to study novel crystal structures, whilst there is also a fully equipped molecular beam epitaxy (MBE) system attached to the end-station that can be used to produce samples *in situ*, as demonstrated by the successful growth of Gadolinium doped europium oxide (EuO) thin film structures. The Nano-ARPES branch has been attracting an increasing number of users that want to understand not only the electronic structure on a macroscopic scale but also to establish the real space distribution of those states. This is now possible with sub-micron resolution on the branchline and changes in the focussing optics aim to improve the resolution to less than 500 nm. Beamline I07 has been in a period of stable operation for the last few years; it is now in the process of upgrading its monochromator to a Diamond designed system. This will increase the stability of the photon beam, the first stage in improving the focusing optics to reduce the beam dimensions to a planned size of ~10 µm. Plans are also underway to upgrade the sample environments, in particular the UHV system for *in situ* MBE studies.

The diversity of the science programme is a strength of this group with studies ranging from the observation of novel electronic states in complex crystals to experiments on the structure of lipid layers at the air-liquid interface. This year's science highlights cover two specific areas from this broad range of applications, namely understanding the mechanism by which ozone reacts with organic molecules in seawater and two highlights on understanding materials related to spintronics. Jones *et al*, used I07 to highlight the unexpected result that rather than ozone attacking organic molecules at the surface of a water layer, it seems to produce radicals in the liquid that then affect the structure of the layer. This result will cause a rethink in understanding the mechanisms occurring in atmospheric chemistry and interactions in seawater. More conventional surface science studies were undertaken on I09, where Pincellii *et al* have demonstrated the role of dimensionality in affecting the electronic structure in important spintronic materials. Dilute magnetic semiconductor (GaMnAs) and strained strontium doped lanthanum manganite (LSMO) samples were studies by photoelectron spectroscopy (PES) at different energies, to establish the changes in electronic structure with depth by relating specific peaks to carrier mobility in the materials. ARPES measurements on beamline I05 by Sunko *et al*, studied the spin-orbit splitting in the layered oxide compounds $PtCoO_2$ and $PdCoO_2$ both terminated with CoO_2. The surprisingly large spin splitting is unexpected but can be explained by large inversion symmetry breaking related to the top surface layer. The CoO_2 layer has oxygen atoms above and below the Co atoms and it is the movement of electrons through these two different routes (caused by the different environment at the surface) that produces the large asymmetry.

The members of the Structures and Surfaces Group are committed to continuing the high quality scientific output from the beamlines, through enhanced interaction with our user community. Please contact us, if you would like to discuss any of the techniques or possible experiments and how the synchrotron studies could help in your research.

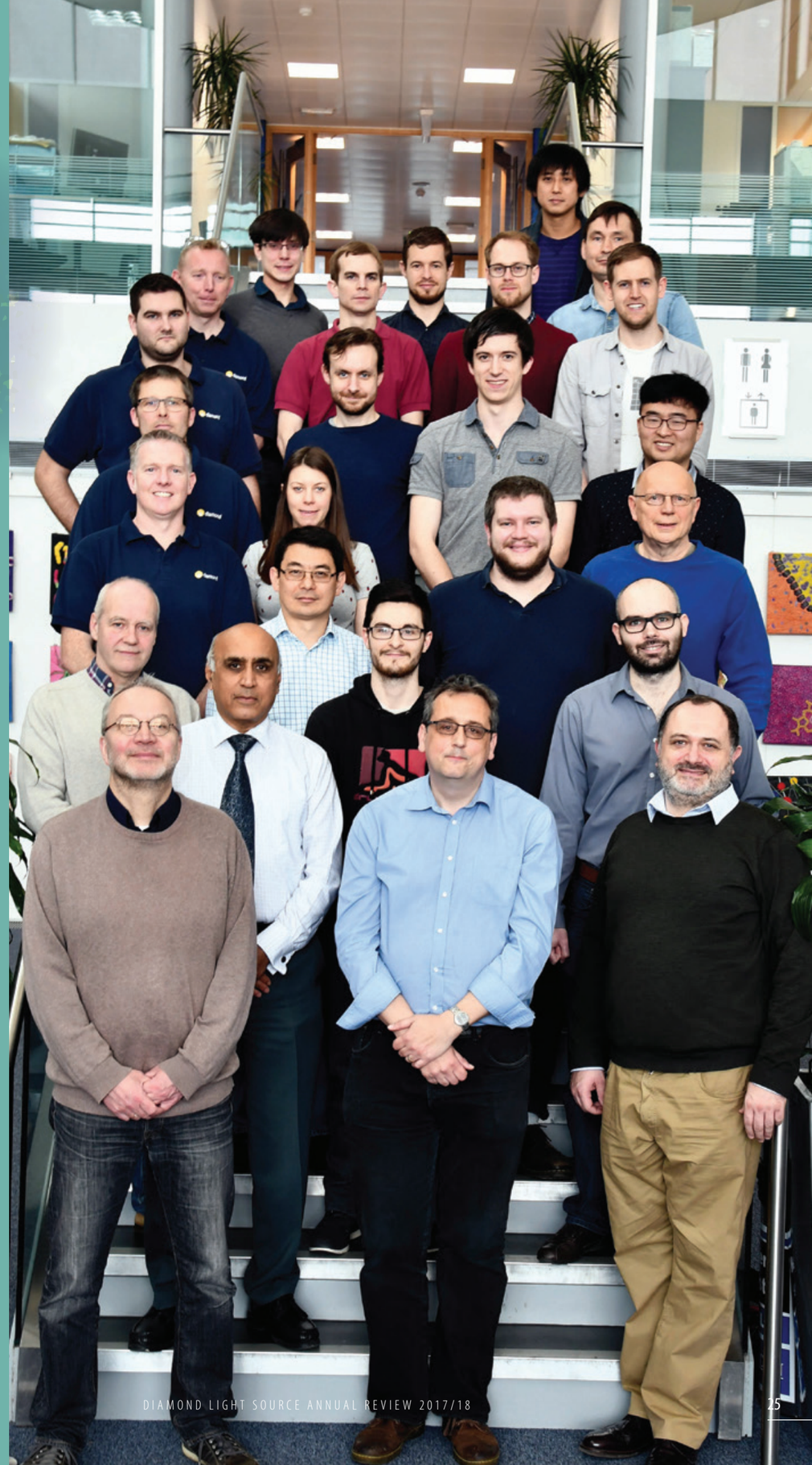

Figure 1: The scientists, engineers, technicians and PDRAs that make up the Structures and Surfaces Group.

Achieving maximal spin splitting at a crystal surface

Related publication: Sunko V, Rosner H, Kushwaha P, Khim S, Mazzola F, Bawden L, Clark OJ, Riley JM, Kasinathan D, Haverkort MW, Kim TK, Hoesch M, Fujii J, Vobornik I, Mackenzie AP, King PDC. Maximal Rashba-like spin splitting via kinetic- energy-coupled inversion-symmetry breaking. *Nature* **549**, 492–496, doi:10.1038/nature23898 (2017).

Publication keywords: Spin-orbit coupling; Rashba; Spin-splitting; Delafossite; ARPES

The surfaces of materials can host unique electronic properties, where the electrons behave very differently from the interior. All electrons possess a magnetic moment, their spin, but in most non-magnetic materials electrons with different spins behave in the same way. This may not be the case at surfaces, where a splitting of states of opposite spin may be observed. This leads to novel electronic phases, an interesting area of fundamental research but also for potential applications in spin-controlled devices. For spin-splitting to be useful in electronic devices, it is often necessary to maximise the size of the splitting.

Researchers from the University of St Andrews and the Max Planck Institute for Chemical Physics of Solids in Dresden investigated the origin of large spin-splitting on cobalt-based delafossite oxides. They used high-resolution angular resolved photoemission measurements on the dedicated beamline (I05), which has a small light spot, high flux and excellent manipulator control that makes it ideal for measurements on small samples.

Their results show that spin-splitting in delafossite oxides reaches as much as the full strength of the spin-orbit coupling of the relevant orbitals. This highly surprising result is a consequence of unusually strong symmetry breaking at the surface, enabled by the crystal structure. This insight could be used to design new materials exhibiting record-breaking spin-splitting.

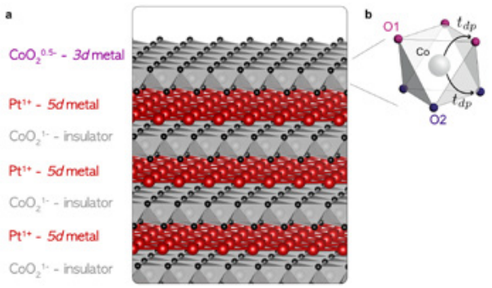

Figure 1: (a) Crystal structure of $PtCoO_2$. In the bulk, triangular Pt layers (red) are separated by insulating CoO_2 layers. If the CoO_2 layer is found on the surface it becomes effectively hole-doped and metallic. (b) One CoO_2 octahedron, a basic structural unit of the CoO_2 layer. At the surface the hopping path through the top oxygen (O1) is preferred, causing the large inversion symmetry breaking, and eventually the large spin-splitting.

Delafossites are layered oxide compounds of the general formula ABO_2, in which triangularly coordinated noble metal (A, A=Pt,Pd) layers are separated by transition metal oxide (BO_2, B=Co, Rh, Cr) blocks (Fig. 1a). The platinum and palladium based delafossite metals have a single, fast Pt/Pd based band crossing the Fermi level, and making a hexagonal Fermi surface. Their room temperature conductivities are among the highest of any metal, and higher per carrier than that of elemental copper[1]. Their low temperature mean free paths are extremely long, reaching as much as 20 μm (~10^5 lattice spacings) in as-grown $PdCoO_2$. The long mean free path has led to the observation of a number of anomalous transport properties, including hydrodynamic electron flow.

While this fascinating transport is taking place in the noble metal, the transition metal oxide layer of $PtCoO_2$ and $PdCoO_2$ is insulating. This is because the Co^{3+} is in the d^6 configuration, with the t_{2g}-like orbitals completely occupied and e_g-like orbitals empty. The bulk compound can thus be thought of as a natural heterostructure, with alternating metallic and insulating layers.

The natural layers make delafossites particularly suitable for the study of their surfaces, which can quite generally be expected to exhibit behaviour different to that of the bulk layers[2,3]. This is easy to see using a simple ionic picture to describe the charge of the layers; in the bulk each A ion donates half an electron to the oxygen below and half an electron to the oxygen above it. This obviously cannot take place at the surface; if the BO_2 layer is at the surface, this should become hole-doped with respect to the bulk layer, and could be expected to become metallic.

In this work, angle-resolved photoemission (ARPES) showed two Fermi surfaces arising from the CoO_2 terminated surfaces of $PtCoO_2$ and $PdCoO_2$, in addition to the bulk Fermi surface (Fig. 2a). Further spin-resolved ARPES measurement revealed the two surface Fermi surfaces to carry an in-plane chiral spin polarisation of opposite sign, similar to the well-known Rashba effect (Fig. 2b). While a combination of time-reversal symmetry and inversion symmetry ensure the spin degeneracy of electronic states, the natural breaking of inversion symmetry at every surface enables such a spin polarisation to develop.

The qualitative observation of the spin-split states on a surface is thus not unexpected, however the size of the splitting observed is surprising. To see this, one needs to compare the size of the splitting in the delafossites with other well-known systems. The splitting in momentum in the delafossite reaches as much as 0.13 $Å^{-1}$, comparable to 0.1 $Å^{-1}$ in BiTeI and 0.26 $Å^{-1}$ in Bi/Ag surface alloys[4]. Those are some of the largest momentum splittings known, and it is no accident they are typically found in bismuth containing compounds, as the atomic spin-orbit coupling (SOC) of bismuth 6p orbitals is as large as 1500 meV. The spin-orbit coupling of Co is only 70 meV, 20 times weaker! The observation of such large splitting in the delafossites is thus highly surprising, and requires further explanation.

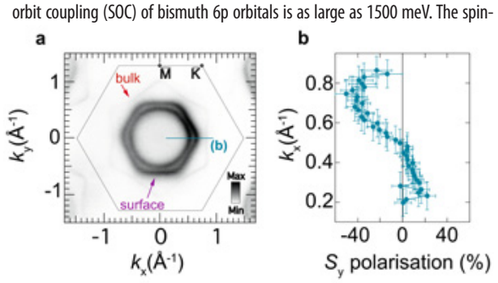

Figure 2: (a) Fermi surface of $PtCoO_2$, measured by angle resolved photoemission. In addition to the bulk Fermi surface, two concentric surface Fermi surfaces are clearly observed. (b) Expected value of spin polarisation in the y direction as a function of momentum in the x direction, measured along the line shown in (a). The measurement shows switching of spin polarisation between the two Fermi surfaces, indicating Rashba-like spin splitting.

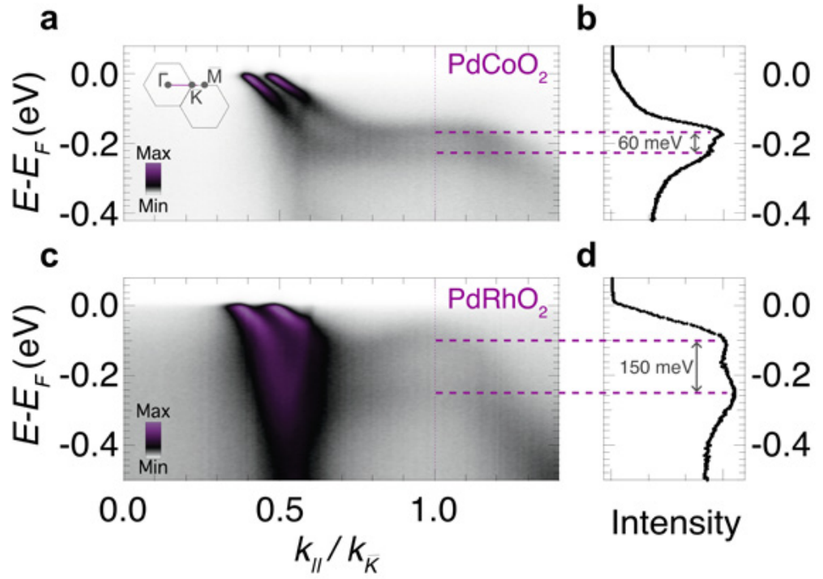

Figure 3: Spin-split surface states of $PdCoO_2$ (a) and $PdRhO_2$ (c), indicating a spin splitting that scales with the SOC strength of the B-site transition metal. The splitting retains the strength of the atomic SOC of the transition metal even as this strength is increased by a factor of approximately 2.5 on moving from Co to Rh. This is particularly evident from the spin splitting at the K point (dashed lines in a and c), which is clearly visible in the energy distribution curves shown in (b) and (d).

To understand the large splitting it is necessary to realise that the atomic spin-orbit coupling is not the only relevant energy scale; rather the size of the splitting is determined by the relative magnitude of the spin-orbit coupling and inversion symmetry breaking (ISB) energy scales, with the smaller scale limiting the splitting. In the vast majority of spin-split states the ISB scale is small, limiting the splitting to a moderate fraction of the atomic spin-orbit coupling. In delafossites the splitting at some points of the zone becomes comparable to the atomic spin-orbit coupling (Fig. 3), indicating that the inversion symmetry breaking energy scale is larger than the spin-orbit one, enabling the maximum possible spin splittings to be achieved. Understanding the mechanism of this symmetry breaking is highly relevant for design of future spintronic materials.

The key point is the structure of the top CoO_2 layer (Fig. 1b). Co electrons can hop from one Co to another either via the oxygen in the layer above (O1), or via the oxygen in the layer below (O2). In the bulk these two paths are equivalent, however the top oxygen has no noble metal above it. This causes an on-site energy shift between the two oxygens, and makes the hopping path through the surface oxygen much more likely. The inversion symmetry breaking is no longer a small perturbation of the dominant kinetic hamiltonian; rather the kinetic hamiltonian itself becomes asymmetric. This asymmetry of hopping integrals is estimated to be about 40%, or about 150 meV. This is more than twice the atomic spin-orbit coupling of cobalt, allowing the spin splitting to assume the full atomic spin-orbit coupling strength, as observed.

What is more, this kinetic mechanism of inversion symmetry breaking has a potential for achieving truly large spin splitting scales in compounds containing heavier ions with larger spin-orbit coupling. Usually increasing the atomic spin orbit coupling causes the splitting to be limited by the smaller inversion symmetry breaking scale, however the kinetic inversion symmetry breaking is proportional to the bandwitdh, and will also grow as heavier atoms with larger orbitals are used. This suggests a route to stay in the 'strong inversion symmetry breaking' limit even when the absolute size of spin orbit coupling is large. A proof that this is indeed possible is found by measuring the surface electronic structure of previously unstudied $PdRhO_2$. Similar surface states are observed to the cobalt-based compound, but the energetic spin splitting in the rhodate reaches a ~2.5 times larger value of 150 meV, a record for an oxide, reflecting the 2.5 times larger atomic spin-orbit coupling. This therefore confirms the kinetic energy-coupled inversion symmetry breaking mechanism.

To conclude, it has been shown here that a 'recipe' for achieving large spin-splitting is to use heavy elements with large atomic spin orbit coupling and large orbital overlaps in a structure where the preferred hopping paths are out of plane. Due to the loss of bonding at a surface such kinetic energy will become asymmetric, and introduce a large inversion symmetry breaking energy scale, allowing the full spin-orbit coupling energy to be utilised in spin-splitting surface states.

References:

1. Mackenzie, A. P. The properties of ultrapure delafossite metals. *Reports on Progress in Physics* **80(3),** doi: 10.1088/1361-6633/aa50e5 (2017).
2. Noh, H. J. *et al.* Anisotropic Electric Conductivity of Delafossite $PdCoO_2$ Studied by Angle-Resolved Photoemission Spectroscopy. *Physical Review Letters* **102**, 256404, doi: 10.1103/PhysRevLett.102.256404 (2009).
3. Mazzola, F. *et al.* Itinerant ferromagnetism of the Pd-terminated polar surface of PdCoO, arXiv:1710.05392 (2017).
4. Ishizaka, K. *et al.* Giant Rashba-type spin splitting in bulk BiTeI. *Nature Materials* **10**, 521–526, doi: 10.1038/NMAT3051 (2011).
5. Park, R. P. *et al.* Microscopic mechanism for the Rashba spin-band splitting: Perspective from formation of local orbital angular momentum. *Journal of Electron Spectroscopy and Related Phenomena* **201**, 6-17, doi: 10.1016/j.elspec.2014.12.009 (2015).

Funding acknowledgement:

The work was supported by the European Research Council (via the QUESTDO project), the UK Engineering and Physical Sciences Research Council, the Royal Society, the Max-Planck Society, and the International Max-Planck Partnership for Measurement and Observation at the Quantum Limit.

Corresponding author: Veronika Sunko, University of St Andrews & Max Planck Institute for Chemical Physics of Solids, vs61@st-andrews.ac.uk

Using X-rays to investigate cloud chemistry

Related publication: Jones SH, King MD, Ward AD, Rennie AR, Jones AC, Arnold T. Are organic films from atmospheric aerosol and sea water inert to oxidation by ozone at the air-water interface? *Atmospheric Environment* **161**, 274-287, doi:10.1016/j.atmosenv.2017.04.025 (2017).

Publication keywords: Atmospheric aerosol; Sea-water; Thin film; Heterogeneous oxidation; Ozone; OH radical; X-ray reflectivity

Aerosols – tiny particles in the air – are key to the formation of clouds, as all cloud droplets form when water droplets condense around aerosols. If the chemical properties of aerosols are modified, this can affect the size and number of droplets within a cloud, and hence how much light the cloud reflects and how much rain falls. A small chemical change can cause a climatic difference, and although this process has a significant effect on Earth's climate, it is not well understood.

A large number of aerosols are coated with a thin organic film. Previous studies of how these organic films react with atmospheric oxidants, such as ozone, have used proxy organic material. Researchers from Royal Holloway, University of London report the first X-ray reflectivity study of real samples of atmospheric aerosols, employing the unique capabilities of the Surface and Interface Diffraction beamline (I07) to capture information on the changes that occur when the samples are exposed to atmospheric oxidants.

Surprisingly, they found that the samples did not react with ozone, although they did react with hydroxyl radicals. This may indicate that aerosols in the atmosphere are less reactive than previously thought. The organic films tested were composed mainly of saturated material, indicating that future studies should concentrate on saturated materials, rather than the unsaturated proxies generally studied. Future studies will test samples from different environments, to investigate how their behaviour may differ.

Atmospheric aerosols critically affect the Earth's climate by directly scattering and absorbing solar radiation and indirectly through their involvement in cloud formation and their influence on cloud radiative properties[1]. Numerous aerosols are coated in a thin organic film, which affects their physical properties and therefore their contribution to the Earth's climate[2]. As the atmosphere is an oxidising medium, it is likely that an aerosol will be oxidised in its lifetime, which will also affect the physical properties of the aerosol such as its ability to uptake water and whether it will act as cloud condensation nuclei (CCN), the precursor to a cloud droplet. Therefore, it is important to study oxidation reactions of atmospheric aerosols coated in a thin film to better understand aerosol contribution to cloud formation and cloud radiative properties and thus the Earth's climate.

An X-ray reflectivity experiment was conducted on I07 at Diamond to study the oxidation of real organic films at the air-water interface with common atmospheric oxidants (gas-phase ozone and the aqueous phase radicals, hydroxyl and nitrate). The thickness and scattering length density of the film were monitored throughout the experiment using X-ray reflectivity. Scattering length density provides information on the chemical composition and amount of material present at the air-water interface. I07 was used because a good signal-to-noise ratio can be obtained up to high reflection angles and because of the availability of fast acquisition times.

Atmospheric aerosol samples were collected at Royal Holloway University of London using filter samplers and sampling cartridges. The site is close to central London and some of the UK's busiest motorways. The sampling cartridges contained coated denuders to remove ambient gaseous ozone to prevent the oxidation of the material collected on the filter prior to the oxidation experiment. Surface sea-water samples were collected at Milford-on-sea on the south coast of England using a long reach sampler. In all cases, organics were extracted and stored at -18°C until use.

X-ray reflectivity studies were performed on monolayer films of atmospheric or sea-water material at the air-water interface formed on a Langmuir trough. A custom trough was set up on an anti-vibration table on the I07 beamline and reflectivity of the film was monitored before and during addition of an oxidant. For experiments conducted using ozone as the oxidant, ozone was generated using an ozoniser and the trough was contained in a sealed chemically inert plastic bag. Kapton windows allowed X-rays to pass into the bag. For aqueous phase radical experiments, hydroxyl or nitrate radicals were generated in the aqueous subphase from photolysis of a precursor solution. UV lamps were located directly above the trough along its length to evenly illuminate the subphase.

X-rays were specularly reflected from the liquid surface onto a defined region of interest on a detector and the reflectivity of the film was measured as a function of momentum transfer of the X-rays perpendicular to the interface. The X-ray data was modelled using a simple parallel layer model consisting of the thin film located between two semi-infinite media (air and the liquid subphase) as shown in Figure 1.

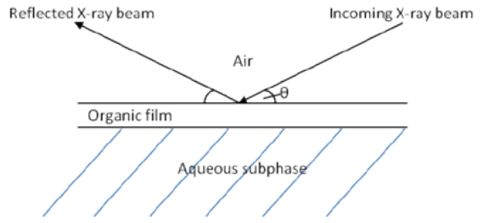

Figure 1: Model for an organic film at the air-water interface.

No reaction was observed between gas-phase ozone and a thin film of material extracted from atmospheric aerosol or sea-water. The amount of material at the air-water interface remained constant throughout the experiment. Owing to this surprising result, a thin film of material extracted from atmospheric aerosol was exposed to the aqueous phase hydroxyl radical and a reaction was observed. Figure 2 shows the reflectivity profile for the reaction, the reflectivity increases as shown by the direction of the arrow as time proceeds indicating a reaction. The X-ray data was modelled[3] (Fig. 3), and a clear decrease in scattering length density and film thickness was observed in comparison to the constant values observed when atmospheric film material was exposed to gas-phase ozone.

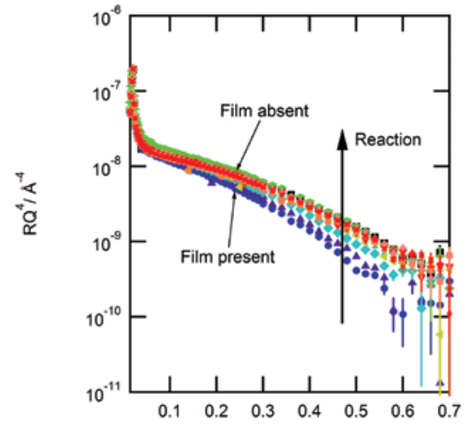

Figure 2: X-ray reflectivity profile for a monolayer of atmospheric film material exposed to the aqueous phase hydroxyl radical.

As a reaction was observed with the aqueous phase hydroxyl radical and no reaction was observed with gas-phase ozone, it suggests that the organic film material in both atmospheric and sea-water samples contains a lack of unsaturated material. Unsaturated material contains double bonds which ozone would cleave resulting in the formation of smaller molecules that would either partition to the gaseous or aqueous phase resulting in a decrease in the amount of material at the air-water interface. Aqueous radicals react by abstraction of a hydrogen atom and can therefore react with material that contains no double bonds. Similarly no reaction was observed between sea-water film material and gas-phase ozone, however, a reaction was observed (decrease in the amount of material at the air-water interface) between sea-water film material and the aqueous phase nitrate radical.

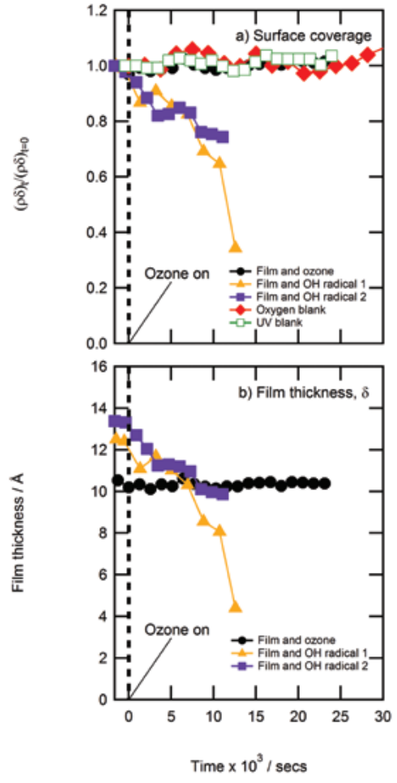

Figure 3: (a) the upper panel shows the modelled relative scattering length (amount of material) of atmospheric film material when exposed to gas-phase ozone and the aqueous phase hydroxyl radical. An oxygen blank (film exposed to oxygen only) and a UV blank (film exposed to UV only, with no precursors present in the subphase) are also shown and no reaction is observed. (b) the lower panel shows the modelled film thickness of atmospheric film material when exposed to gaseous ozone and the aqueous phase hydroxyl radical.

Atmospheric aerosol and sea-water samples were also analysed by mass spectrometry techniques. No unsaturated material was detected, which could mean that the concentration of unsaturated material in the samples is very low and could even be below the detection limit of the techniques, or, that the samples contain a much greater proportion of saturated material. In support of the lack of reaction observed with gas-phase ozone, a number of studies[4,5] in the literature have shown that unsaturated material exists in much lower concentrations compared to saturated material in atmospheric aerosol samples.

In conclusion, organic material extracted from real atmospheric aerosol and sea-water samples forms stable films at the air-water interface. The oxidation of these films has been studied using X-ray reflectivity and shown that such films are unreactive to gaseous ozone and can be modelled as a constant amount of material at the air-water interface. It is proposed that the samples either do not contain unsaturated material or contain it in very low concentrations, which is supported by multiple studies in the literature[4,5] which propose that unsaturated material in atmospheric aerosol is present in very low concentrations when compared to saturated material. X-ray reflectivity has shown that a thin organic film extracted from atmospheric aerosol does react with the aqueous phase hydroxyl radical and a thin organic film extracted from sea-water does react with the aqueous phase nitrate radical. Therefore heterogeneous oxidation by gas-phase ozone may not be important in the atmosphere, whereas radical oxidation appears to be important. Thus it is recommended that future proxy studies focus on radical oxidation of saturated organics. Future studies of real aerosol samples collected at different stages throughout an aerosol lifetime are also recommended to determine whether gas-phase oxidation by ozone is important at specific times.

References:

1. Stocker, T.F. *et al.* Climate Change 2013 – The Physical Science Basis. doi:10.1017/CBO9781107415324 (2014).
2. Donaldson, D.J. *et al.* The influence of organic films at the air-aqueous boundary on atmospheric processes. *Chemical Review* **106 (4)**, 1445-1461, doi:10.1021/cr040367c (2006).
3. Abeles, F. La théorie générale des couches minces. *Journal de Physique et de Radium* **11**, 307–309, doi:10.1051/jphysrad:01950001107030700 (1950).
4. Rogge, W.F. *et al.* Quantification of urban organic aerosols at a molecular level: Identification, abundance and seasonal variation. *Atmospheric Environment Part A General Topics* **27** (**8**), 1309-1330, doi:10.1016/0960-1686(93)90257-Y (1993).
5. Gilardoni, S. *et al.* Regional variation of organic functional groups in aerosol particles on four U. S. east coast platforms during the International Consortium for Atmospheric Research on Transport and Transformation 2004 campaign. *Journal of Geophysical Research: Atmospheres* **112** (**D10**), doi:10.1029/2006JD007737 (2007).

Funding acknowledgement:

Diamond beamtime grants: SI8744 and SI9632 and NERC funding grant: NE/H019103/1.

Corresponding author: Dr Stephanie H. Jones, University of Toronto, stephanie.jones@utoronto.ca

Understanding the behaviour of electrons in spintronic materials

Related publication: Pincelli T, Lollobrigida V, Borgatti F, Regoutz A, Gobaut B, Schlueter C, Lee TL, Payne DJ, Oura M, Tamasaku K, Petrov AY, Graziosi P, Miletto Granozio F, Cavallini M, Vinai G, Ciprian R, Back CH, Rossi G, Taguchi M, Daimon H, van der Laan G, Panaccione G. Quantifying the critical thickness of electron hybridisation in spintronic materials. *Nature Communications* **8**, 16051, doi:10.1038/ncomms16051 (2017).

Publication keywords: Ferromagnetism; Magnetic properties and materials; Spintronics; Surfaces; Interfaces; Thin films; Hard X-ray photoelectron spectroscopy

As the interface between magnetic and non-magnetic materials is a key feature of spintronic devices, it is crucial to characterise and understand both the surface and bulk electronic and magnetic properties of the materials used in their production. For transition metal oxides it appears that thicknesses on the scale of several nanometers are critical for the appearance or disappearance of desired properties, but the presence of these critical thicknesses is extremely difficult to assess.

A team of researchers led by a group from National Research Council (CNR) Trieste developed a technique to reliably and precisely detect variations in electronic structure with depth. They used the Surface and Interface Structural Analysis beamline (I09), which allows photoelectron spectroscopy at tunable probing depths by changing the photon energy. The researchers applied their technique to two prototypical spintronic materials, and advanced theoretical modelling allowed them to attribute the results to the ability of carriers to move freely through the solid, and to precisely define the depths at which such variations take place. This is a step towards achieving the necessary precise control of spatially-confined spintronic materials.

Complex materials at the focus of modern research display unusual characteristics, often termed as quantum properties. In many cases, these exhibit a critical dependence on small variations of external parameters such as temperature, electric and/or magnetic field, photoirradiation and strain. Spintronics is a highly active field, exploiting quantum properties to achieve simultaneous manipulation of transport and magnetic ordering, with the perspective of realising extremely compact and efficient devices.

The integration in nanoscale components, however, faces spintronics with the challenges of spatial confinement. Lattice distortions, stoichiometry changes, surface states and orbitals population rearrangements alter the electronic structure when the crystal is interrupted. The unperturbed configuration is recovered only in the bulk. The introduction of a long-range order parameter such as magnetic alignment adds a further characteristic spatial scale that concurs with the ones of charge-driven interactions to create an intricate picture.

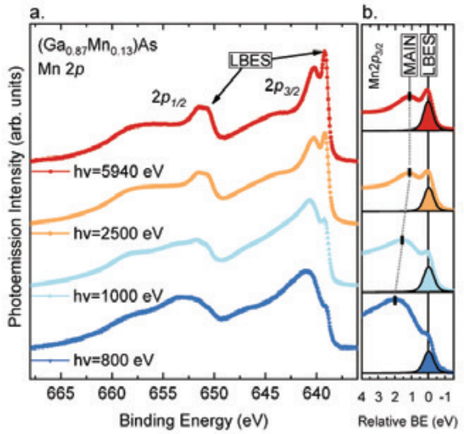

Figure 1: (a) Photon energy dependent Mn 2p core level spectra of GMA (measured with linear polarisation at T = 300 K). The spectra are shifted vertically for ease of comparison after integral background subtraction. The multiplet structures of the $2p_{½}$ and $2p_{3/2}$ are clearly resolved. The arrows indicate the position of the well-screened satellites for each spin-orbit partner; (b) Expanded view of the Mn 2p3/2 peak around 640 eV BE. The evolution the peak-fit component reproducing the LBES structure is shown as a function of increasing photon energy.

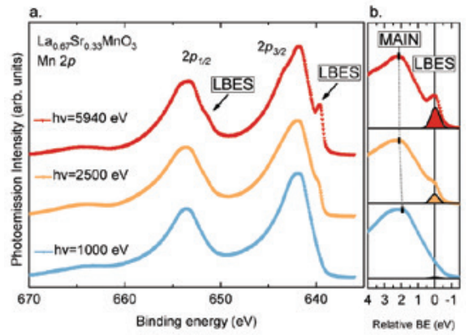

Figure 2: (a) Photon energy dependent Mn 2p core level spectra of LSMO (measured with linear polarisation at T = 200 K). The spectra are shifted vertically for ease of comparison after integral background subtraction. The arrows indicate the position of the well-screened satellites for each spin-orbit partner; (b) Expanded view of the Mn $2p_{3/2}$ peak around 640 eV BE. The evolution the peak-fit component reproducing the LBES structure is shown as a function of increasing photon energy. Note that at hv = 1000 eV the well screened intensity is clearly present in GMA, while almost absent for LSMO.

Evidence is accumulating that *critical thicknesses* are encountered frequently when assessing properties such as two dimensional conductivity[1], magnetoresistance[2] and ferroelectricity[3]. The term indicates the region of the solid in which radical changes in the electronic structure are produced by the crystal interruption: films below these thicknesses do not possess the desired emergent properties (although they may bear other ones).

It often difficult to understand whether critical thicknesses arise from intrinsic effects, controllable by interface engineering, or from extrinsic, uncontrollable processes. Such a problem indeed requires the resolution of the electronic structure of a single system, and virtually a single sample, by a technique of intrinsic probing depth tuneable across the surface region.

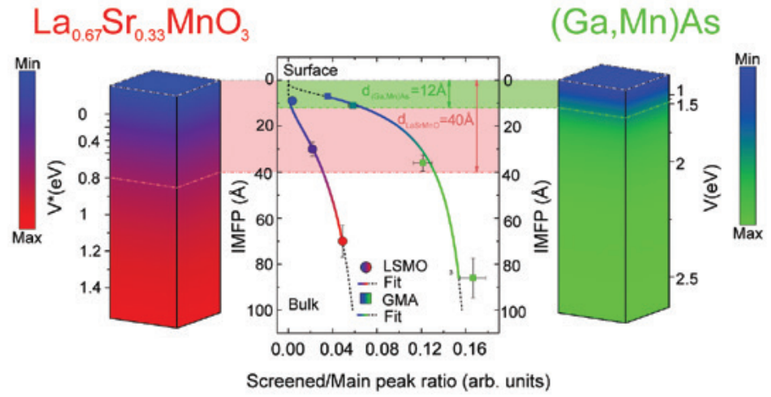

Figure 3: Central panel: relative amplitude of LBES plotted as scatter points for LSMO (circles) and GMA (squares). The vertical error-bar is 10% of the IMFP. The horizontal one is obtained by propagation of uncertainty on peak-fitting parameters. The curves show the fitted functions, dashed outside the data-points. The green (red) shaded area defines the crossover thickness for GMA (LSMO). The parallepipeda schematise the solid: a gradient reproduces the relative intensity of the LBES in GMA (LSMO), blue corresponding to zero and green (red) to the maximum in the 0-100 Å range; a tick-scale shows the evolution of the theoretical hybridisation parameter.

An effective approach has been achieved by the study of core-level satellites in photoelectron spectroscopy (PES)[4,5]. Indeed, during the photoemission process, photoionised atoms are projected in a set of final states depending on the mechanisms available to screen the core charge, giving rise to satellites. A subset of these, observed at lower binding energy than the main line (low binding energy satellites, LBES), is sensitive to carrier mobility. Cluster-model calculations[4,5] define such sensitivity with the *hybridisation parameter*, which quantifies the contribution of mobile states to the equilibrium electronic structure.

In complex materials, LBES are enhanced (or appear altogether) when the probing depth of PES is increased to deeper regions below the surface. Indeed, by increasing the excitation photon energy from 800 eV to 6 keV, the depth probed by PES extends from 1 nm to 10 nm, thus spanning the transition from surface to bulk properties. In order to use this approach to confirm or disprove interpretations, however, it must achieve quantitative precision.

This possibility is offered by the combination of hard and soft X-ray photoelectron spectroscopy (respectively HAXPES and SX-PES) in consistent experimental conditions at Diamond's Beamline I09. It was applied to two prototypical spintronics systems: the rare-earth-doped manganite, $La_{1-x}Sr_xMnO_3$ (LSMO), and the most representative diluted magnetic semiconductor, (Ga,Mn)As. In both systems, the relationship between electronic reconstruction and magnetic properties, as well as the competition between electron localisation and hybridisation, are relevant in determining the Curie temperature (T_C) and ferromagnetic state.

The Mn 2p core-level spectra (Fig. 1a, Fig. 2a, respectively) were measured for (Ga,Mn)As (20 nm film, Mn doping 13%, epitaxially grown on GaAs(100) substrate) and LSMO (40 nm film, x=0.33, epitaxially grown on LSAT(100) substrate), as a function of increasing photon energy, i.e. with increasing probing depth. The LBES features were clearly observed.

The evolution of the intensity of the LBES versus photon energy could be determined by a line shape analysis (Fig. 1b, Fig. 2b), allowing for the development of a quantification procedure (Fig. 3). The relative amplitude of the LBES component was plotted, for each photon energy, against the corresponding inelastic mean free path (IMFP) of the electrons, defining the corresponding probing depth. The resulting plot was fitted by considering an exponential attenuation of the LBES through the surface layer, whose thickness *d* was the fitting parameter. A value *d*=1.2 nm was found for (Ga,Mn)As and *d*=4 nm was obtained for LSMO. LSMO was also measured in three strain states induced by substrate mismatch, finding no detectable modifications in *d*.

The relative energy distance between the LBES and the main line also provided a precise method to compare experiments with state-of-the-art cluster-model calculations, and thus to create (Fig. 3) a vertical scale of the variation of the hybridisation parameter, which, consistently, changed more drastically within the critical thickness in both materials.

In conclusion, it has been demonstrated that the combination of SX-PES and HAXPES can be used to quantify the characteristic scale of the modifications of the electronic structure produced by the surface in complex materials. Such an approach paves the way for methodical discrimination between competing models of the effects of vertical confinement. Finally, precise means to draw a comparison with calculated spectra has allowed reliable attribution of the bulk properties to the increased hybridisation of the ground state with high mobility states.

References:

1. Ohtomo, A. *et al*. A high-mobility electron gas at the $LaAlO_3/SrTiO_3$ heterointerface. *Nature* **427(6973)**, 423-426, doi:10.1038/nature02308 (2004).
2. Park, J. H. *et al*. Magnetic Properties at Surface Boundary of a Half-Metallic Ferromagnet $La_{0.7}Sr_{0.3}MnO_3$. *Phys Rev Lett* **81(9),** doi:10.1103/PhysRevLett.81.1953 (1998).
3. Junquera, J. *et al*. Critical thickness for ferroelectricity in perovskite ultrathin films. *Nature* **422**, 506-509, doi:10.1038/nature01501 (2003).
4. Horiba, K. *et al*. Nature of the Well Screened State in Hard X-ray Mn 2p Core-Level Photoemission Measurements of $La_{1-x}Sr_xMnO_3$ Films. *Phys Rev Lett* **93(23)**, 236401, doi:10.1103/PhysRevLett.93.236401 (2004).
5. Fujii, J. *et al*. Identification of Different Electron Screening Behavior Between the Bulk and Surface of (Ga,Mn)As. *Phys Rev Lett* **107(18)**, 187203, doi:10.1103/PhysRevLett.107.187203 (2011).

Funding acknowledgement:

This work has been partly performed in the framework of the nanoscience foundry and fine analysis (NFFA-MIUR Italy) facility.

Corresponding authors: Dr Tommaso Pincelli, CNR-IOM, pincelli@iom.cnr.it, Dr Giancarlo Panaccione, CNR-IOM, giancarlo.panaccione@elettra.eu

Magnetic Materials Group

Sarnjeet Dhesi, Science Group Leader

The newly formed Magnetic Materials Group concentrates on emergent phenomena in quantum materials using the capabilities of beamlines I06, I10, I16, B16 and I21. The research encompasses a variety of challenges and opportunities at the frontiers of condensed matter physics and materials science ranging from topological states of matter, superconductivity, spintronics, two-dimensional systems, skyrmions and multiferroics. The key insights made by researchers exploit the high sensitivity of polarised X-ray spectroscopy, microscopy and scattering available across the beamlines. For instance, polarised soft X-rays combined with the PhotoEmission Electron Microscope (PEEM) on the Nanoscience beamline (I06) have visualised the domain dynamics underpinning antiferromagnetic spintronics while the resonant soft X-ray scattering on the BLADE: X-ray Dichroism and Scattering beamline (I10) has been used to understand the topological properties of skyrmions. On the Materials and Magnetism beamline (I16), interference effects in hard X-ray scattering have led to a deeper understanding of long-range magnetic ordering in canted antiferromagnets. The Inelastic X-ray Scattering beamline (I21) is in a commissioning phase, but has had already performed ground breaking experiments measuring orbital excitations, magnon dispersion and electron-phonon coupling in several highly-correlated systems. In this inaugural contribution to the annual highlights we present research from our user community that uniquely demonstrates how polarised X-ray science can uncover dramatic changes in the magnetic properties of materials from subtle changes to the geometric and electronic structure.

The origin of many complicated magnetic structures arises from short-range and long-range interactions. The understanding of long-range order arising from the Dzyaloshinskii-Moriya interaction (DMI) is, therefore, fundamental to developing new devices based on magnetoelectric effects. Building on previous work that determined the sign of the DMI for the weak ferromagnet, $FeBO_3$, researchers on beamline I16 have gone a step further and unearthed the relationship between band filling and the sign of the DMI by studying a series of isostructural weak ferromagnetic carbonates. The change in sign of the DMI is correlated to the electronic structure using first-principles calculations and is a dramatic demonstration of how magnetic properties, that can be determined using polarised X-rays, are influenced by subtle changes to the electronic structure.

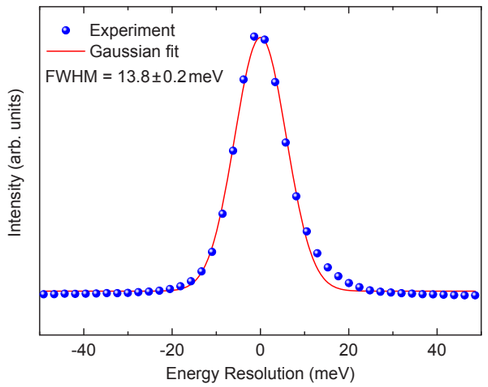

Figure 1: Combined energy resolution at the Oxygen K-edge using the 2000 l/mm VPG3 beamline grating and the 2700 l/mm SVLS2 spectrometer grating on beamline I21.

By depositing thin films of $BiFeO_3$ on vicinal surfaces researchers on beamline I06 were able to grown single ferroelectric domain samples leading to deterministic and robust room-temperature control of the magnetic orientation of a Co overlayer. $BiFeO_3$ is a multiferroic with a DMI that leads to a spin cycloid structure with a ~63 nm period. At first glance it might seem that such a complicated magnetic structure would have little effect on a Co overlayer. However, the combined use of Neutron Diffraction, at the nearby ISIS facility, and the PEEM on beamline I06 demonstrated that the interface region of the $BiFeO_3$ structure has a collinear antiferromagnetic component that, upon reversal of the $BiFeO_3$ electric polarisation using a bias voltage, is able to reproducibly switch the Co film magnetisation direction. These nanoscale insights into the interface region of single domain thin film $BiFeO_3$ are only possible using the PEEM combined with polarised soft X-rays and show how controlling film structure can lead to new and robust functionality.

When inversion symmetry is broken using interface engineering in trilayers, the spin-orbit interaction leads to the spin-orbit torque (SOT) effect that can then be used to switch the magnetisation of a thin magnetic film. The size of the SOT depends sensitively on interface properties, but can also be tuned by altering the resistivity of the materials in the trilayer using ion sputtering during growth. On I10 researchers have employed this approach to relate the changes in the resistivity of a Pt layer, in a $Pt/Co/AlO_x$ trilayer, to changes in the Co spin and orbital moments determined using X-ray Magnetic Circular Dichroism (XMCD).

In terms of technical developments across the beamlines we start with the latest addition to the suite of Diamond beamlines. I21 is a polarised soft X-ray beamline covering the energy range 250 eV to 3000 eV and dedicated to Resonant Inelastic X-ray Scattering. In the past few months the beamline team have started user operation and welcomed eight international research groups for first experiments. The novel collection geometry on I21 means that the beamline leads the world in detection efficiency and can perform scans in a fraction of the time that would otherwise be possible. The beamline has already achieved a resolution of 13.8±0.2 meV at the O *K*-edge (Fig. 1) and is now pressing ahead with further developments to reach higher photon energies covering the 4*d* and 5*d* transition metal 2*p* and 3*p* edges respectively, provide polarisation analysis of the scattered X-rays and install more efficient detectors. I10 is in the closing stages of installing a new electromagnet facility, to complement the existing low-temperature 14 T magnet, for fast XMCD measurements and is also installing a new versatile electromagnet in the RASOR diffractometer. I06 is completing the refurbishment of the branchline, which will permanently house the vector magnet and time-resolved soft X-ray diffraction systems. Beamline I06 has also started the process of installing a new Medipix3RX quad detector for the PEEM with a higher quantum efficiency with respect to the existing detector. In the coming year, I06 will also upgrade the PEEM manipulator to reach lower temperatures using liquid He enabling researchers to explore the phase diagrams of, for instance, multiferroics and superconductors. I16 have upgraded the polarisation analyser to house an area detector and is continuing to develop versatile polarisation control of the incoming X-rays. The main upgrade to the B16 Test beamline has been the design and development of a pink-beam compatible X-ray camera system, which overcomes the challenges from the high flux of white beam, including degradation of image quality due to accumulated contamination on the scintillator during intense X-ray exposure. This camera system will facilitate fast imaging on B16 using pink/white beams. Furthermore, in the B16 science highlight, a novel approach to selecting a single bunch using surface acoustic waves is presented.

The Magnetic Materials Group will continue developing the beamlines and off-line laboratories for the research community and would welcome input on how we can maintain the world-leading facilities developed at Diamond. In the long-term we are also working on the development of the facilities ready for an upgrade to the low-emittance Diamond-II machine. Our aim is to realise a family of polarised X-ray beamlines with intuitive software, underpinned by advanced on-site sample characterisation facilities and supported by state-of-the-art data visualisation tools.

Figure 2: The scientists, engineers, technicians and PDRAs that make up the Magnetic Materials Group.

Imaging exchange coupling in multiferroic, multifunctional devices

Related publication: Saenrang W, Davidson BA, Maccherozzi F, Podkaminer JP, Irwin J, Johnson RD, Freeland JW, Íñiguez J, Schad JL, Reierson K, Frederick JC, Vaz CAF, Howald L, Kim TH, Ryu S, Veenendaal MV, Radaelli PG, Dhesi SS, Rzchowski MS, Eom CB. Deterministic and robust room–temperature exchange coupling in monodomain multiferroic $BiFeO_3$ heterostructures. *Nature Communications* **8(1583)**, 1-8, doi:10.1038/s41467-017-01581-6 (2017).

Publication keywords: Multiferroics; Exchange coupling; Spintronics

The data storage on which out smartphones, tablets and computers rely works via electrical fields (e.g. flash drives) or magnetic fields (e.g. hard drives), but research into magnetoelectric materials could lead to a new generation of multifunctional devices that use a combination of the two.

Magnetoelectric materials have both electrical and magnetic functionality, and changing one induces a change in the other – it's called 'cross-coupling'. Developing an understanding of cross-coupling involves studying how the magnetic properties change when an electric field is applied, but most magnetoelectric materials have very complicated structures. Researchers simplified the process by simplifying the material itself, developing a unique process for making a simplier magnetoelectric material.

They then used I06's X-ray PhotoEmission Electron Microscope (XPEEM) to image – in real time- how changing the electric properties results in a change in the magnetic state. Their results are an important step towards exploiting cross-coupling to make new multifunctional devices that work well at room temperature, opening up new directions for creating low 'spintronic' devices that make use of an electron's spin, as well as its charge.

We find ferromagnets and ferroelectrics all around us: our latest credit cards have both a magnetic stripe and a ferroelectric memory chip on it. Yet usually they are different materials placed in separate locations, just like on the card. Multiferroics are materials in which both magnetic and ferroelectric properties coexist intrinsically in the same material, and offer the possibility to combine normally spatially–separated functions into a single device with multiple functions, as well as drive new device paradigms. This could drastically increase the performance and reduce the size of future circuits. The biggest challenge is to understand just how these properties are internally coupled and then how to exploit this coupling to design new multifunctional devices. On Diamond Light Source's I06 Nanoscience beamline, researchers have made an important step to show how multiferroic coupling can be exploited to make a new, robust multifunctional device working at room temperature. Using monodomain epitaxial thin film heterostructures of the most promising multiferroic, $BiFeO_3$, I06's X-ray photoemission microscope (XPEEM) has imaged how the ferroelectric properties can deterministically control the magnetic orientation of a ferromagnetic overlayer only a few atoms thick.

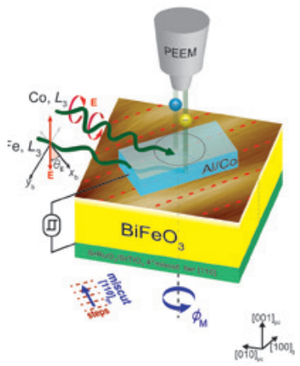

Figure 1: Schematic diagram of in situ ferroelectric switching during XPEEM imaging to study exchange coupling between monodomain $BiFeO_3$ and Co overlayer, whose magnetic end electric configurations are depicted in the right panel. The magnetoelectric heterostructure is shown as mounted in the XPEEM, with incoming circular and linear polarised light used for circular dichroism (XMCD) on Co and linear dichroism (XMLD) on Fe, respectively. The antiferromagnetic configuration of the sub-surface (i.e. bulk) $BiFeO_3$ has been determined by neutron diffraction. The ferroelectric state of the $BiFeO_3$ can be switched by 71° from the 'down' to 'up' state, allowing the properties of the ferromagnetic Co and surface antiferromagnetic $BiFeO_3$ layers to be characterised in both states.

Switching the $BiFeO_3$'s ferroelectric state between 'up' and 'down' controllably and reproducibly rotates the ferromagnetic orientation of the overlayer by 90°. This opens up new directions for creating fast, low-power 'spintronic' devices (microelectronic devices that use the electron's spin as well as its charge) by exploiting the multiferroic properties of $BiFeO_3$.

Staying ahead of Moore's Law – which predicts a doubling of the number of transistors in microelectric circuits every two years – is driving the search for new device functionalities, which in turn require the discovery of materials with new properties that can be controlled by applying a voltage or current. Multiferroic materials, especially 'magnetoelectrics' that show coupled magnetic and ferroelectric properties in the same phase, offer great promise to satisfy these requirements[1,2]. Thin films are necessary for any device that should eventually be integrated into a large-scale circuit, and epitaxial growth of films also offers the opportunity to control and even improve certain properties of a material as compared to its bulk counterpart. For example, in silicon films the electron mobility can increase under certain conditions of epitaxial strain (i.e. squeezing or stretching the crystal in two directions, leaving the third direction free to adjust), thus allowing higher operating speeds. Epitaxial strain can also improve the properties of ferroelectric films influenced by the size and distribution of domains, adjacent volumes in which the polarisation points in different directions. For $BiFeO_3$, the deleterious effect of multiple domains was eliminated by creating large-area $BiFeO_3$ films possessing only a single ferroelectric domain – 'monodomain' films, with the desirable property that there is only one, well-defined direction of the polarisation **P** in either the 'up' and 'down' states[3]. In magnetoelectric $BiFeO_3$, the magnetic organisation of spins on the Fe sites is antiferromagnetic, i.e. moving from one Fe site to the next, the magnetic spins point in opposite directions. In bulk $BiFeO_3$, the spins have the added complexity that they rotate slightly going from one site to the next, completing a full rotation over a distance of about 62 nm in bulk (the period of the so-called 'spin–cycloid'). The cycloid is expected to create problems for any $BiFeO_3$–based magnetic device, since over large areas there is no single direction of the magnetisation, as there is in simple collinear antiferromagnets. To complicate matters even more, in $BiFeO_3$ crystals there are 8 possible ferroelectric domains, each with 3 cycloids of different orientations – 24 different configurations in all, making multidomain $BiFeO_3$ a complex material difficult to incorporate in a well-behaved, deterministic magnetic device.

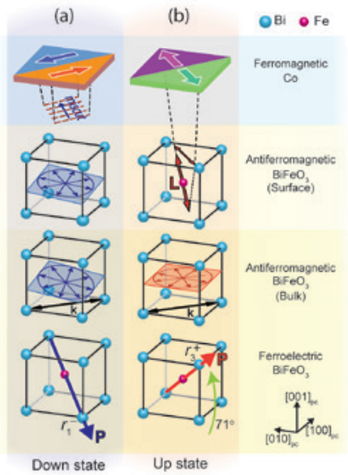

Figure 2: Combining the XPEEM results with neutron diffraction measurements that measure the bulk antiferromagnetic properties, the results are shown in a and b. The top-most panel in (a-b) shows how the Co layer rotates in-plane by ~90° when the $BiFeO_3$ ferroelectric polarisation (P) is switched 71° from 'down' to 'up' states (bottom panel). The coupling mechanism is through the antiferromagnetic spin–cycloid (circle with radial arrows) at the $BiFeO_3$ surface that converts from a pure cycloid in the 'down' state to a collinear axis L only in the 'up' state.

One of the building blocks of spintronic devices is an 'exchange–coupled' bilayer, based on an effect discovered in the 1950s but still not well understood, in which the spins in a simple antiferromagnetic layer are coupled to the spins in a ferromagnetic overlayer. Since the spin axis **L** in a collinear antiferromagnet is fixed, exchange coupling across the interface serves to effectively fix the direction of the ferromagnetic layer. New functionality can be introduced by creating a magnetoelectric exchange–coupled bilayer, in which the spin axis **L** in the antiferromagnetic layer rotates when the ferroelectric polarisation is switched; then exchange–coupling between **L** and the spins in the ferromagnetic overlayer would cause the ferromagnetic spins to rotate as well, in a deterministic and controllable way[4].

Precisely this new type of magnetoelectric exchange coupling is demonstrated by the XPEEM data (Figs. 1-3). Several improvements to the samples constructed for these experiments were crucial to achieving unambiguous interpretation of the data. Most important is the use of monodomain $BiFeO_3$ films under epitaxial strain: neutron diffraction confirms that each ferroelectric monodomain is correlated to a single antiferromagnetic domain, even after hundreds of ferroelectric switching cycles. Thus monodomain $BiFeO_3$ films eliminate the 24 different polarisation–cycloid configurations mentioned previously for bulk $BiFeO_3$. In the presence of a strong exchange coupling to the ferromagnetic overlayer, the stability of the monodomains ensures (a) one-to-one correlation between the $BiFeO_3$ ferroelectric state and the overlayer spin orientation and (b) deterministic control over the spins orientation of the overlayer.

Ferroelectric switching of the monodomain $BiFeO_3$ between 'up' and 'down' states was accomplished inside the XPEEM by installing the Ferroelectric Tester (Radiant Technologies) in the high–voltage rack of the microscope. Antiferromagnetic properties of the $BiFeO_3$ were monitored by X-ray Magnetic Linear Dichroism (XMLD) on the Fe $L_{2,3}$ absorption edge (~710 eV) and the magnetic orientation of spins in the ferromagnetic Co overlayer was monitored by X-ray Magnetic Circular Dichroism (XMCD) on the Co $L_{2,3}$ edge (~770 eV). The instrument setup allowed for the first time *in situ* reading and writing of the ferroelectric polarisation of a thin film device, while the XPEEM imaged the effect of the ferroelectric switching on the $BiFeO_3$ antiferromagnetic and Co ferromagnetic configuration. The exact knowledge of the ferroelectric, antiferromagnetic and ferromagnetic configuration of the multiferroic device was key to unveiling the physics behind its functionalities. Crucially, the submicron size of the device made possible the deterministic nature of the multiferroic coupling, and only the combination of microscopic (XPEEM) and bulk (neutron diffraction) techniques has made it possible to disentangle the roles played by each one of the three previously mentioned ferroic orders.

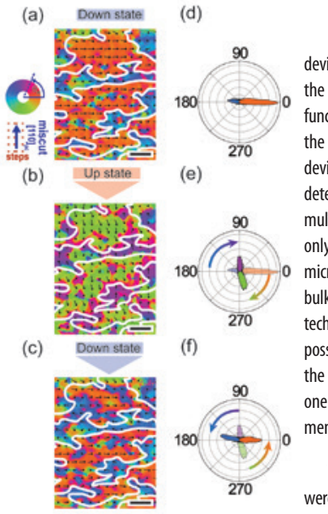

Figure 3: ~90° magnetisation rotation with ferroelectric switching. XMCD-PEEM vector maps of Co local magnetisation for $BiFeO_3$ polarisation switching from the (a) 'down' to (b) 'up' and back to (c) 'down' state consecutively (scale bar 1 µm). The polar plots show the angular distribution of the Co magnetisation. Magnetic domain boundaries are indicated by the white lines. The polar plots indicate an average Co magnetisation rotation of nearly 90° from the (d) 'down' state to (e) 'up' state and then back to the (f) 'down' state.

The $BiFeO_3$-based devices were switched successfully at room temperature more than 1000 times, a breakthrough result for multiferroic devices. This suggests that the strain enginneering of heterostructures is a promising path for the realisation of practical, new multiferroic devices.

References:

1. Eerenstein, W. *et al*. Multiferroic and magnetoelectric materials. *Nature* **442**, 759-765, doi:10.1038/nature05023 (2006).
2. Catalan, G. & Scott, J. F. Physics and Applications of Bismuth Ferrite. *Adv. Mater.* **21**, 2463-2485, doi:10.1002/adma.200802849 (2009).
3. Jang, H. W. *et al.* Domain Engineering for Enhanced Ferroelectric Properties of Epitaxial (001) $BiFeO_3$ Thin Films. *Adv. Mater.* **21**, 817-823, doi:10.1002/adma.200800823 (2009).
4. Bibes, M. & Barthélémy, A. Multiferroics: Towards a magnetoelectric memory. *Nat. Mater.* **7**, 425-426, doi:10.1038/nmat2189 (2008).

Funding acknowledgement:

This work was supported by the Army Research Office through grant W911NF-10-1-0362 and W911NF-13-1-0486. PEEM measurements at Diamond Synchrotron (UK) were performed at the I06 beamline under proposals nt12084, nt13225 and si11589. Part of this work was performed at the Surface/Interface: Microscopy (SIM) beamline of the Swiss Light Source, Paul Scherrer Institut, Switzerland. Work at Argonne National Laboratory was supported by the US DOE, Office of Science, Office of Basic Energy Sciences, under Contract No. DEAC02-06CH11357. M. V. V. is supported by the U.S. DOE under Award No. DE-FG02-03ER46097. R.D.J. acknowledges STFC for the provision of beam time on the WISH instrument at ISIS, proposal number RB1600019, and P. Manuel for data collection. R.D.J. acknowledges support from a Royal Society University Research Fellowship. J.Í. acknowledges support from the Luxembourg National Research Fund (Grant number FNR/P12/4853155).

Corresponding authors: Prof Chang-Beom Eom, University of Wisconsin, eom@engr.wisc.edu, Dr W Saenrang, Suranaree University of Technology, Thailand, Prof B A Davidson, CNR-Istituto Officina dei Materiali, Italy & Temple University, USA

Engineering platinum resistivity to enhance spin-orbit torque

Related publication: Lee JW, Oh YW, Park SY, Figueroa AI, Van Der Laan G, Go G, Lee KJ, Park BG. Enhanced spin-orbit torque by engineering Pt resistivity in Pt/Co/AlOx structures. *Physical Review B* **96**, doi:10.1103/PhysRevB.96.064405 (2017).

Publication keywords: Spin-orbit torque; Spin Hall angle; Magnetic memory

Spin-orbit torque (SOT) arises from spin-orbit coupling in heavy metal/ferromagnet bilayers, and can be used to control the magnetisation direction. It is of considerable interest as a way to efficiently switch the magnetisation of spintronic devices, which have advantages over traditional electronic devices, including non-volatile memory and logic applications. In order to engineer materials with enhanced SOT, for lower power consumption, scientists are investigating the microscopic origin of SOT.

A team of researchers based in Korea and the UK used X-ray Absorption Spectroscopy (XAS) and X-ray Magnetic Circular Dichroism (XMCD) measurements on Diamond's BLADE: X-ray Dichroism and Scattering beamline (I10) to investigate the relationship between the resistivity and the spin-Hall angle of platinum. They found that the SOT strength increases with heavy metal resistivity. Their results are expected to provide an efficient route for material engineering towards improved SOT-based spintronic devices.

The manipulation of the magnetisation by in-plane current utilising spin-orbit torque (SOT) has been receiving a great deal of attention due to its possible applications in spintronic devices such as magnetic memories and spin-logic devices[1-3]. For wider applications of spintronic devices, it is essential to find an efficient way to switch the magnetisation. In this respect, many attempts are being made in order to improve the SOT efficiency, for instance, by finding heavy metal (HM) electrodes with high spin Hall angle.

In order to efficiently engineer materials with large spin Hall angle, it is important to address the so-far unanswered question concerning the microscopic origin of the SOT. One of these questions is the relation between the resistivity of the HM layer and the spin Hall angle. In this work, the effect of the resistivity on the spin Hall angle was investigated using Pt(5 nm)/Co(0.8 nm)/AlO_x(1.8 nm) structures (Fig. 1a), in which the resistivity of Pt is modulated by varying Ar deposition pressures ranging from 3 to 50 mTorr. The resistivity of the Pt layer shows a gradual increase with Ar pressure and reaches a value of almost 1.6 times larger for Pt deposited under 50 mTorr than that grown under 3 mTorr (Fig. 1b). This is expected because the reduced kinetic energy of sputtered atoms under a higher pressure leads to imperfections in the crystal structure.

Next, the effect of the Pt resistivity on the spin Hall angle and resultant SOT is investigated by measuring SOT-induced effective magnetic fields and the critical current for SOT-induced magnetisation switching. The effective magnetic fields are measured using a harmonic lock-in technique: the measurement of the first and second harmonic Hall voltages with respect to the in-plane magnetic fields, allowing us to extract the effective spin Hall angle ($\theta_{SH,eff}$). Figure 1c shows that the $\theta_{SH,eff}$ increases ~3 times while the resistivity of Pt layer increases by a factor of 1.6. The increase in $\theta_{SH,eff}$ is confirmed by SOT-induced switching experiments where the magnetisation direction was monitored by measuring the anomalous Hall resistance (R_H) while sweeping a pulsed driving current up to ±25 mA. The results, shown in Figure 1d, demonstrate deterministic SOT-induced switching of perpendicular magnetisation and show a reduction in the switching current I_{sw} for a larger Ar deposition pressure or a larger Pt resistivity. The decrease in switching current, or enhancement in the switching efficiency (Fig. 1e), is in good agreement with the enhancement in $\theta_{SH,eff}$ obtained by the harmonic lock-in technique.

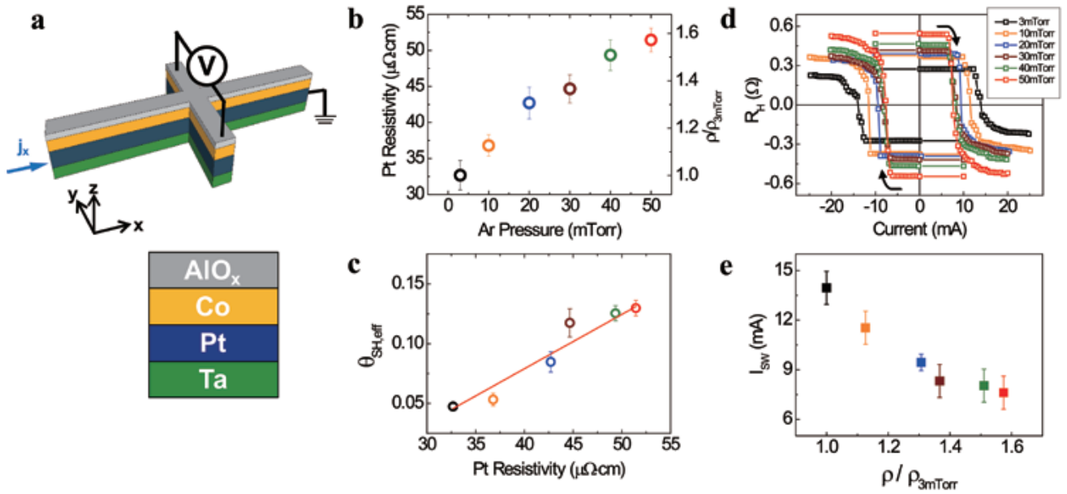

Figure 1: Dependence of the spin-orbit torque (SOT) on the Pt resistivity. (a) Schematic of sample structure. (b) Pt layer resistivity as a function of Ar deposition pressure. (c) Extracted effective spin-Hall angle vs. Pt resistivity, obtained by harmonic lock-in measurements. (d) SOT-induced magnetisation switching for Pt/Co/AlO_x stack with various Pt deposition pressures. (e) Switching current (Isw) as a function of Pt resistivity.

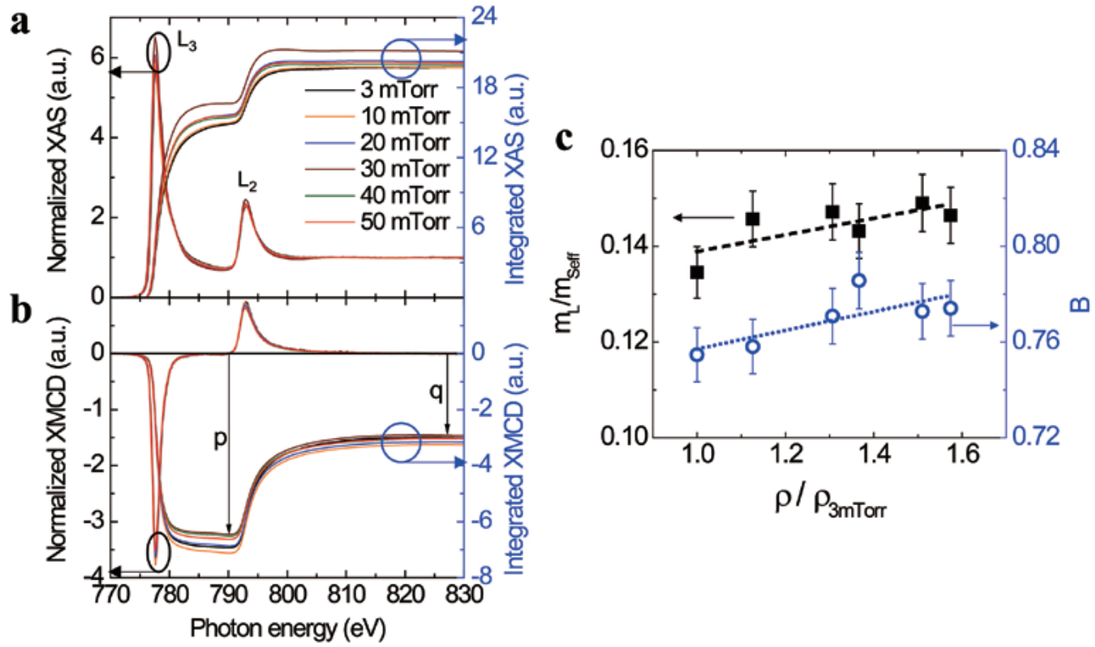

Figure 2: X-ray absorption spectroscopy (XAS) and X-ray magnetic circular dichroism (XMCD) measurements and analysis for samples with Pt layers grown under varying pressure conditions. (a) XAS spectra and their Integrated intensities at the Co L2,3 edge. The branching ratio B is obtained from the latter. (b) Corresponding XMCD spectra and their integrated intensities. The vertical arrows indicate the values of p and q for application in the magneto-optical sum rules. (c) m_L/m_{seff} ratio (left axis) and B (right axis) vs. Pt resistivity. Dashed lines are guides to the eye.

It has been experimentally shown that the $\theta_{SH,eff}$ of Pt increases with the Pt resistivity, however, the enhancement factor of the spin-Hall angle is 3.0 while the enhancement factor of the Pt resistivity is 1.6. This may imply that there is a significant interface contribution to the enhancement in $\theta_{SH,eff}$ since more current flows near the Co/Pt interface as the Pt resistivity increases. To account for this additional contribution to the SOT, the interface contribution needed to be experimentally addressed, which is related to the spin-orbit coupling-induced band splitting originating from the inversion-symmetry breaking at the interface. X-ray Absorption Spectroscopy (XAS) and X-ray Magnetic Circular Dichroism (XMCD) measurements were performed to verify whether the interface spin-orbit coupling is influenced by the Pt resistivity. Two quantities associated with the spin-orbit coupling of the Co atoms were obtained: the branching ratio (B) and the orbital-to-spin magnetic moment ratio ($m_L/m_{S,eff}$) using the XAS and XMCD spectra and their integrated intensities for Pt(5 nm)/Co(0.8 nm)/AlO_x (1.8 nm) samples (Fig. 2a,b). The obtained values of B and $m_L/m_{S,eff}$ show a gradual increase with Pt resistivity indicating that the spin-orbit interaction of the Co indeed increases with the resistivity of the Pt layer. These results are in good agreement with the theoretical prediction[4] which emphasises the important role of interfacial spin-orbit interaction that contributes to the increase in $\theta_{SH,eff}$. Therefore, our result, the efficient control of $\theta_{SH,eff}$ and hence of SOT by controlling the HM resistivity, opens up a novel way to improve the switching efficiency in SOT-active devices.

References:

1. Žutić, I. *et al*. Spintronics: fundamentals and applications. *Reviews of Modern Physics* **76(2)**, 323-410, doi:10.1103/RevModPhys.76.323 (2004).
2. Miron, I. M. *et al*. Perpendicular switching of a single ferromagnetic layers induced by in-plane current injection. *Nature* **476**, 189-193, doi:10.1038/nature10309 (2011).
3. Liu, L. *et al*. Spin-Torque Switching with the Giant Spin Hall effect of Tantalum. *Science* **336(6081),** 555-558, doi:10.1126/science.1218197 (2012).
4. Wang, L. *et al*. Giant Room Temperature Interface Spin Hall and Inverse Spin Hall Effects. Phys *Rev Lett* **116 (19)**, 196602, doi: 10.1103/PhysRevLett.116.196602 (2016).

Funding acknowledgement:

This work was supported by the National Research Foundation of Korea (2017R1A2A2A05069760, 2017M2A2A6A01071238)

Corresponding author: Prof Byong-Guk Park, Materials Science and Engineering, KAIST, bgpark@kaist.ac.kr

Adding electrons to switch magnetic chirality

Related publication: Beutier G, Collins SP, Dimitrova OV, Dmitrienko VE, Katsnelson MI, Kvashnin YO, Lichtenstein AI, Mazurenko VV, Nisbet AGA, Ovchinnikova EN, Pincini D. Band Filling Control of the Dzyaloshinskii-Moriya Interaction in Weakly Ferromagnetic Insulators. *Physical Review Letters* **119,** 167201, doi:10.1103/PhysRevLett.119.167201 (2017).

Publication keywords: Dzyaloshinskii-Moriya interaction; Weak ferromagnetism; Resonant X-ray diffraction

The Dzyloshinskii-Moriya interaction (DMI) was first introduced in 1957 to explain 'weak ferromagnetism'. It causes a twisting of the pattern of atomic magnets, and is now considered to be the driving force behind the exotic magnetic vortexes called Skyrmions. A predictive theory hadn't been developed, however, as until now a detailed study of the amplitude and sign of the DMI hadn't been carried out.

A team of researchers has used the Materials and Magnetism beamline (I16) to carry out a systematic study of the DMI in a series of magnetic crystals. I16 offers the very high X-ray flux needed to observe the tiny signals associated with magnetism. Even more importantly, it has the space and versatility to allow the development and testing of novel techniques. For these experiments, the researchers installed a movable magnet to drag around the whole magnetic pattern without moving the sample, yielding data of much higher quality than traditional scans. Their novel technique could be applied to small crystal grains, with one of the samples ($NiCO_3$) being around 50 microns in size.

Their results showed a spectacular change in the magnitude and sign of the DMI as electrons were added to 3d shells, confirming theoretical calculations and a simple model based on the number of electrons carried by the magnetic ion. The study brings us a step closer to systematic prediction of important material properties. The possibility of controlling and changing the sign of the DMI is an essential step towards finding suitable materials for spintronics applications.

Magnetic order at the atomic scale is ruled by exchange interactions, which are mostly symmetric upon exchange of the spins. In 1957, Dzyaloshinskii introduced an antisymmetric part to explain the weak ferromagnetism observed in a some crystals[1]. This new term, known as the Dzyaloshinskii-Moriya interaction (DMI), is a key ingredient in many modern magnetic phases, such as multiferroics and skyrmions. Despite the intense research effort on these materials, the DMI still lacks a simple understanding at the microscopic level, in particular because many experimental studies on the DMI address only its magnitude, not its sign. The sign of the magnetic twist is accessible in a handful of long-period magnetic structures, with complex phase diagrams that defy systematic investigations versus band filling.

Weak ferromagnets with the carbonate structure offer an opportunity to perform such a systematic study: $MnCO_3$, $FeBO_3$, $CoCO_3$ and $NiCO_3$ share the same crystal structure and the same low temperature magnetic ground state: weak ferromagnetism due to a small canting of the spins away from the collinear antiferromagnetic arrangement (Fig. 1). The main difference is the nature of the transition metal ions, which carry the magnetic moments, and it is expected that the number of valence electrons has a large influence on the DMI. The sign of the DMI in these crystals is directly connected to the direction of the canting of the spins with respect to the antiferromagnetic sequence (Fig. 1), but the determination of this direction is not straightforward. Specifically, the canting direction can easily be driven in any direction of the basal plane by a small magnetic field, which is convenient to ensure a single magnetic

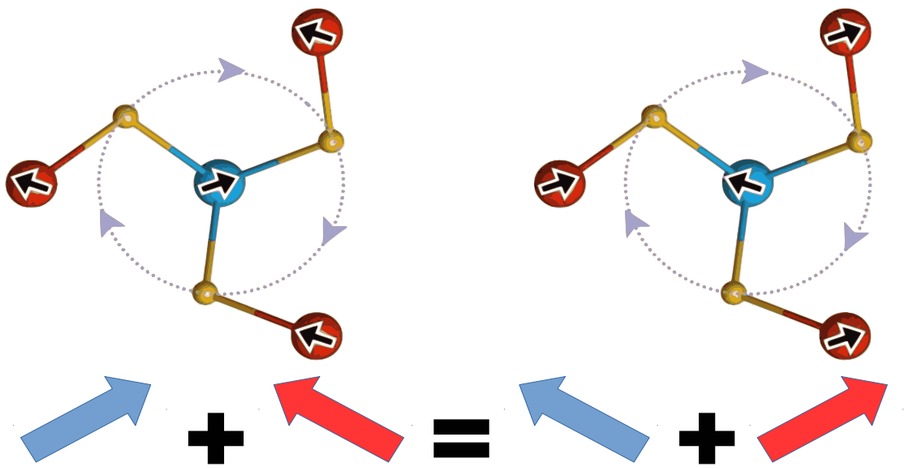

Figure 1: Local atomic and magnetic structures in the series of weak ferromagnets. The ions of the two magnetic sublattices are represented by blue (site 1) and red (site 2) spheres, with black arrows denoting the direction of their spins. Oxygen atoms between the two adjacent transition metal layers are represented as yellow spheres. The dotted circles highlight the twist of the oxygen layer. The left and right panels show the two possible magnetic configurations which depend on the sign of the DMI, for an applied magnetic field pointing toward the bottom of the figure.

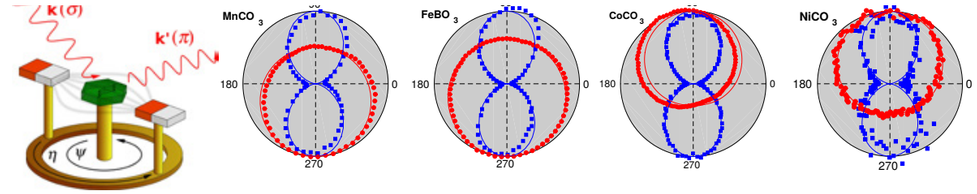

Figure 2: X-ray diffraction experiment: schematic view and main results. Normalised experimental values of the diffraction intensity versus magnet angle η, for the series of weak ferromagnets. The blue curves are measured away from the resonance and show the pure magnetic scattering intensity, which is symmetric and insensitive to the scattering phase. The red curves are on resonance and include a strong interference term that breaks the symmetry and gives the phase of the magnetic scattering, revealing the sign of the DMI. Experimental data (symbols) are shown with their fits (plain lines) against the model given in Beutier et al.[3].

domain in the sample, but the phase of the antiferromagnetic structure is needed to extract the sign of the DMI.

A new diffraction method was developed for this purpose[2]. Magnetic scattering encodes the magnetic structure, but the measurement of pure magnetic reflections cannot capture its phase and therefore the pattern of stacking of the canted moments. Interference was needed with a reference wave independent of the magnetic structure: here Resonant Elastic X-ray Scattering (REXS) is used, which contributes to the same 'crystallographically forbidden' reflections as the antiferromagnetic structure. The sign of the REXS amplitude must of course be known. Despite the rather exotic nature of the REXS amplitude in this case (pure electronic quadrupole scattering), it can be reliably modelled with a modern X-ray spectroscopy software.

The measurements were performed at beamline I16, with a monochromatic X-ray beam tuned to the K absorption edge of the transition metal of each sample. The 'spacegroup forbidden' 009 reflection, allowed for the antiferromagnetic structure and quadrupole resonant scattering, was measured in the low temperature magnetic phase. In order to exploit the interference effect, a weak magnetic field was rotated in the basal plane of the sample, dragging the whole magnetic structure without moving the sample. The interference intensity varied in proportion to σ sin(η), where σ is the sign of the DMI and η is the azimuthal angle of the magnetic field in the basal plane. This simple scan yields directly the sign of the DMI, as shown in Figure 2. It is characterised by the deviation of the measured intensity toward η = 90° or η = 270°, i.e., whether the red rings in Figure 2 go up or down. The results are remarkably clear: the sign of the DMI is the same in $FeBO_3$ and $MnCO_3$, which are both opposite to $CoCO_3$ and $NiCO_3$. More precisely, the canting angle is negative (Fig. 1, left) in $FeBO_3$ and $MnCO_3$, and positive (Fig. 1, right) in $CoCO_3$ and $NiCO_3$. These signs represent the missing information from the absolute values of the canting angles that are reported in the literature and complete our knowledge of the relative strength of the DMI in this series of materials. The experimental signed values of the canting angles are in agreement with state-of-the-art first-principle calculations within local density approximation taking into account the on-site Coulomb interaction U and spin-orbit coupling (LDA + *U* + SO).

The results[3] show a nearly monotonic variation of the canting angle (and the DMI) as a function of the filling of the 3*d* band, with a change of sign between $FeBO_3$ and $CoCO_3$. This can be understood with a simple model based on partial inter-orbital contributions to the DMI (IO-DMI), following the super-exchange-based approach developed by Moriya[4]: considering two interacting ions, one considers each of the partial contributions for DMI between one orbital of one ion and one orbital of the other ion. By changing the occupation of the 3*d* states we change the balance between empty and fully occupied channels for the IO-DMI. It results in the change of sign and magnitude of the total DMI.

This work, relying on a novel diffraction method, provides thus a simple microscopic understanding of the DMI in insulator systems.

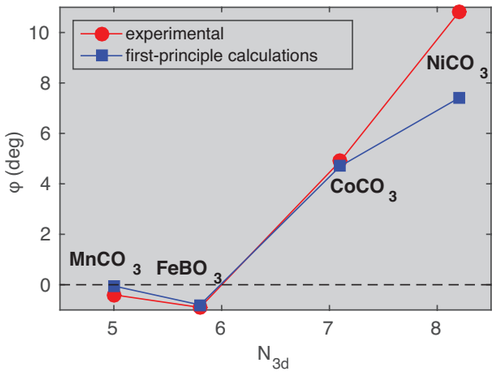

Figure 3: Experimental and theoretical values of the canting angle (φ) against the filling of the 3d band. The experimental signs and the ab initio values are taken from this work. The sign of the canting angle corresponds to the sign of the DMI. N_{3d} is the number of the 3d electrons per transition metal ion obtained from first-principles calculations.

References:

1. Dzyaloshinsky I. A thermodynamic theory of "weak" ferromagnetism of antiferromagnetics. *Journal of Physics and Chemistry of Solids* **4(4),** 241-255, doi: 10.1016/0022-3697(58)90076-3 (1958).
2. Dmitrienko, V. E. *et al*. Measuring the Dzyaloshinskii–Moriya interaction in a weak ferromagnet. *Nature Physics* **10,** 202–206, doi:10.1038/nphys2859 (2014).
3. Beutier, G. *et al*. Band Filling Control of the Dzyaloshinskii-Moriya Interaction in Weakly Ferromagnetic Insulators. *Phys. Rev. Lett.* **119**, 167201, doi:10.1103/PhysRevLett.119.167201 (2017).
4. Moriya, T. Anisotropic Superexchange Interaction and Weak Ferromagnetism, *Phys. Rev.* **120**, 91, doi:10.1103/PhysRev.120.91 (1960).

Funding acknowledgement:

We acknowledge Diamond Light Source for time on Beamline I16 under Proposals No. 7703 and 11751, and ESRF for time on Beamline BM28 (XMaS) under Proposal BM28-01-966. The work of V. V. M. is supported by the grant of the President of Russian Federation Grant No. MD-6458.2016.2. A. I. L. acknowledges the support of Grant No. DFG SFB-668 and the excellence cluster CUI. M. I. K. acknowledges support from ERC Advanced Grant No. 338957 FEMTO/NANO. Y. O. K. acknowledges the computational resources provided by the Swedish National Infrastructure for Computing (SNIC) and Uppsala Multidisciplinary Center for Advanced Computational Science (UPPMAX).

Corresponding authors: Dr Guillaume Beutier, SIMAP, guillaume.beutier@grenoble-inp.fr and Prof Steve P. Collins, Diamond Light Source, steve.collins@diamond.ac.uk

Fast Active Optics for Synchrotron Radiation

Related publication: Vadilonga S, Zizak I, Roshchupkin D, Petsiuk A, Dolbnya I, Sawhney K, Erko A. Pulse picker for synchrotron radiation driven by a surface acoustic wave, *Optics Letters* **42 (10)**, 1915-1918, doi:10.1364/OL.42.001915 (2017).

Publication keywords: Surface acoustic waves; Optics; Pulse picker

Synchrotron light sources produce a strong and stable pulsed beam, for which the pulse sequence is dependent on the circumference of the storage ring. Many experiments only require some of the pulses, including 'pump and probe' experiments that activate a process and then measure it. Experiment hutches are equipped with pulse pickers that are used to select which pulses reach the sample. Currently, pulse pickers rely on mechanical systems rotating at high velocities, such as crystals or mirrors. They are limited by their rotation speed, and other design factors.

To overcome these limitations, a team of researchers has developed a new type of pulse picker, based on an active optic system that uses surface acoustic waves (SAW) rather than mechanical components. It provides a flexible method of selecting pulses, via electron modulation of the amplitude of the acoustic waves.

For their experiments they used B16, which is equipped with the special optics needed to focus the beam onto the detector. Having successfully demonstrated that this new type of pulse picker is feasible for pulses separated by at least 120 ns, the team has plans to install a second one at the BESSY II facility in Germany.

X-ray time-resolved experiments allow the investigation of the dynamics of chemical reactions or physical phenomena. Various pump-probe experiments can be conceived, and the studied processes span different time scales from picosecond to millisecond. In pump-probe experiments, a fast change in the sample is triggered by external activation (pumping). A short time after the activation, an X-ray pulse is used to measure the state of the studied sample (probe). Ideally, no additional X-ray pulses should reach the sample.

Synchrotron radiation facilities provide strong and stable X-ray beam pulses that can be used for time-resolved measurements. Since at synchrotron light sources many experiments are served simultaneously, a pulse picker is preferably implemented in each experimental station.

Modern pulse pickers are mechanical choppers rotating at high velocities. Depending on the design, mechanical bunch pickers can select X-ray pulses separated by at least several hundred nanoseconds. Another limitation common to most of the pulse pickers actually in use is the low repetition rate, in the kilohertz region. However, synchrotron sources commonly operate with a repetition rates in the megahertz region.

In 1984 Kikuta *et al*. foresaw the possibility of using the surface acoustic wave (SAW) to manipulate an X-ray beam[1] and in 1997 Tucoulou *et al*. presented a different kind of pulse picker based on X-ray diffraction from a multilayer modulated by SAW trains[2]. The SAW induces a sinusoidal deformation on the multilayer surface, which acts as a grating. When illuminated by X-rays it produces diffraction satellites[3]. The SAW propagates with a constant velocity, usually between 2000–5000 m/s [4]. The time resolution is defined as the time that the SAW train needs to enter and leave the X-ray beam footprint. To be of practical value for Diamond, the time resolution has to be smaller than the 400 ns wide ion clearing gap.

In this highlight a feasibility test for an X-ray pulse picker built taking advantage of diffraction of a SAW in sagittal geometry is reported. In this geometry, the wavefront is parallel to the scattering plane[5]. This has the advantage of diminishing the time resolution to values that are at least one order of magnitude lower, compared to meridional geometry. The necessary time resolution to isolate the single bunch was achieved.

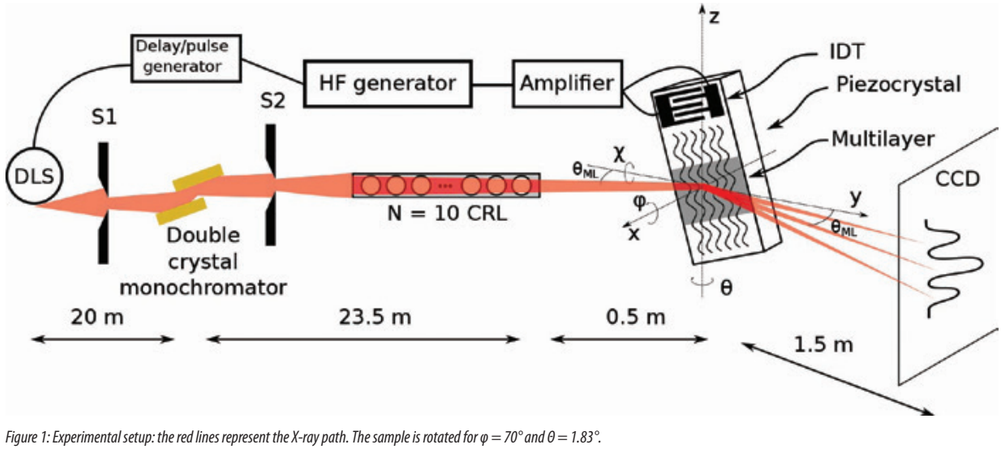

Figure 1: Experimental setup: the red lines represent the X-ray path. The sample is rotated for φ = 70° and θ = 1.83°.

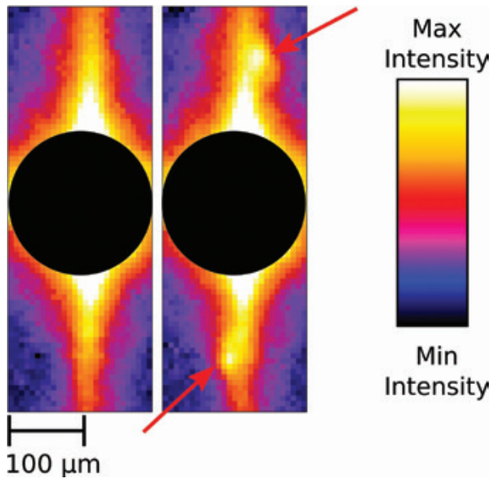

Figure 2: Experimental CCD camera images. The exposure time was 1 s. Surface plane is horizontal, scattering plane vertical. The saturating multilayer Bragg reflection in the middle was covered by a filled circle to avoid distraction from the important parts of the image. SAW is off (left). The two small peaks (arrows) are the m =1 diffraction satellites due to the scattering on the SAW grating (right). They are separated from the main peak horizontally, as well as vertically, which facilitates the detection. The colour scale was modified to emphasise the diffraction satellites.

The substrate was a Y cut of Lithium Niobate ($LiNbO_3$), a piezoelectric crystal. For our sample, the resonance frequency was 289 MHz, and the SAW wavelength was 12 µm. The propagation velocity was 3468 m/s.

X-ray diffraction from a SAW-modulated Si/W multilayer was studied in a four-circle diffractometer at the B16 beamline at Diamond. The X-ray energy of 8 keV was selected by a double Si crystal monochromator. The beam was focused on the detector using 10 refractive Be lenses. The focal spot on the detector was 6 µm. A charge-coupled device (CCD) camera detector was used to measure the diffracted intensity. The SAW was excited using a high-frequency generator, and a wideband radio frequency amplifier with 5 W power. The Bragg angle θ at the SiB4 C multilayer was 1.83, and the sample was tilted about the x axis by φ 70°. SAW trains were emitted with 100 ns duration, see Figure 1. The emission of the SAW was correlated with the Diamond storage ring in order to scatter the X-rays emitted from the selected electron bunch. The delay, and consequently the selected bunch, was controlled by a delay generator.

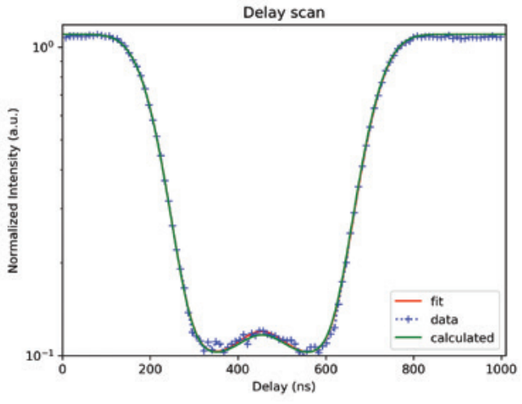

Figure 3: Measured data (blue), the Gaussian fit (red), and the calculated shape of the curve (green). The resolution of the measured curve is 10 ns.

In the CCD camera images (Fig. 2) the peaks are rather well separated, even though they are not entirely decoupled from the halo of the main beam. Calculated from experimental data, including the scattered intensity from the non-disturbed area, the rejection ratio is about 50%. However this does not reflect the real rejection ratio of a SAW pulse picker, which is proven in static experiments to be around 0.1% [4,5]. To calculate the time resolution of the pulse picker, the integrated intensity from the satellites was correlated to the delay time. The integration area in the CCD image was automatically selected by a numerical algorithm. For a given delay between the storage ring signal and the SAW trigger, the SAW crosses the footprint of the X-ray beam in the moment when a specific bunch is being scattered. When the SAW train reaches the beam footprint and interacts with the multibunch, the intensity is maximal, normalised to 1 in the plot in Figure 3. The intensity decreases when the delay is such that the SAW train reaches the footprint during the ion gap, and it has a relative maximum in the middle of the gap due to the interaction with the single bunch. The time resolution corresponds to the full width at half-maximum of the peak at the single bunch position; in our experiment it was 117 ns.

References:

1. Hiramoto, T. *et al.* High Frequency Time Modulation of the X-ray Beam Diffracted from a LiNbO3 Crystal by Surface acoustic Waves, *Japanese J of App Phys* **24 (2)**, doi:10.1143/JJAP.23.L193 (1985).
2. Tucoulou, R. *et al.* High frequency electro-acoustic chopper for synchrotron radiation, *NIM B* **132**, 207-213, doi:10.1016/S0168-583X(97)00405-9 (1997).
3. Irzhak, D. & Roshchupkin, D. X-ray diffraction on the x-cut of a Ca3TaGa3Si2O14 single crystal modulated by a surface acoustic wave, *J App Phys* **115**, 244903, doi:10.1063/1.4884875 (2014).
4. Erko, A. *et al*. Modern Developments in X-ray and Neutron Optics, *Springer Series in Optical Sciences* (2008)
5. Vadilonga, S. *et al.* Observation of sagittal X-ray diffraction by surface acoustic waves in Bragg geometry, *J Appl Cryst* **50**, 525-530, doi:10.1107/S1600576717002977 (2017).

Funding acknowledgement:

This work was carried out with the support of Diamond Light Source.

Corresponding author: Simone Vadilonga, Helmholtz Zentrum Berlin, simone.vadilonga@helmholtz-berlin.de

Imaging and Microscopy Group

Paul Quinn, Science Group Leader

Imaging and Microscopy is a newly formed science group, which brings together eight experimental facilities (I08, J08, DIAD, I12, I13-1, I13-2, I14 and ePSIC) with a new imaging group leader to coordinate and drive the group's activities. These facilities use electrons and X-rays to image samples under different experimental conditions across a diverse range of length scales and time scales. Different contrast mechanisms allow for imaging of sample properties such as elemental composition, density and structure and this ability to extract image sample properties in minute detail lends itself to a wide range of scientific areas from chemistry and catalysis to environmental science, materials science, biology, medicine, and cultural heritage.

The Scanning X-ray Microscopy (SXM) beamline (I08) is for morphological, elemental and chemical speciation on a broad range of organic-inorganic interactions in a 250 - 4400 eV photon energy range, and sample investigations under ambient or cryogenic conditions. I08 has a range of applications including biological and biomedical sciences, earth and environmental science, geochemistry, and materials science. During the reporting period, the performance for lower photon energies on I08 was improved significantly, in particular for carbon Near Edge X-ray Absorption Fine Structure (NEXAFS) spectromicroscopy. I08 faced its first major upgrade as a result of the Scanning and Mapping projects. This upgrade is now finalised and offers users superior performance in data collection and software interfaces to the user community. The design and construction of a soft X-ray spectro- and tomo-ptychography branchline (J08) progresses according to plan. This instrument is expected to be available for experiments in the second half of 2019.

The Dual Imaging and Diffraction (DIAD) beamline (K11) will be the first beamline to offer two X-ray microscopy techniques (imaging and diffraction) applied synchronously with a switching time of a few milliseconds. This enables *in situ* structural characterisation experiments taking advantage of both techniques simultaneously.

DIAD is being built to use light from a ten pole permanent magnet wiggler. The diffraction technique is conducted using monochromatic light, whereas the imaging technique can be performed with monochromatic or polychromatic ('pink') beam. The X-ray energy can be chosen separately for both techniques in the range from 7 - 38 keV. The beamline is under construction and is expected to start commissioning activities in the middle of 2019. First users are expected by the end of that year. The user-community is already heavily engaged in many aspects of beamline operation, particularly in the selection and specification of dedicated sample environments. A mechanical test-rig for diffraction and tomography will be one of the main instruments to allow *in situ* experiments for a variety of scientific disciplines like engineering and material science, bio-materials and hard tissues, geology and mineralogy, and soil-plant interactions. The beamline will also aim to provide sample environments for other communities such as energy, electro-chemistry and corrosion science.

The I12 (JEEP) beamline uses a 4.2 T superconducting wiggler to provide polychromatic and monochromatic X-rays in the energy range 50 - 150 keV. The high photon energies provide good penetration through large or dense samples. The beamline offers beam sizes ranging from 50 x 50 microns for diffraction, up to 90 x 25 mm for imaging. These beam characteristics enable the study of materials and processes inside sample environments without unacceptable attenuation of the beam, using macro-scale samples that are more representative of the process under study. X-ray techniques available are radiography, tomography, energy-dispersive diffraction, monochromatic and white-beam 2D diffraction/scattering and small-angle X-ray scattering. The beamline's two flexible experimental hutches allow users to bring their own rigs and sample chambers. I12 has a diverse user community (materials science and engineering; chemical processing; biomedical engineering; geoscience; environmental science; physics, palaeontology) who make full use of the beamline's versatility. On the technical side, I12 has commissioned a new IR lamp furnace ("Helios"), designed for diffraction and imaging experiments on small samples and capillaries at temperatures > 1000° C. In the optics hutch, there is a new heat load management filter which removes photons below 50 keV. The new rotating disc design replaces the original fixed SiC filter design, which was unreliable. The rotating filter was developed and tested over an extended period to ensure robustness and reliability. This was achieved without disrupting beamline user operations.

The I13 imaging and coherence beamline aims for multiscale imaging in the energy range of 6 - 30 keV. The achievable resolution ranges from several microns to some tens of nanometers with two branchlines operating independently for this purpose. The Diamond-Manchester imaging branchline performs mainly in-line phase contrast tomography with a strong emphasis on dedicated sample environments. Failure of lithium batteries, material cracks, the structure of ice cream, bones under load, the storage of CO_2 in brine and sandstone are some examples of the studies conducted under realistic conditions. Two projects are currently under development for submicron and phase sensitive imaging. A new full-field microscope will perform Zernike phase contrast imaging over a field of view of 50-100 µm and a resolution of 50 - 100 nm and a grating interferometry setup will provide superb image quality, measuring the absolute phase and providing small angle information allowing us to identify nano-sized structures from micrometer resolution X-rays. The highest spatial resolution, of 30 nm,is achieved on the coherence branch with ptychographic imaging. Our most important development is that we are now able to use the EXCALIBUR photon counting detector at 50 Hz frame rate which has reduced ptycho-tomography scans from days to a few hours. We can now routinely perform ptychography as a standard user experiment, enabling the beamline's ambition for multi-scale imaging. A large number of pilot experiments are currently underway, many of which previously used the imaging branch but can now exploit higher resolution ptychographic imaging. Examples are the study of battery failure, the origin and structure of particles from the Fukushima accident, or the micro- and nano-structure of insects.

Figure 1: Construction of the hutches nearing completion for DIAD.

Figure 2: The scientists, engineers, technicians and PDRAs that make up the Imaging and Microscopy Group.

I14, the Hard X-ray Nanoprobe beamline, welcomed its first users in March 2017 which kicked off an exciting year of commissioning, developments and experiments. I14 offers a small beam of 100 - 200 nm for high resolution imaging. Over the last year I14 has offered X-ray fluorescence, diffraction and XANES mapping with spatial resolutions down to 100 nm. Thermal spray coatings, corroded metal surfaces, meteorites, metallic particles in cells, photovoltaic films and radionuclide particles are just a sample of the many science areas and successful experiments conducted so far. The beamline is still in its optimisation phase and over the coming year the spatial resolution will improve to ~50 nm and new techniques and facilities such as ptychography, cryogenic sample handling and *in situ* sample environments will be rolled out for routine use.

In 2017 the Electron Physical Sciences Imaging Centre (ePSIC) at Diamond welcomed its first users. The two transmission electron microscopes which make up the centre, a JEOL ARM 200 and a JEOL GRAND ARM 300, were brought to Diamond through collaboration with Johnson Matthey and Oxford University. The ARM 200 is a state-of-the-art probe-corrected analytical microscope capable of atomic resolution electron energy loss and X-ray spectroscopy. The ARM 300 is a dedicated imaging instrument aligned across a wide range of accelerating voltages (30 - 300 keV). It is both probe- and imaging-corrected and has numerous detectors including a fast direct electron detector (operating at up to 2000 fps). These combined capabilities make this a unique resource for electron microscopy within the UK. With *in situ* sample holders, users at ePSIC can perform variable temperature measurements from 100 to 1600 Kelvin to directly image the atomic structure of materials during thermally driven transitions. This *in situ* capability will be expanded upon over the coming year. An Oxford Instruments EDX detector has been added to the ARM 300 to allow combined X-ray spectroscopy and high-resolution imaging. The state of the art instrumentation available at ePSIC has attracted both established electron microscopists looking to develop new techniques and scientists with limited previous electron microscopy experience interested in the atomic structure of their samples. The collaboration of the expert staff at ePSIC with this range of users is helping to bring cutting edge microscopy techniques to the wider material science community.

Revealing the reactivity of iron in the Lena River basin

Related publication: Hirst C, Andersson PS, Shaw S, Burke IT, Kutscher L, Murphy MJ, Maximov T, Pokrovsky OS, Mörth C-M, Porcelli D. Characterisation of Fe-bearing particles and colloids in the Lena River basin, NE Russia. *Geochimica et Cosmochimica Acta* **213**, 553-573, doi:10.1016/j.gca.2017.07.012 (2017).

Publication keywords: Arctic; River; Iron; Organic matter; X-ray absorption spectroscopy; Transmission electron microscopy

With the melting Arctic ice cap causing its rivers to swell, understanding how organic carbon (C) is transported to the ocean and crucially trapped by these rivers is important for climate change modelling and mitigation. Reactive iron (Fe)-bearing mineral particles trap organic C in soils and continental shelves, yet the amount of reactive Fe and how it reacts with organic C in large Arctic rivers is poorly understood. Using a transmission electron microscope and the Scanning Transmission X-ray Microscopy beamline (I08) at Diamond Light Source, the size, mineralogy, and form of Fe particles in a sample obtained from a representative Arctic river basin – the Lena River and its major tributaries – were characterised. X-ray Absorption Near Edge Structure (XANES) spectroscopy and X-ray Fluorescence (XRF) mapping at I08 confirmed that Fe is transported as particles and colloids in the Lena River, and that 70% of these particles are composed of poorly crystalline ferrihyrite, which is a reactive form of Fe. Distinguishing between C and Fe at nanoscale resolution, the ferrihydrite was revealed to be in the form of discrete particles within networks of organic C, and transported by attachment to the surface of larger organic matter (>0.7 µm) and clay particles. These important insights into the reactivity of Fe-bearing particles in the Lena River basin, and thus how well Fe traps and transports organic C, show that the Lena River supplies reactive Fe to the ocean, a significant proportion of which is already associated with organic C. The result confirms that Fe-bearing particles contribute towards natural C sequestration on the continental shelf.

Iron (Fe) is abundant in the Earth's continental crust but only exists in low concentrations in the ocean. Rivers are important suppliers of Fe to the ocean. Fe is mainly transported as particles spanning a range of size, mineralogy and speciation, which together determine their reactivity. Chemically reactive Fe-bearing particles are characterised by poorly-crystalline mineral nanoparticles (e.g. ferrihydrite, lepidocrocite)[1]. These natural nanoparticles settle onto the continental shelf and are a source of dissolved, bioavailable Fe and have surfaces that sequester and transport organic carbon (OC). Globally, organic carbon associated with reactive Fe on continental shelves is 2900 – 6900 times the amount of carbon in the atmospheric carbon pool[2]. Reactive Fe therefore plays an important role in regulating the carbon cycle on Earth's surface.

Large Arctic rivers (Yenisei, Ob, Lena, Yukon, Mackenzie rivers) are important suppliers of Fe to the continental shelf in the Arctic Ocean[3]. These rivers drain areas of permafrost (ground that remains at or below 0ºC for more than two consecutive years) that preserves a vast stock of organic matter (OM) (Fig. 1). The Arctic is subject to severe climate change and higher surface temperatures are increasing the thickness of the summer active layer (the upper surface of permafrost that thaws every summer), possibly increasing the supply of organic matter to the continental shelves[3]. The capacity for reactive Fe to mobilise, transport and sequester organic carbon in the Arctic remains poorly understood, and so the aim of this study was to quantify and characterise Fe-bearing particles and their relationship with OM in a large Arctic River, the Lena River in northeast Russia.

The Lena River basin contributes the second largest discharge to the Arctic Ocean, supplying a substantial portion of particulate material to the Laptev Sea estuary and continental shelf[3]. Water samples were collected from stations along the Lena River and its major tributaries during the post-spring flood period. These stations span a wide range of topography, permafrost and latitudinal extent. Fe was separated into different size fractions: particles (> 0.22 µm), colloids (< 0.22 µm – 1 nm), aqueous (< 1 nm) Fe. The particulate fraction contained the highest proportion of Fe (~70 %) and the aqueous fraction contained the highest proportion of OC (~60 %), in all samples. Transmission Electron Microscopy (TEM) and synchrotron based Scanning X-ray Spectromicroscopy (SXM) on beamline I08 were performed on particles from the main channel and tributaries, to characterise the size, mineralogy, Fe speciation and association with organic carbon.

Photograph by Liselott Kutscher

Figure 1: The Lena River is the seventh longest river on Earth. The river and tributaries drains a basin underlain by permafrost and spans a wide range in topography and lithology.

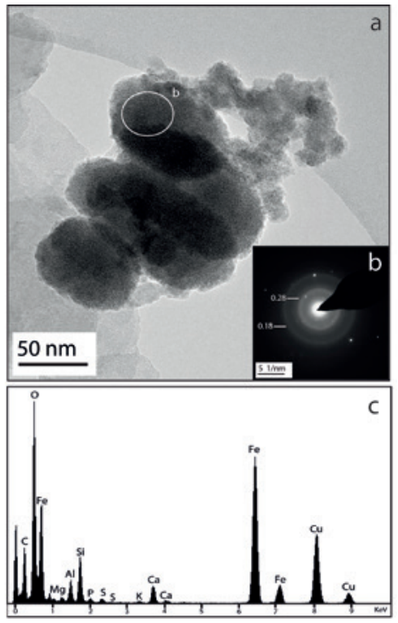

Figure 2: TEM image of a 150 nm long aggregate composed of 20-50 nm particles (a). The nanoparticles are sub-rounded and have an amorphous to poorly crystalline structure and the SAED pattern shows two major rings at 0.18 nm and 0.28 nm (b) and the EDX spectra shows that the nanoparticles are composed of Fe and O, alongside other minor elemental concentrations. The Cu signal comes from the underlying copper grid.

Reactive Fe-bearing particles were present as poorly crystalline particles (200 nm – 1 µm) composed of aggregates of smaller (< 30 nm) spherical nanoparticles (Fig. 2a). The Selected Area Electron Diffraction (SAED) patterns with two broad rings at 0.18 nm and 0.28 nm (Fig. 2b) and Energy Dispersive X-ray (EDX) peaks of Fe and O (Fig. 2c), are indicative of 2-Line ferrihydrite[4]. Poorly reactive Fe-bearing particles were identified as clay particle aggregates (illite, 500 nm to 1 µm) and crystalline iron oxides (haematite, 100 to 200 nm), that are not readily available for biological uptake or surface complexation with OM.

Organic matter structures were identified using TEM as micron-sized web-like networks of fibrils (Fig. 3a) and micron-sized bacteria cells (Fig. 3b). Darker 'inclusions' were observed within these structures and these were analysed using STXM on beamline I08. TEM and SXM were applied on the same particles, enabling novel comparison between the mineralogy and speciation of Fe associated with organic matter. X-ray fluorescence (XRF) mapping on Beamline 108 is optimised to map particles at a 50 nm resolution and can distinguish between carbon (C), nitrogen (N) and iron (Fe) in the particulate material. Maps in Figures 3c and 3d show that Fe is sitting as discrete nano-sized particles amongst C and N rich regions, suggesting that these OM structures trap and transport Fe in the Lena River basin.

X-ray spectroscopy was used to analyse the oxidation state Fe in the nanoparticles associated with the organic matter structures. Beamline I08 is optimised for this task due to the 280 – 4400 eV photon energy range and spectral resolution of 4000 over the photon energy range. Stacks of SXM energies were acquired at different photon energies within range of the Fe L-edge. These energies were used to make Fe L-edge NEXAFS (Near Edge X-ray Absorption Fine Structure) spectra with a spatial resolution of 50 nm (Fig. 3e). The acquired spectra were compared with spectra of Fe-bearing colloids in Southern Ocean waters[5], and correspond with Fe(III)-rich particles (Fig. 3e). The combined use of TEM and SXM shows that organic fibrils trap discrete Fe(III)-particles, composed of reactive ferrihydrite, in the Lena River basin, with no evidence of Fe-OC complexation or a reduced or mixed valence Fe. Hence, larger particles of reactive Fe and organic carbon are transported together in large Arctic rivers.

In this study, SXM and TEM imaging were used to characterise Fe-bearing particles and colloids in the Lena River and major tributaries. Chemically reactive Fe is identified as ferrihydrite, that accounts for 70 ± 15% of the total suspended Fe in the Lena River. Aggregates of ferrihydrite (Fig. 2) will be deposited in estuarine and shelf sediments and contribute to organic carbon degradation or traps and sequester organic carbon in Arctic shelf sediments. Nanoscale ferrihydrite associated with networks of OM or attached to the surface of clay minerals (Fig. 3) will be transported further across the continental shelf, providing a source of bioavailable Fe to the Arctic Ocean. The Arctic is subject to severe climate change threatening to alter terrestrial and ocean biogeochemical cycles. We demonstrate that the Lena River, a major Arctic River, is an important contributor of reactive Fe to the continental shelf of the Arctic Ocean. This work places constraints on the present day supply of Fe from a large Arctic river to the Arctic Ocean.

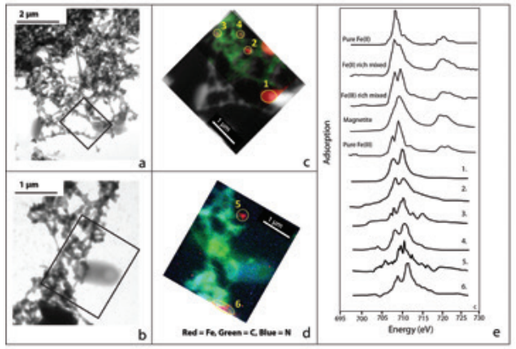

Figure 3: TEM images of web-like organic fibrils (a) and bacterial cells and organic fibrils (b), show darker 'inclusions', investigated using SXM on beamline 108. The XRF maps of these organic structures shows carbon-rich (green), nitrogen-rich region (blue) and iron-rich (red) regions (c, d). The NEXAFS spectra of Fe-rich regions were compared with spectra of Fe particles from the Southern Ocean[5], showing that Fe(III) oxides are associated with organic matter (e).

References:

1. Raiswell, R. *et al*. The iron biogeochemical cycle past and present. *Geochemical Perspectives* **1**, doi:10.7185/geochempersp.1.1 (2012).
2. Lalonde, K. *et al*. Preservation of organic matter in sediments promoted by iron. *Nature* **483**, 198-200, doi:10.1038/nature10855 (2012).
3. Holmes, R. M. *et al.* Seasonal and annual fluxes of nutrients and organic matter from large rivers to the Arctic Ocean and surrounding seas. *Estuaries and Coasts* **35(2)**, 369-382, doi:10.1007/s12237-011-9386-6 (2012).
4. Janney, D. E. *et al*. Transmission electron microscopy of synthetic 2- and 6- Line ferrihydrite. *Clays and Clay Minerals* **48(1)**, 111-119, doi:10.1346/CCMN.2000.0480114 (2000).
5. Von der Heyden, B. P. *et al.* Chemically and geographically distinct solid-phase iron pools in the Southern Ocean. *Science* **338(6111)**, 1199-1201, doi:10.1126/science.1227504 (2012).

Funding acknowledgement:

This study was funded by MetTrans, (a European Union Seventh Framework Marie Curie ITN) [Grant No.290336] and the Swedish Research Council [VR 621-2010-3917]. Beamtime was funded by Diamond Light Source [Grant No. SP11282].

Corresponding author: Dr Catherine Hirst, Department of Geological Sciences, Stockholm University, catherine.hirst@nrm.se

Investigating lithium ion battery failures

Related publication: Finegan DP, Darcy E, Keyser M, Tjaden B, Heenan TMM, Jervis R, Bailey JJ, Vo NT, Magdysyuk OV, Drakopoulos M, Di Michiel M, Rack A, Hinds G, Brett DJL, Shearing P. Identifying the cause of rupture of Li-ion batteries during thermal runaway. *Advanced Science* **5**, doi:10.1002/advs.201700369 (2017).

Publication keywords: Li-ion batteries; High-speed X-ray imaging; Thermal runaway

The 18650 cylinder is the most widely used lithium ion (Li-ion) cell geometry, powering everything from laptops to electric vehicles. Its capacity has been steadily increasing, and now more than ever, the safety of Li-ion batteries is of the utmost importance. Cell failure is extremely rare during normal operation, but under abusive conditions the active materials within Li-ion batteries break down exothermically, generating large amounts of heat that can lead to a positive feedback loop, fire and even explosions – a phenomenon known as thermal runaway.

Rupture of 18650 cells during thermal runaway is one of the most hazardous types of failure, and yet the stages leading to rupture are not well understood. Researchers are investigating the cause of rupture to further our understanding of failure mechanisms and to guide the development of safe next-generation Li-ion cells. To capture the dynamic sequence of events with enough detail, they need to use Diamond's high-speed X-ray imaging capabilities. The I12 JEEP beamline offers a large field of view for high speed and high energy imaging of Li-ion battery failures. Their results show that the introduction of a bottom vent on commercial cells can help reduce the risk of rupture and improve the safety of the cell.

High-energy density lithium ion batteries are used for a wide range of applications, from portable electronics and medical devices to aerospace and manned spaceflight. Maintaining a high standard of safety for lithium ion cells is more important now than ever before particularly since high-energy density cells are expected to operate under challenging conditions for applications that are often 'mission critical'. For example, when a battery pack for the auxiliary power unit caught fire on a Boeing Dreamliner in 2014, the entire fleet of aircraft was grounded for several months due to passenger safety concerns[1].

Catastrophic failure of lithium ion batteries stems from the occurrence of 'thermal runaway' where, at a critical temperature, a series of exothermic reactions cascade throughout the cell. This process generates a lot of heat and produces large amount of product gas, both of which present significant safety challenges to mitigate hazards. For example, the rapid generation of heat and gas inside an 18650 cell can lead to violent ruptures and fires. One of the most violent failure mechanisms occurs when the pressure inside cylindrical 18650 cells reaches a critical point where the cell bursts and generates projectiles from its ejecting contents. The ejected contents consist of hot, electrically conducting, reacting material that can lead to propagation of thermal runaway to neighbouring cells via heat dissipation or short circuiting elsewhere. Identifying the cause of rupture is crucial for manufacturers to carry out an informed approach to engineering safer cell designs. However, in a previous study[2], bursting was shown to occur in less than 0.01 s, which along with the events occurring inside a steel casing, makes the dynamic occurrences particularly challenging to capture and characterise.

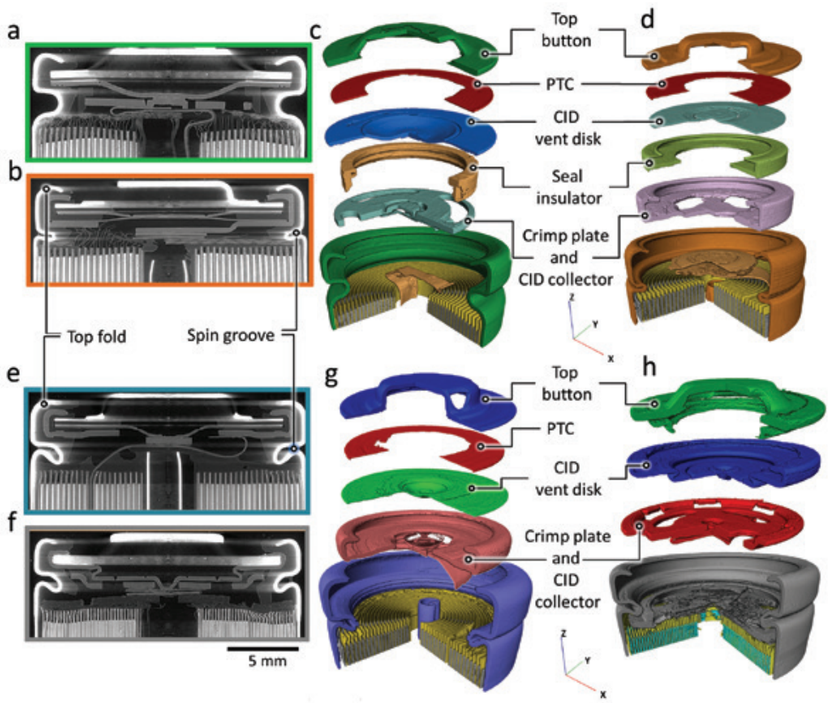

Figure 1: Greyscale orthoslices and 3D reconstructions from X-ray CT of 18650 cells manufactured by (a,c) LG, (b,d) Panasonic, (e,g) Sanyo, and (f,h) Samsung.

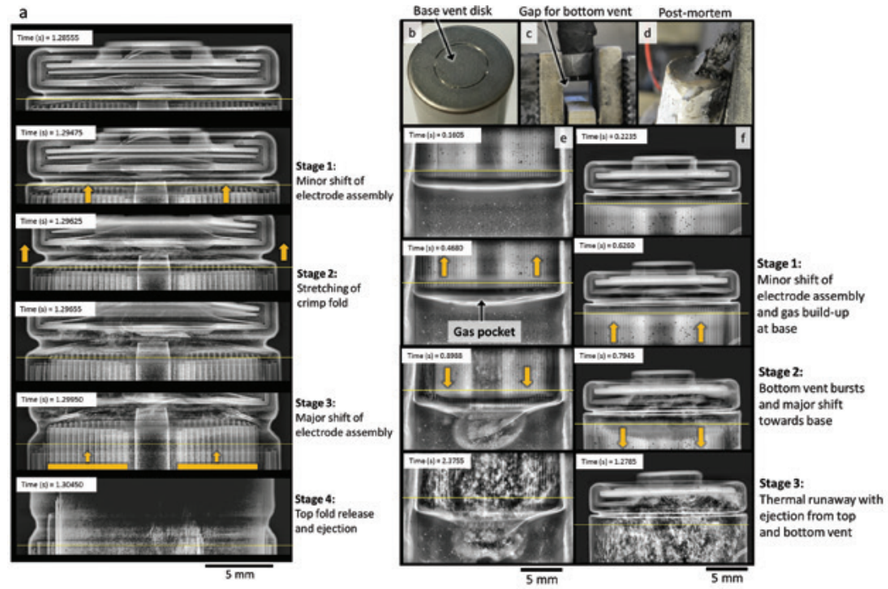

Figure 2: (a) Time-stamped radiographs showing the stages leading to the rupture of an 18650 Panasonic cell. (b-d) Photographs showing the bottom vent feature in its fresh state, during the experiment, and following thermal runaway. (e,f) Radiographs taken at the top and bottom of a base-vent cell showing the movement of the electrode assembly during thermal runaway.

High energy and high flux synchrotron X-ray sources such as Diamond Light Source hold the exceptional capability of carrying out high-speed and high-resolution X-ray imaging with a high energy beam[3]. Even the most rapid failure mechanisms of lithium ion batteries can be captured in detail and the interaction between the mechanical design of commercial cells and the rapid internal structural dynamics during thermal runaway can be examined. In this study[4], high speed X-ray imaging at up to 4000 frames per second (fps) was used to elucidate the stages that lead to violent rupture of 18650 cells. The failure mechanisms of different commercial cell designs (Fig. 1) were characterised and compared with respect to safety and merits associated with their respective designs. Failure mechanisms were characterised into four different types: controlled ejection, cell bursting, top button puncture and escape of internal mandrel. The unprecedented spatial and temporal resolution achieved at I12 allowed the distinct stages that lead to each type of failure to be classified (Fig. 2). For example, across all cell designs, three consistent steps preceded violent rupture and ejection of cell contents. First, the spin-groove extended (see labelling of components in Figure 1), followed by the electrode assembly shifting and clogging the vent, and finally, the top-fold straightened out and released the header components leading to ejection of the entire electrode assembly.

The shift of the electrode assembly towards the vent that led to clogging, is thought to have resulted from an insufficient gas flow being able to pass through the core of the assembly from the base of the cell. This led to the electrode assembly shifting in the direction of the escape path towards the vent, hindering the flow of escaping gas, and leading to a rapid pressure rise within the casing of the cell. A practical application of this result was then explored by introducing a second vent on the base plate of an 18650 cell. The simultaneous relief of pressure from the top and bottom of the cell was shown to drastically reduce the risk of violent rupture and ejection, most notably by improving the relief of generated gas and avoiding the shift of the electrode assembly that previously caused clogging.

The insights achieved in this work indicate that to achieve a high standard of safety for next generation lithium ion batteries, cell designs must evolve alongside their increasing energy density and propensity to catastrophically fail. This study presented the first example of high-speed X-ray imaging being used to link internal structural dynamics to external risks posed during thermal runaway, and demonstrates the potential of this diagnostic approach to be combined with other metrics of risk such as heat generation, gas generation, and internal temperature measurements.

References:

1. Air Accidents Investigation Branch, Report on the serious incident to Boeing B787-8, ET-AOP London Heathrow Airport on 12 July 2013. *Aircraft accident report 2/2015* (2015).
2. Finegan, D. P. *et al.* In-operando high-speed tomography of lithium-ion batteries during thermal runaway. *Nature Communications* ***6***, 6924, doi:10.1038/ncomms7924 (2015).
3. Drakopoulos, M. *et al.* I12: the Joint Engineering, Environment and Processing (JEEP) beamline at Diamond Light Source. *Journal of Synchrotron Radiation* ***22*** **(3)**, 828-838, doi:10.1107/S1600577515003513 (2015).
4. Finegan, D. P. *et al.* Identifying the Cause of Rupture of Li-Ion Batteries during Thermal Runaway. *Advanced Science* **5**, 1700369, doi:10.1002/advs.201700369 (2017).

Funding acknowledgement:

The authors would like to acknowledge funding from the EPSRC (EP/ N032888/1 and EP/M009394/1), the Royal Academy of Engineering, the STFC (ST/N002385/1), and the UK National Measurement System. These experiments were performed between beamlines ID19 at the ESRF (Grenoble, France) and I12 at Diamond Light Source (Harwell, UK). Finally, the authors would like to acknowledge the help and support from the NASA Johnson Space Center.

Corresponding author: Dr Donal Finegan, National Renewable Energy Laboratory, USA, donal.finegan@nrel.gov

Corrective glasses provide sharper X-ray vision

Related publication: Seiboth F, Schropp A, Scholz M, Wittwer F, Rödel C, Wünsche, M, Ullsperger T, Nolte S, Rahomäki J, Parfeniukas K, Giakoumidis S, Vogt U, Wagner U, Rau C, Boesenberg U, Garrevoet J, Falkenberg G, Galtier EC, Lee HJ, Nagler B, Schroer CG. Perfect X-ray focusing via fitting corrective glasses to aberrated optics. *Nature Communications* **8**, 14623, doi:10.1038/ncomms14623 (2017).

Publication keywords: X-ray optics; Aberration correction; Phase plate; Ptychography

The intense X-ray light produced by modern synchrotron radiation sources and X-ray free-electron lasers (XFELs) allows the fine structure and dynamics of matter to be studied in exquisite detail. In principle, beams should be able to be focused to a few nanometres and below. Such small intense X-ray nanobeams are crucial to concentrate the radiation onto a given sample. However, the beam's short wavelength places stringent requirements on today's X-ray optics, which limit resolution due to refractive, diffractive, or reflective distortions (known as aberrations) of the resulting image.

To understand and correct these distortions, an X-ray microscopy technique known as Ptychography, was performed at Diamond Light Source's X-ray Imaging and Coherence beamline (I13), which offers a very flexible optics and sample environment, ideal for testing new X-ray optics. Using the Coherence Branchline (I13-1), built specifically to provide resolution beyond the limitations of X-ray optics and scintillator-coupled detectors, Ptychography elucidated the wavefield created by the X-ray optics with high spatial resolution and sensitivity. From this, wavefield errors from the optics alone were plotted in great detail to design appropriate corrective glasses. Capable of correcting optics beyond current manufacturing limitations, the glasses consist of an X-ray phase plate placed on the optical path following the lens to achieve focusing that is largely insensitive to small shape and surface errors. These glasses were further refined via Ptychography by measuring the optics with the corrective glasses on, to determine and correct any remaining distortions. Applied in next-generation synchrotrons and XFELs, the method could dramatically improve resolution in fields such as X-ray microscopy, serial crystallography, single-molecule imaging and many more.

The ever-increasing brightness of modern storage ring sources and XFELs enables studying the structure and dynamics of matter with unprecedented spatial and temporal resolution. To fully benefit from the power of these sources, it is crucial to confine the X-ray beam and concentrate the radiation onto the sample. This is essential to improve not only the spatial resolution and sensitivity of X-ray analytical techniques, but also to generate highly intense X-rays that facilitate the generation of extreme states of matter and enable the study of non-linear X-ray phenomena. However, this requires X-ray optics with high numerical aperture (NA) that can withstand the extremely bright pulses of modern sources. Unfortunately, suitable X-ray optics are limited by fabrication technology, and trade-offs need to be made between aberration-free performance and highest possible NA.

Ptychography[1], an X-ray scanning coherent diffraction microscopy technique, has evolved to one of the most important methods for X-ray beam and optics characterisation. Here, a nano-structured sample, positioned in the vicinity of the focal plane was scanned across the beam while far-field diffraction patterns were recorded with appropriate spatial overlap. With the help of elaborate phase retrieval algorithms[2] the complex wavefield at the sample position could be retrieved unambiguously. From these data the wavefront error in the exit pupil of the focusing optics was calculated with highest sensitivity and spatial resolution[3] (Fig. 1). For focusing a stack of 20 beryllium compound refractive lenses (Be CRLs) with a radius of curvature of 50 µm and a geometrical aperture of 300 µm was used at an X-ray energy of 8.2 keV. The rotational symmetric phase error shown in Fig. 1, a clear signature for spherical aberration, originates from tiny but repetitive shape errors of individual Be CRLs within the large lens stack. To reproduce the wavefield error in Fig. 1, numerical simulations have been performed where the lens shape deviation from an ideal parabola was iteratively refined. The retrieved deformation of an individual lens surface is shown in Fig. 2. As Be CRLs are fabricated via a coining process by pressing two parabolic stamps into a Be foil, an improvement of the already very small deformation error of 500 nm by a significant amount appears very challenging.

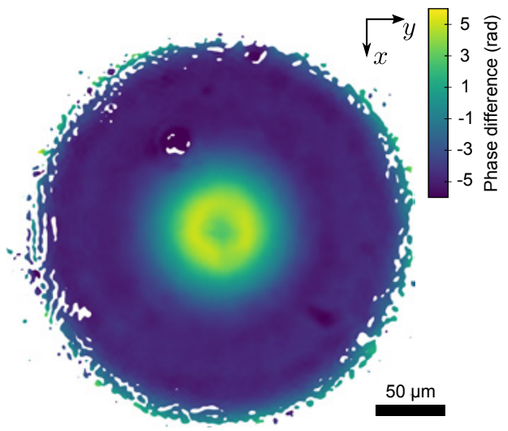

Figure 1: Measured wavefront deformation at the lens exit pupil compared to a spherical wave.

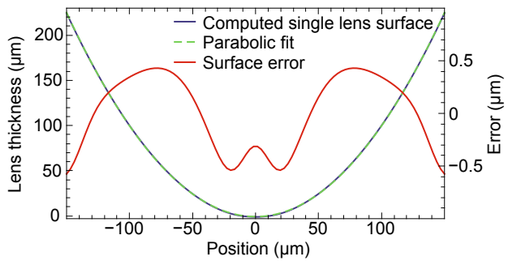

Figure 2: Modelled lens deformation of a single lens surface within the stack of 20 bi-concave Be CRLs.

Instead, a general scheme to correct for residual aberrations in any X-ray optics was employed. By introducing corrective glasses into the optical path -- tailor-made to the specific optics -- true diffraction-limited focusing could be achieved. From the phase error in Fig. 1 a corrective phase plate was modelled that corrects the wavefield deformation by introducing an opposing phase shift. Fig. 3 shows the phase plate made out of fused silica by ultrashort-pulse laser ablation[4].

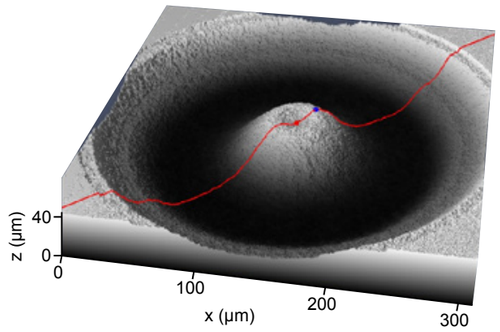

Figure 3: A tailor-made phase plate was manufactured by ultrashort-pulse laser ablation from fused silica to correct the whole lens stack at once for aberrations

Due to spherical aberration, the nanofocus using the uncorrected optics was spoiled by X-rays being partly focused further upstream, highlighted by the arrow in Fig. 4a. This led to unwanted radiation around the focal spot, shown by the solid green line in the focal plane profile of Fig. 4c. Compared to a perfect lens (dashed red line in Fig. 4c), intensities in side lobes were increased by over an order of magnitude. In practice, these side lobes reduce the attainable resolution in X-ray microscopy applications due to an effective spot size broadening, illustrated by the radially integrated intensity profile in Fig. 4d. In addition, the peak intensity in the main focal spot is significantly reduced, as most of the radiation is distributed in the outer lobes.

By installing the tailor-made glasses behind the Be CRLs, the performance of the optics was strongly improved. With the suppression of spherical aberration, most X-rays were now focused within the same focal plane, illustrated by the clean beam caustic in Fig. 4b. This resulted in lowered intensities by an order of magnitude in lobes surrounding the focal spot, shown by the dotted blue line in Fig. 4c, and ultimately a reduced effective focal spot size as shown in Fig. 4d. The corrective glasses transformed the Be CRL optics from an aberrated system into a diffraction-limited hard X-ray optics. While the uncorrected optics could only focus less than 30 % of the radiation compared to the ideal optics (Strehl ratio below 0.3), the corrected focus gathered more than 85 % (Strehl ratio 0.85). At the same time the geometrical aperture and NA of the optics is unaffected.

With this novel scheme, many X-ray optics can be improved in performance beyond current manufacturing limitations. The principle is not only applicable to refractive optics as shown here, but can also be transferred to reflective and diffractive optics as well. As the glasses are very compact and easy to align, they can also be retrofitted to existing beamline optics. This benefits not only the resolution and sensitivity in classical X-ray microscopy schemes, but may also lead to new opportunities for isochoric X-ray heating and non-linear X-ray optics at XFEL sources.

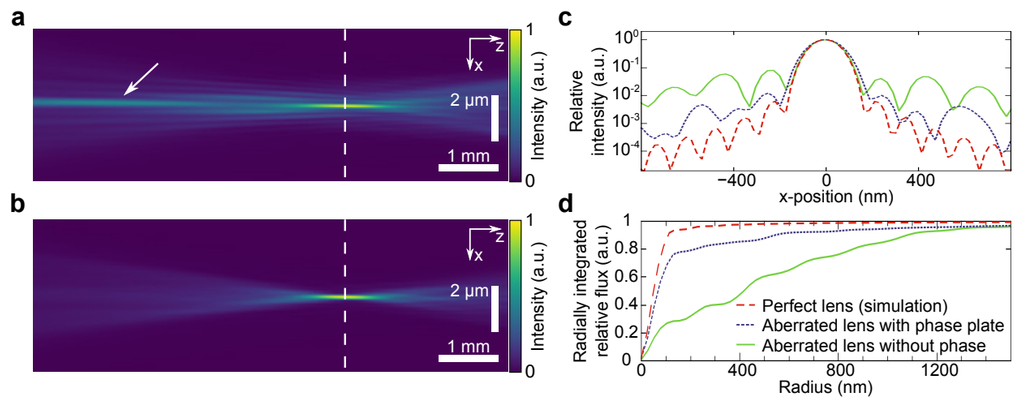

Figure 4: (a) Beam caustic in horizontal projection along the optical axis. For Be CRLs with spherical aberration the paraxial rays are focused further upstream (arrow), leading to pronounced side lobes in the main focal plane (dashed vertical line). (b) The Be CRLs equipped with the phase plate show almost no aberration. (c) While the central focal spot is unaffected in size, intensity in side lobes is reduced due to the phase plate. (d) By concentrating most of the radiation in the central speckle, the effective focal spot radius is reduced from over 800 nm to 125 nm.

References:

1. Thibault, P. *et al*. High-Resolution Scanning X-ray Diffraction Microscopy. *Science* **321(5887),** 379-382, doi:10.1126/science.1158573 (2008).
2. Maiden, A. M. *et al*. An improved ptychographical phase retrieval algorithm for diffractive imaging, *Ultramicroscopy* **109(10)**, 1256-1262, doi:10.1016/j.ultramic.2009.05.012 (2009).
3. Seiboth F. *et al*. Quantitative characterisation of aberrations in X-ray optics. *SPIE Proceedings* **9963**, doi:10.1117/12.2237646 (2016).
4. Chichknov, B. N. *et al*. Femtosecond, picosecond and nanosecond laser ablation of solids. *Applied Physics A* **63(2)**, 109-115, doi:10.1007/BF01567637 (1996).

Funding acknowledgement:

This work was supported by the German Ministry of Education and Research (BMBF) under Grant Number 05K13OD2, the DFG under Grant SCHR 1137/1-1 and the Swedish Research Council. Frank Seiboth, Andreas Schropp and Christian Rödel acknowledge funding from a Peter Paul Ewald fellowship of the Volkswagen Foundation. Parts of this research were carried out at the coherence branch of beamline I13 at Diamond Light Source and beamline P06 at PETRA III at DESY, a member of the Helmholtz Association. Use of the Linac Coherent Light Source, SLAC National Accelerator Laboratory, is supported by the US Department of Energy, Office of Science, Office of Basic Energy Sciences under Contract No. DE-AC02-76SF00515. The MEC instrument is supported by the US Department of Energy, Office of Science, Office of Fusion Energy Sciences under Contract No. SF00515.

Corresponding author: Dr Frank Seiboth, DESY, Germany and LCLS, USA, frank.seiboth@desy.de

Imaging multiphase fluid flow in permeable media

Related publication: Singh K, Menke H, Andrew M, Lin Q, Rau C, Blunt MJ, Bijeljic B. Dynamics of snap-off and pore-filling events during two-phase fluid flow in permeable media. *Scientific Reports* **7**, 5192, doi: 10.1038/s41598-017-05204-4 (2017).

Publication keywords: Multiphase flow; Permeable media; Snap-off; Capillary trapping; Pore-scale displacement

Knowing how fluids move through micron-sized voids (or 'pores') in rock kilometres below the Earth's surface is crucial information to help understand and optimise underground carbon dioxide (CO_2) sequestration, oil recovery from reservoir rocks, and a host of other processes. Oil and gas can be trapped in pores as water flows through the rock, with strong trapping beneficial for CO_2 storage and weak trapping preferable for efficient oil recovery. However, the exact nature of trapping at the pore scale is not well-understood, with inhibiting viscous and driving capillary forces both thought to play an important role in controlling flow during trapping events.

To illuminate this process, an innovative flow apparatus was engineered to replicate the high pressures and temperatures seen in reservoirs. With the Diamond Manchester Imaging Branchline (I13-2) within the X-ray Imaging and Coherence beamline (I13) at Diamond Light Source, fluid flow was imaged in 3D, at the micron scale, and with a time resolution of around a minute. I13-2 offers photon flux over a million times higher than that of a laboratory X-ray source, perfect for studying rapid dynamic processes like fluid displacement. As a result, the time-resolved imaging provided pore-by-pore analysis of the local capillary pressure during trapping events. Results reveal that water pushes oil into pore spaces in approximately 10 minutes – orders of magnitude slower than the opposite process when oil pushes out water from the pore space. After trapping, the oil rearranges in the pore space to find a new position of minimum energy and the local capillary pressure increases rapidly. These new insights provide useful information to build novel models predicting how these fluids flow and how much oil or gas is trapped.

Multiphase fluid flow in permeable media is a complex pore-scale phenomenon, which has many applications in natural and industrial processes, such as water infiltration in soils, oil recovery from reservoir rocks, geo-sequestration of supercritical CO_2 to address global warming, and subsurface non-aqueous phase liquid contaminant transport. At the pore scale, the two most important processes that compete during the displacement of a non-wetting (hydrophobic) fluid by a wetting (hydrophilic) fluid are pore-filling or piston-like displacement and snap-off; this latter process can lead to trapping of the non-wetting phase[1]. The trapping of the non-wetting phase is important: for CO_2 storage, a maximum trapping efficiency is desired whereas for oil recovery, less trapping is preferable for efficient production. Although, there are several studies reported on two-dimensional visualisation of fluid displacement and trapping, the dynamics of imbibition processes (displacement of a non-wetting fluid by a wetting fluid) leading to snap-off have not been investigated in such details in realistic three-dimensional geometry. The time-dependent information is important to validate models of pore-scale displacement and to quantify how the balance of viscous and capillary forces controls the exact nature of trapping.

We conducted dynamic flow experiments in a 3.8 mm diameter and 10 mm long Ketton limestone sample. The sample was first saturated with the brine. The system was pressurised to 10 MPa, followed by injection of oil (a

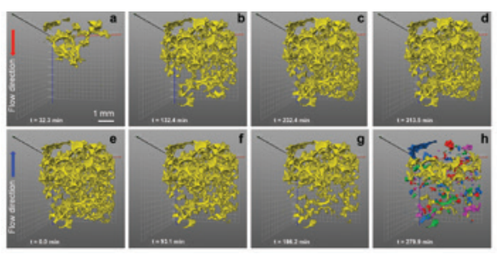

Figure 1: Drainage at t = 32.3 min (a), 132.4 min (b), 232.4 min (c) and 313.5 min (d). Sequence of imbibition at t = 0 min (e), 93.1 min (f), 186.2 min (g) and 279.9 min (h). Various colors in (h) represent disconnected oil clusters (trapped phase) after complete imbibition.

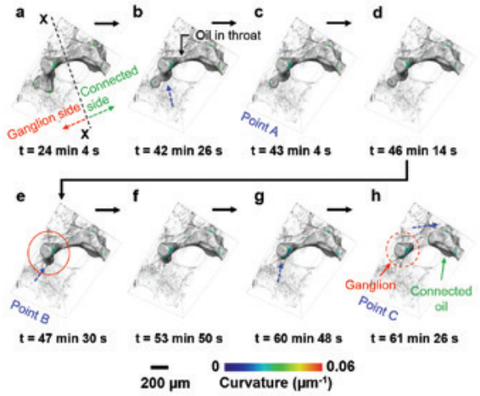

Figure 2: Snap-off during imbibition in a throat between two adjacent pores. Various times during brine injection showing oil progression and trapping in a water-wet Ketton rock sample. The rock and brine are shown semi-transparent and transparent respectively for effective visualisation. The dashed blue arrows indicate the approximate direction of interface migration. Points a-c show the events marked in Fig. 3. Time t = 0 denotes the start of the imbibition process (after acquiring the first tomographic image in imbibition). Time (t) represents the end of each tomographic image acquisition. (Singh et al.[5])

drainage process for water-wet porous media) from the top of the sample by establishing a pressure gradient of 50 kPa. The sample was imaged in three dimensions continuously during drainage using a pink beam (with photon energies up to 30 keV) at beamline I13-2. We used a voxel size of 3.28 µm and a time-step of 38 s between each three-dimensional data collection. After the completion of the drainage process (identified when there was no longer any visible change in fluid saturations), the flow was reversed by injecting brine (imbibition process) from the base of the sample at a pressure gradient of 22 kPa. The sample was imaged continuously during imbibition.

Figure 1 shows the oil phase at various time steps during drainage (Fig. 1a-d) and imbibition (Fig. 1e-h). The residual oil at the end of imbibition contains

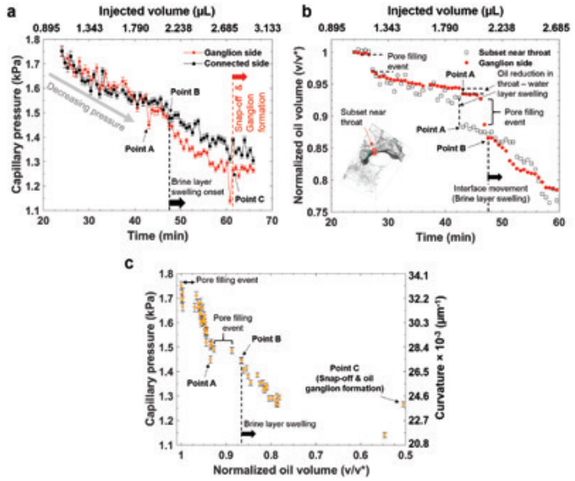

Figure 3: Local capillary pressure and oil saturation analysis during pore-filling and snap-off processes. (a) Capillary pressure is plotted against time and injected volume in the ganglion and connected side subsets that are shown in Fig. 2. (b) Oil volume (v) normalised to the oil volume (v) at t = 24 min 4 s in the ganglion-side subset and in a subset near throat (red box in inset) as a function of time and injected volume. (c) Capillary pressure in the ganglion-side subset as a function of normalised oil volume (v/v*) in the ganglion-side subset. Figure from (Singh et al.[5]).*

a number of disconnected oil ganglia (trapped phase), represented by different colours (Fig. 1h). A complete three-dimensional image sequence of drainage and imbibition processes is shown in videos (Video 1 and 2)[6].

In this study, our aim was to obtain a complete understanding of various pore-scale displacement and snap-off events that result in trapping of the non-wetting phase in the pore space. Figure 2 shows snapshots of one of the pore-filling and trapping events during imbibition. The complete three-dimensional sequence of the oil displacement process is shown in the video (Video 3)[6]. During brine injection, the brine-oil interface moves from pore to pore in a piston-like displacement without oil trapping, until it reaches the pore space marked by the red circle (Fig. 2e). Here, the brine (not shown for effective visualisation) in the adjacent oil-filled throats starts to swell. The brine layers in the throat corners continue to grow until the brine-oil interface is no longer stable, resulting in snap-off of the interface and trapping of the oil.

To explain the snap-off process quantitatively, we analyse the local capillary pressure (calculated from the Young-Laplace equation, $P_c = \sigma\kappa$, where P_c is the capillary pressure, σ is the interfacial tension between oil and brine, and κ is the total curvature estimated from an analysis of the segmented image) as a function of time and injected brine volume during the pore-filling and snap-off events observed in Figure 2. The relationship of capillary pressure, time and normalised oil volume is shown in Figure 3. Here, the ganglion and connected side represent the values measured on the left and right side of the X-X section respectively (shown in Fig. 2a). The X-X section was selected in the throat where the snap-off occurred (Fig. 2h). From Figure 3a, we observe that the capillary pressure on both sides decreases approximately linearly with injected brine volume and time. The brine-oil interface migrates from left to right without any trapping (representing pore-filling events). At point A (Fig. 3b), we observe a rapid decrease in the oil volume in the subset near the throat (open symbols in Fig. 3b corresponding to the red box in the inset picture). This is linked to the capillary pressure gradient, caused by a sudden decrease in the local capillary pressure in the ganglion side (Fig. 3a), which drives the brine flow towards the throat. Then just after 46 minutes, we observe a pore-filling event that occurs between points A and B where the capillary pressure remains approximately constant (Fig. 3c) while locally the oil saturation decreases rapidly (Fig. 3b). This type of pore-filling behaviour, however, has not been seen or hypothesised hitherto: in drainage instead we see rapid changes in capillary pressure at a constant saturation[2].

Beyond point B (Fig. 3), there is an apparent disparity in capillary pressure across the system, which drives brine in layers to flow from the ganglion to the connected side. This represents a swelling of wetting layers in the throat, as can be seen by an incremental reduction in oil volume in the throat subset in Figure 3b (open symbols). Eventually at point C (Fig. 3a, 3c), we see snap-off, resulting in the trapping of oil ganglion in the pore body. When this happens, there is a rapid rise in capillary pressure as the ganglion rearranges to find a lower energy configuration. The remarkable feature of this analysis is that the swelling of wetting layers proceeds over approximately 14 minutes. This is many orders of magnitude slower than the sub-millisecond filling observed during a Haines jump in drainage[3,4]. We have investigated three different snap-off events for different pore topologies and fluid configurations, which are reported in Singh *et al.*[5]. The time-scale for brine layer swelling in all the studied events are of the order of tens of minutes, followed by instantaneous snap-off processes. After snap-off the local pore-scale capillary pressure rises as the ganglion rearranges to find a lower energy configuration.

In conclusion, the time-resolved X-ray micro-tomography provides new insights into pore-scale fluid displacement in three-dimensional porous media. This has led us to investigate the pore-filling and snap-off events that lead to the trapping of the non-wetting phase. These findings have important implications in many fields such as oil recovery, CO_2 sequestration and remediation of oil contaminated sites.

References:

1. Blunt, M. J. Multiphase Flow In Permeable Media: A Pore-Scale Perspective. 2017. Cambridge University Press.
2. Morrow, N. R. Physics and thermodynamics of capillary action in porous media. *Ind. Eng. Chem.* **62 (6)**, 32-56, doi:10.1021/ie50726a006 (1970).
3. DiCarlo, D. A. *et al.* Acoustic measurements of pore-scale displacements. Geophysical Research Letters **30(17)**, 1901, doi:10.1029/2003GL017811 (2003).
4. Armstrong, R. T. *et al*. Interfacial velocities and capillary pressure gradients during Haines jumps. *Phys. Rev. E* **88**, 043010, doi:10.1103/PhysRevE.88.043010 (2013).
5. Singh, K. *et al*. Dynamics of snap-off and pore-filling events during two-phase fluid flow in permeable media. *Scientific Reports* **7**, 5192, doi:10.1038/s41598-017-05204-4 (2017).
6. Videos: Drainage in carbonate rock oil-phase visualization doi:10.6084/m9.figshare.4232330.v1; Waterflooding in carbonate rock oil phase visualization doi:10.6084/m9.figshare.4232354.v1; Curvature mapping during pore-filling and snap-off event in water wet carbonate rock doi:10.6084/m9.figshare.4235381.v1

Funding acknowledgement:

We gratefully acknowledge funding from the Qatar Carbonates and Carbon Storage Research Centre (QCCSRC), provided jointly by Qatar Petroleum, Shell, and Qatar Science & Technology Park. We thank Diamond Light Source for providing experimental time on Beamline I13-2 (MT11587).

Corresponding author: Dr Kamaljit Singh, Imperial College London, kamaljit.singh@imperial.ac.uk

State-of-the-art electron microscopy offers clarity on diamond defects

Related paper: Olivier EJ, Neethling JH, Kroon RE, Naidoo SR, Allen CS, Sawada H, van Aken PA, Kirkland AI. Imaging the atomic structure and local chemistry of platelets in natural type Ia diamond. *Nature Materials* **17**, 243-248, doi:10.1038/s41563-018-0024-6 (2018).

Publication keywords: Type Ia diamonds; Platelet defects; STEM; TEM; EELS

Flawless diamonds are extremely rare and expensive. Most diamonds contain defects, and for scientific and industrial applications, the defects are very important. In a naturally-formed diamond, the presence and structure of defects can be used to accurately determine the geological environment in which it was formed. The defects also shape the electronic and optical properties of diamonds, and exploiting these properties in synthetic diamonds could lead to next-generation optical storage devices, high-frequency field-effect transistors (FETs) and high-power switches.

Research into the nature of diamond defects has uncovered more than a hundred different optically-active types, many of which have an unknown atomic configuration. For more than 50 years, researchers have been investigating the platelet defect. A number of theoretical structure models have been proposed, but imaging techniques were unable to give experiments the atomic-level resolution necessary to confirm or discard them.

Now a team of researchers have made use of recent advances in electron microscopy, at the state-of-the-art electron Physical Science Imaging Centre (ePSIC), to solve the mystery of the platelet's structure. They used a combination of atomically-resolved scanning transmission electron microscopy (STEM), transmission electron microscopy (TEM) and electron energy-loss spectroscopy (EELS) to uncover the structural details of a natural diamond, and confirm the correct structural model. Further studies could shed light on how the platelet defect is formed, or structures of other types of defect, and this remarkable step forward could bring new opportunities for tailoring optical and electronic properties of diamond.

The nature of defects in diamonds has attracted considerable scientific interest, mainly due to their role in shaping electronic and optical properties[1]. They may well hold the key to next-generation devices, including optical storage, high-frequency field effect transistors and high-power switches.

Over 100 different types of optically-active defects have been identified, and in a natural diamond the presence and structure of defects plays an important role in defining colour and quality, and can be used to accurately determine the geological environment in which it formed.

Nitrogen is a common impurity in diamond, forming several different types of defect[2]. The presence and quantity of nitrogen-related defects are fundamental to diamond classification (Fig. 1). Type I diamonds have a high concentration of nitrogen, and related absorption bands in their spectra. They are further classified depending on whether nitrogen is present in an aggregated form (type Ia), or in isolated substitutional sites (type Ib). Diamonds with a low concentration of nitrogen, which do not show the absorption bands, are classified as type II.

In natural type 1a diamonds, nitrogen aggregates occur with and within extended defects on {100} planes, called platelets. Platelets have a typical diameter of tens to hundreds of nanometers. They are optically active in the infrared, with a frequency that depends upon the size of the platelet. Platelet defects are common in both natural and synthetic diamonds, but their exact atomic configuration has been a mystery for more than 50 years.

In 1940, Raman and Nilakantan used X-ray diffraction to make the first observations of platelets in diamonds, and these defects were characterised by Evans and Phaal in 1962 using TEM. A number of theoretical structural models were proposed, but until now these could not be tested experimentally.

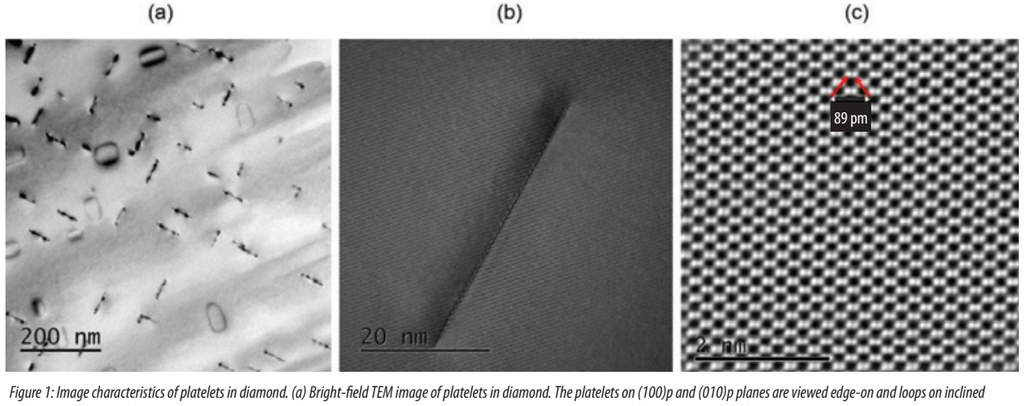

Figure 1: Image characteristics of platelets in diamond. (a) Bright-field TEM image of platelets in diamond. The platelets on (100)p and (010)p planes are viewed edge-on and loops on inclined {111} planes are also visible. (b) High-resolution TEM image showing a single platelet. The beam direction is parallel to <110> (c) HAADF STEM image of diamond viewed along an beam direction showing the 89 pm {004} separation (indicated by red arrows). [Reprinted by permission from Springer Nature: Olivier EJ et al. doi:10.1038/s41563-018-0024-6 (2018)].

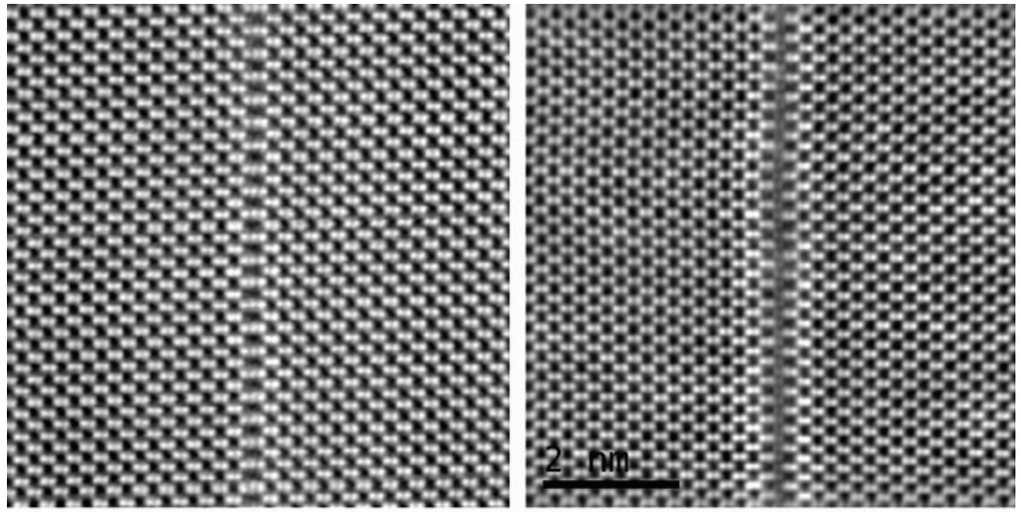

Figure 2: High-resolution HAADF STEM images of two platelets viewed edge-on along <110> directions showing the asymmetric nature of the platelet structure. (a) Image of platelet A. (b) Image of platelet B. [Reprinted by permission from Springer Nature: Olivier EJ et al. doi:10.1038/s41563-018-0024-6 (2018)].

Using STEM and TEM to image carbon materials is particularly challenging, as the light atoms show a low contrast and are easily displaced by electron irradiation. The interatomic distances that need to be resolved are shorter than most other elements, and it is only now that recent advances in aberration-corrected electron microscopy at low voltage have made it possible to image platelets with sub-Ångström spatial resolution and sufficiently high contrast.

Using atomically-resolved scanning STEM, TEM and EELS, a team of researchers from the UK and South Africa have imaged the atomic structure and local chemistry of platelets in a natural type Ia diamond.

Previous work found evidence of a strong link between nitrogen and platelets, suggesting that nitrogen may play an important role in the formation and structure of these defects. EELS spectra from the core of several platelet defects revealed the presence of a nitrogen K-edge, and subsequent studies (also predominantly using EELS) confirmed the detection of measurable quantities of nitrogen in platelets. However, the quantities detected are generally too low to suggest a nitrogen-only platelet structure; the presence of carbon is also necessary.

The new study presents aberration-corrected high-resolution STEM images, which show the atomic arrangement in the platelet core. Its findings are supported by EELS data from the core, which enable a complete description of the platelet structure.

The team used aberration-corrected STEM imaging in high-angle annular dark field (HAADF) mode, together with EELS spectrum imaging, to study the atomic structure and chemical composition of platelets in greater detail (Fig. 2). They also recorded high-resolution TEM (HRTEM) images, and then qualitatively compared HRTEM and STEM images to simulated images generated from the various theoretical structural models.

High spatial-resolution EELS spectrum imaging was used to investigate the presence, distribution and coordination environment of nitrogen in the platelets, taking care to use sufficient flux for accurate signal detection while avoiding progressive electron-beam-induced damage of the platelet structure. The results showed clear evidence for the presence of nitrogen within the defect.

The change in the EELS structure of the carbon K-edge at the defect core, and its similarity to the nitrogen K-edge, indicates that the defect core contains both atomic species in an interstitial arrangement. The presence of a pre-edge feature in both carbon K- and nitrogen K-edges indicates trigonal distortion of the lattice with the consequent coordination environment of the interstitial atoms being three-fold rather than four-fold.

The experimental results favour one particular structural model, the 'zigzag' model, in which interstitials of carbon or nitrogen are arranged at alternating (zigzag) sites. They also confirm earlier studies showing that the platelet is primarily composed of carbon, with a small fraction of nitrogen.

It is still unclear how these platelets form and the role of nitrogen in their formation, and further studies at different stages of platelet formation could further our understanding. However, this is a remarkable step forward in characterising a challenging material, and it is hoped that these new imaging capabilities will also shed light on other diamond defects with unknown structures. A new level of clarity on the atomic structure of these defects will offer up new opportunities for tailoring the optical and electronic properties of diamond.

References:

1. Bosak, A. *et al.* Symmetry of platelet defects in diamond: new insights with synchrotron light. *Acta Cryst* **B66**, 493-496, doi: 10.1107/S0108768110031071 (2010).
2. Goss, J.P. *et al.* Interstitial nitrogen and its complexes in diamond. *Phys Rev B* **70**, 235208, doi:10.1103/PhysRevB.70.235208 (2004).

Funding acknowledgment:

E.J.O., J.H.N., R.E.K. and S.R.N. acknowledge the financial support of the NRF and DST in South Africa and the DST-NRF Centre of Excellence in Strong Materials at the University of the Witwatersrand. A.I.K. acknowledges financial support from EPSRC and the Royal Society. We thank Diamond Light Source for access and support in use of the electron Physical Science Imaging Centre during part of this work.

Corresponding author: Prof Angus Kirkland, ePSIC and Oxford University, angus.kirkland@diamond.ac.uk

Crystallography Group

Heribert Wilhelm, Science Group Leader

The Crystallography Science Group comprises beamlines I11, I15, I15-1, and I19, members of the former Engineering & Environment and the Materials Villages. The reorganisation of the beamlines into Science Groups will enhance the collaboration across Diamond. Furthermore, the technical and scientific expertise within the Crystallography Science Group can be fully exploited to provide the basis for future development and pioneering experiments.

The Crystallography Science Group beamlines employ various X-ray scattering and diffraction techniques to study structural properties of crystalline, amorphous, and liquid materials at ambient and different non-ambient conditions. These powerful facilities are used for a wide range of science disciplines, from Condensed Matter Physics, Chemistry, Engineering, Earth and Materials to Life Sciences. Important research fields cover *in situ* studies of batteries, synthesis of new materials as well as structural studies at extreme temperature and/or pressure conditions. The high demand and productivity of the beamlines are reflected by the output of about 150 publications in 2017.

I11 Update

The High-Resolution Powder Diffraction Beamline (I11) uses monochromatic X-ray beams with high brightness and energies in the range of 6 - 25 keV for high-resolution and time-resolved powder diffraction experiments, either in the first experimental hutch (EH1) or for long duration experiments (LDE) in EH2. The beamline provides a suite of different sample environments for EH1 to study the changes of structural properties under the influence of an external control parameter, such as temperature or gas exposure (see highlight by E. Tsang). The unique LDE facility, in operation only for a few years, is in high demand for studying processes happening on time scales of months to years. Currently, there are 10 experiments running, each under specific conditions, that are exposed to the X-ray beam periodically to track any structural changes. Each two-dimensional diffraction pattern is automatically calibrated and reduced to a one-dimensional diffractogram ready for refinement analysis.

New sample environments and equipment are continuously developed. Recent examples are the benzene-vapour panel for absorption work of porous frameworks and the high-temperature capillary furnace (design stage) to study material behaviour up to 1200° C, both for EH1. A cold-cell for LDE has been commissioned recently. It operates in a moderate temperature range around 0°C, but achieves cooling rates as low as 0.3°C per day. This specification was required for the investigation of slow mineral formation in sea-ice. Furthermore, coin cells for *in operando* battery research are now in use in both experiment hutches.

I15 Update

The Extreme Conditions beamline (I15) provides poly- and monochromatic X-rays in the energy range 20 – 80 keV. The majority of experiments aim to reveal the structural properties of materials under extreme pressure conditions by using the diamond-anvil cell, also in combination with resistive or laser heating.

During the last year, a laser-heating system has been fully integrated into the micro-focussing station of I15. It provides double-sided heating with an off-axis YAG laser-delivery combined with the possibility to adjust remotely the position of the heated part of the sample to the spot of the focussed X-rays. Thermal emission spectra from both sides of the sample are recorded during *in situ* diffraction and can be processed automatically post heating for temperature determination. The set-up has already been used in a number of experiments (see highlight by D. Laniel). Improving user-friendliness, such as alignment of the pressure cell with respect to the lasers and the installation of a new laser are under way.

The beamline also provides tools and special beam conditions for various research fields. One example is the high demand for pressure equipment from users outside the high-pressure community studying structural changes in porous materials induced by pressure ranging from a few bar to several 10 kbar. On the other hand, focussed high energy X-rays (76 keV) for diffraction studies or tuning the energy across an absorption edge for anomalous scattering experiments have been used by users from various disciplines.

I15-1 Update

The X-ray Pair-Distribution Function Measurements beamline (I15-1) employs three discrete energies – 40, 65, and 76 keV – of the X-ray spectrum of the horizontally off-centred part of I15's wiggler fan. The beamline is devoted to X-ray Pair-Distribution Function (XPDF) measurements and became operational in April 2017. Since then it has had very successful experiments from a diverse user community. The short- to medium-range structural information that XPDF provides have covered diverse areas such as energy and porous materials, pharmaceuticals, and Earth sciences. The high-quality Pair Distribution Function (PDF) data produced for crystalline, semi-crystalline and amorphous materials is already resulting in high-impact publications, such as a recent study on glassy- and liquid-porous materials (see highlight by T. Bennett).

The beamline team, together with the controls and software groups, continues to make strides towards their vision of providing quality, automatically processed PDF data at the point of data collection. The database, which will store the required sample information, is complete. The collected two-dimensional scattering data are already automatically processed into one-dimensional data instantaneously, suitable for input into external PDF analysis software. PDF data processing within Diamond's DAWN software is undergoing further improvements before an anticipated release later in 2018.

Proposals to I15-1 have had an increasing emphasis on *in situ* measurements. The initial sample environments which allowed for a 100-1000 K temperature range have been complemented by a range of apparatus allowing to perform PDF studies on reactions under a flow of gas, crystallisation during hydrothermal synthesis, and phase changes during electrochemical cycling. I15-1 is now developing a range of liquid-based sample environments to enable time-resolved measurements on reacting solutions. Since April 2018, I15-1 offers rapid access beamtime via a mail-in route and hope to welcome their first proprietary industrial users.

I19 Update

The Small-Molecule Single-Crystal Diffraction beamline (I19) uses X-rays with energies in the range of 5 – 25 keV to determine the structures of single-crystalline small-molecule systems, both as a means of characterising newly synthesised molecules or for the study of structural change induced by a physical variable, such as high-pressure (see highlight by E. Brechin) or gas exposure.

The transport of pre-mounted samples to Diamond and a cryogenic storage has been realised during last year. It ensures that the samples are stored under controlled conditions until they are loaded into the robot immediately prior to beamtime. This has paved the way for remote-access operation of the beamline. Users from the North-East England BAG have moved to operating the beamline completely remotely from the University of Newcastle – including sample exchange, data collection and processing. This mode of operating in the first experimental hutch (EH1) makes it possible to carry out chemical crystallography studies in a more responsive manner as beamtime can be scheduled in more regular and shorter periods.

An on-axis viewing camera has been installed in EH2 to improve the alignment of the crystals. The system also includes a spectrometer for *in situ* ruby-fluorescence measurements, needed for the determination of the pressure exerted to the samples contained within gas-membrane driven diamond-anvil cells. Now a series of high-pressure structure determinations can be carried out without the need to remove the pressure cell from the diffractometer for each pressure change. Furthermore, a static liquid-cell has been developed in collaboration with the University of Edinburgh. It operates between a few hundred bar to several kbar of pressure, i.e. a pressure range of most interest to technological applications. It allows the pressure to be adjusted in fine steps and structural information to be obtained to a high degree of crystallographic detail.

Figure 1: The scientists, engineers, technicians and PDRAs that make up the Crystallography Group.

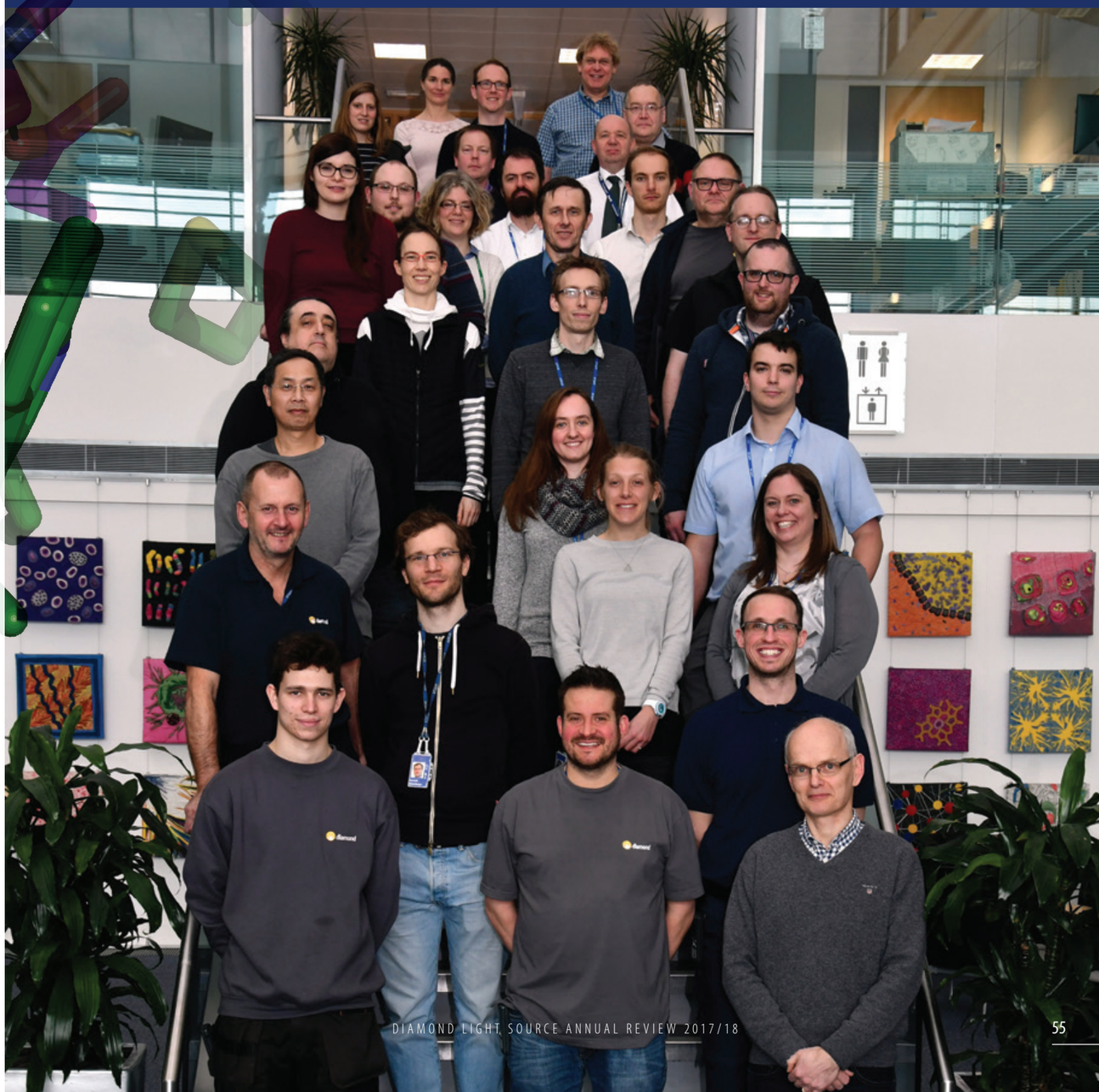

Moving towards renewable raw material sources

Related publication: Ye L, Song Q, Lo BTW, Zheng J, Kong D, Murray CA, Tang CC, Tsang SCE. Decarboxylation of Lactones over Zn/ZSM-5: Elucidation of the Structure of the Active Site and Molecular Interactions. *Angewandte Chemie* **56 (36)**, 10711-10716, doi:10.1002/anie.201704347 (2017).

Publication keywords: Decarboxylation; Synchrotron X-ray diffraction; Zn/ZSM-5

The world currently relies on coal, oil and gas, not only for fuel but also as raw materials for the production of chemicals. With reserves of these fossil fuels running out, and a growing awareness of the CO_2 pollution their use causes, it is becoming increasingly important to develop sustainable carbon sources. One option is to use biomass, dry plant matter, and a team of researchers have demonstrated a new method for converting biomass into butene gas, which in turn can be processed into the chemicals used in the production of polymers and resins.

Their work uses Gamma-valerolactone (GVL), a chemical processed from biomass raw material, and the catalyst Zn/ZSM-15, and demonstrates that it is possible to use a renewable source material to produce benzene, toluene and xylene.

They used high-resolution X-ray powder diffraction (SRXD) on III to examine the structure of their samples, which yielded important information about the reaction mechanism. This was the first time that SXRD had been used to investigate the structures of adsorbed structures of the Gamma-valerolactone GVL and immobilized Zn-species used in the research. The results are a step towards affordable, sustainable chemical prodction.

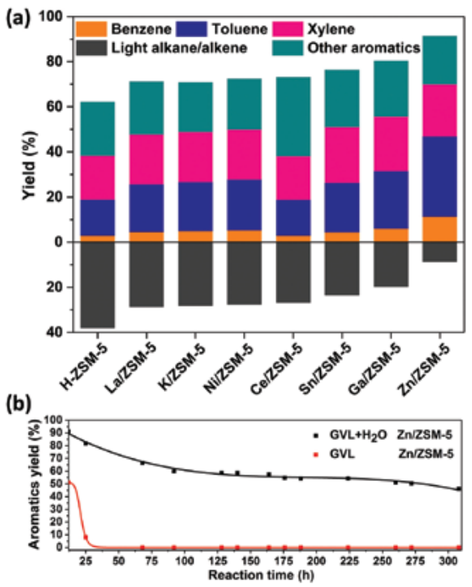

Figure 1: (a) Product distribution over various ZSM-5 based catalysts (5 g) by feeding 40 wt% aqueous GVL solution to the preheated catalyst bed with weight hourly space velocity (WHSV) 1.0 h^{-1} at 10 bar after 12 h (the time to collect the liquid products for analysis) at complete GVL conversions. The mole % yield is based on the moles of the GVL reactant to the products. (b) Long term catalytic performance of Zn/ZSM-5 with WHSV 1.0 h^{-1} at 450 °C. [Reused from doi:10.1002/anie.201704347(2017)]

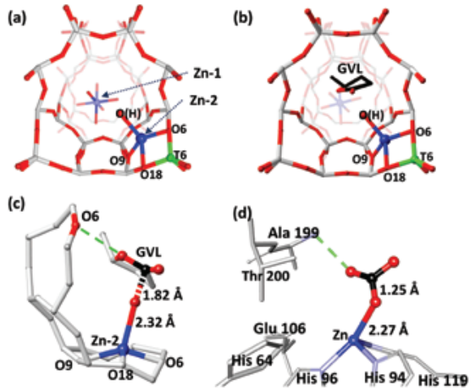

Figure 2: The refined structures of Zn/ZSM-5 catalyst derived from SXRD and refinements. (a) Fresh Zn/ZSM-5; (b) GVL adsorbed on fresh Zn/ZSM-5; (c) A close-up view of Zn(2)-OH interacting with the carbonyl of GVL; BAS (Brønsted acidic sites) in O6 assists the regeneration of depleted Zn-OH by water molecule activation (d) A published crystal structure showing a complex intermediate of Zn-OH of T199A-CA II enzyme with adsorbed CO_2 for comparison (PDB: 1CAM) [Crystal Database from National Center for Biotechnology Information][4]. In all the refined structures, the stick/ball model is used O = red, Si = grey, Al = green, Zn = blue, C = black. In (c) and (d), only the activated complexes with carbonyl adsorbates are colored. A mirror plane symmetry has been disregarded for clarity, view down the x-axis (the sinusoidal channel). Site 199 assists the regeneration of depleted Zn-OH by water molecule activation. [Reused from doi:10.1002/anie.201704347(2017)]

The depleting supplies of non-renewable oil, coal and gas and their associated CO_2 emissions are of significant concerns[1]. Biomass has long been regarded as a potential alternative to mitigate these problems. Lactones, such as gamma-valerolactone (GVL) can be favourably produced from lignocellulosic biomass and be applied to the production of BTX (benzene, toluene, xylene)[2]. However, the commercialisation of a biomass process is commonly limited by the process efficiency, tolerance to impurities and the stability of catalyst, etc. In the GVL conversion, the key challenges are to reduce the catalysis into a single simple step without the need for water separation and keeping high productivity in BTX[3].

After screening a number of modified ZSM-5 samples, aluminosilicate zeolites, we have identified the Zn incorporation into H-ZSM-5 which gives the best catalytic activity (Fig. 1a). The long-term testing shows that water molecule is essential for keeping the high yield of BTX over the Zn/ZSM-5 (Fig. 1b). We are interested to elucidate the structure of Zn/ZSM-5 and its interaction with GVL/water for the production of BTX in this catalysis.

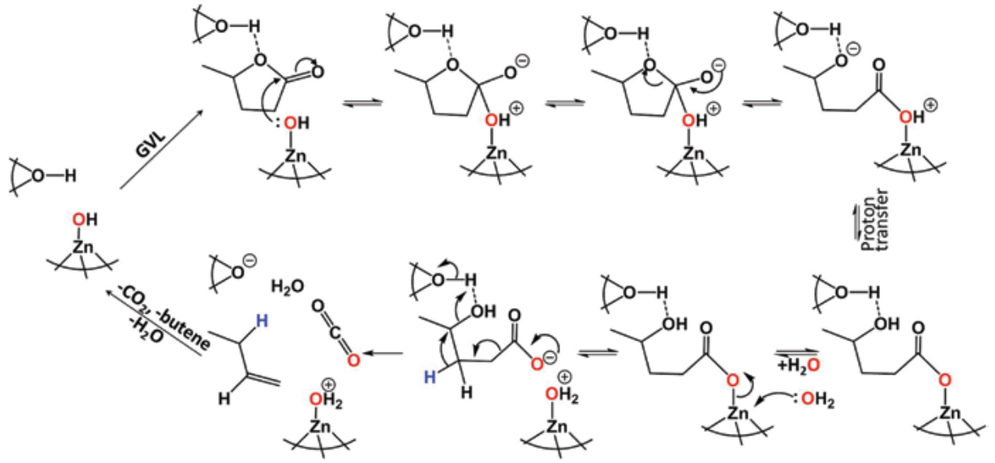

Figure 3: The proposed mechanism for aromatics production via butene formation whereby the initial step of cooperative ring opening hydrolytic decarboxylation of gamma-valerolactone (GVL) with water molecule activation over Zn/ZSM-5 is similar to that of Zn-containing enzymatic catalysis. [Reused from SI of doi:10.1002/anie.201704347(2017)]

However, the modified zeolite powder although is in microcrystalline form, it is difficult to get single crystal for its structure determination. In addition, the common lab-source X-rays techniques for powder diffraction are not sensitive and accurate to determine the Zn/ZSM-5 structure. Recently, the significant advancement of modern X-ray diffraction facilities using the high brightness synchrotron has provided chemists with a powerful tool in studying powder crystalline materials. The environment of Zn and the adsorption geometry of GVL in the H-ZSM-5 were therefore elucidated by SXRD in Beamline I11 in combined with Rietveld refinement in order to rationalize the catalytic mechanism of this reaction.

The best-fit synchrotron X-ray powder diffraction (SXRD) result (Fig. 2a) shows the space group of the Zn/ZSM-5 is *Pnma*. Two isolated Zn species have been identified within the zeolite cavity. One hexa-aqua Zn^{2+} (named Zn-1) with Zn-O(H_2) distance of 2.12(3) Å is found located at the intersection region of the sinusoidal and straight channels. The site occupancy factor (SOF) of the Zn-1 is 0.104(2). Taking the symmetry of the *Pnma* space group into account, there are $0.104 \times 4 = 0.42$ Zn-1 per unit cell of Zn/ZSM-5. Interestingly, another tetra-coordinated Zn^{2+} (named Zn-2) attached to three wall-oxygens (next to Al(T6)) of ZSM-5 and one oxygen of dissociated H_2O is also identified. The SOF of Zn-2 is 0.071(3) corresponding to $0.071 \times 8 = 0.57$ Zn-2 per unit cell.

By controlling the GVL adsorption, only trace amount of GVL is exposed to the Zn/ZSM-5. The SXRD result shows (Fig. 2b) the carbonyl of GVL molecule only aligns itself to the terminal hydroxyl group of Zn-2, implying that this is likely to be the active site whereas, no interaction of GVL with the Zn-1 species containing no terminal OH (spectator in catalysis) in the structure is found. The detailed adsorption geometry of Zn/ZSM-5 (Fig. 2c) suggests a strong dative bonding between the GVL and Zn-OH of Zn-2 species with a short O-C carbonyl distance of 1.82(4) Å has been formed. This indicates that the nucleophilic attack to the carbonyl of GVL by Zn-OH to create ring opening and decarboxylation may be the first step of the catalysis. The depleted OH group may be regenerated by H_2O with the involvement of the nearby Brønsted acid sites in the zeolite within the atomic distance. We suspected that such catalytic reaction induced by Zn-OH is similar to that of the natural occurring Zn-OH containing enzyme, the carbonic anhydrase (CA) which can catalyze the reversible hydration of CO_2. Comparing the structure of the GVL adsorbed Zn-2 site in Zn/ZSM-5 (Fig. 2c) with the published crystal structure of the T199A CAII enzyme-CO_2 complex (Fig. 2d), both active Zn^{2+} is indeed in a similar tetrahedral coordinated environment with a terminal -O(H)[4]. During bio-catalysis, the -OH of the amino acid in site 199 near the Zn^{2+} is known to activate the incoming water molecule cooperatively. The nucleophilic OH^- on Zn site can then attack CO_2 to form a Zn-hydrogen carbonate species with extremely high turnover frequency (TOF)[6]. Taken the reaction result and the structure characterisation into account, we believe that the enzymatic like structure of the Zn/ZSM-5 can accelerate the ring opening and decarboxylation of the GVL by Zn-OH, followed by the regenerating the deleted Zn-OH by involving the nearby Brønsted acid site (Fig. 2c) to re-activate water molecule in a similar atomic distance as that of amino acid site 199 in the enzyme.

In conclusion, using SXRD combined with Rietveld refinement, we demonstrate for the first time the presence of Zn-OH and neighbour Brønsted acid site in Zn/ZSM-5. They provide the synergetic active sites to convert the GVL and water to BTX via the initial ring opening and decarboxylation of the GVL molecule (Fig. 3). The catalytic mechanism is also shown to be comparable to that of the reported CA II enzyme containing similar Zn-OH framework. Thus, the immobilized Zn^{2+} for catalytic hydrolysis may provide inspirations to the chemical industry on how to harness biomass to produce useful products.

References:

1. Rahimpour, M.R. *et al.* Progress in catalytic naphtha reforming process: A review. *Applied Energy* **109**, 79-93, doi:10.1016/j.apenergy.2013.03.080 (2013).
2. Alonso, D.M. *et al.* Gamma-valerolactone, a sustainable platform molecule derived from lignocellulosic biomass. *Green Chemistry* **15**, 584-595, doi:10.1039/c3gc37065h (2013).
3. Bond, J.Q. *at al.* Integrated catalytic conversion of gamma-valerolactone to liquid alkenes for transportation fuels. *Science* **327 (5969)**, 1110-1114, doi:10.1126/science.1184362 (2010).
4. Xue, Y. *et al.* Structural-analysis of the zinc hydroxide-thr-199-glu-106 hydrogen-bond network in human carbonic anhydrase-II. *Proteins: Struct, Funct, and Bioinf* **17 (1)**, 93-106, doi: 10.1002/prot.340170112 (1993).
5. Fisher, Z. *et al.* Structural and kinetic characterisation of active-site histidine as a proton shuttle in catalysis by human carbonic anhydrase II. *Biochemistry* **44(4)**, 1097-1105, doi:10.1021/bi0480279 (2005).

Funding acknowledgement:

The authors wish to thank EPSRC, UK and Diamond Light Source Ltd and SRIFT-SINOPEC for the financial support of this collaborative work and are grateful to the Office of China Postdoctoral Council to grant a fellowship to LY to work at Oxford.

Corresponding author: Prof Edman Tsang, University of Oxford, edman.tsang@chem.ox.ac.uk

Using high temperature and pressure to form novel materials

Related publication: Laniel D, Dewaele A, Anzellini S, Guignot N. Study of the iron nitride FeN into the megabar regime. *Journal of Alloys and Compounds*, **733**, doi:10.1016/j.jallcom.2017.10.267 (2017).

Publication keywords: Laser-heated diamond anvil cell; High pressure chemistry; Powder X-ray diffraction; Crystal structure determination

Chemistry drastically changes at very high pressures, allowing exotic types of chemical interactions leading to the formation of novel materials. For mixtures of iron (Fe) with a significant amount of nitrogen (N), theoretical calculations suggested that new Fe-N compounds could be synthesised at high pressures, and are expected to have enhanced properties such as increased hardness, superconductivity, or the ability to act as a catalyst.

A team of researchers used I15 to carry out this research, because this beamline provides an intense and highly focalised X-ray diffraction beam that allows investigations into the atomic structure of the compounds produced. A new laser-heating setup on I15 allowed the experiment to reach temperatures of up to 1700°C and pressures of 128 GPa - more than a million times the atmospheric pressure - by employing a laser-heated diamond anvil cell.

Over the course of their experiments, the scientists saw the development of three compounds, ZnS-type FeN, Fe_2N and NiAs-type FeN, which they were able to characterise using X-ray powder diffraction. Above 17.7GPa, the FeN compound adopting a NiAs-type structure was formed, remained stable as the pressure was reduced, and could be removed for analysis of its physical and mechanical properties. However, they did not observe the iron pernitride FeN2 that was predicted by the theoretical calculations. Their results will help to increase the accuracy of the theoretical calculations, and will lead to new insights into the intriguing chemistry of Fe-N compounds at high pressures.

The membrane diamond anvil cell (DAC) allows the generation of extreme pressures by squeezing a small sample in between two diamond anvils. The synthesis of new compounds in this hand-sized device can be noticed and characterised using synchrotron X-ray diffraction. Indeed, the interaction of energetic X-rays with a periodic atomic arrangement, such as crystals, produces an interference pattern (diffraction pattern) from which the periodic atomic lattice, the atoms' position and the solid's stoichiometry can be precisely determined. To help cross energy barriers impeding a possible chemical reaction towards the most stable compound at a given pressure, heating the sample up to 2000 K is vital and is achieved by focusing two high power infrared lasers on the sample. This complex, double-sided laser-heating setup was recently put in place on Diamond's I15 beamline. The Psiché beamline of the SOLEIL synchrotron, equipped with a similar setup, was also used for this project. For the experiments performed at both beamlines, a thin, micrometer-sized iron flake was loaded in the DAC and entirely embedded in a much greater quantity of nitrogen. Iron can chemically react with the diamond of the anvils at high pressure and temperature, forming parasitic carbon compounds known to hinder further chemical reactions between iron and nitrogen. To avoid this, the iron was not directly positioned on the diamond anvil but instead placed on top of c-BN micrograins or a thin layer of KCl, which are both known to be chemically inert. A microphotograph of a Fe-N sample is shown in Figure 1. The loaded sample was then brought to the beamline where the formation of a new iron-nitrogen compound under extreme pressure-temperature conditions was investigated by performing powder X-ray diffraction.

Below 12 GPa, laser-heating of the samples resulted in the synthesis of the previously discovered Fe_2N compound[1]. However, upon reaching pressures above 17 GPa and after further laser-heating, new diffraction lines that did not match any previously known Fe-N, pure Fe or N structures, were noticed. The new crystal's lattice was determined to be hexagonal and, based on the absence of specific diffraction lines, belonging to the space group $P6_3/mmc$. An identical amount of nitrogen and iron atoms were found to compose the new

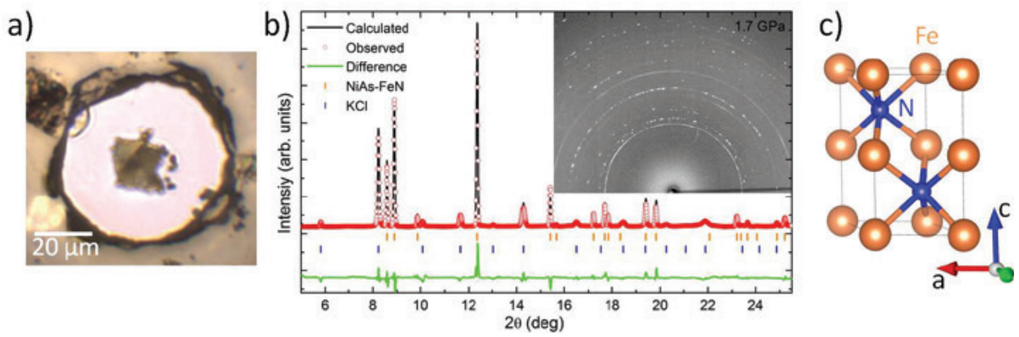

Figure 1: (a) Microphotograph of an iron flake inside the DAC experimental cavity at a pressure of 9.1 GPa. The sample is placed on c-BN micrograins and completely embedded in pure molecular nitrogen; (b) Rietveld refinement of a diffractogram obtained from a FeN sample at 1.7 GPa, decompressed from 25.3 GPa. The observed diffraction lines can be assigned to FeN in the NiAs-type of structure (orange) and KCl (blue). (Inset) A two-dimensional diffraction data image at 4.7 GPa showing several diffraction rings. (c) Arrangement of Fe and N atoms in the hexagonal (P63/mmc) structure of FeN. The blue and orange spheres represent nitrogen and iron atoms, respectively.

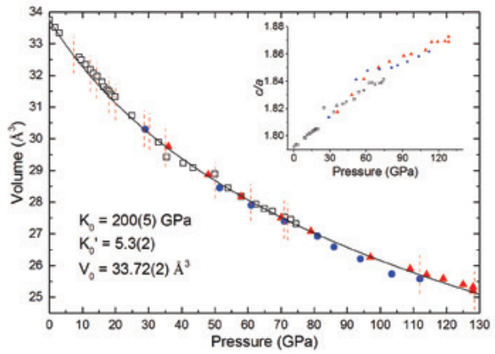

Figure 2: Unit cell volume of hexagonal FeN as function of pressure and at ambient temperature. The solid line represents a fit of a third order Birch-Murnaghan equation of state to the data. The vertical red lines mark the pressures where the sample was laser-heated. The various symbols represent different experimental runs, with the full and empty symbols indicating data obtained at the Diamond Light Source I15 beamline and the Soleil synchrotron Psiché beamline, respectively. (Inset) The evolution of the c/a ratio of the hexagonal FeN indicates that the c-axis is less compressible than the a-axis.

solid, thus yielding a stoichiometry of FeN, and they were determined to adopt the common NiAs-type atomic arrangement, found in the well-known NiAs solid. The structural determination was achieved by a Rietveld refinement. FeN in its NiAs-type structure along with a Rietveld refinement are also shown in Figure 1. These findings are in agreement with similar studies reported in the literature[2,3].

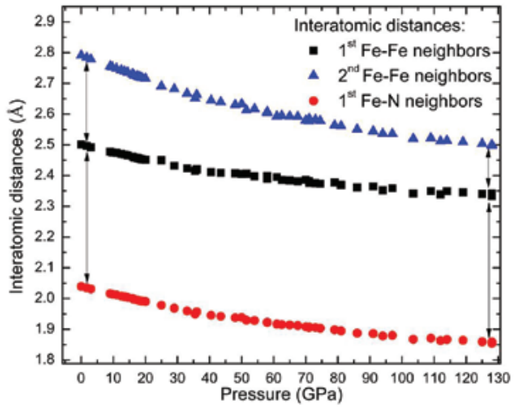

Figure 3: Evolution of the interatomic distances of FeN in the NiAs-type of structure with respect to pressure. The interatomic distance that is most reduced by pressure is the distance of Fe to its second-nearest Fe neighbor, followed by the distance to its nearest N and Fe neighbors. With increasing pressure, the interatomic distances of the first and second Fe-Fe shells become similar.

The FeN compound was characterised by powder X-ray diffraction up to 128 GPa with frequent laser-heating but no further chemical or structural transformations were observed. The evolution of the FeN compound's unit cell lattice parameters and volume with respect to pressure is shown in Figure 2. Based on these measurements, valuable information regarding the compound's equation of state, its compressibility as well as the evolution of the chemical interactions between the Fe and N atoms could be inferred. By fitting a third order Birch-Murnaghan equation of state to the pressure-volume data, a bulk modulus of $K_0 = 200(5)$ GPa with a pressure derivative $K_0' = 5.3(2)$ were obtained for a fixed, measured volume of $V_0 = 33.72(2)$ Å^3 at ambient pressure. The bulk modulus of FeN in its high pressure structure is slightly higher than what was found in nitrogen-poor iron nitrides, which agrees with the trend that the addition of nitrogen atoms strengthens the crystalline structure by increasing the crystal's overall covalent interactions[1].

As shown in Figure 2, the *c*/*a* ratio progressively increases with pressure, indicating that the *a*-axis is more compressible than the *c*-axis. The anisotropic behavior of the lattice parameters has consequences regarding the interatomic distances within the crystal. As shown in Figure 3, the interatomic distance of the six second-nearest Fe neighbors surrounding a given Fe atom is more compressible than the shortest Fe-Fe and Fe-N distances. Based on previous studies of compounds with the NiAs-type structure, this particular change of interatomic distances is indicative of a weakening of the solid's ionicity, i.e. a lower charge transfer from the metallic Fe atoms to the nitrogen atoms[4].

The FeN compound in its NiAs-type of structure proved to be retrievable down to ambient conditions after the complete release of pressure. However, a partial structural phase transition of FeN in its NiAs-type of structure into FeN in a ZnS-type of structure was detected, with the latter being a phase previously produced exclusively in thin films. Interestingly, neither of those two phases are thermodynamically favored below 10 GPa, where the Fe_2N compound, although of different stoichiometry, is energetically favored. This result underlines the large activation barriers impeding chemical reactions necessary for a change in stoichiometry (FeN → Fe_2N) as opposed to an effortless structural transition (NiAs-FeN → ZnS-FeN). With this conclusion in mind, the laser-heating of the NiAs-type FeN compound to higher temperatures could very well result in the synthesis of yet another nitrogen-rich Fe-N solid, such as the theoretically predicted iron pernitride FeN_2.[5]

References:

1. Hasegawa, M. *et al.* Systematic study of formation and crystal structure of 3d-transition metal nitrides synthesized in a supercritical nitrogen fluid under 10 GPa and 1800 K using diamond anvil cell and YAG laser heating. *Journal of Alloys and Compounds*, **403 (1-2)**, 131-142, doi:101016/jjallcom200504197 (2005).
2. Clark W. P. *et al. Angewbante Chemie International Edition*, **56**, 7302, doi: 10.1002/anie.201702440 (2017).
3. Niwa, K. *et al.* Highly Coordinated Iron and Cobalt Nitrides Synthesized at High Pressures and High Temperatures. *Inorganic Chemistry*, **56 (11)**, 6410-6418, doi: 10.1021/acs.inorgchem.7b00516 (2017).
4. Onodera, A. *et al.* Structural and electrical properties of NiAs-type compounds under pressure. *Journal of Physics and Chemistry of Solids*, **60**, 167-179, doi:10.1016/S0022-3697(98)00278-9 (1999).
5. Wessel, M. *et al.* A New Phase in the Binary Iron Nitrogen System? -The Prediction of Iron Pernitride, FeN2. *Chemistry European Journal*, **17,** 2598-2603, doi:10.1002/chem.201003143 (2011).

Funding acknowledgement:

The authors gratefully acknowledge the Centre National d'Etudes Spatiales (CNES) and the Natural Sciences and Engineering Research Council of Canada (NSERC) for financially supporting the Ph.D. of D.L.

Corresponding authors: Dominique Laniel, CEA-DAM, dominique.laniel@cea.fr, Dr Agnès Dewaele, CEA-DAM, agnes.dewaele@cea.fr

Metal Organic Framework Liquids and Glass: Moving Away From the Ordered Domain

Related publication: Gaillac R, Pullumbi P, Beyer KA, Chapman KW, Keen DA, Bennett TD, Coudert F-X. Liquid metal–organic frameworks. *Nature Materials* **16**, 1149-1154, doi:10.1038/nmat4998 (2017).

Publication keywords: Metal-organic framework; Liquid; Glass; Amorphous; Porous

Building on previous work conducted at Diamond, researchers have used X-ray Pair Distribution Function (XPDF) on the I15-1 beamline to probe the structure of a Metal Organic Framework (MOF) in its glassy state, from which they inferred the structure of its liquid form.

MOFs are crystalline materials, which are receiving a lot of interest due to their porous nature, which allows them to accommodate guest molecules within their structure. Potential applications include drug delivery, catalysis, and the capture or separation of gases. There are around 60,000 MOFs, and until very recently research had focused on their solid form.

For this new study, the team investigated the structure of ZIF-4 at Diamond, the Advanced Photon Source in Chicago and ISIS Neutron and Muon source, using their results to produce a computational model of the glassy state from which they could infer the structure of the liquid state. Their results show that this MOF retains its porous structure in its liquid form. This opens up a whole new area of research, investigating whether other MOFs also behave in this way, as well as discovering the properties and potential applications of liquid and glass MOFs.

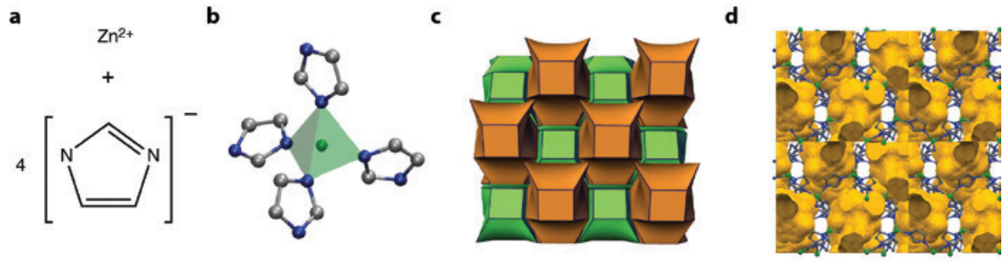

Figure 1: (a) The construction from metal ion and linker of Zn(Im)4 tetrahedra, the basic building unit of ZIF-4 (Im, imidazolate; Zn, green; N, blue; C, grey). (b) Representation of the cage topology adopted by ZIF-4, where each polyhedra corner corresponds to one Zn(Im)4 tetrahedron. (c) Crystalline structure of ZIF-4, (d) with free volume represented in orange.

Metal-organic frameworks (MOFs) continue to be of interest for a variety of applications such as gas sorption, separations, drug delivery, harmful waste storage and catalysis. The overwhelming majority of research concentrates on the chemical opportunities afforded by crystalline structures created by ordering inorganic nodes and ligands in nano-porous network architectures[1]. Our studies have recently shown that one family of MOFs, the zeolitic imidazolate frameworks (ZIFs), undergoes solid-liquid transitions upon heating. The structures, which adopt identical network topologies to inorganic zeolites, consist of M^{n+} ions linked by imidazolate $C_3H_3N_2^-$ ligands (Fig. 1). Interestingly, quenching the liquid formed by melting one such system, ZIF-4, at 865 K, results in a glass, which resembles amorphous SiO_2 ($aSiO_2$), though with the $Zn(Im)_2$ chemical formula[2].

A sample of the melt-quenched glass arising from ZIF-4 was prepared *ex situ*, before X-ray total scattering data were collected using the I15-1 (XPDF) beamline at Diamond Light Source, UK. These data, combined with neutron

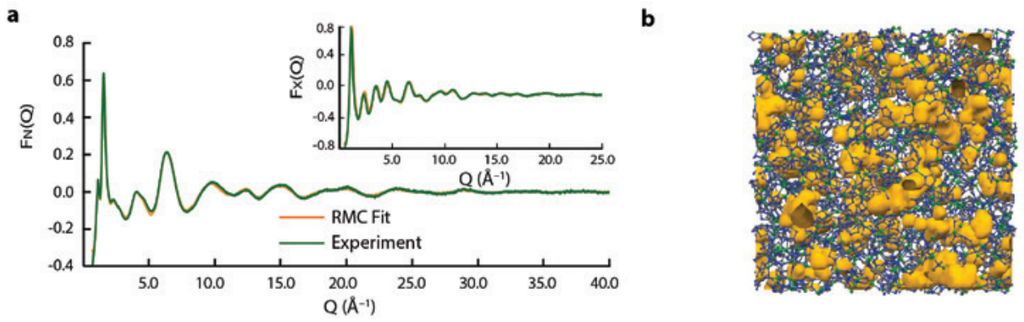

Figure 2: (a) Experimental neutron structure factor F(Q) data and the fit from the configuration shown in (b). Inset: X-ray data and fit. (b) Atomic configuration of the melt-quenched glass, gained from modelling synchrotron and neutron total scattering data.

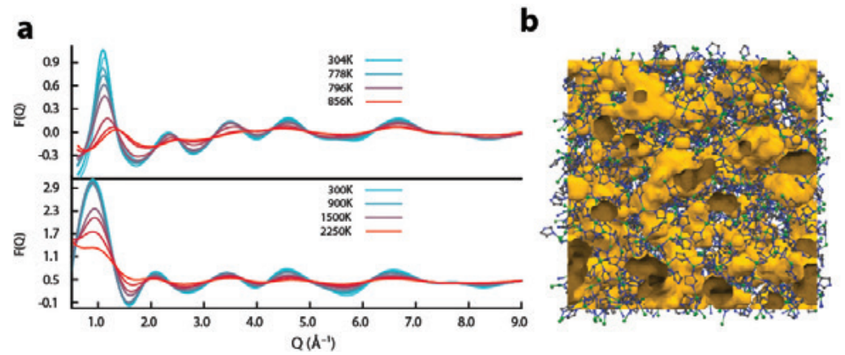

Figure 3: (a) Experimental glass (top) and computational ZIF-4 (bottom) X-ray structure factors upon heating. (b) Atomic configuration of the ZIF melt, gained from reverse Monte Carlo modelling of the total scattering data collected at 856 K. Free volume is represented in orange, Zn atoms in green, N in blue, and C in grey.

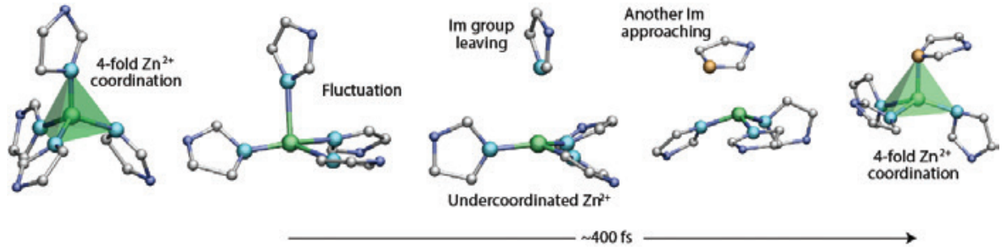

Figure 4: Visualisation of a representative imidazolate exchange event. Zn, green; N (initially coordinated), light blue; N, blue; N (coordinated after exchange), orange; C, grey.

data collected using the GEM Diffractometer at the ISIS Neutron and Muon Source, UK, were then modelled using reverse Monte-Carlo modelling – software which gradually alters a starting atomic configuration to fit the experimental data collected[3]. For this task, we used a model of an amorphous $Zn(Im)_2$ network from a solid amorphous (non melt quenched) $Zn(Im)_2$ phase, itself gained by adjusting a Continuous Random Network (CRN) model for $aSiO_2$ (Fig. 2)[4]. The resultant configuration, the first model for a melt-quenched glass, was gained without changing network topology, and resulted in a good fit to the experimental structure factors.

To investigate the mechanism of melting, synchrotron X-ray diffraction data were collected at the Advanced Photon Source, USA (APS), to evaluate structural changes in the glass upon heating. The pair distribution functions (PDFs) contain the expected peaks at approximately 1.3 Å, 2 Å, 3 Å, 4 Å and 6 Å, which correspond to C–C/C–N, Zn–N, Zn–C, Zn–N and Zn–Zn pair correlations, respectively. Constant temperature molecular dynamics simulations were also carried out, with the PDFs obtained showing similar trends to the experimental ones (Fig. 3). The high temperature experimental data on the liquid MOF phase at 865 K was modelled using RMC Profile[3], providing the first configuration for a liquid MOF (Fig. 3b). Simulation also provided the opportunity to build up a molecular picture of the melting process (Fig. 4), showing it to proceed via dissociation of an imidazole ligand from a Zn^{2+} centre, followed by association of a different Im ligand – not unlike hydrogen bond switching between water molecules.

Importantly, analysis of the pore volume of the ambient temperature glass using a probe diameter of 2.4 Å showed only 4.8% accessible volume. Upon melting at 865 K, this increased to 16.2 %. Hence, our conclusion was that even at high temperatures, the liquid contains porosity. This is also greater than ionic liquids containing the imidazolium ion ($C_3H_3N_2^+$). Elaborating on the generality of the melting phenomenon will be important, as the activation energy required to break the coordination metal-ligand bonding is above that which causes thermal decomposition of some MOFs, including the prototypical ZIF-8.

Given the retention of coordinative bonding between crystal and liquid forms, the term 'MOF-liquid' was introduced, to refer to liquids formed from melting crystalline MOF structures. The research will add to the developing community of researchers interested in the combination of flexibility, defects and disorder in MOFs[5].

References:

1. Furukawa, H. *et al.* The Chemistry and Applications of Metal-Organic Frameworks. *Science* **341**, 6149, doi:10.1126/Science.1230444 (2013).
2. Bennett, T.D. *et al.* Hybrid glasses from strong and fragile metal-organic framework liquids. *Nat Comms* **6**, 8079, doi:10.1038/ncomms9079 (2015).
3. Tucker, M.G. *et al.* RMCProfile: reverse Monte Carlo for polycrystalline materials. *J Phys Condens Mat* **19(33)**, doi:10.1088/0953-8984/19/33/335218 (2007).
4. Bennett, T.D. *et al.* Structure and Properties of an Amorphous Metal-Organic Framework. *Phys Lett Rev* **104**, 115503, doi:10.1103/PhysRevLett.104.115503 (2010).
5. Bennett, T.D. *et al.* Interplay between defects disorder and flexibility in metal-organic frameworks. *Nat Chem* **9**, 11-16, doi:10.1038/nchem.2691 (2017).

Funding acknowledgement:
We thank A. Boutin, A. Fuchs, A. Cheetham and R. Vuilleumier for fruitful discussions. This work benefited from the financial support of ANRT (thèse CIFRE 2015/0268). We acknowledge access to HPC platforms provided by a GENCI grant (A0010807069). T.D.B. would like to thank the Royal Society for a University Research Fellowship.We also thank Diamond Light Source for access to beamline I15-1 (EE15676), and D. Keeble and P. Chater for assistance with data collection on I15-1 during its initial commissioning phase. We gratefully acknowledge the Science and Technology Facilities Council (STFC) for access to neutron beamtime at ISIS on the GEM instrument. This research used resources of the Advanced Photon Source (Beamline 11-ID-B, GUP44665), a US Department of Energy (DOE) Science User Facility operated for the DOE.

Corresponding author: Dr Thomas Douglas Bennett, University of Cambridge, tdb35@cam.ac.uk

Putting the squeeze on Re^{IV}

Related publication: Woodall CH, Craig GA, Prescimone A, Misek M, Cano J, Faus J, Probert MR, Parsons S, Moggach S, Martínez-Lillo J, Murrie M, Kamenev KV, Brechin EK. Pressure induced enhancement of the magnetic ordering temperature in rhenium(IV) monomers. *Nature Communications* **7**, 13870 doi:10.1038/ncomms13870 (2016).

Publication keywords: Rhenium; High pressure X-ray crystallography; High pressure SQUID magnetometry; Magnetic order

Materials that have long range magnetic order are fundamental to modern technologies, including data storage devices, space research, cancer therapy and biomedical imaging techniques. Future miniaturisation of these components depends on designing molecules that behave in the same way as larger magnets, and to do this we need an improved understanding of the connection between molecular structures and their resulting properties.

Although high-temperature- and high-magnetic-field-based studies are common in molecular chemistry, the effect of high pressures is less well explored. A team of researchers has therefore studied the effect of increasing hydrostatic pressure on rhenium(IV) compounds that exhibit long range magnetic order. They used small-molecule single-crystal diffraction on Diamond's I19 beamline to provide high-precision measurements able to monitor small changes in the structure, and high-pressure magnetometry to explore the link between the structural changes and changes in magnetic behaviour.

Their results showed that applying pressure to single crystals of rhenium(IV) compounds shortens distances between molecules in the crystal, with corresponding changes to magnetic behaviour, including an increase in the temperature at which long range magnetic order occurs.

$[ReCl_4(MeCN)_2]$·MeCN (**1**) (Me=methyl) and $[ReBr_4(bpym)]$ (**2**) (bpym=2,2′-bipyrimidine) are characterised by large magnetic anisotropies and significant intermolecular magnetic exchange interactions mediated through Re–X···X–Re type contacts (X = halogen), resulting in spin canting (the non-collinearity of neighbouring spin centres) and magnetic order at low temperature (T_c(**1**) = 6.5 K, T_c(**2**) = 18.0 K)[1,2,3]. The dipolar exchange pathways arise as a result of the spin density from the metal ion being delocalised onto the peripheral atoms of the ligand. Intermolecular magnetic exchange interactions can be modified by changing intermolecular distances, *i.e.* making these distances shorter would be expected to increase the strength of the exchange and increase the ordering temperature, and one method of achieving this is to exert hydrostatic pressure. By combining high-pressure single-crystal X-ray crystallography and high-pressure SQUID magnetometry, in tandem with detailed theoretical analysis, the relationship between changing structure and changing magnetic behaviour can be extracted, and the underlying physical origins of the behaviour revealed.

Compounds **1** (*Pnma*) and **2** ($P2_12_12_1$) crystallise in orthorhombic space groups, with the metal ion occupying a distorted octahedral environment, bonded to two N-atoms and four halides. The extended structures display staggered zig-zag chains that propagate along the *a*-axis of the unit cell *via* interhalide dispersive interactions (Fig. 1). Under pressures of up to 4.30 GPa unit cell volumes decrease by 20% (**1**) and 14% (**2**), the principal component of compression occurring along the *c*-axis of the unit cell in both cases. **2** undergoes a phase transition between 1.93 GPa and 3.06 GPa to a monoclinic phase with space group $P2_1$, and when subjected to complete compression-decompression cycles to 4 GPa, both **1** and **2** return to their original ambient pressure unit cell/space group. In addition, ambient pressure crystal structures solved at $T = 4$ K show both species retain their room temperature structures. The most significant structural changes observed under pressure in **1** and **2** occur in the intermolecular Re-X···X–Re distances. For **1** the Re–Cl(4)···Cl(2)–Re distance shortens by ~0.6 Å to 3.362(11) Å, while for **2** the Re-Br(2)···Br(4)-Re distance decreases by 0.31 Å to 3.5718(2) Å.

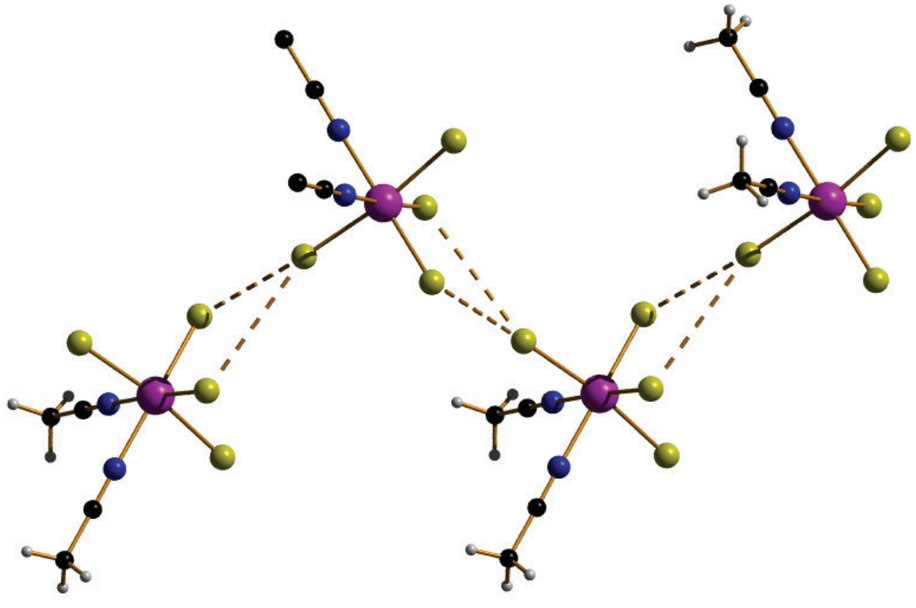

*Figure 1: The structure of compound **1**, highlighting the zig-zag chains and the short halide-halide contacts (dashed lines). Colour code: Re = pink, C = black, N = blue, Cl = yellow, H = white.*

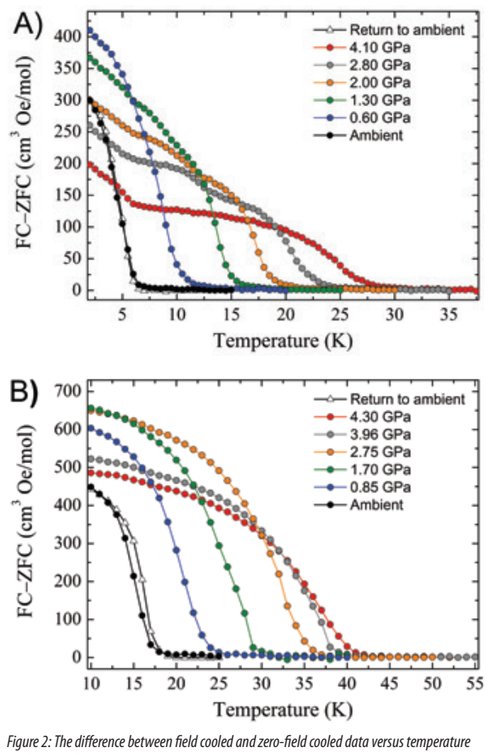

*Figure 2: The difference between field cooled and zero-field cooled data versus temperature for **1** (a) and **2** (b).*

High pressure SQUID magnetometry, performed on microcrystalline samples of **1** and **2** in a turnbuckle diamond anvil cell[4], shows that the application of hydrostatic pressure leads to an increase in ordering temperature (Fig. 2). At the highest pressures measured, T_c (determined from field cooled and zero-field cooled measurements as a function of temperature) reaches 28 K at 4.10 GPa for **1**, and 42 K at 4.30 GPa for **2**. For **1**, this represents a four-fold enhancement, with the rate at which T_c increases being 5.1 and 5.4 K GPa^{-1} for **1** and **2**, respectively. The phase transition observed for compound **2** does not affect the monotonic increase of the ordering temperature, and in both cases the changes in T_c are reversible; recovery of the ambient pressure T_c is observed when the pressure is released from the cell. Density functional calculations show that the shortest Re-X···X-Re pathways generate the most efficient magnetic exchange interactions (*J*) at all pressures, and that an increase in the magnitude of *J* in **1** and **2** is observed when external pressure is applied, in agreement with increasing T_c in both systems. Indeed, the correlation between parameters is straightforward, external applied pressure produces a linear increase in *J* and a linear increase in T_c (Fig. 3).

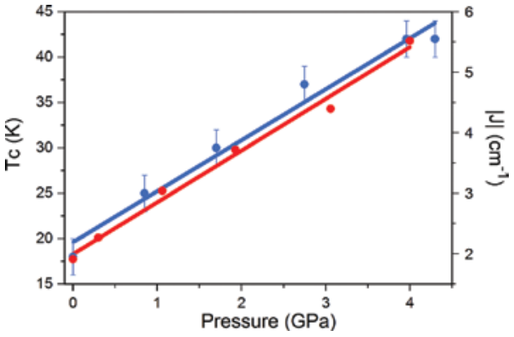

*Figure 3: Pressure dependence of the ordering temperature, T_c (blue circles), and the strongest magnetic exchange, *J* (red circles). The lines represent the linear best-fit.*

The use of multiple high pressure techniques is a simple and efficient methodology for probing structure-property relationships. For synthetic chemists it has the added advantage of negating the need to make families of compounds that may differ electronically. In this instance, the pressure-induced enhancement of the magnetic ordering temperatures of two spin-canted Re^{IV} systems can be directly correlated to changes in structure, specifically Re-X···X-Re distances, through the combined use of single-crystal X-ray crystallography and SQUID magnetometry, allowing unprecedented insight into the underlying physical origins of behaviour in a step-by-step manner.

References:

1. Kunz, P.C. *et al.* Attempted abstraction of the halogenides in $(HNEt_3)[Re(CH_3CN)_2Cl_4]$ and crystal structures of cis-$[Re(CH_3CN)_2Cl_4]$·CH_3CN and cis-$[Re(NHC(OCH_3)CH_3)_2Cl_4]$. *J Inorg and Gen Chem* **15**, 633, doi:10.1002/zaac.200700265Z (2007).
2. Volkov, S.V. *et al*. Synthesis and structure of rhenium(IV) chloride complexes with acetonitrile. *Russian J Inorg Chem* **52**, 2, doi:10.1134/S0036023607020088 (2007).
3. Chiozzone R. *et al.* A novel series of rhenium-bipyrimidine complexes: synthesis, crystal structure and electrochemical properties. *Dalton Trans* **0**, 653-660, doi:10.1039/B615136A (2007).
4. Giriat, G. *et al.* Turnbuckle diamond anvil cell for high-pressure measurements in a superconducting quantum interference device magnetometer. *Rev Sci Instrum* **81**, 073905, doi:10.1063/1.3465311 (2010).

Funding acknowledgement:

EPSRC EP/N01331X/1 "Putting the Squeeze on Molecule-Based Magnets" We acknowledge Diamond Light Source for time on Beamline I19 under Proposal MT11879.

Corresponding author: Prof Euan K. Brechin, EaStCHEM School of Chemistry, The University of Edinburgh, ebrechin@ed.ac.uk

Biological Cryo-Imaging Group

Martin Walsh, Deputy Director of Life Sciences

Biological imaging at Diamond now has a new home with the recent formation of the Biological Cryo-Imaging Group. This brings together dedicated facilities for X-ray, light and electron microscopy at Diamond. The bending magnet beamline B24 is the source of X-rays for the full field cryo-transmission X-ray microscope dedicated to biological X-ray imaging and the beamline has also established a cryo super resolution fluorescence microscopy facility which is a joint venture between Diamond and the University of Oxford. The Biological Cryo-Imaging Group is completed with the recently established national centre for cryo-electron microscopy at Diamond, eBIC (Electron Bio-Imaging Centre).

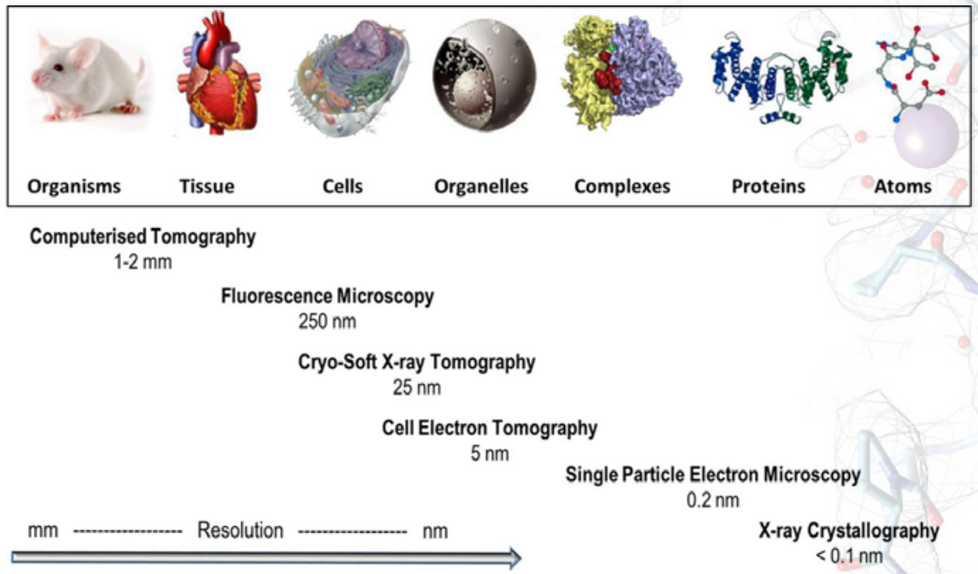

Figure 1: Biological imaging in context. Representative techniques developed for the investigation of structure in biological systems at different scales, in order of resolution attainable. (Reproduced with permission from Harkiolaki et al. Emerg Top Life Sci (2018))

B24 exploits cryo-soft X-ray tomography (cryo-SXT), which is a powerful technique for imaging intact cells in their near native state to resolutions of 25 - 40 nm. The technique sits neatly in the resolution gap that exists between electron and light microscopies and its real power lies in its ability to provide 3D imaging of whole cells with little or no chemical or mechanical modification. A schematic of the various imaging techniques available to biologists and how B24 and cryo-SXT fits into this tool set is shown in Figure 1. Cryo-SXT provides a unique tool to aid biologists to understand many key cellular and disease processes. One of the first external user experiments at B24 aptly illustrates the power of the technique where Hale *et al* used B24 to visualise red blood cells infected with the malaria parasite *Plasmodium falciparum*. This work is summarised in more detail in the accompanying highlight. Sitting alongside the X-ray microscope at B24 is a cryo super resolution fluorescence microscopy facility, which is in the early stages of commissioning. It has also carried out first

Figure 2: B24 experimental hutch with the X-ray microscopy in the background.

Figure 3: Super resolution cryo fluorescence Microscopy facility at B24.

Figure 4: (a) eBIC Krios hall housing Titan Krios II, III and IV microscopes; (b) Titan Krios I located next to I20 in the experimental hall of Diamond; (c) the SCIOS cryo focused ion beam scanning electron microscope at eBIC.

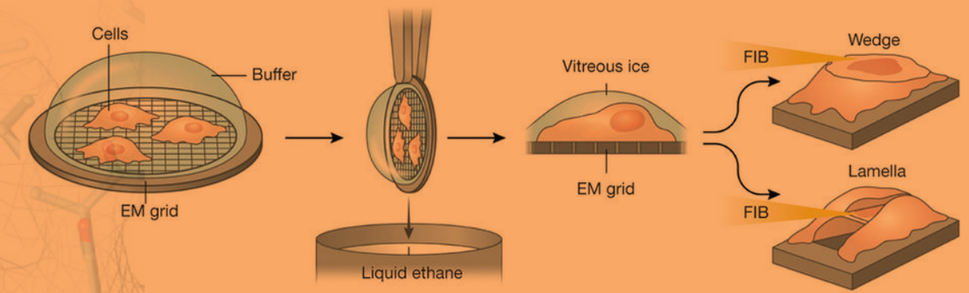

Figure 5: Schematic of the workflow for cryo-FIB milling of cells with the SCIOS microscope at eBIC (Figure from Narayan K & Subramaniam S Nature Methods 12, 1021-1031 (2015)). Cells are grown on special grids for Transmission Electron Microscopy (TEM) and are rapidly plunge-cooled in liquid ethane and transferred to the SCIOS under cryogenic temperatures. A chosen area is FIB-milled tangentially either from one direction to produce a wedge or from above and below to produce a lamella, revealing the region to be imaged either using the scanning electron transmission mode in the SCIOS or it can be transferred to an eBIC Titan Krios under cryogenic conditions and imaged at high resolution using cryo-ET.

experiments with B24 users in the last year. Use of cryo-structured illumination microscopy (cryo-SIM) has allowed correlative imaging with the B24 X-ray microscope to be developed and workflows are currently being optimised which also paves the way for use with cryo-electron tomography (cryo-ET) at eBIC. The development of the facility is a joint collaboration with the advanced bioimaging unit, Micron, at the University of Oxford. B24 is now in the final round of commissioning and optimisation with users and will enter full user operations in the autumn of 2018.

eBIC is the first high-end cryo-electron microscopy (cryo-EM) facility worldwide to be embedded in a synchrotron and user operations have been set up to mirror the well-established synchrotron beamline model. The centre is funded by the Wellcome Trust, the Medical Research Council (MRC) and the Biotechnology and Biological Sciences Research Council (BBSRC). eBIC has rapidly developed since it welcomed the first user group in July 2015. A key aim of the centre, enabled by the synchrotron access model, was to provide a state-of-the-art-facility for single particle cryo-EM and cryo-ET through cost-effective, peer-reviewed access based on scientific excellence. The rapid provision of high-end microscopes and the embedding within Diamond allowed this vision to be realised at breakneck speed and the success of the eBIC model has inspired other synchrotron sites worldwide to follow suit.

In addition to providing cost-effective access to high-end microscopes for cryo-EM and cryo-ET, eBIC provides a focus for future hardware and software developments and advanced training for the community. The latter has been exemplified by specialised 'hands-on' training workshops in sample preparation for cryo-EM as well as specialised training courses in collaboration with the Collaborative Computational Project for electron cryo-microscopy (CCP-EM, ccpem.ac.uk) which is funded by the MRC and based at the Research Complex at Harwell. These courses and 'hands on' workshops have been extremely successful, although are heavily oversubscribed. This is due to sample preparation for cryo-EM remaining a major bottleneck and expertise in the community is lacking which is reflected in the greater than 10-fold oversubscription for the first two practical workshops dedicated to this topic at eBIC in January and October of 2017. Advanced training with support from CCP-EM, and the European funded Horizon 2020 project iNEXT (inext-eu.org), with which Diamond is a partner, will continue through 2018-19.

On the computing front, on-the-fly processing of data has been rolled out and management of data collected and processed at eBIC will be presented in the information system ISPyB that is now being developed for use by cryo-EM. The latter project is being coordinated by Diamond through the H2020 iNEXT project and will be available for use in the near future at all the European cryo-EM centres. These software developments have been carried out in collaboration with CCP-EM and the developers of the Scipion framework which brings together numerous software packages for EM and presents them to the user in a unified interface for both biologists and developers. This has enabled the accelerated development of these automated workflows at eBIC and ISPyB will provide added value and provides a key tool for users to allow remote access use of eBIC to be realised.

The user program at eBIC has continued to grow rapidly in 2017 with two new Titan Krios 300 KeV microscopes (Thermofisher) brought online, taking the total number of high-end microscopes to 4. eBIC is also heavily engaged in developing a user program for cellular studies and during 2017 a cryo focused ion beam scanning electron microscope (SCIOS, Thermofisher) has been in commissioning with in-house users. The microscope allows the cryo-milling of cellular samples into thin slices (up to 100 nm) making them suitable for imaging by cryo-ET (a schematic of the workflow is illustrated in Fig. 4). Whereas X-rays are more penetrating and cryo-SXT at B24 can image samples as thick as 10-15 mm, cryo-ET requires thin cellular slices with the advantage that imaging at much higher resolutions are achievable (Fig. 1). Again, here a correlative approach that combines light and electron microscopy provides a powerful tool to image cellular regions of interest. In collaboration with B24 development of workflows that combine live-cell fluorescent light microscopy, cryo-fluorescent microscopy, and cryo-ET to provide a structural and dynamic view of cellular processes are in development. A call for proposals from external users for commissioning of the SCIOS microscope at eBIC was announced in April 2018 for experiments in early autumn 2018.

In summary the new Biological Cryo-Imaging Group at Diamond is at an exhilarating stage of development and we expect research and development to continue at a fast and exciting pace through 2019 as we bring all the instruments in the group fully online.

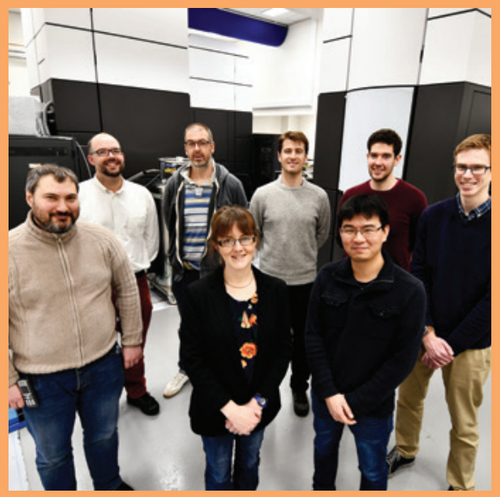

Figure 6: Some members of the eBIC team in the Krios Hall.

How malaria parasites break out of red blood cells during the infection cycle

Related publication: Hale VL, Watermeyer JM, Hackett F, Vizcay-Barrena G, van Ooij C, Thomas JA, Spink MC, Harkiolaki M, Duke E, Fleck RA, Blackman MJ, Saibil HR. Parasitophorous vacuole poration precedes its rupture and rapid host erythrocyte cytoskeleton collapse in *Plasmodium falciparum* egress. *Proceedings of National Academy of Sciences* **114(13)**, 3439-3444, doi:10.1073/pnas.1619441114 (2017).

Publication keywords: Malaria; Egress; Electron tomography; Soft X-ray microscopy; Electron energy loss spectroscopy

Malaria is a highly infectious disease that is widespread in tropical and sub-tropical regions of the world. It is caused by a group of parasitic single-celled microorganisms, which are carried by mosquitoes. When malaria parasites enter a human via a mosquito bite, they rapidly multiply in red blood cells within a protective casing known as the parasitophorous vacuole. Once the newly made parasites mature they have to break through this vacuole as well as the membrane of the red blood cell in order to infect other red blood cells.

The exact mechanisms underpinning these crucial, clinical stages of malaria infection were unclear, so 3D images of infected cells were obtained using X-ray tomography at B24 at Diamond. Using special additives to arrest the breakage of the parasites' double enclosures at different steps, the process was explored in detail and compared with live cell video microscopy. 3D electron tomography was also employed to scour tiny slices of the infected cells to examine their structural details.

The work revealed that rather than the parasites causing a gradual breakdown of the red blood cell membrane, the process happened far more abruptly. At a very late stage, the infected host cell underwent a dramatic shape change and then broke to liberate the parasites. Furthermore, the study showed that the membrane of the vacuole became permeable just prior to its breakage. These new insights could help to develop novel antimalarial therapies that target this critical process.

Malaria parasites have a complex life cycle with very distinct stages in their mosquito and mammalian host tissues, but the clinical symptoms all arise from cycles of infection in the blood stage. Once a parasite enters a red blood cell, it wraps itself in a piece of membrane originally derived from the host cell, and then, hidden away from immune detection, proceeds to divide into up to 32 daughter cells. During this process, the parasites take control of the red blood cell and insert all the machinery they need to proliferate and to protect the infected cell from detection and attack by the host immune system. Comfortably installed, they proceed to consume the cell's haemoglobin, fuelling their growth. Once the parasite progeny are mature, they release signals to begin the process of egress, by which they will successively break their surrounding membrane and then the outer membrane of the red blood cell, with its cytoskeleton support layer, culminating in their explosive release into the bloodstream where they quickly find new red blood cells to infect and restart the cycle. For the major human parasite species, *Plasmodium falciparum*, this cycle takes around 2 days, and results in the cyclical fever and chills typical of the disease.

Egress takes place through a highly orchestrated sequence of events triggered by secretion of proteases or other factors from the parasites into their vacuole, leading to a further cascade of protease activation[1,2]. Two chemical blockers have been discovered that arrest egress at different points: The first block (compound 1 or the closely related compound 2) prevents the parasites from breaking out of their vacuole by blocking secretion of the protease Sub1, so that the infected cell remains full of mature parasites packed tightly inside their own compartment, with the blood cell retaining a rigid but distorted shape. The second block (the cysteine protease inhibitor E64) arrests egress just before the final escape of the parasites, trapping them inside the remnants of the red blood cell, which has lost its mechanical integrity but still loosely retains the parasites inside a floppy bag-like cell (Fig. 1).

In this study[3], three-dimensional (3D) reconstructions of these two arrested states were obtained by both electron and X-ray tomography. The electron microscopy (EM) images revealed an initial, previously unknown, step in which the vacuole membrane becomes leaky and allows mixing of the cell contents with those of the vacuole. To track the changes in composition of the vacuole and red cell compartments, we used electron energy loss spectroscopy, which confirmed that the two compartments were initially distinct in composition but then became equalised.

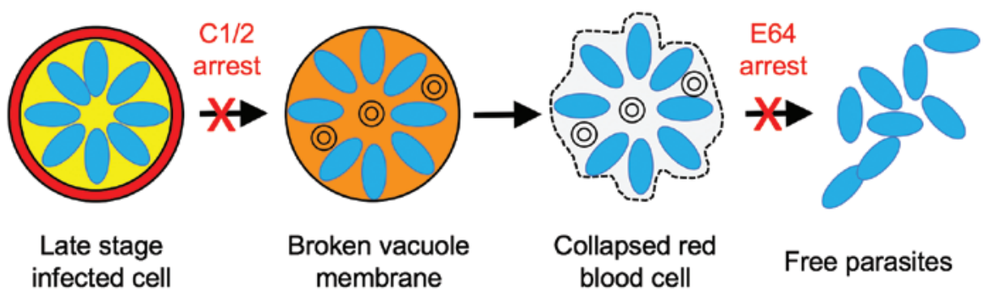

Figure 1: Schematic diagram of the main steps in egress, with points of arrest by compound 1/2 and E64 indicated.

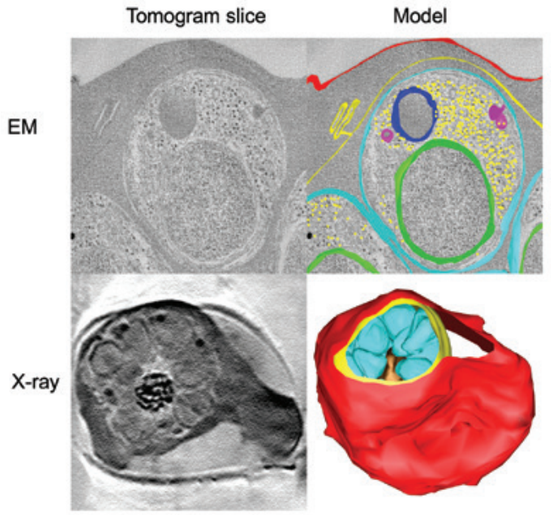

Figure 2: Electron and X-ray tomograms of cells arrested early in egress by Compound 1 or 2. Red cell membrane, red; vacuole membrane, yellow; parasite cell membranes, cyan. Other colours, parasite organelles and ribosomes.

The EM and electron spectroscopy observations were made on the very thin sections needed for transmission EM imaging, so that it was not possible to determine whether the leak arose from tiny holes distributed over the membrane or from a localised broken region that was not captured in the thin sections. A unique feature of soft X-ray beamlines like Diamond's B24 is that they enable 3D imaging of structures as thick as a whole cell in the native, frozen-hydrated state. The B24 images provided an overview of the cells, allowing us to search for localised regions of breakage. However, the data suggested that vacuole membrane did not have any large lesions and that the leakage arises from pores that are too small to detect even by electron tomography. The X-ray overview also revealed the overall shape of the cells, which retain their original biconcave disk shape, albeit distorted by a huge bulge to accommodate the parasite-containing vacuole (Fig. 2). The cytoskeleton underlying the blood cell membrane confers its rigidity.

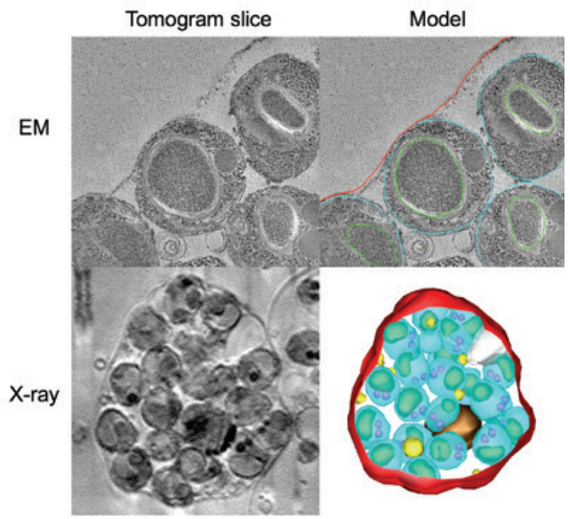

Figure 3: Electron and X-ray tomograms of cells arrested late in egress by E64. Colour code as in Figure 2.

In contrast, EM of the late stage arrested cells showed the parasites loosely enclosed in the remnants of the blood cell, with whorls of membrane left behind by the broken vacuole (Fig. 3). The X-ray view showed how the late stage cells had collapsed and lost their rigidity, likely due to some proteolytic degradation or disassembly of the cytoskeletal network in the later part of the cascade.

We used time lapse video microscopy of live cells and a modified form of the parasites expressing a fluorescent protein in the vacuole, in order to track membrane leakage. The resulting movies, along with a body of previous studies in the literature, show that the egress process is a programme of intense cellular activity punctuated by visible, dramatic changes in cell shape, lasting about 30 minutes from the first detectable step (vacuole membrane permeabilisation) to parasite exit. 10-20 minute pauses between visible steps likely reflect intracellular processes on the subnanometer scale that are not visible by cellular imaging. This sequence of steps is diagrammed in Figure 1.

This study illustrates the power of multiscale imaging with a range of microscopy techniques from optical to X-ray to electron, including fluorescence and spectroscopy, to reveal events on the cellular and subcellular scales. These approaches can be extended to the molecular level if cryo-electron tomography can be applied to slices of vitrified cells produced by the emerging technique of focussed ion beam milling. However, robust procedures for identification and tracking of the region of interest through the various imaging and milling steps are not yet established. This workflow will make it possible to computationally extract large macromolecular complexes from cryo tomograms and combine them to get detailed views of the cellular machinery in situ.

References

1. Blackman, M. J. *et al*. Recent insights into apicomplexan parasite egress provide new views to a kill. *Current Opinion in Microbiology* **16**, 459-464, doi:10.1016/j.mib.2013.04.008 (2013).
2. Thomas, J. A. *et al*. A protease cascade regulates release of the human malaria parasite *Plasmodium falciparum* from host red blood cells. *Nature Microbiol* **3(4)**, doi:10.1038/s41564-018-0111-0 (2018).
3. Hale, V. L. *et al.* Parasitophorous vacuole poration precedes its rupture and rapid host erythrocyte cytoskeleton collapse in *Plasmodium falciparum* egress. *PNAS* **114 (13)**, 3439-3444, doi:10.1073/pnas.1619441114 (2017).

Funding acknowledgement: This work was supported by Gatan BBSRC CASE PhD Studentship BB/F016948/1 (to V.L.H.), MRC Project Grant G1100013 (to H.R.S., M.J.B., and R.A.F.), Wellcome Equipment Grants 101488, 079605, and 086018 (to H.R.S., M.J.B., and R.A.F.), by the Francis Crick Institute, MRC Grant U117532063 (to M.J.B.), Wellcome Trust ISSF2 funding to the London School of Hygiene and Tropical Medicine, and a Wellcome Trust Career Re-Entry Fellowship 095836/Z/1/Z (to C.v.O.).

Corresponding Authors: Victoria L Hale*, Helen R Saibil, ISMB, Birkbeck College, h.saibil@mail.cryst.bbk.ac.uk

*Present address: MRC Laboratory of Molecular Biology, vhale@mrc-lmb.cam.ac.uk

Red light photosynthesis

Related publication: Qian P, Siebert CA, Wang P, Canniffe DP, Hunter N. Cryo-EM structure of *Blastochloris viridis* LH1-RC complex at 2.9 Å. *Nature* **556**, 203-208, doi:10.1038/s41586-018-0014-5 (2018).

The structure of a photosynthetic protein complex that absorbs infrared light in aquatic bacteria has been determined for the first time, using cryo-electron microscopy (cryo-EM) at eBIC. The work outlined in the journal *Nature*, showed every component of the photosynthetic complex to an impressive 2.9 Å resolution.

In photosynthesis, light harvesting (LH) complexes funnel absorbed solar energy to reaction centre (RC) complexes, which transiently trap and store the harvested energy in the form of a charge separated state. Thereafter, a series of electron and proton transfers within the RC converts a quinone acceptor to its reduced form, a quinol. Plants and algae usually absorb light energy at wavelengths of up to 700 nm, but one particular phototrophic bacterium *Blastochloris* (Blc.) *viridis* can absorb and utilise wavelengths far greater than these. Remarkably, these bacteria have adapted RCLH complexes with the capacity to absorb energy above 1000 nm – near infrared light that is inaccessible to other photosynthetic organisms.

The central RC component of the Blc. viridis photosynthetic complex was the first ever membrane protein structure to be successfully determined by X-ray crystallography which resulted in the awarding of the Nobel prize in 1985 to Deisenhofer, Huber and Michel[1,2]. However, the structure of the LH1-RC complex in its entirety had eluded scientists until now. To understand the structural basis of the extraordinary infrared absorption, researchers from the University of Sheffield collaborated with scientists at eBIC and utilised Titan Krios I to determine the structure of the LH1-RC complex. The resulting 2.9 Å resolution structure revealed the positions of all bacteriochlorophyll, carotenoid, haem and quinone cofactors, as well as the protein-protein interactions that form the structural basis for infrared light absorption, charge-trapping electron transfers and export of the quinol product.

Plants and algae use chlorophyll *a* to absorb solar energy at wavelengths up to 700 nm. However, it has been known for decades that some phototrophic bacteria can make use of other, lower energy regions of the solar spectrum, by absorbing light in the 750–900 nm region. Most of these bacteria use bacteriochlorophyll *a*, which absorbs at around 770 nm in methanol, and their LH1-RC complexes red-shift the absorption maximum to 870–880 nm. *Blc. viridis* uses bacteriochlorophyll *b* (BChl b) which, when solubilised in methanol, absorbs at 795 nm, and remarkably, achieves a red shift of 220 nm from the pigments, enabling photosynthesis to occupy a spectral niche above 1000 nm.

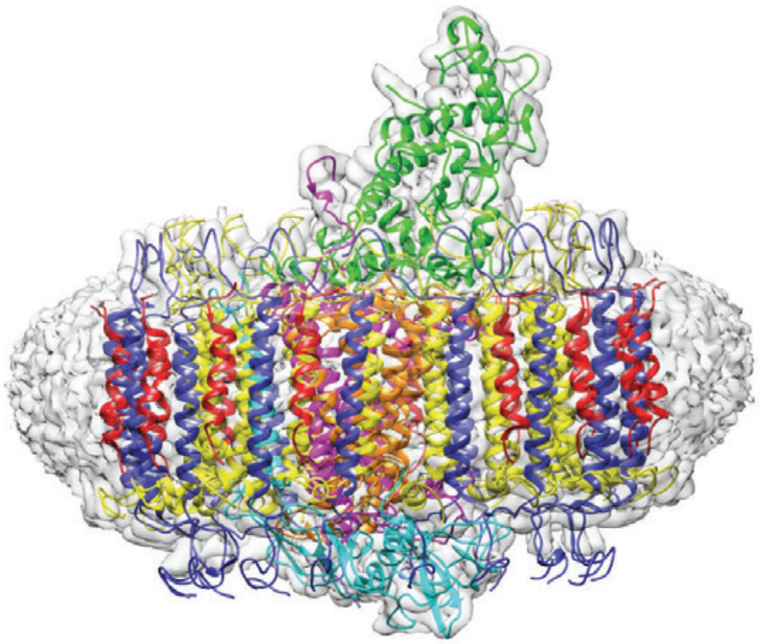

Figure 1: The cryo-EM structure of the Blc. viridis LH1-RC complex, with the electron density map in grey and ribbon representations of LH1-α (yellow), LH1-β (dark blue), LH1- γ (red), RC-C (green), RC-H (cyan), RC-L (orange) and RC-M (magenta).The LH1 complex is surrounded by a belt of detergent and other disordered molecules.

The application of cryo-electron microscopy (cryo-EM) was crucial to understand the whole intact complex and its role in photosynthetic growth as the reaction centre alone cannot harvest sufficient light. The LH1 ring that surrounds the RC and co-ordinates a bacteriochlorophyll array harvests and delivers captured light energy extremely efficiently to the RC special pair. This process is illustrated in fine detail in the published structure.

The cryo-EM structure of the *Blc. viridis* LH1-RC complex showed that the organism employs a range of strategies to allow it to harvest light at 1000 nm. The presence of BChl *b* alone is insufficient to explain the absorption and the high-resolution structure indicated a number of additional contributory factors. As has been demonstrated in related organisms by site-specific mutagenesis, H-bonding between BChl *b* and LH1 Trp residues is likely responsible for a component of the red shift[3]. Additional contributions are due to the size, stiffness and extensive cooperativity within the complex between the proteins and co-ordinated pigments. The *Blc. viridis* LH1 complex also contains a novel gamma subunit and this enables a triple ring structure which further rigidifies the entire array thereby promoting the red shift.

The product of energy trapping is a quinol molecule, which must escape the confines of the LH1 ring that surrounds the RC and move into the quinone pool for subsequent utilisation by the cytochrome bc_1 complex[4]. The *Blc. viridis* LH1-RC structure illustrates how quinols may traverse the surrounding LH1 ring. A small pore is apparent in the LH1 ring, near a binding pocket, which houses a quinol, designated Q_P. This binding pocket provides a folding template that imposes a compact conformation and a suitable orientation on Q_P prior to its entry to the pore in the LH1 ring. Thus, the RC-LH1 complex of *Blc. viridis* reveals a new strategy for fostering quinol/quinone exchange across an LH1 ring.

The structural insights gained from this study could enable near infrared light absorption to be engineered into biosynthetic, bioinspired or biohybrid photosynthetic structures. In particular, bacteria could be adapted to have a wide input of solar energy with applications for novel solar cell technologies.

The team will continue looking at this bacterium and they plan to apply genetic engineering to remove the critical outer ring to see if they can force the complex to absorb light towards higher energy wavelengths. Building on the success of this structural study at eBIC they will also explore other photosynthetic systems using cryo-EM.

References:

1. Deisenhofer, J. *et al*. Structure of the protein subunits in the photosynthetic reaction centre of *Rhodopseudomonas viridis* at 3 Å resolution. *Nature* **318**, 618–624, doi:10.1038/318618a0 (1985).
2. Deisenhofer, J. & Michel, H. Nobel lecture: The photosynthetic reaction centre from the purple bacterium *Rhodopseudomonas viridis*. *EMBO* **8**, 2149–2170 (1989).
3. Olsen, J. D. *et al*. Modification of a hydrogen bond to a bacteriochlorophyll a molecule in the light-harvesting 1 antenna of *Rhodobacter sphaeroides*. *Proc Natl Acad Sci USA* **91**, 7124–7128 (1994).
4. Blankenship, R. E. Molecular Mechanisms of Photosynthesis 2nd edn. *John Wiley &* Sons, Oxford (2014).

Funding:

C.N.H. and P.Q. acknowledge support from the Biotechnology and Biological Sciences Research Council (BBSRC) UK, award number BB/M000265/1, the European Research Council Advanced Award 338895 and the Sheffield University Imagine programme. C.N.H. was also partially supported by the Photosynthetic Antenna Research Center (PARC), an Energy Frontier Research Center funded by the US Department of Energy, Office of Science, Office of Basic Energy Sciences (Award number DE-SC0001035). D.P.C. acknowledges funding from the European Commission (Marie Skłodowska-Curie Global Fellowship 660652). We acknowledge Diamond for access and support of the Cryo-EM facilities at the UK national electron bio-imaging centre (eBIC), funded by the Wellcome Trust, MRC and BBSRC.

Corresponding authors: Prof Neil Hunter, Dept of Molecular Biology and Biotechnology, University of Sheffield, c.n.hunter@sheffield.ac.uk, Dr Alistair Siebert, eBIC, Diamond Light Source, alistair.siebert@diamond.ac.uk

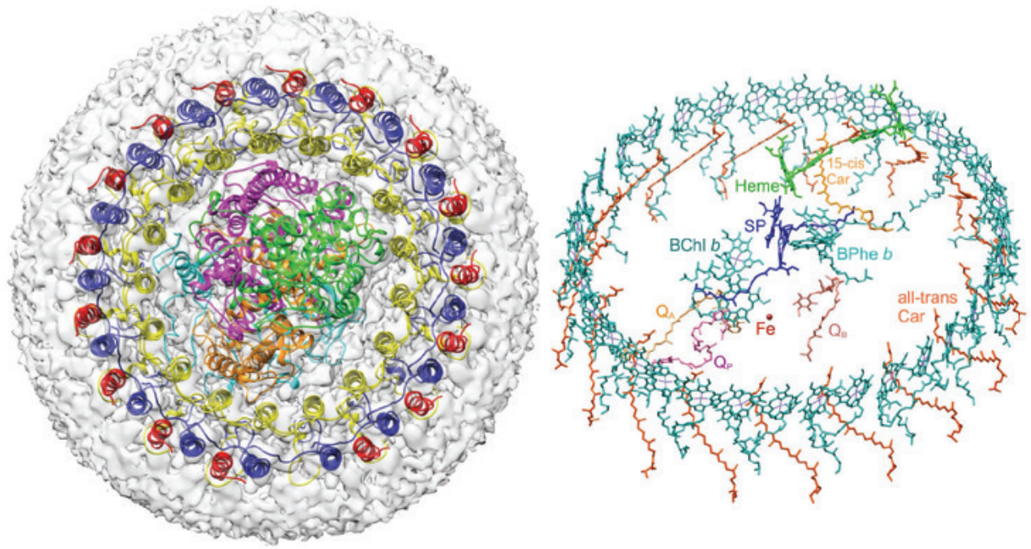

Figure 2: (Left) Top view of the periplasmic face of the complex. The 'missing' LH1- γ in the outer ring at the bottom of the figure is the location of the pore for quinol export and for oxidised quinones to gain access to the RC. (Right) Closely spaced LH1 bacteriochlorophyll b (sea green) and carotenoid (orange) pigments surrounding central RC pigments, as well as haem cofactors (green) for electron transfer to the RC, and quinones (Q) for transport of protons and electrons away from the RC.

Spectroscopy Group

Sofia Díaz-Moreno, Science Group Leader

Following the restructuring of the Diamond Science Division, the Diamond Spectroscopy Group is built around four beamlines; the Microfocus Spectroscopy beamline (I18) the Core X-ray Absorption Spectroscopy (XAS) beamline (B18) and the two independently operating branches of the Versatile X-ray Absorption Spectroscopy beamline, I20-scanning and I20-EDE. These four beamlines are complementary in many aspects, such as the energy range they cover, the size of the focussed beam spot delivered to the sample, and the time resolution they are able to reach.

Nevertheless, each beamline has its unique characteristics and they are optimised for performing different types of experimental studies. Over the last year more than 1,350 peer-reviewed experimental shifts were delivered using the Spectroscopy Group beamlines, covering many different scientific disciplines, from chemistry and catalysis to environmental and life sciences, materials science, hard condensed matter and cultural heritage.

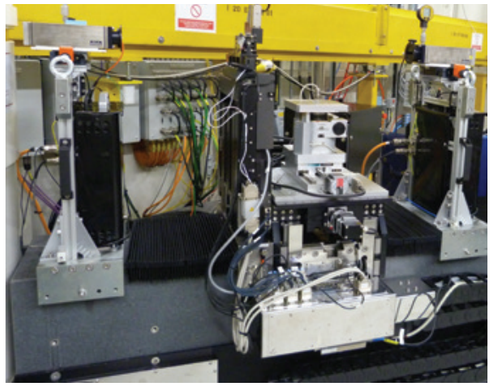

Figure 1: Turbo-XAS end-station mounted on the I20-EDE branch.

As well as supporting a very vibrant user programme, many technical developments have also been implemented on the beamlines during the last year. Some of the developments have improved data quality and collection times, while others have added new capabilities to the beamlines.

I18 Update

The Microfocus Spectroscopy beamline (I18) uses a 2x2 µm beam to examine heterogeneous material on the micrometre scale using a variety of techniques, such as X-ray Fluorescence (XRF), X-ray Absorption Near Edge Structure (XANES) spectroscopy and X-ray Diffraction (XRD). During the last year considerable effort has gone into optimising the new mapping perspective used to collect XRF maps, as well as its integration into the Diamond General Data Acquisition program (GDA). This new software, originally installed in November 2016 along with a new motor control platform, has dramatically improved the efficiency of XRF map collections. This has allowed the routine collection of full fluorescence XANES map stacks; about a hundred maps at different incident energies are acquired over the same region of a sample to give hundreds of XANES scans when the energy dimension of the dataset is probed. The software has been fine tuned to give a much smoother user experience over the last year.

In addition, a new silicon drift Vortex-ME4 detector has been installed to operate together with the already existing detector. The two silicon detectors are now routinely used for data collection in a set-up shown in Figure 2. The use of these detectors has replaced the need to use a liquid nitrogen cooled germanium detector, simplifying significantly the beamline operation, as well as improving the count rate performance for the energy range covered by the beamline.

B18 Update

The Core XAS beamline (B18) uses an X-ray beam covering a broad energy range to collect X-ray Absorption Spectroscopy (XAS) data on all elements heavier than phosphorus. The capability of the monochromator for continuous scanning together with a flexible experimental space with the availability of a large range of sample environment equipment, make this beamline ideal to perform experiments *in situ* and under *operando* conditions.

The fluorescence capabilities of B18 have been expanded with the development of an X-ray spectrometer with medium energy resolution working in Von Hamos geometry. This spectrometer has been designed to overcome the limitations of the traditional solid state detectors when the fluorescence detection of the element of interest is affected by the presence of overlapping emission lines and intense backgrounds. The spectrometer has demonstrated very good performance not only for the study of complex samples, but also for very dilute systems. The implementation of streamlined alignment procedures and an increase of the collected solid angle are on-going developments. We expect to be able to make this spectrometer available to the user community in late spring 2018.

Upgrades to the beamline in 2017 also included the redesign of the low energy section of the experimental table. With this new development, the set-up time for low energy experiments that are not compatible with high vacuum conditions is significantly reduced, increasing the efficiency and the reliability of the beamline.

The implementation of a simplified framework has improved the software interface for experiments with a large number of samples. The measurements can be programmed in one go using a spreadsheet-like interface, minimising the chances of errors during the experiment preparation. This functionality has already been used during the Block Allocation Group access mode reducing the time needed for the experiment.

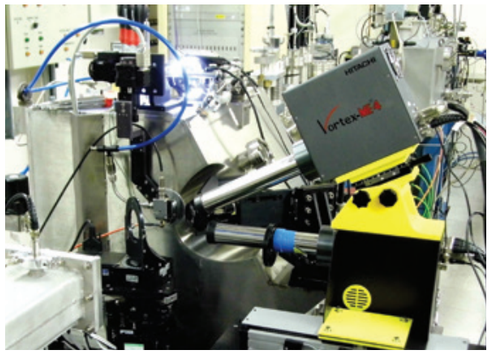

Figure 2: Two silicon detectors configured for use on I18 to increase count rate performance.

Figure 3: The scientists, engineers, technicians, PDRAs and PhD students that make up the Spectroscopy Group.

I20 Update

The scanning branch of I20 (I20-scanning) provides high intensity X-rays for the study of very low concentration samples by XAS. It also provides the capabilities to perform X-ray Emission Spectroscopy (XES) using a Rowland circle spectrometer, enabling the performance of high-resolution studies of the electronic structure of samples.

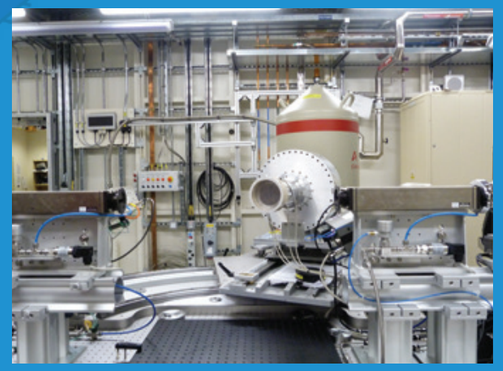

Figure 4: I20-Scanning fluorescence detector mounted on the new rotational stage that enhances flexibility for sample environment integration.

This year the main developments on this branch have been focussed on improving its ability to perform XAS on challenging samples. A new experimental table has been installed to allow the integration of a large rotational stage for the 64 element monolithic germanium solid state detector. With this stage the detector can be located at different angles with respect to the incident X-ray beam which allows the use of sample environments that leave very limited space for the collection of the fluorescence emission. To further improve the beamline performance, new read-out electronics has been developed and integrated with the germanium detector. This new system is the Xspress-4 digital pulse processor that has been developed in-house by the Diamond Detector Group. Xspress-4 is able to deliver a factor of three increase in detector system count rate whilst maintaining the data quality that could be achieved using the previous read-out system. This new read-out system consequently allows the beamline to study samples where the element of interest is surrounded by many other heavy elements that otherwise would saturate the detector signal at high count rates.

The development project for a new monochromator for the scanning branch of I20 is still ongoing with the aim of delivering a device that is to enable better use of the high photon flux delivered by the wiggler source, and extend the energy range of the beamline up to 34 keV.

The I20-EDE branch is designed to perform XAS experiments in dispersive configuration, and has been optimised for *in situ* and *operando* time-resolved studies over time scales ranging from seconds down to milliseconds or even microseconds. The optimisation of this branch has continued during the last year and significant effort has been invested in the development of the software necessary to visualise and analyse the large amount of data that can be collected. In addition, the development and integration into the beamline of a sequential data acquisition mode, turbo-XAS, is very well advanced. This mode of data collection is well suited to the investigation of systems in transmission mode when small angle scattering from the samples is significant, or in fluorescence mode when the concentration of the element of interest is low. Two successful user experiments have been performed during the last year that makes use of this new development.

In parallel to supporting the beamlines and the operational science programme, the Spectroscopy Group was also busy last year organising and hosting the *International Workshop on Improving Data Quality on XAFS Spectroscopy, Q2XAFS2017*. At this event, more than 50 participants met to review international standards and protocols, and to revise recommendations for best practice when performing XAFS experiments.

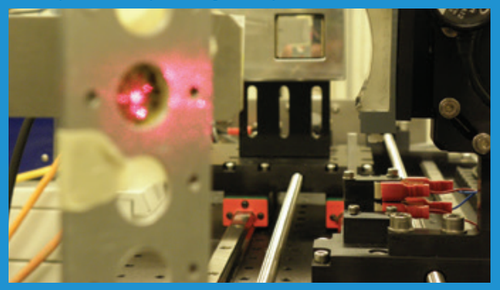

Figure 5: The Von Hamos spectrometer installed at B18.

Nanocrystallites on micro-catalysts brought into focus

Related publication: Price SWT, Martin DJ, Parsons AD, Sławiński WA, Vamvakeros A, Keylock SJ, Beale AM, Mosselmans JFW. Chemical imaging of Fischer-Tropsch catalysts under operating conditions. *Science Advances* **3**, e1602838, doi:10.1126/sciadv.1602838 (2017).

Publication keywords: Catalysis; Tomography; Diffraction; Fluorescence

The Fischer-Tropsch process is used to convert hydrogen and carbon monoxide to hydrocarbons. It relies on the use of catalysts, which make the process more efficient and can control which products are produced, from long hydrocarbon chains to heavy waxes. A team of researchers developed a novel technique to investigate how cobalt catalysts change, at both the micro- and nanoscale, during the Fischer-Tropsch process. They used the Microfocus Spectroscopy beamline (I18) which allowed them to focus X-rays down to the microscopic sizes (5 µm) needed for the study, and to collect all of the different modes of characterisation (absorption, diffraction, fluorescence, mass spectrometry) simultaneously. This was the first simultaneous measurement of all the characterisation techniques on the beamline.

Their work investigated the influence of the deposition sequence on the chemical and physical structure of the catalyst, in 3D, under conditions close to those used in large scale reactors, so the observed structure and activity relationships from the experiment are relevant to the full scale reactors. Their results show that even small modifications in how catalysts are made can significantly affect their performance.

Many active catalysts consist of metal nanoparticles supported on larger grains of refractory oxides, such as silica (SiO_2), titania (TiO_2), alumina (Al_2O_3), or a mixture thereof. This helps optimise the metal nanoparticles dispersion and improve the long term stability. Recently, additional metals have been added to the catalyst in small amounts to 'promote' the activity further (e.g. rhenium, platinum), and help control the long term stability of the particles[1]. These compound systems are now the catalyst of choice at many plants. However, with the increase in constituents comes and increase in complexity, both in how they can be synthesised, and the resultant chemical and physical structures that are formed. One factor that can affect this is the order in which the catalyst and promoters are added to the support. To that end, two samples were prepared with identical elemental compositions (10 wt% cobalt, 1 wt% rhenium, 5 wt% titanium, supported on silica – CoRe/Ti/SiO_2). The Re is a promoter for the Co to lower the temperature needed to reduce it from an oxide to a metal, the state required to perform FTS, and the Ti is a modifier for the silica support to aid the interaction with Co. The difference between the two samples being whether Ti was added first or last to the support material. Differing activity (conversion of CO) and selectivity (formation of desired long chain hydrocarbon products) were observed between the two catalysts, however the reasons for this were not fully understood. Previous studies of similar materials to determine the active state of the catalyst were bulk measurements of an area in a reactor and therefore only revealed the average composition present[2]; supported catalysts possess complex micro- and nano- structures that need to be considered to fully understand the relationship between structure and performance. To this end, the multimodal tomography set up was developed on beamline I18. A microreactor was developed that could be scanned through the highly focussed X-ray beam (5 µm), and X-ray diffraction (XRD), X-ray fluorescence (XRF) and X-ray absorption data collected simultaneously. By rotating the reactor in the path of the beam as well as scanning it, this data could be collected at different angles (computed tomography, CT), which when reconstructed revealed the location of each grain within the reactor, and the locations of each element and crystalline phase present within each individual grain[3].

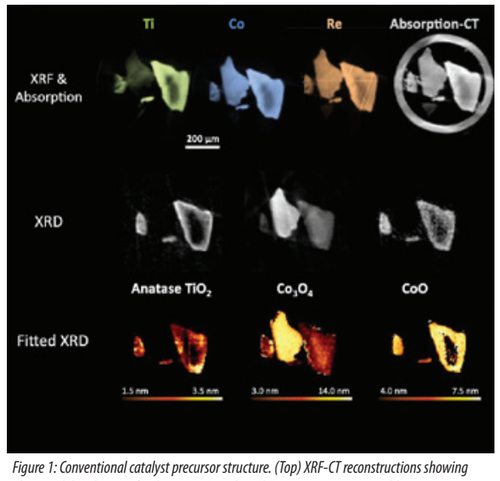

Figure 1: Conventional catalyst precursor structure. (Top) XRF-CT reconstructions showing elemental distributions for the conventional catalytic precursor. Green, Ti; blue, Co; orange, Re. Absorption-CT reconstruction (grey) also shows the capillary wall surrounding the particles. (Middle) XRD-CT reconstructions of the conventional catalyst revealing the phases present. (Bottom) Average crystallite size per pixel for each phase identified. Each pixel is 5 µm × 5 µm. Gas flow was 6 ml min^{-1} He at 25°C.

When Ti is added first it is oxidised and partially crystallises on the large SiO_2 grains forming the anatase polymorph of titania (TiO_2). Typically, in the precursor material, the Co is present in the spinel form Co_3O_4, however in regions where anatase is concentrated a small proportion is reduced to CoO (Fig. 1). A typical bulk XRD measurement would not have been able to reveal this relationship. Once the cobalt oxide is reduced to metallic cobalt (400 °C H_2), no traces of either oxidic phase remain. However, once FTS conditions are started (200 °C $2H_2$:CO), the smallest Co nanoparticles that are co-located with anatase are susceptible to re-oxidation back to CoO (Fig. 2).

For the catalyst where Ti is added second, after the Co and Re, it does not crystallise, however there is still a small an amount of CoO present in the precursor material in regions with high Ti concentration, indicating that the formation of CoO is not dependent on crystalline TiO_2. Once through the reduction cycle and into FTS conditions, the catalyst is stable against reoxidation, with only metallic Co forming.

Furthermore fitting of the diffraction patterns revealed information on the nature of the metallic Co. Typically, metallic Co packs together in two different forms, cubic and hexagonal (Fig. 3). A third, disordered, form of packing known as intergrown Co is also possible; as this is a random mixture of cubic and hexagonal packed layers, it results in broader, less intense diffraction peaks, and is harder to quantify. For both catalysts studied here, fitting of the XRD data revealed the degree of intergrowth can be directly correlated with the Ti modification on the silica support. When Ti is deposited before the Co, it increases the strength of the metal support interaction and results in smaller, strained Co nanoparticles (a result of a higher degree of intergrowth) therefore explaining why they are prone to reoxidation under FTS conditions (Fig. 2). The weaker metal support interaction when Co is deposited first means the Co atoms are more mobile, forming larger crystallites that are less strained, with a lower degree of intergrowth and therefore more stable once under FTS conditions.

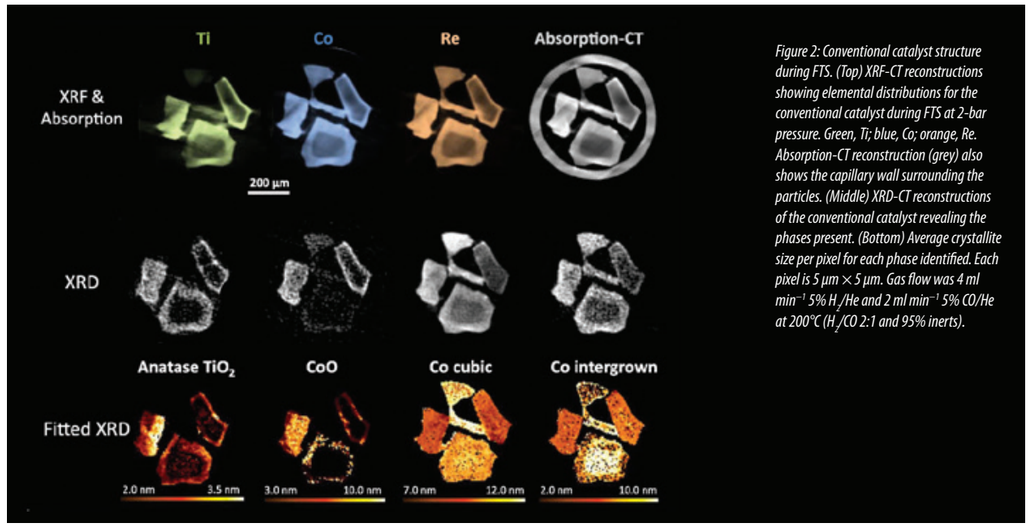

Figure 2: Conventional catalyst structure during FTS. (Top) XRF-CT reconstructions showing elemental distributions for the conventional catalyst during FTS at 2-bar pressure. Green, Ti; blue, Co; orange, Re. Absorption-CT reconstruction (grey) also shows the capillary wall surrounding the particles. (Middle) XRD-CT reconstructions of the conventional catalyst revealing the phases present. (Bottom) Average crystallite size per pixel for each phase identified. Each pixel is 5 µm × 5 µm. Gas flow was 4 ml min^{-1} 5% H_2/He and 2 ml min^{-1} 5% CO/He at 200°C (H_2/CO 2:1 and 95% inerts).

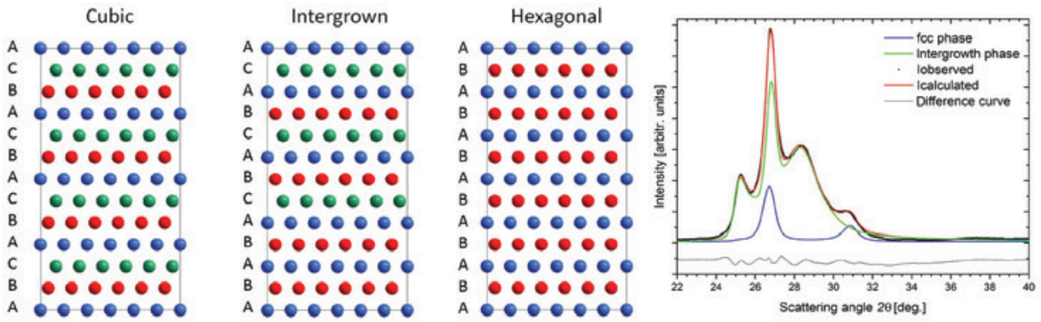

Figure 3: Simulation of diffraction patterns. (Left) Co crystal structures used for XRD simulations: Cubic (fcc) with ABC stacking, intergrown with fully random stacking, and hexagonal (hcp) with ABAB layer sequence. (Right) Exemplar fit of the XRD pattern generated from cluster analysis of inverse catalyst after reduction using DISCUS. Black points, experimental pattern; red, fitted pattern; blue, fit to cubic phase; green, fit to intergrown phase; grey, difference curve.

In both cases, however, the degree of intergrowth (i.e. disorder) in the Co is linked to the concentration of Ti and not its crystallinity. The Co nanoparticles formed when Ti is deposited first are smaller and more active to CO conversion, whereas when Ti is deposited second, the Co nanoparticles formed are larger and have greater selectivity towards longer chain hydrocarbon products.

The complex relationships between elemental and crystalline phase distributions could only be revealed by the multimodal tomography technique developed and, crucially, correlation of structure with activity and selectivity was possible as the data was recorded whilst the catalyst was operating. The understanding of how the degree of disorder affects catalyst activity and selectivity has not been considered to the same extent as the effect of nanoparticle size has. This opens the way to new means to tune catalyst selectivity for FTS, and in a broader sense, the techniques developed here can pave the way for studying other catalytic reactions.

References:

1. Jacobs, G. *et al.* Fischer–Tropsch synthesis: Study of the promotion of Re on the reduction property of Co/Al203 catalysts by *in situ* EXAFS/XANES of Co K and Re LIII edges and XPS. *Appl. Catal. A-Gen.* **264**, 203-212, doi:10.1016/j.apcata.2003.12.049 (2004).
2. Tsakoumis, N. *et al*. Fischer–Tropsch synthesis: An XAS/XRPD combined in situ study from catalyst activation to deactivation. *Journal of Catalysis* **291**, 138, doi:10.1016/j.jcat.2012.04.018 (2012).
3. Price, S.W.T. *et al*. In situ microfocus chemical computed tomography of the composition of a single catalyst particle during hydrogenation of nitrobenzene in the liquid phase. *Angew. Chem. Int. Ed. Engl.* **54,** 9886-9889, doi:10.1002/ange.201504227 (2015).

Funding acknowledgement:

We thank Diamond Light Source for access to beamtime. We acknowledge the University of Oslo for access to high-performance computing (NN2875k), the Engineering and Physical Sciences Research Council (EP/K007467/1), Vetenskapsrådet (Sweden; VR-2012-5240) and the Science and Technology Facilities Council for additional funding,

Corresponding author: Prof Andrew Beale, UCL, andrew.beale@ucl.ac.uk

Atomically Dispersed Gold Species Can Act as Catalysts

Related publication: Malta G, Kondrat SA, Freakley SJ, Davies CJ, Lu L, Dawson S, Thetford A, Gibson EK, Morgan DJ, Jones W, Wells PP, Johnston P, Catlow CRA, Kiely CJ, Hutchings GJ. Identification of single-site gold catalysis in acetylene hydrochlorination. *Science* **355(6332)**, 1399-1403, doi: 10.1126/science.aal3439 (2017).

Publication keywords: Gold; Single site catalysis; Acetylene hydrochlorination; *In situ* measurements

Current production process for vinyl chloride, the monomer used in PVC and everything from piping and tubing to gels and lubricants, relies on a mercury-based catalyst. Mercury is one of the most toxic substances on the planet, and the UN recently ratified the Minamata Convention, meaning that a more environmentally-friendly alternative is required.

It has been shown that gold supported on carbon could be used as an alternative catalyst for this reaction, and although it is currently being commercialised its behaviour under harsh reaction conditions has never been investigated. The reaction is typically carried out at 200°C, using corrosive gas mixtures that can rapidly deactivate catalysts. X-ray absorption spectroscopy (XAS) is the ideal tool for observing the reaction *in situ*, and the quick acquisition time available on B18 gave a team of researchers the time resolution needed to see activation and deactivation during the reaction.

Their results offer the first example of a single site catalyst remaining atomically dispersed and working under such harsh reaction conditions, and will enable more rational catalyst design to find a replacement for the current mercury catalyst.

The production of vinyl chloride monomer (VCM) as the precursor to polyvinyl chloride (PVC) is a major industrial process. In particular, 42 million tonnes of PVC had being consumed in 2016, constituting 16% of total plastic demand[1]. The production of VCM through acetylene hydrochlorination (the reaction of acetylene with HCl) using a mercuric chloride based catalyst is the dominant method of VCM production in coal rich areas such as China. However, the catalyst losses significant amounts of mercury, posing a great risk to the environment. The recently ratified Minamata convention has outlined that VCM production must move to mercury free production by 2022, necessitating the development of a new commercial catalyst for VCM production.

This need had been recognised previously and led, in 1985, to the prediction of gold based catalysts as effective for this reaction. This prediction was based on correlation of activity with the standard electrode potential of metal chlorides supported on carbon and has been subsequently proven experimentally, leading to the exponential growth in the field of gold catalysis. With the legislative pressure to replace the current catalyst system Au/C has become a viable alternative due to its stability, limited metal toxicity via loss to the environment and high selectivity to the desired product[2].

To date effective catalysts have been studied which were prepared by impregnation of a gold precursor ($HAuCl_4$) with an acidic solution of aqua regia (a mixture of nitric and hydrochloric acid). This impregnation method prevents the agglomeration of large metallic Au nanoparticles which are readily seen when impregnating the precursor in aqueous solution and have been shown to be inactive. Despite this observation, there remained in the literature confusion about the active form of the catalyst with many active catalysts appearing to contain metal nanoparticles. Multiple examples of active catalyst showed the predominant species present to be metallic Au by characterisation methods such as X-ray photoelectron spectroscopy (XPS) despite no observation of metallic gold by bulk diffraction methods such as X-ray diffraction (XRD). Commonly, minority cationic components of Au (I) and Au (III) were observed which led to the hypothesis that cationic Au at the periphery of the larger nanoparticles was the active site for the acetylene hydrochlorination reaction[3].

To prepare the most active catalyst the highest utilisation of the active phase is desirable, therefore the determination of the cationic species as either the active sites or a spectator species is essential. It has also been reported that $HAuCl_4$ can be susceptible to photo-reduction by XPS which could result

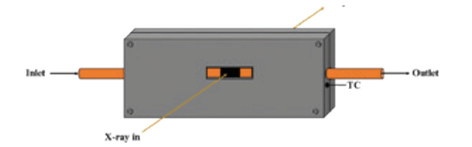

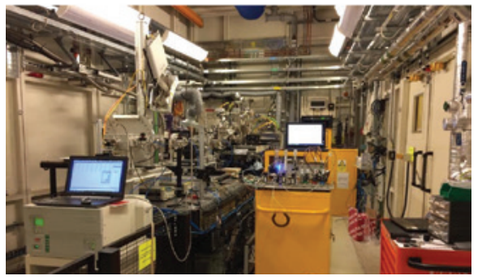

Figure 1: Experimental setup to carry out acetylene hydrochlorination with simultaneous acquisition of X-ray absorption spectra.

in the metallic phase being over estimated in these catalysts materials when analysed ex situ. In addition, characterisation of these materials by TEM revealed the presence of some amorphous Au-chloride structures which sintered to nanoparticles under the electron beam. These observations demonstrate the limitations of characterising this material ex situ because of the sensitive nature of the nanostructures to beam damage[3].

To gain a greater understanding of the active form of the catalyst under operating conditions, a reactor system was designed in consultation with beamline B18. The designed reactor allowed the research team to simultaneously acquire X-ray absorption spectra, at the Au L_3 absorption edge, while carrying out an acetylene hydrochlorination reaction at realistic reaction conditions with product analysis by mass spectrometry (Figure 1). This allowed for the correlation of the performance of the catalyst with Au oxidations state and co-ordination environment as determined by the X-ray absorption spectra. Reactions were carried out at 200 °C with 100 mg of 1% Au/C catalyst prepared using the aqua regia impregnation method and 50 ml min^{-1} of gas flow containing acetylene (C_2H_2) (2.35 vol%), Hydrogen Chloride (HCl) (2.4

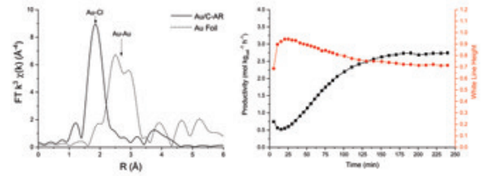

Figure 2: (a) k3- weighted c EXAFS Fourier transform of aqua regia prepared 1% Au/C catalyst and Au foil standard (b) Normalised white line intensity correlated with VCM productivity over the course of the reaction induction period.

vol%) and Argon (Ar) as carrier gas. Using the quick acquisition time available and the x-y movable stage it was possible to record XAS spectra at three points through the catalyst bed, every three minutes during the extended reaction.

Utilising the quick acquisition times and element specific absorption the resulting smaller absorption cross sections, when compared to XPS, made it possible to characterise the catalysts with minimal photo reduction. This gave a more representative characterisation of the Au species present in the catalyst, which are particularly sensitive to photoreduction.

The first key observation was in the characterisation of the fresh catalyst material. Analysis of the X-ray Absorption Near Edge Structure (XANES), specifically using the normalised whiteline absorption height and a linear combination fitting analysis, with Au(III), Au(I) and metallic Au standards, revealed that the Au in the catalyst was in a cationic form with no indication of metallic Au. This was further confirmed by the Extended X-ray Absorption Fine Structure (EXAFS) analysis which demonstrated no intensity in the Fourier-transform characteristic of Au-Au but only Au-Cl bond distances, signifying that the Au species were isolated in the catalyst rather than forming metallic nanoparticles[4].

The catalyst samples were then heated to 200 °C under an inert atmosphere, where the XAS again suggested that the samples were free of any metallic Au nanoparticles structure. During this it was possible to observe the decomposition of the $AuCl_3$ type species into AuCl like species corresponding the decomposition temperature of $AuCl_3$ to AuCl at around 160 °C. On the introduction of the reactant gases the Au speciation evolved, initially through re-oxidation to a Au(III) species before equilibration to a stable Au(III) [30%] : Au(I) [70%] ratio with no characteristic Au – Au scattering distances present throughout this equilibration process. Analysis of the VCM productivity acquired at the same time as the XAS, revealed an induction period where the

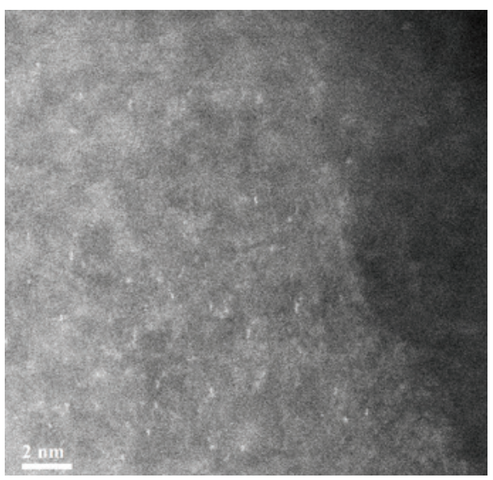

Figure 3: Representative STEM-HAADF image showing mono dispersed single site isolated Au species.

catalyst is becoming more active over time until equilibration at steady state. This induction period was able to be correlated with the Au(III) : Au(I) ration of the catalyst material (Fig. 2). At all points, no metallic Au was detected. A subsequent high-angle annular dark-field scanning electron transmission microscopy (HAADF-STEM) analysis, optimised to reduce beam damage, confirms the observation of isolated Au species in the fresh catalyst material (Fig. 3).

This study provided the evidence that the isolated cationic Au species present in the catalyst were in fact the active species and damage and photoreduction of the catalyst materials through ex situ characterisation masked and confused the interpretation of the active form of the catalyst in previous studies. By characterising the catalyst during the reaction, the research team were able to conclusively show that the active catalyst for this reaction is isolated cationic Au sites akin to homogenous catalysts. This provides an opportunity to design the ligand environments around the Au centre to improve catalyst activity and stability which could result in Au becoming the replacement for the mercury based catalysts for VCM manufacture. In fact Au/C catalysts have been successfully operated at a commercial scale and look set to lead the reduction in mercury usage in this large scale industrial process[5].

References:

1. Polyvinyl Chloride (PVC) – Market Study|Ceresana, http://www.ceresana.com/en/market-studies/plastics/polyvinyl-chloride/, accessed 27 July 2017.
2. Hutchings, G. J. Vapor phase hydrochlorination of acetylene: Correlation of catalytic activity of supported metal chloride catalysts. *Journal of Catalysis* **96(1)**, 292-295, doi:10.1016/0021-9517(85)90383-5 (1985).
3. Liu, X. *et al.* Investigation of the active species in the carbon-supported gold catalyst for acetylene hydrochlorination. *Catalysis Science & Technology* **6**, 5144-5153, doi:10.1039/c6cy00090h (2016).
4. Malta, G. *et al.* Identification of single-site gold catalysis in acetylene hydrochlorination. *Science* **355(6332)**, 1399-1403, doi:10.1126/science.aal3439 (2017).
5. Johnston, P. *et al.* Discovery, Development, and Commercialization of Gold Catalysts for Acetylene Hydrochlorination. *J. Am. Chem. Soc* **137(46)**, 14548-14557, doi:10.1021/jacs.5b07752 (2015).

Funding acknowledgement:

We acknowledge Cardiff University for support as part of the MAXNET Energy Consortium. UK Catalysis Hub is thanked for resources and support provided through our membership of the UK Catalysis Hub Consortium and funded by the Engineering and Physical Sciences Research Council (EPSRC) (grants EP/K014706/1, EP/K014668/1, EP/K014854/ 1EP/K014714/1, and EP/M013219/1). We used the B18 beamline at the Diamond Light Source (allocation numbers SP10306, SP11398, and SP15214) C.J.K. acknowledges funding from the National Science Foundation Major Research Instrumentation program (GR no. MRI/DMR-1040229). Calculations were performed through our membership of the UK's High-End Computing (HEC) Materials Chemistry Consortium, which is funded by EPSRC (EP/L000202); this work used the Advanced Research Computing High-End Resource (ARCHER) UK National Supercomputing Service (www.archer.ac.uk). Local high performance computing (HPC) services at University College London (UCL) were used on the Grace computer.

Corresponding author: Prof Graham Hutchings, Cardiff Catalysis Institute, Cardiff University, Hutch@cf.ac.uk

Phosphorylation Enhances Cytochrome *c* Dynamics to Modulate its Function

Related publication: Moreno-Beltrán B, Guerra-Castellano A, Díaz-Quintana A, Del Conte R, García-Mauriño SM, Díaz-Moreno S, Gonzalez-Arzola K, Santos-Ocaña C, Velázquez-Campoy A, De la Rosa Ma, Turano P, Díaz-Moreno I. Structural Basis of Mitochondrial Dysfunction in Response to Cytochrome *c* Phosphorylation at Tyrosine 48. *Proceedings of the National Academy of Sciences* **114 (15),** 3041-3050, doi:10.1073/pnas.1618008114 (2017).

Publication keywords: Cytochrome *c*; Mitochondrial dysfunction; Nuclear magnetic resonance; Phosphorylation; Respiratory supercomplexes

Some diseases, including cancer and ischemia (an inadequate blood supply to an organ or part of the body), involve reversible phosphorylation at a given site on the cytochrome c protein. Cytochrome c is essential for human metabolism and contains a heme iron, which allows it to function as an electron carrier. To understand the molecular basis underlying the effects of phosphorylation, an international team of researchers has used several methods to analyse the structure, dynamics and functional features of an engineered, stable variant of cytochrome c.

The aim of the work was to understand how a change in the protein affects its function within the cell, and the team used X-ray Absorption Spectroscopy (XAS) to determine the protein's structural features. They chose the Versatile X-ray Spectroscopy beamline (I20), in particular the I20-Scanning branchline for its ability to measure highly diluted biological samples. Nuclear Magnetic Resonance (NMR) showed that cytochrome c phosphorylation only induces local structure changes, hardly affecting the overall protein conformation. Both XAS and NMR experiments showed an increase in the mobility of the protein region surrounding the mutation and the heme group, explaining the observed functional changes.

The response of cells to physiological changes and oxidative stress involves the modulation of mitochondrial respiration. This affects the intrinsic activities of the electron transport chain components and their assembly within the internal mitochondrial membrane. In fact, hypoxia induces the grouping of these proteins into the so-called supercomplexes, which facilitates the transfer of electrons between the distinct components of the electron transport chain, while decreasing the generation of reactive oxygen species (ROS). The best known supercomplex is called the respirasome, and encompasses the membrane complexes I, III and IV. Alterations in the formation of the supercomplex lead to the development of hypoxia-dependent pathologies, such as cancer or ischemia. A key modulator of the mitochondrial activity is cytochrome *c* (Cc)[1]. Cc is a small heme-protein which acts as an electron carrier between complexes III and IV; and is highly conserved throughout evolution. Cc also participates in cell life and death decisions in mammals[2] and plants[3]. This pleiotropic role of Cc makes post-translational modifications an essential mechanism to regulate its functions tightly. Phosphorylation and nitration of tyrosine residues stand out among these modifications. Indeed, they affect the conformational equilibria of the protein along with its ability to bind physiological partners[3,4].

Specifically, post-translational Cc phosphorylation at tyrosine 48 is key in modulating mitochondrial signalling. Nevertheless, the mechanism by which it alters the conformation and function of this protein is barely understood. To address this subject requires solving the 3D structure of the phosphorylated species. However, cell-extract phosphatases reverse Cc phosphorylation, hampering the isolation of the modified protein from tissues. This makes any structural analysis a highly challenging task. Hence, we solved the 3D solution-structure of a Cc phosphomimic obtained by replacing tyrosine 48 with the synthetic amino acid *p*-carboxy-methyl-L-phenylalanine (*p*CMF)[5].

In order to do this, the effects of the mutation on the heme iron coordination sphere were tested. First, distance restraints relative to the axial coordination of iron were necessary for the structure computations. All the reported mutants mimicking phosphorylation in this position displayed altered biophysical properties related to conformational stability of the heme moiety[3,5]. Thus, a precise assessment of the changes in coordination geometry of the heme iron was required. Figure 1a shows the XAS fluorescence spectra

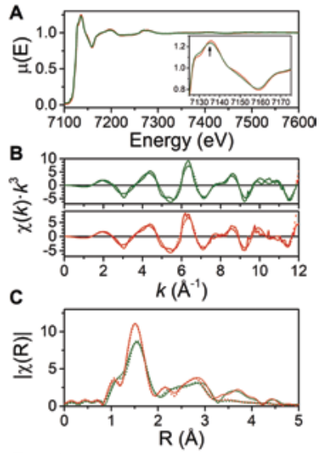

Figure 1

Figure 1: X-ray absorption spectra. (a) Overlay of the X-ray absorption spectra for reduced WT (red) and Y48pCMF (green). Insert: detailed view highlighting the differences within the XANES region. (b) EXAFS extracted signals. (c) Overlay of the Fourier transforms of the EXAFS spectra. In panels (b) and (c), continuous lines correspond to experimental data and dotted lines to theoretical fits.

at the Fe K-edge of wild-type (WT) and mutant (Y48*p*CMF) Cc species at cryogenic temperatures, recorded at the I20-Scanning beamline. Notably, the absorption spectra of the two proteins are very alike. Both spectra include the pre-edge feature at *ca.* 7113 eV, indicative of the octahedral geometry for the first iron coordination sphere. Overall, the X-ray Absorption Near Edge Structure (XANES) region of the spectra for the two Cc species are almost identical, as can be seen in the figure. The absorption edge appears at 7126 eV in both cases, indicating that the oxidation state of the metal ion is not affected by the mutation. However, some spectral features are broadened for the Y48*p*CMF Cc, as is the case of the feature at 7136 eV, related to porphyrin plane distortion.

The Extended X-ray Absorption Fine Structure (EXAFS) signals and the corresponding Fourier transforms are shown in Figure 1b and Figure 1c respectively. The Fourier transforms indicate an increase in disorder for the first coordination sphere around the iron centre for the mutant species. After an initial estimation of the distances between metal and ligand using X-ray diffraction data, a cyclic refinement was performed by selecting coordinates from 10000 snapshots of Molecular Dynamics computations, which determined the lowest squared deviations in distances for the distinct scattering paths selected. Interestingly, there was no significant difference in metal-to-ligand distances in between the two species. Nevertheless, Debye-Waller factors indicated an increase of the disorder in the equatorial ligands – those belonging to the phophyrin ring – in agreement with the broadening of the 7136 eV feature in the XANES region and the decrease of intensity of the first peak of the Fourier transform.

The solution structure of the phosphomimic mutant revealed small, but significant conformational changes in loops containing the phosphorylation site and adjacent residues providing axial ligands for the heme iron (Fig. 2). Furthermore, NMR relaxation data and the presence of signals undergoing slow chemical exchange indicated that phosphorylation enhanced the dynamics of the above-mentioned loops – which surround the heme group. Notably, this facilitates the access of water molecules into the heme pocket. To summarise, the NMR and XAS data indicated that the mutant showed both similar overall 3D structure and iron coordination geometry to the WT protein, but exhibited enhanced dynamics.

Phosphorylation may affect the interaction between Cc and its partners by several means. The addition of a phosphate results in Cc carrying a negative charge, with a significant impact. Additionally, enhanced dynamics in the unbound species increases the conformational entropy penalty. In fact, NMR and Isothermal Titration Calorimetry (ITC) data indicate that one of the two reported docking sites for Cc at its electron donor (complex III) is lost. In the context of the respirasome supercomplex, the docking site which the modified Cc no longer bind lies on the pathway towards its electron acceptor (complex IV). This site was proposed to be involved in restraining the diffusion path of Cc across the respirasome surface (Fig. 3).

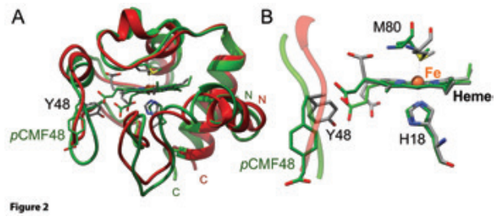

Figure 2

Figure 2: Structural changes in cytochrome c upon phosphorylation. (a) Richardson's ribbons representation of the NMR structures of WT (red; pdb code: 2N9I) and Y48pCMF (green; pdb code: 2N3Y) species. The positions of the N- and C- termini are labelled. (b) Overlay of the heme groups of the two cytochrome species. The targeted residue is also shown. Bonds are represented by sticks. Heavy atoms are in CPK colors, except for Y48pCMF carbons (in green).

To test this hypothesis, yeast mitochondria preparations were prepared under conditions, either avoiding or eliciting supercomplex formation. The performance of WT and mutant Cc species was tested. No difference was found between the two species when supercomplex formation was inhibited. However, when supercomplex assembly was favoured, the activity of Cc as an electron carrier for complex IV increased – according to oxygen evolution measurements – but the activity of the phosphomimic mutant was substantially lower when compared to the WT species.

High complex IV activity has been related to ROS generation[1]. Hence, the inhibition of the electron shuttling from complex III by phosphorylation of Cc may downregulate such a harmful side-reaction. In addition, phosphorylated Cc shows an enhanced peroxidase activity – probably due to higher heme accessibility – which makes it a better ROS scavenger. These findings will eventually aid the development of a robust therapeutic approach, either to foster or silence, as required, the pro-survival action of phosphorylated Cc reported here.

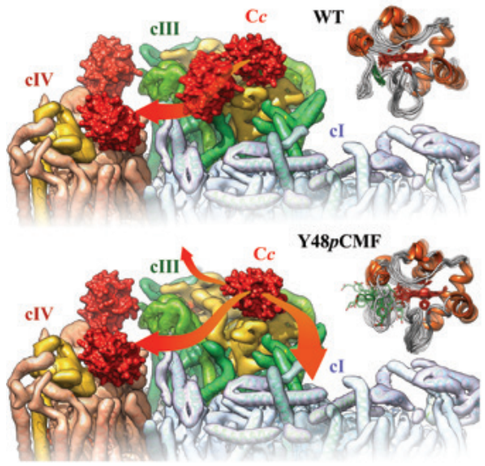

Figure 3

Figure 3: Paths for cytochrome c diffusion from cytochrome c_1 to cytochrome oxidase across the respirasome surface, according to NMR and functional data. Upper: Cytochrome c (Cc) undergoes diffusion restraints (channelling) when carrying electrons from complex III to complex IV that yields a higher performance of the electron carrier. Lower: Phosphorylation enhances the internal motions of Cc and the loss of a secondary binding site in complex III makes Cc drift towards the bulk mitochondrial intermembrane space.

References:

1. Díaz-Moreno, I. *et al.* Cytochrome *c* signalosome in mitochondria, *Eur Biophys J* **40**, 1301-1315, doi:10.1007/s00249-011-0774-4 (2011).
2. González-Arzola, K. *et al.* Structural basis for inhibition of the histone chaperone activity of SET/TAF-1β by cytochrome *c*, *PNAS* **112 (32)**, 9908-9913, doi:10.1073/pnas.1508040112 (2015).
3. González-Arzola, K. *et al*. Histone chaperone activity of *Arabidopsis thaliana* NRP1 is blocked by cytochrome *c*, *Nucleic Acids Res* **45(4)**, 2150-2165, doi:10.1093/nar/gkw1215 (2017).
4. Guerra-Castellano, A. *et al.* Structural and functional characterisationof phosphomimetic mutants of cytochrome *c* at threonine 28 and serine 47, *Biochim Biophys Acta* **1857 (4)**, 387-395, doi:10.1016/j.bbabio.2016.01.011 (2016)
5. Guerra-Castellano, A. *et al.* Mimicking tyrosine phosphorylation in human cytochrome *c* by the evolved tRNA synthetase technique, *Chemistry* **21(42),** 15004-12, doi:10.1002/chem.201502019 (2015).

Funding acknowledgement:

We acknowledge the NMR services at the Centro di Ricerca di Risonanze Magnetiche [CERM; Florence], Centro de Investigación, Tecnología e Investigación [CITIUS; Seville], and Biointeractomics Platform [BIP-cicCartuja; Seville], as well as TA Instruments. We also thank Diamond Light Source for access to beamline I20-Scanning [Proposal SP-6011]. Experimental work was performed in part at the Grenoble INSTRUCT Centre [ISBG; UMS 3518 CNRS-CEA-UJF-EMBL], with support from FRISBI [ANR-10-INSB-05-02] and GRAL [ANR-10-LABX-49-01] within the Grenoble Partnership for Structural Biology. Financial support was provided by the Spanish Ministry of Economy and Competitiveness [Grants BFU2015-71017-P/BMC and BFU2015-19451/BMC, cofounded by FEDER EU], European Union [Bio-NMR-00130 and CALIPSO-312284], Ramon Areces Foundation, and Andalusian Government [BIO198]. B.M.-B. was awarded a PhD fellowship from the Spanish Ministry of Education [AP2009-4092] and a short-term traveling fellowship from the European Bio-NMR Project. A.G.-C. was awarded a PhD fellowship from the CSIC [JaePre-2011-01248]. A.D.Q. thanks Diamond Light Source for supporting him as a visitor scientist.

Corresponding author: Prof Irene Díaz-Moreno, Instituto de Investigaciones Químicas, cicCartuja (Universidad de Sevilla – CSIC), idiazmoreno@us.es

Soft Condensed Matter Group

Robert Rambo, Science Group Leader

The Soft Condensed Matter Group provides the infrared (IR) and Circular Dichroism (CD) spectroscopy and, both Small and Wide Angle X-ray Scattering (SAXS and WAXS) imaging capabilities of Diamond. The Soft Condensed Matter Group comprises of four beamlines B21, B22, I22 and B23. This unique portfolio of beamlines can analyse a range of samples that include two-dimensional thin films (photovoltaics), living mammalian cells, three-dimensional matrices (metal-organic frameworks) and nano-particles in non-crystalline states.

The Soft Condensed Matter Group maintains a dedicated laboratory space for our visiting users. The laboratory houses vital equipment for sample preparation and analysis such as a centrifuges, a small tissue-culture facility, spectroscopy equipment (including CD, standalone IR and UV spectroscopy, multi-angle and quasi-elastic light scattering) and the ability to work with different gases. Laboratory and offline instrumentation usage can be reserved through the User Administration System at any time throughout the operational year of Diamond. Since the start of 2017, both B21 and B23 now offer mail-in services for solution-state SAXS and CD measurements.

Figure 1: Participants at the WIRMS 2017 Workshop hosted in the UK for the first time, by Diamond at Worcester College.

B23 Update

Operational since 2009, the Circular Dichroism beamline (B23) uses circularly polarised light to characterise the structure of complex materials in solution and in solid state films. Many molecular systems have a handedness (chirality) to them akin to our right and left hands. This molecular handedness will preferentially absorb light that is either right-polarised or left-polarised and at B23, measurements are made that precisely quantify how much of each type of light is absorbed by the sample. In thin films, quantification of the polarisation at micron resolution can inform on how materials prefer to orient themselves and for biological samples, CD spectra can be used to demonstrate conformational changes, drug binding or instabilities in a protein.

B23 has pioneered development of high-throughput screening (HTCD) and CD Imaging (CDi) technologies and most recently, the B23 team has developed a unique extreme-environment high pressure cell (HPC). The high pressure sample cell can withstand 2500 times atmospheric pressure while allowing researchers to measure the sample CD spectra. For the life sciences, this sample cell allows researchers to investigate the stability of proteins and enzymes in the solution state under extreme conditions.

B22 Update

The Multimode Infrared Imaging and Microspectroscopy (MIRIAM) beamline (B22) is used to assess the molecular composition and microscopic spatial distribution of a sample at the highest, optically-achievable resolution. B22 operates two end-stations that are dedicated to confocal infrared spectromicroscopy and IR imaging, with a suite of single and array detectors that cover the whole IR range. B22 is used for a wide variety of applications such as the analysis of inorganic-organic combinations and polymers, as well as studying live cells in situ.

The beamline is developing the novel use of adaptive optics to enable the highest contrast IR images in full field microscopy. The adaptive optics instrument uses an innovative double set of deformable mirrors for shaping the IR beam intensity profile. The multipixel detection and image oversampling aims to prove the ultimate spatial resolution and sensitivity achievable in IR imaging via synchrotron radiation. This unique instrumentation capability will be able to study inter-/intra-cellular structures, gas/liquid inclusions evolution in mineralogical sections driven by temperature, hyperspectral imaging of thin film/polymer interfaces, biofilms composition, microcrystal gas-solid reactions *in situ*, as well as catalysis dynamics in microfluidic devices.

I22 update

The Small Angle Scattering and Diffraction beamline (I22) offers combined Small and Wide Angle X-ray Scattering studies (SAXS and WAXS) on a range of low order biological and synthetic samples. It is particularly adept at providing structural information on partially ordered materials ranging from bone and thin-films to large helical structures such as collagen.

I22 pioneered the first in-vacuum Pilatus 2M WAXS detector. Recent optimisations combining simultaneous SAXS and WAXS measurements have enabled measurements that cover a resolution range of nearly 10000. This resolution range can provide information at length scales from the size of a single bond to the width of a bacteria cell. This optimised X-ray camera generates a massive amount of data for Diamond users and I22 has also focused on integrated pipelines for data reduction and processing in the scientific software platform DAWN. In the coming year, I22 will be introducing an integrated microfocus capability allowing for rapid changes in beam sizes ideal for scanning experiments.

B21 update

The High Throughput SAXS beamline (B21) is dedicated to the study of non-crystalline, randomly oriented particles. SAXS measurements can be made on any type of sample and in any physical state. For the life sciences community, solution state SAXS measurements allow for the opportunity to study biological machines in conditions that are comparable to their liquid, hydrated environment. This ability complements the many solid-state studies performed at Diamond using X-ray crystallography and cryo-electron microscopy. The B21 end-station can be configured for low-throughput, syringe-pump based experiments and high-throughput batch-mode experiments using either the bioSAXS sample delivery robot or high-performance liquid chromatography (HPLC) instrument for inline size-exclusion chromatography (SEC) coupled SAXS.

In the continued quest to lower the instrumentation background, B21 relocated the sample and detector downstream by nearly five metres (Fig. 2). This move, coupled with the recent optics upgrade, increased the operational flux at the sample position by nearly 21-fold with a comparable decrease in instrumentation background in the highest resolution region of the detector. This optimised sample position enabled further improvements in the SEC-SAXS sample cell reducing the exposed sample volume from 24 to 10 uL. The new configuration will be complemented by in-line multi-angle light scattering that will not only inform on the sample's molecular mass but also, enable measurements at smaller scattering angles.

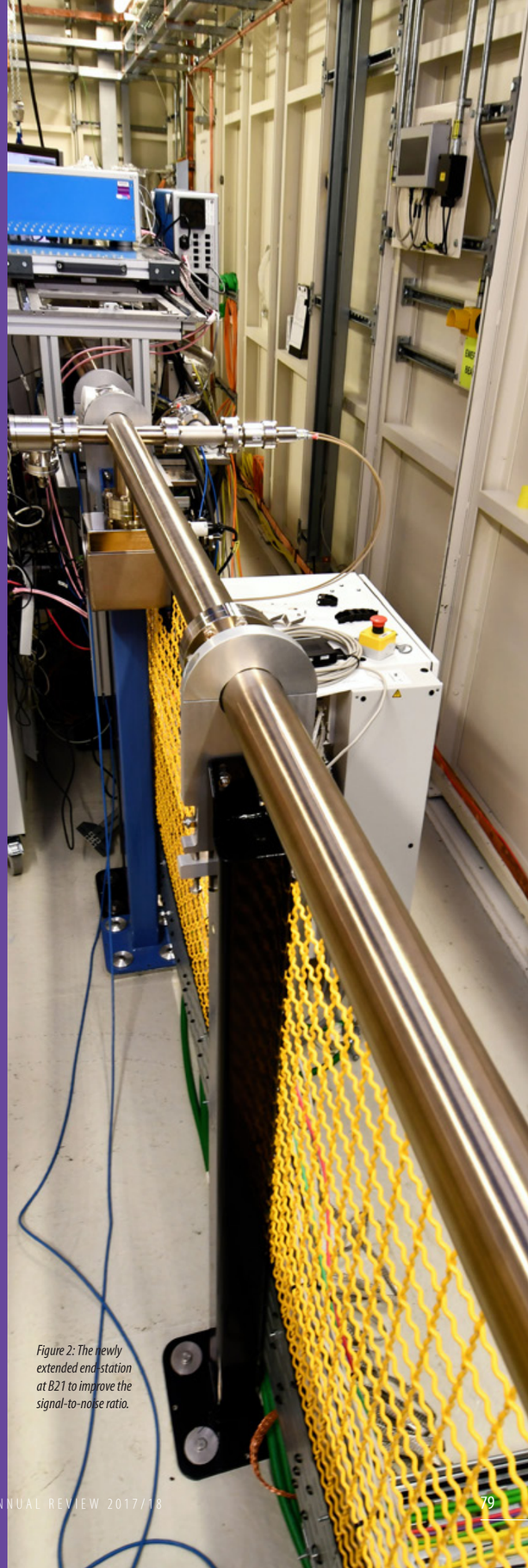

Figure 2: The newly extended end-station at B21 to improve the signal-to-noise ratio.

Complex Self-assembly Inside Atmospheric Aerosol Droplets?

Related Publication: Pfrang C, Rastogi K, Cabrera-Martinez ER, Seddon AM, Dicko C, Labrador A, Plivelic TS, Cowieson N, Squires AM. Complex three-dimensional self-assembly in proxies for atmospheric aerosols. *Nature Communications* **8**, 1724, doi:10.1038/s41467-017-01918-1 (2017).

Publication keywords: Atmospheric aerosols; Small-angle X-ray scattering (SAXS); Raman spectroscopy; Acoustic levitation; Lyotropic liquid crystalline phases

Aerosols are significant to the Earth's climate, with nearly all atmospheric aerosols containing organic compounds that often contain amphiphilic molecules. However, the nature of how these compounds are arranged within an aerosol droplet remains unknown. It was recently demonstrated that fatty acids in proxies for atmospheric aerosols self-assemble into highly ordered three-dimensional nanostructures known as lyotropic liquid crystalline phases. This finding may have implications for environmentally important processes. In this research, acoustically trapped droplets of oleic acid/sodium oleate mixtures in a sodium chloride solution were analysed by simultaneous synchrotron small-angle X-ray scattering (SAXS) and Raman spectroscopy in a controlled gas-phase environment. It was demonstrated that the droplets contained crystal-like lyotropic phases including hexagonal and cubic close-packed arrangements of spherical and cylindrical micelles, and stacks of bilayers, whose structures responded to atmospherically relevant humidity changes and chemical reactions. Further experiments showed that self-assembly reduces the rate of reactions with atmospheric oxidants. These experiments at the High Throughput SAXS beamline (B21) demonstrated that lyotropic-phase formation also occurs in more complex mixtures more closely resembling compositions of atmospheric aerosols. This suggests that lyotropic-phase formation likely occurs in the atmosphere, with potential implications for cloud formation and properties, lifetimes of molecules in the atmosphere, and other important aerosol characteristics.

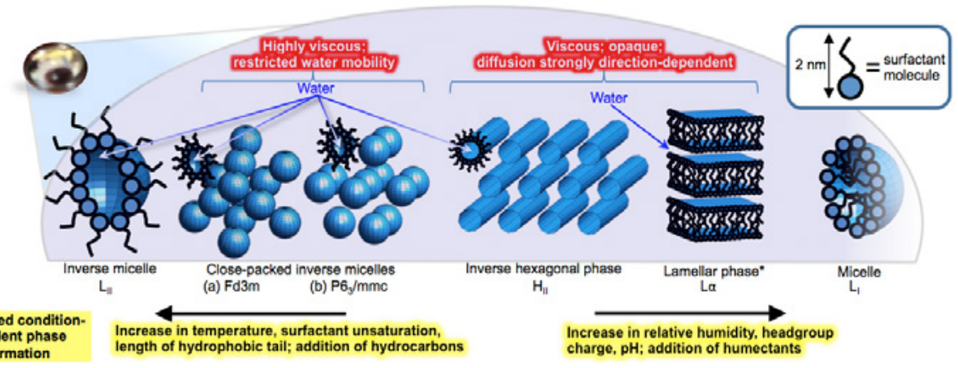

*Figure 1: Complex 3D self-assembly of surfactant molecules in proxies for atmospheric aerosols: lyotropic phases formed; impact on key properties of atmospheric aerosols (highlighted in red); and proposed condition-dependent phase changes (yellow). All depicted phases were observed during the experiments on levitated aerosol droplets. *The lamellar phase can exist over a much wider range of relative humidities than the other phases, accommodating variations in water content by changing the spacing between the surfactant bilayers.*

In these experiments single droplets were held in levitation and followed changes in these droplets at the same time using X-rays to track the arrangement of the molecules and Raman spectroscopy to follow chemical changes. These droplets were exposed to conditions encountered in the atmosphere: changes in humidity and presence of the atmospheric oxidant ozone. In all humidities, the droplets exhibited highly complex self-assembled three-dimensional structures. Exposure to ozone eventually broke down the molecules and destroyed the complex molecular arrangement; however, the molecules survived much longer in those arrangements than expected. This could explain longer lifetimes of such molecules found in the atmosphere compared to laboratory experiments where the complex arrangements that may be encountered in atmospheric conditions is not taken into account.

It was demonstrated that complex 3D self-assembly occurs in proxies for atmospheric aerosols. Many of these 3D structures are strongly anisotropic and are known to significantly affect optical properties, diffusion, viscosity, surface tension and water uptake; and therefore, in an atmospheric context, may have a dramatic impact on aerosol behaviour (Fig. 1).

Fatty acids represent a significant proportion of marine (up to 15 ng m^{-3}) and urban aerosol; cooking organic aerosol emissions was recently estimated to be surprisingly high at 7400 tons per year, thus corresponding to nearly 10% of the total man-made small particle ($PM_{2.5}$) load in the United Kingdom based on measurements in London. Nevertheless, atmospheric aerosol composition is far more complex. Thus further studies were carried out at Diamond's High Throughput SAXS beamline (B21) of more complicated organic mixtures, specifically mirroring aerosol compositions found in urban environments by adding additional components to our aerosol proxy. Surprisingly, this more accurate model of real atmospheric material retained complex 3D arrangements as detailed below.

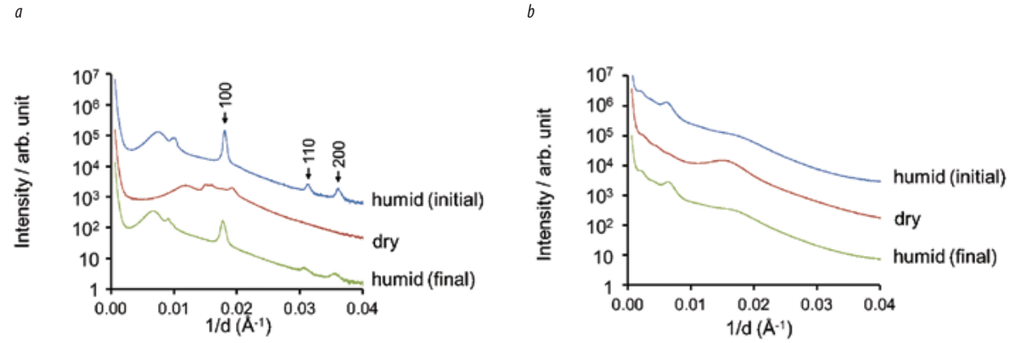

Figure 2: SAXS of more complex atmospheric aerosol proxies collected at B21. a Fatty acid/sugar (sodium oleate:oleic acid:fructose ratio 1:1:1.8) and b fatty acid/sugar/hydrocarbon (sodium oleate:oleic acid:fructose:hexadecane ratio 1:1:1.8:0.6) mixtures based on aerosol compositions found in the Chinese city Chongqing in winter. In each experiment, SAXS data were obtained from capillary coatings first in a humidified environment (N_2, relative humidity, RH, >90%), that was then dried (N_2, RH <20%) and finally re-humidified (N_2, RH >90%). The SAXS patterns are shown in sequence from top to bottom in each case.

During the experiments on more complex mixtures on B21, two further atmospheric aerosol components were introduced: first sugar (fructose) and then hydrocarbon (hexadecane). Two mixtures were prepared: fatty acid/sugar and fatty acid/sugar/hydrocarbon. The fatty acid/sugar/hydrocarbon ratios were chosen according to ratios found by Wang *et al*[1]. in field studies of real atmospheric aerosols in the Chinese city of Chongqing in winter, where the three main classes of organic components were fatty acids, sugars and alkanes (3244, 2799 and 948 ng m^{-3}, respectively). For experimental ease, the mixtures were analysed not as levitated droplets but as dry coatings on the inside of X-ray capillary tubes, which were exposed to high and low relative humidities. As demonstrated in Figure 2, both the sodium oleate/oleic acid/fructose and the sodium oleate/oleic acid/fructose/hexadecane systems showed complex 3D self-assembly. SAXS patterns from the sodium oleate/oleic acid/sugar system on humidification clearly show three Bragg peaks from the inverse hexagonal (H_{II}) phase, with further peaks indicating additional coexisting phases. On drying, the structure changes, but different Bragg peaks are nonetheless observed; rehumidifying showed the changes to be reversible, suggesting that they represent thermodynamic phases in equilibrium with water vapour in the surrounding environment. The sodium oleate/oleic acid/sugar/hydrocarbon mixture showed a different self-assembly; here, while it was not possible to assign the peaks to a particular symmetry phase—indeed, more than one phase may be present—the presence of multiple peaks shows the existence of periodic ordering on the nanometre-length scale, while the reversible responses to humidity changes again show lyotropic-phase formation.

While it is clear that further studies are urgently needed to test the impact of this complex self-assembly on the atmosphere, this work demonstrates the potential of these arrangements to explain substantially extended atmospheric lifetimes found for reactive organic molecules. Further investigations combining laboratory and field studies are required to establish the influence of complex three-dimensional self-assembly on a wider range of properties such as light scattering, hygroscopicity, viscosity and diffusion in aerosol particles. These properties potentially affect cloud nucleation and albedo, and atmospheric reaction rates, and so are key to understanding the impact of aerosols on the environment and climate change.

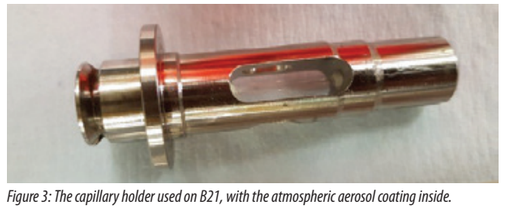

Figure 3: The capillary holder used on B21, with the atmospheric aerosol coating inside.

The research is a collaboration between Universities of Reading, Bath, Bristol and Lund with experiments carried out mainly at large-scale facilities in Sweden (MAXIV-lab) as well as Diamond Light Source.

Current work on acoustically levitated droplets is ongoing at Diamond's I22 beamline in collaboration with Prof. Nick Terrill and Dr Andy Ward harvesting the capability of the microfocus set-up to map dynamic structural changes at different locations within the levitated droplets such as core–shell effects in atmospheric aerosol proxies.

Experiments on more complex mixtures (Fig. 2) were carried out on samples coated inside glass capillary tubes (Fig. 3). Oleic acid, sodium oleate, fructose and hexadecane were dissolved in ethanol (oleic acid and hexadecane) and methanol (fructose and sodium oleate), respectively. The solutions were combined in the volume ratios oleic acid:sodium oleate:fructose 1:1:1.8 and oleic acid:sodium oleate:fructose 1:1:1.8:0.6 to mimic the aerosol composition found by Wang *et al*[1]. Approximately 50–80 mL of the solution was introduced into a 1.5-mm-diameter thin-walled glass capillary tube embedded in a metal cylinder (custom-made at B21 beamline). This produced a coating on average of 0.1-mm thickness, although considerable variations in thickness could be seen visually. For humidity control, the tube was connected to a nitrogen line, either via a water bubbler for high humidity (>90% RH) or directly, for low humidity (<20% RH), and analysed using SAXS.

Reference:

1. Wang, G. *et al*. Molecular, seasonal, and spatial distributions of organic aerosols from fourteen Chinese cities. *Environ Sci Technol* **40**, 4619–4625, doi:10.1021/es060291x (2006).

Funding acknowledgment:

C.P. received financial support for the development of the acoustic levitator from the Royal Society (2007/R2) and NERC (Grant number NE/G000883/1). NERC (Grant number NE/G019231/1) provided financial support for the acoustic levitator to be interfaced with a Renishaw inVia Raman microscope. K.R. is grateful for his NERC studentship. E.R.C.M. is thankful to the Department of Science, Technology and Innovation (Colciencias), Colombia, for studentship funding. Beamtime was awarded under MAX-lab Proposal IDs 20120333 and 20140459. Additional funding was awarded under Bio-Struct X travel funding Grants 4206 and 9487. We are grateful to the University of Reading's Chemical Analysis Facility, CAF, for providing access to a Renishaw InVia Raman microscope for complementary experiments. Additional capillary experiments on the more complex atmospheric aerosol proxies were carried out on Diamond Light Source beamline B21 under experiment SM16578–3.

Corresponding authors: Dr Christian Pfrang, University of Reading, c.pfrang@reading.ac.uk, Dr Adam Squires, University of Bath, a.squires@bath.ac.uk

Building 3D nanomaterials with sticky DNA bricks

Related publication: Brady RA, Brooks NJ, Cicuta P, Di Michele L. Crystallization of amphiphilic DNA nanostructures, *Nano Letters* ***17*** **(5),** 3276-3281, doi:10.1021/acs.nanolett.7b00980 (2017).

Publication keywords: Amphiphilic molecules; DNA crystallisation; DNA nanotechnology; Hydrophobic interactions; Self-assembly; Single crystals

Several technological applications, spanning from energy storage to biomedicine, require the preparation of new materials with a finely organised 3D nanoscale structure. To achieve such delicate structures, they must be assembled from the bottom up, much like the iconic Lego bricks. However, unlike Lego, the building blocks in these scenarios are too small to be handled directly, so they must be encouraged to self-assemble.

Over recent years, some nanomaterials have been developed based on DNA, but they have been limited in size and shape. To overcome this barrier, a new type of DNA nanomaterial has been devised with the aid of the Small Angle X-ray Scattering (SAXS) beamline (I22) .

The novel building material (termed C-Stars) was made from single-stranded DNA molecules that were adorned with cholesterol molecules to help them stick together. Through these sticky interactions, they self-assembled into crystals which were analysed at I22. The invaluable structural data showed that the C-Stars adopted a crystal lattice arrangement. This lattice geometry could be changed by altering the shape of the C-Stars, but more interestingly, the DNA network also could be engineered to change its structure in response to an external stimulus.

With such a flexible and robust building material, the resulting crystal arrangements are almost limitless. The 3D crystals are a completely new class of DNA nanostructures, which will have applications in advanced technologies such as biosensors, light harvesting and molecular sieving.

Reliable self-assembly methods for the fabrication of nano-structured materials with prescribed properties would bring about a manufacturing revolution in many areas of advanced technology, including, but not limited to, (bio)sensing, photonics, light harvesting, energy storage, and molecular sieving.

Over the last two decades, the ever-expanding research field of DNA Nanotechnology has demonstrated how synthetic nucleic acid molecules can be used to create nanoscale motifs of near arbitrary shape[1]. DNA is indeed an ideal nanoscale construction material, mostly owing to the exquisite selectivity of the Watson-Crick base-pairing interactions, responsible for holding together double-helical DNA and enabling most of DNA's biological functionalities. By carefully designing the base-sequence of synthetic DNA strands, it is possible to exploit base pairing to create complex shapes[1]. Furthermore, synthetic DNA can be commercially produced at relatively low cost, is robust against degradation, highly biocompatible, and can be connected to a plethora of other molecules that can impart advanced functionalities[1].

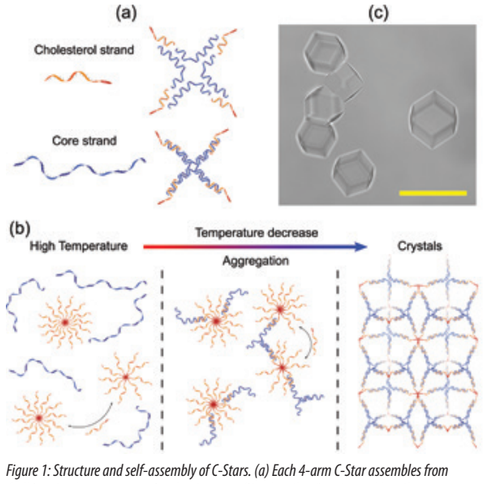

Figure 1: Structure and self-assembly of C-Stars. (a) Each 4-arm C-Star assembles from 4 different ssDNA molecules forming the core of the junction (blue) and 4 identical cholesterol-functionalised strands (orange). (b) All single-stranded components are mixed in stoichiometric ratio and brought to high temperature, where cholesterol-DNA micelles coexist with free core strands. Upon slow cooling, the C-Star cores form and cross-link the micelles, leading to aggregates that grow over time into network. (c) Aggregation leads to the appearance of macroscopic single crystals, shown in bright-field light microscopy. Scale bar 50 µm.

A long-term goal of structural DNA Nanotechnology has been the creation of motifs that can support long-range order in three dimensions, forming macroscopic *crystalline materials*. Until recently, however, only very few examples of DNA nanostructures have proven capable of achieving this result[2,3], substantially limiting our opportunity of tailoring the characteristics of the DNA crystals to specific technological needs.

Most of the available routes for creating ordered nanostructured materials rely on the self-assembly of *amphiphilic molecules*. These include lipids, soap molecules and specifically designed synthetic polymers, and feature, on each individual molecule, both *hydrophobic* and *hydrophilic* domains. When dispersed in water, the hydrophobic parts of amphiphilic molecules cluster with each other, leaving the hydrophilic segments in contact with the solvent. Depending on the geometry of the molecule, this *frustrated phase separation*, leads to a variety of different self-assembled structures, from small clusters, to filaments, to 2D membranes (*e.g.* lipid bilayers), to macroscopic 3D arrays[4]. Compared with the specific lock-and-key interactions between DNA Nanostructures, the self-assembly mechanism of amphiphiles is far more robust. However, the production of amphiphilic molecules often requires laborious chemical synthesis, and lacks all of the aforementioned practical advantages that make DNA-based materials so appealing.

In a recent contribution[5], the team featuring Mr R. Brady, Prof P. Cicuta, Dr L. Di Michele (University of Cambridge), and Dr N. Brooks (Imperial College London), combined the best of both worlds, introducing a new type of amphiphilic DNA nanostructures, dubbed *C-Stars*[5], capable of effectively forming macroscopic 3D crystalline aggregates. C-Stars are simple branched motifs self-assembled from a small number of synthetic single-stranded (ss)DNA molecules (Fig. 1a). Some of these strands are modified with a hydrophobic cholesterol molecule, ultimately positioned at the tip of each DNA arm. Since DNA itself is very hydrophilic, cholesterol modifications make C-Stars amphiphilic, and capable of self-assembling through the robust frustrated phase separation mechanism. At the same time, C-Stars retain all of the advantages of DNA-based materials, including the facile design and prototyping of different shapes, the easy functionalisation and the biocompatibility.

Figure 1 demonstrates the self-assembly principle of C-Stars. The ssDNA components are dispersed in buffered aqueous solution, and heated up to 90°C. At this high temperature, the DNA double helices (duplexes) cannot form, but

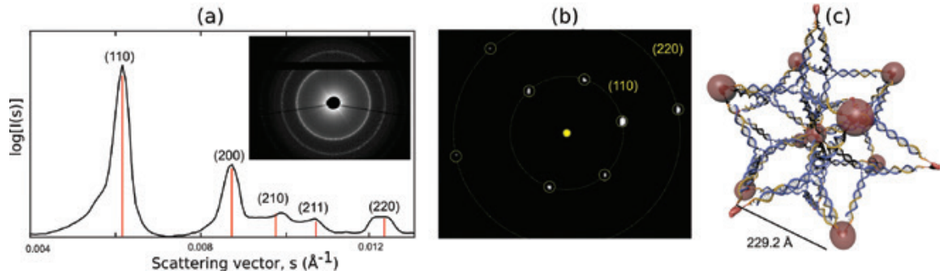

Figure 2: SAXS characterisation of C-Star crystals performed at Diamond I22 beamline. (a) SAXS powder diffraction pattern collected by illuminating a large number of individual crystallites. The black solid line shows the radial average of the 2D patterns shown in the inset. Red vertical lines mark the Bragg peaks. (b) Single crystal diffraction pattern collected using the microfocus end-station. Spots are highlighted by yellow circles. Both measurements are consistent with a BCC unit cell. (c) Plausible arrangement of the C-Stars in the BCC unit cell, with the micelle-like hydrophobic cores located at the lattice points, highlighted by red beads.

the hydrophobic forces are still active, causing the cholesterol-bearing ssDNA strands to cluster into *micelles* (Fig. 1b). As the temperature is slowly decreased, the duplexes forming the C-Star junction start to self-assemble, linking together the micelles and forming a network whose structure is determined by the shape of the C-Stars, and thus encoded in the chosen sequence of DNA bases. The resulting

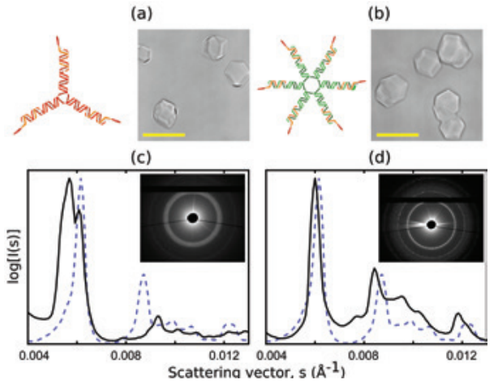

Figure 3: Self-assembly of C-Stars with 3 and 6 arms. Both 3-arm (a) and 6-arm (b) C-Stars form macroscopic single crystals, shown in bright field light microscopy. Scale bars 20 µm. SAXS powder diffraction patterns (insets) and radial intensity profiles (black solid lines) for 3-arm (c) and 6-arm (d) samples. The radial intensity profile for the 4-arm sample (dashed blue line), overlaid for easier visual comparison, highlights the difference in internal structure of the crystals formed by difference C-Star designs.

aggregates grow over time and coalesce (Fig. 1b), eventually forming macroscopic networks exceeding 40 µm in size, equivalent to billions of individual C-Stars. When inspected with light microscopy, the aggregates display a polyhedral shape, strongly hinting at an underlying crystalline structure (Fig. 1c).

Small Angle X-ray Scattering (SAXS), performed at Diamond beamline I22, was used for the microscopic structural characterisationof aggregates self-assembled from 4-arm C-Stars. Powder diffraction experiments were performed at small-angle length scales by illuminating dense, millimeter-size, pellets prepared by concentrating a large number of DNA crystals. The generated diffraction patterns are the result of several crystals being exposed to the X-rays at once, and show well defined rings (Fig. 2b), which when averaged radially highlight clear Bragg peaks indicative of an ordered network.

Using the *microfocus* end-station available at I22, which can reduce the cross-section of the X-ray beam down to 10 µm, we could illuminate individual C-Star crystallites and obtain *single crystal* diffraction patterns (Fig. 2b).

The positions of the peaks in the powder diffraction and the spots of the single-crystal diffraction patterns are compatible with a body-centered cubic (BCC) lattice. Combining this information with the size of the individual C-Stars (imposed by design), and the coordination of cholesterol DNA micelles, we could identify the likely arrangement of the DNA building blocks in the BCC network (Fig. 2c). In our model, the unit cell, the elementary cube periodically tiling the 3D space, has a size (lattice parameter) of 23 Å, and contains 6 C-Stars. Interestingly, C-Star networks are extremely empty, with DNA and cholesterol occupying only about 15% of the volume of the crystal. In other words, C-Star aggregates have a very high porosity (~85%), which makes them ideal to encapsulate other molecules within the DNA.

Powder diffraction experiments were also performed on C-Stars featuring different numbers of arms. Remarkably, 3-arm and 6-arm building blocks are also capable of effectively supporting long-range 3D order, but form crystals with a different geometry compared to the 4-arm stars (Fig. 3).

That the large size of the unit cell, the intrinsic low contrast of DNA samples, and the very porous nature of C-Star crystals, make the use of synchrotron-based X-ray scattering strictly necessary. In view of this, the facilities of Diamond I22, optimized for the study of soft and biological matter, and the support of expert beamline scientists such as Dr. Andy Smith, played a crucial role in the study of this new class of nanomaterials.

Owing to their robust and flexible self-assembly mechanism, C-Stars will ultimately allow to significantly expand the range of shapes and sizes of DNA building blocks capable of sustaining long-range order in 3D. This design flexibility makes it possible to incorporate functional molecules within the DNA network, which can make the crystalline materials responsive to external stimuli. With the support of the I22 Diamond team, we are planning to demonstrate this possibility in an upcoming SAXS session.

References:

1. Seeman, N. C. & Sleiman, H. F. DNA nanotechnology, *Nature Reviews Materials* **3**, 17068, doi:10.1038/natrevmats.2017.68 (2017).
2. Zheng, J. *et al.* From molecular to macroscopic via the rational design of a self-assembled 3D DNA crystal, *Nature* **461**, 74-77, doi:10.1038/nature08274 (2009).
3. Simmons, C. R. *et al.* Construction and Structure Determination of a Three-Dimensional DNA Crystal, *J Am Chem Soc* **138 (31),** 10047-10054, doi:10.1021/jacs.6b06508 (2016).
4. Mai, Y. & Eisenberg, A. Self-assembly of block copolymers, *Chem Soc Rev* **41(18)**, 5969-85, doi:10.1039/C2CS35115C (2012).
5. Brady, R.A. *et al*. Crystallization of amphiphilic DNA nanostructures, *Nano Letters* ***17*** **(5),** 3276-3281, doi:10.1021/acs.nanolett.7b00980 (2017).

Funding acknowledgement:

The authors of the study (Ref. 5) acknowledge support from the EPSRC Programme Grant CAPITALS number EP/J017566/1, the Oppenheimer Fund, Emmanuel College Cambridge, the Leverhulme Trust, and the Isaac Newton Trust through an Early Career Fellowship (ECF-2015- 494) and the EPSRC CDT in Nanoscience and Nanotechnology (NanoDTC), grant number EP/L015978/1. The authors also acknowledge Diamond Light Source for provision of synchrotron beamtime (SM14217, SM15530, and SM15030), and thank Dr. Andy Smith for assistance in operating beamline I22.

Corresponding author: Dr Lorenzo Di Michele, Cavendish Laboratory, University of Cambridge, email: ld389@cam.ac.uk

Shocking protein crystals into action: combining electrochemistry and infrared microscopy provides insight into [NiFe] hydrogenase mechanism

Related publication: Ash PA, Carr SB, Reeve HA, Skorupskaite A, Rowbotham JS, Shutt R, Frogley MD, Evans RM, Cinque G, Armstrong FA, Vincent KA. Generating single metalloprotein crystals in well-defined redox states: electrochemical control combined with infrared imaging of a NiFe hydrogenase crystal. *Chemical Communications* **53**, 5858-5861, doi:10.1039/C7CC02591B (2017).

Publication keywords: Protein crystallography; Infrared microspectroscopy; Infrared spectroscopy; Redox protein; Metalloprotein; Electrochemistry

Proteins are the nanoscale 'machines' that control almost all processes in cells, and revealing their structures is paramount to understanding how they work. X-ray crystallography is a valuable tool for providing 'snapshot' images of working proteins at an atomic level; however, some proteins are very tricky to freeze at particular moments in time.

[NiFe] hydrogenase enzymes are proteins that allow microbes to survive using hydrogen gas as their only energy source. These enzymes have drawn much attention because of their potential applications in future green energy technologies, but to fully determine how they work, it is imperative to image them at specific stages of their reactions.

Fortunately, [NiFe] hydrogenases naturally contain markers that are easily studied using infrared light, which made them ideal subjects for the Infrared Microspectroscopy beamline (B22, MIRIAM). Crystal forms of the enzymes were analysed at B22 within a custom-built electrochemical cell which allowed their reactions to be slowed down. This setup provided the opportunity to study an otherwise extremely fast reaction in unprecedented detail.

The demonstration that hydrogenase protein crystals could be controlled using electrochemistry is an important finding as many other proteins can be studied in the same way, including proteins that convert carbon dioxide into useful chemicals.

Understanding the structures of individual proteins at the atomic level has been key in building up our understanding of how they contribute to the function of cells. In particular, X-ray crystallography has been extremely valuable in providing 'snapshot' images of many different proteins at the level of individual atoms. It is often difficult to trap proteins in specific states relevant to their function, however. This is particularly true for redox proteins, which catalyse chemical reactions involving the transfer of electrons, where crystallographic structures can represent structural averages from mixtures of states at similar redox levels. The benefits of using complementary spectroscopic techniques alongside protein crystallography, at the single crystal level, are becoming more widely acknowledged in order to gain a more complete understanding of biomolecular structure and function[1]. However, methods which offer direct control over the oxidation state of a redox protein crystal and simultaneous microspectroscopic measurement are lacking. It is timely that new tools are developed for studying redox proteins because they catalyse many chemical reactions which are relevant to solving big global challenges, including how to use hydrogen as a sustainable fuel, how to capture the greenhouse gas carbon dioxide and turn it into useful chemicals, and how to efficiently produce the fertilisers needed to sustain the world's growing population.

Nickel-iron ([NiFe]) hydrogenases are an important class of redox proteins, which allow bacteria such as *E. coli* to live using hydrogen gas as their sole energy source. Hydrogenases are inspirational catalysts as they catalyse the reversible oxidation of H_2 at active sites based around cheap, abundant metals, and at high turnover frequencies (>9,000 s^{-1}). The active site of [NiFe] hydrogenases incorporates biologically unusual ligands, CO and CN^-, bound to iron (Fig. 1a). Vibrational stretching bands of these ligands can be probed readily using infrared (IR) light, and the precise wavenumber positions of the bands (in particular of the CO chromophore) are diagnostic of specific redox states of the [NiFe] active site (Fig. 1b)[2]. Electrochemistry has proved critical to understanding the catalytic activity of [NiFe] hydrogenases and has been used in conjunction with spectroscopic methods to navigate between the equilibrium redox states of the active site, or to study the distribution of active site states during steady-state catalytic turnover[3,4]. Here, unprecedented electrochemical control over the redox state of single crystals of hydrogenase is combined with *in situ* synchrotron IR microspectroscopy to tease out chemical reactivity that is too fast to see in solution studies but is slowed in the crystal state.

This study exploited the synchrotron IR source of the Multimode IR Imaging and Microspectroscopy (MIRIAM) beamline, Diamond Light Source, to monitor the active site of [NiFe] hydrogenase 1 from *E. coli* in the crystalline state as a case study[5]. Hydrogenase 1 yields large well-diffracting crystals, with a typical cross-section of 50 × 50 μm^2 and axial length of 1000 – 2000 µm. A custom-built reflection-absorption three-electrode electrochemical cell allowed precise potential control, with a cocktail of redox mediators in solution employed to facilitate electron transfer between the crystal and working electrode. Spectra recorded following alternating reductive and oxidative potential steps confirmed that electrochemical control of the hydrogenase 1 active site was fully reversible over multiple reduction-oxidation sequences. The brightness of the MIRIAM source enabled collection of high signal-to-noise spectra at discrete 15 × 15 μm^2 sub-sections along the length of single hydrogenase 1 crystals, and electrochemical control was shown to extend over the whole crystal length. Spectral changes were complete within 30 minutes of application of a potential step.

The [NiFe] hydrogenase catalytic cycle (Fig. 1b) consists of both electrochemical steps and chemical steps involving proton transfer. The most reduced equilibrium state of the [NiFe] hydrogenase active site, Ni_a-R, actually consists of three sub-states at the same redox level. The precise nature of the Ni_a-R sub-states is unknown but they are thought to represent differently protonated forms of the [NiFe] active site, possibly indicative of discrete proton transfer events following initial activation of H_2[2]. In solution and steady-state

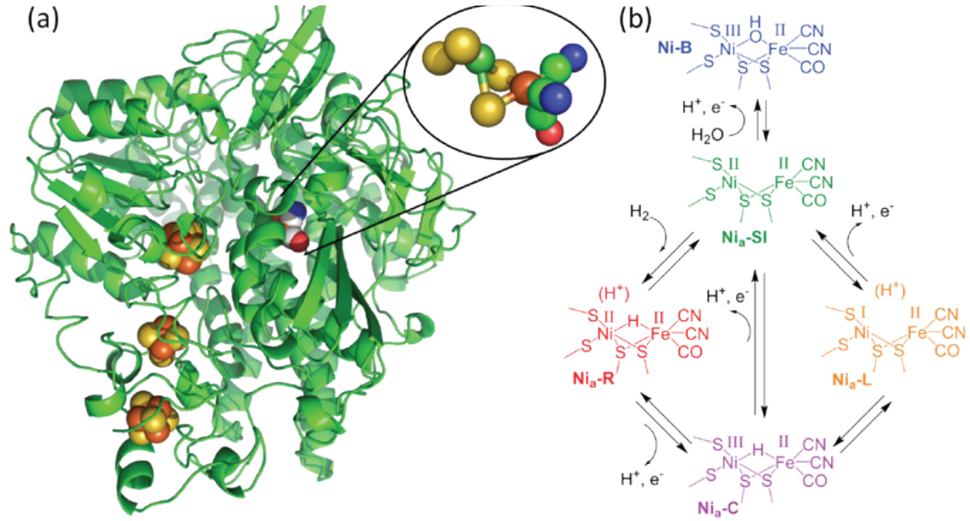

Figure 1: (a) Structure of the [NiFe] hydrogenase I from Escherichia coli in cartoon form, with the metal centres and their ligands shown as spheres in elemental colours (nickel: green, iron: orange, sulphur: yellow, carbon: grey, oxygen: red, nitrogen: blue); (b) Proposed catalytic cycle at the active site of [NiFe] hydrogenases.

turnover studies the different Ni_a-R sub-states states are observed at constant ratio, regardless of the potential, presumably interchanging on a timescale faster than the spectroscopic measurement. Interestingly in the crystalline state the interconversion of individual Ni_a-R sub-states can be temporally resolved, providing the first evidence that these sub-states might be sequential intermediates in the catalytic cycle (Fig. 2).

Figure 2: This sequence of infrared spectra highlight the time dependent formation of two of the Ni_a–R sub-states, Ni_a–RII and Ni_a–RIII in hydrogenase I from Escherichia coli. Spectra are presented as reduced minus oxidised baseline-corrected difference spectra following application of a reducing potential step from +241 to -359 mV (vs the standard hydrogen electrode, SHE)

The results of this study have two important implications. Firstly, the ability to control, electrochemically, the redox state of a metalloprotein in a single protein crystal offers possibilities for obtaining 'snapshots' of complex redox proteins in well-defined states that have not been accessible previously. When combined with imaging of crystals using IR microspectroscopy, the state of the protein in the crystal can be checked before X-ray crystallography is used to obtain a structural 'snapshot', and afterwards to check whether there has been any damage to the crystal during the structural measurement. Secondly, our observation that chemistry is slowed down inside the hydrogenase crystal offers possibilities of trapping out specific states that react too fast to be detected in alternative solution studies. Thus, this body of work represents an important advance for understanding the interplay between structure and function in some of the complex metal-containing proteins that are critical to life.

References:

1. Pearson, A. R. *et al*. If You Can Get a Crystal Structure, Why Bother with Anything Else? *Synchrotron Radiation News* ***28(6),*** 10-14, doi:10.1080/08940886.2015.1101321 (2015).
2. Ash, P. A. *et al.* Proton Transfer in the Catalytic Cycle of [NiFe] Hydrogenases: Insight from Vibrational Spectroscopy. *ASC Catalysis* **7(4),** 2471-2485, doi:10.1021/acscatal.6b03182 (2017).
3. Armstrong, F. A. *et al*. Guiding Principles of Hydrogenase Catalysis Instigated and Clarified by Protein Film Electrochemistry. *Acc Chem Res* **49(5)**, 884-892, doi:10.1021/acs.accounts.6b00027 (2016).
4. Hidalgo, R. *et al*. Infrared Spectroscopy During Electrocatalytic Turnover Reveals the Ni-L Active Site State During H_2 Oxidation by a NiFe Hydrogenase. *Angewandte Chemie* **127(24)**, 7216 –7219, doi: 10.1002/anie.201502338 (2015).
5. Ash, P. A. *et al*. Generating single metalloprotein crystals in well-defined redox states: electrochemical control combined with infrared imaging of a NiFe hydrogenase crystal. *Chem Comm* **53**, 5858-5861, doi:10.1039/C7CC02591B (2017).

Funding acknowledgement:

This work was supported by EPSRC grant EP/N013514/1 (to KAV and HAR) and BBSRC grants BB/L009722/1 and BB/N006321/1 (to FAA) and Oxford Interdisciplinary Bioscience Doctoral Training Partnership studentship BB/M011224/1 (to AS) and FAA is a Royal Society Wolfson Research Merit Award holder.

Corresponding authors: Dr Philip Ash, University of Oxford, Department of Chemistry, philip.ash@chem.ox.ac.uk

Prof Kylie Vincent, University of Oxford, Department of Chemistry, kylie.vincent@chem.ox.ac.uk

Unravelling the mechanisms of immune escape by acute myeloid leukaemia

Related publication: Gonçalves Silva I, Yasinska IM, Sakhnevych SS, Fiedler W, Wellbrock J, Bardelli M, Varani L, Hussain R, Siligardi G, Ceccone G, Berger SM, Ushkaryov YA, Gibbs BF, Fasler-Kan E, Sumbayev VV. The Tim-3-galectin-9 Secretory Pathway is Involved in the Immune Escape of Human Acute Myeloid Leukemia Cells. *EBioMedicine* **22**, 44 – 57, doi:10.1016/j.ebiom.2017.07.018 (2017).

Publication keywords: Acute myeloid leukemia; Tim-3, Galectin-9; NK cells; Anti-leukemia immunity

Acute myeloid leukaemia (AML) is a type of blood cancer that originates from white blood cells in the bone marrow. It is often fatal and is considered one of the most common cancers of children and the elderly. The high mortality rate associated with this cancer can partly be ascribed to ineffective current treatments, which consist of aggressive chemotherapy and stem cell transplantation. There is a great need to find alternative treatments for AML patients to improve their outcomes. By understanding the molecular mechanisms employed by AML cells to proliferate and avoid detection by the immune system, it is hoped this unmet need could be fulfilled.

Synchrotron Radiation Circular Dichroism (SRCD) spectroscopy at beamline B23 was used to probe the interactions of proteins involved in a molecular pathway responsible for AML immune escape. It was found that the pathway did not exist in healthy cells and was unique only to AML. The pathway results from a malignant transformation that involves the secretion of an immunoprotective protein, galectin-9, and the expression of a neuronal receptor, latrophilin 1, which triggers exocytosis upon interaction with other cells or soluble factors. The proteins help to impair parts of our immune system that try to destroy the cancer cells. Therefore, targeting this pathway could significantly enhance the patients' immune defences and thus might be considered as a fundamentally new strategy for anti-AML therapy.

Acute myeloid leukemia (AML) is an aggressive blood/bone marrow cancer originating from self-renewing malignant immature myeloid cells. AML rapidly becomes a systemic malignancy and is often a fatal disease since cancerous cells are suppressing anti-cancer immunity by impairing the functional activity of natural killer (NK) cells and T cells with cytotoxic activity[1].

A fundamental biochemical pathway[2] was discovered, which includes ligand-dependent activation of latrophilin 1, a neuronal receptor that facilitates exocytosis and is expressed in malignant but not healthy human myeloid cells[3]. This results in increased translation and secretion of the immune receptor Tim-3 and its ligand galectin-9. The process depends on activities of protein kinase C and mammalian target of rapamycin (mTOR). Tim-3 was found to have a dual role in the whole process by participating in galectin-9 secretion and by being released in a free soluble form. Galectin-9 impairs the anti-cancer activity of NK cells while free soluble Tim-3 attenuates secretion of interleukin-2 (IL-2) required for development of NK cell cytotoxic activity. These results were validated in *ex vivo* experiments using primary samples obtained from AML patients. Tim-3/galectin-9-dependent impairing of anticancer activity of cytotoxic lymphoid cells is summarised in Figure 1.

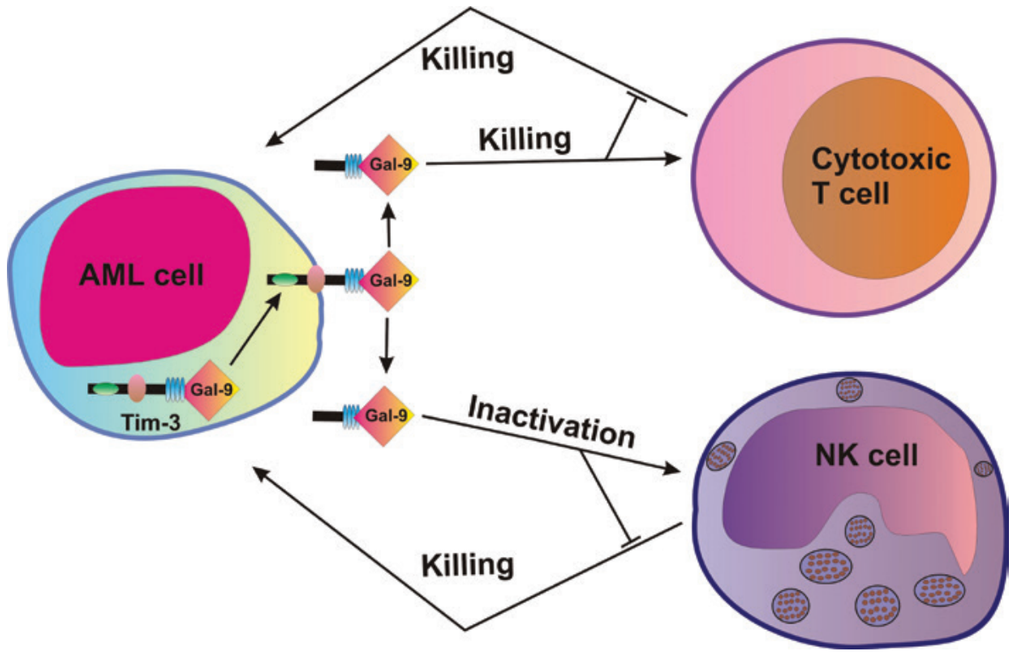

Figure 1: Tim-3-dependent secretion of galectin-9 in human AML cells impairs the anti-leukemic activity of NK cells and cytotoxic T cells (based on Gonçalves Silva, I. et al.[3]).

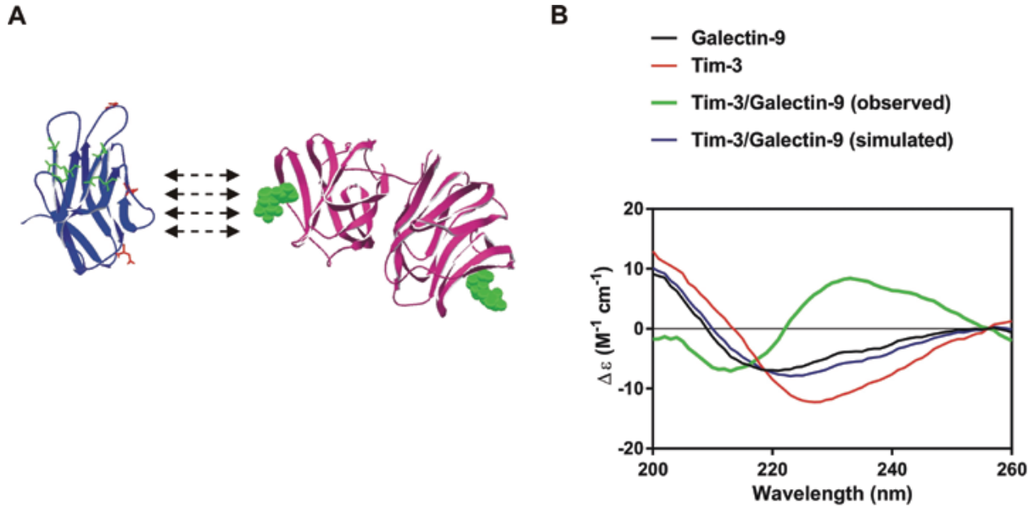

Figure 2: Tim-3-galectin-9 interaction leads to significant conformational changes possibly increasing solubility of the protein complex. (A) The schematic structural models of galectin-9 (on the right) and extracellular domain of the Tim-3 (on the left). In the structural model of the Tim-3, amino acids involved in galectin-9-independent binding are highlighted using green colour. Amino acid residues of the Tim-3, which are potential targets for glycosylation, are highlighted using red colour. (B) The SRCD spectroscopy of galectin-9, Tim-3, and the complex made by both proteins. (Adapted from Gonçalves Silva, I. et al.[2])

Synchrotron radiation circular dichroism (SRCD) spectroscopy at beamline B23 was used to characterise the secondary structure of Tim-3, galectin-9 and the complex made by these two proteins presented in Figure 2a. Structural organisation of both Tim-3 and galectin-9 are presented in the Figure 2a. It was found in earlier studies that galectin-9 interacts with non-glycosylated Tim-3 with high affinity ($Kd = 2.8 \times 10{-}8$ M)[4]. However, this binding is further strengthened by interaction of galectin-9 with sugars of glycosylated Tim-3. In AML cells Tim-3 undergoes glycosylation[2] which means that its affinity to galectin-9 is very high in AML cells. This assumption was confirmed by the fact that the complex is detectable by Western blot analysis, which suggests a strong high affinity binding between the two proteins[2,5]. SRCD spectroscopy was also applied to galectin-9 and Tim-3 mixed to a stoichiometry of 1:1 molar ratio (Fig. 2b). When mixed together with Tim-3, galectin-9 showed a CD spectrum which was clearly different from the simulated spectrum. This suggested that the interaction of Tim-3 with galectin-9 caused a conformational change of both proteins. An obvious increase in β-strand component was observed. Based on these findings, one may suggest that Tim-3 binding possibly alters the conformation of galectin-9. This results in increased capability of galectin-9 to interact with receptors in target cells. Galectin-9 is a protein, which contains two sugar-binding domains. Therefore, one domain could bind Tim-3 (or other proteins/receptor/trafficker) and leave the other domain open for interaction with a receptor molecule (for example Tim-3) associated with the plasma membrane of a target cell (for example NK cell or cytotoxic T cell).

This discovery opens new avenues for development of anti-leukaemia immunotherapy. Targeting this pathway might crucially enhance the patients' immune defences helping them to eliminate leukaemia cells and could fundamentally change existing approaches to leukaemia diagnostics and anti-leukaemia therapy (and possibly the treatment of other cancers).

References:

1. Khaznadar, Z. *et al*. Acute myeloid leukemia impairs natural killer cells through the formation of a deficient cytotoxic immunological synapse. *Eur. J. Immunol*. **44**, 3068–3080, doi:10.1002/eji.201444500 (2014).
2. Gonçalves Silva, I. *et al*. The Tim-3-galectin-9 Secretory Pathway is Involved in the Immune Escape of Human Acute Myeloid Leukemia Cells. *EBioMedicine* **22**, 44-57, doi:10.1016/j.ebiom.2017.07.018 (2017).
3. Sumbayev, V.V. *et al.* Expression of functional neuronal receptor latrophilin 1 in human acute myeloid leukemia cells. *Oncotarget* **7**, 45575–45583. doi:10.18632/oncotarget.10039 (2016).
4. Prokhorov, A. *et al.* The immune receptor Tim-3 mediates activation of PI3 kinase/mTOR and HIF-1 pathways in human myeloid leukemia cells. *Int. J. Biochem. Cell Biol.* **59**, 11–20. doi:10.1016/j.biocel.2014.11.017 (2015).
5. Gonçalves Silva, I. *et al*. The immune receptor Tim-3 acts as a trafficker in a Tim-3/galectin-9 autocrine loop in human myeloid leukemia cells. *Oncoimmunology* **5**, e1195535. doi: 10.1080/2162402X.2016.1195535 (2016).

Funding acknowledgement:

This work was supported by a Daphne Jackson Trust postdoctoral fellowship, University of Kent Faculty of Sciences Research Fund. We thank Prof Giuliano Siligardi and Dr Rohanah Hussain for an excellent and fruitful collaboration and Diamond Light Source for access to B23 beamline (SM12578).

Corresponding author: Dr Vadim Sumbayev, Dr Inna M. Yasinska, Medway School of Pharmacy University of Kent, UK, V.Sumbayev@kent.ac.uk

Phase III Overview

At the end of the 2016/17 Financial Year, there were 31 operational beamlines at Diamond. The remaining five beamlines to join are either in commissioning phases or under construction. By 2020, all Phase III beamlines will be operational with user experiments underway. An overview of their activities and progress is outlined below.

I05 - Angle-Resolved Photoemission Spectroscopy (ARPES)

I05 is a facility dedicated to the study of electronic structures by Angle-Resolved PhotoEmission Spectroscopy (ARPES). This technique is applied to materials with exotic electronic ground states such as unconventional superconductors, solids exhibiting charge and spin density waves, excitonic insulators and non-Fermi liquids. The first branch, which is for HR (high resolution)-ARPES experiments, has been successfully operating since 2013. The second branch is dedicated to nano-ARPES measurements and welcomed its first users in spring 2016. Together these two branches support users studying materials such as oxide superconductors, topological matter and transition metal chalcogenides.

B21 - High Throughput SAXS

Small-Angle X-ray Scattering (SAXS) is used to study particles in solution on B21. SAXS provides a resolution-limited, structural snapshot of the sample and can be used to study slow processes, such as fibre formation. In early 2017, B21 upgraded its X-ray optics with an eighty-fold increase in X-ray intensity and up to a two hundred-fold increase in the signal-to-noise ratio. This upgrade involved replacing the monochromator with a double multilayer monochromator. Coupled with the exceptionally low background scatter, the increased intensity has pushed the sample concentration requirements substantially lower and enabled sub-second measurements. As a result of these enhancements, B21 is now one of the most sensitive beamlines internationally.

I08 - Scanning X-ray Microscopy (SXM)

I08 is the Scanning X-ray Microscopy (SXM) beamline for morphological, elemental and chemical speciation on a broad range of organic-inorganic interactions in a 250-4400 eV photon energy range and sample investigations under ambient or cryogenic conditions, which is unique for an SXM facility. The beamline extended its portfolio of specimen environments to functional cells allowing *in situ* nano-fluidics and electromagnetic biasing. In early 2017, I08 faced its first major upgrade in the frame of Scanning and Mapping projects, which offer optimised and improved data collection and analysis. The design and construction of a dedicated soft X-ray spectro- and tomo-ptychography branch line has begun. This branch is expected to be available to the user communities in 2019.

B24 - Full Field Cryo-Transmission X-ray Microscope (Cryo-TXM)

B24 is a full-field transmission microscope designed specifically to meet the rising demand for tomographic imaging of biological specimens under near physiological conditions. The technique bridges the resolution gap that exists between electron microscopy and conventional light microscopy and allows acquisition of tomographic data from both native and fluorescent-labelled samples. The operational energy range for B24 is 200 eV-2.6 keV, which allows imaging via absorption contrast within the water window as well as phase contrast at higher energies. The beamline is presently operating in optimisation mode. In the future, B24 will be upgraded to allow for the study of samples requiring Containment Level 3.

I23 - Long-Wavelength Macromolecular Crystallography

The Long-Wavelength Macromolecular Crystallography (MX) beamline (I23) is a unique facility dedicated to directly solving the crystallographic phase problem from native proteins. It is the first MX beamline internationally optimised for the long-wavelength region which allows for identification and location of lighter atoms of biological relevance such as chlorine, potassium and calcium as well as assistance with low-resolution model building by locating phosphorus or sulfur atom positions. I23 is uniquely placed for researchers from the UK and worldwide community to solve structures of the most challenging targets which are not amenable to the facilities elsewhere at Diamond or other synchrotrons. The beamline issued its first call for users in 2017.

Beamline	PBS	Status	First User
I05 - Angle-Resolved PhotoEmission Spectroscopy (ARPES)	Cephise Cacho	Operational	2013
B21 - High Throughput SAXS	Robert Rambo	Operational	2013
I08 - Scanning X-ray Microscopy (SXM)	Burkhard Kaulich	Operational	2014
B24 - Cryo-TXM	Liz Duke	Optimisation	2015
I23 - Long-Wavelength Macromolecular Crystallography	Armin Wagner	Optimisation	2016
I15-1 - XPDF	Heribert Wilhelm	Operational	2016
I02-2 - Versatile MX in situ (VMXi)	Thomas Sorensen	Optimisation	2016
B07 - Versatile Soft X-ray (VERSOX)	Georg Held	Optimisation	2017
I14 - Hard X-ray Nanoprobe	Paul Quinn	Commissioning	2017
I21 - Inelastic Soft X-ray Scattering	Kejin Zhou	Optimisation	2017
I02-1 - Versatile MX micro (VMXm)	Gwyndaf Evans	Construction	2018
DIAD: Dual Imaging and Diffraction	Michael Drakopoulos	Construction	2020

XPDF (I15-1): A dedicated X-ray Pair Distribution Function

The XPDF beamline (I15-1) is a side-station to the Extreme Conditions beamline (I15). The design allows both beamlines to operate concurrently. XPDF is dedicated to, and optimised for, pair distribution function measurements. The beamline is applicable to a diverse range of disciplines such as materials chemistry, solid-state physics, earth sciences and pharmaceuticals. Ultimately it provides data collection and analysis software to allow non-expert users to study the local structure of crystalline, amorphous solids, and liquids. A diverse set of commissioning experiments has been performed after its first users in 2016. XPDF is open for peer-reviewed user experiments.

I02-2 - Versatile MX *in situ* (VMXi)

VMXi is the first beamline of its kind solely dedicated to data collection directly from crystallisation experiments *in situ* i.e. from crystals remaining in their crystallisation media, rather than being transferred to a sample holder and exposed to X-rays under cryogenic conditions. The beamline has the facility to store thousands of user crystallisation experiments and features an automated transfer between sample storage and the beamline, as well as highly automated data collection and analysis. VMXi welcomed its first users in late 2016 and is currently under optimisation and is fully open to users. Once fully operational, this beamline will enable users to monitor their crystallisation experiments remotely, and request X-ray analysis without the need for their direct participation in the X-ray experiment. Equipped with an intense X-ray beam, very rapid detector and operating in a fully automated manner, VMXi will accelerate new discoveries in structural biology. This whole approach will allow for the study of crystals as they emerge and for the collection of data from all crystals, including those that are too fragile to handle and those that cannot be cryo-cooled.

B07 - Versatile Soft X-rays (VERSOX)

B07 offers X-ray Photoelectron Spectroscopy (XPS) and X-ray Absorption Spectroscopy (XAS) at ambient pressures. The beamline gives users the ability to carry out studies of catalysts under gas-phase reaction conditions or investigations in atmospheric science and biology with samples under native conditions such as liquid environments. The ambient-pressure beamline/end station is now operational. The first users were welcomed in summer 2017. A second branch line with moderate vacuum restrictions and automated sample manipulation for high throughput XPS and XAS is currently under construction and is expected to open for users in 2019.

I14 - Hard X-ray Nanoprobe

At over 185m long I14 is a scanning probe beamline that uses X-ray fluorescence and diffraction techniques to determine the structure and composition of a wide range of materials. It will deliver X-ray beams of 30-50 nm with energies from 5-23 keV. This small beam size allows for the possibility of studying micron scale samples, such as biological cells, in greater detail and also allows users to study the role of nanoparticles in a range of areas such as catalysis and the environment. The first users were welcomed in early 2017.

I21 - Inelastic Soft X-ray Scattering

I21 is a dedicated Resonant Inelastic Soft X-ray Scattering (RIXS) facility that will produce highly monochromatised, focused and tunable (250-3000 eV) X-ray beams. It is suited to investigate the electronic, magnetic and lattice dynamics of samples particularly those with magnetic and electronic interactions. The beamline is 81 m long with its end station and 15 m long RIXS spectrometer accommodated in an external building adjacent to the Diamond ring. First light in the internal and external beamline was achieved in December 2015 and September 2016 respectively. The beamline construction has been completed and the X-ray commissioning occurred during summer 2017.

I02-1 - Versatile MX micro (VMXm)

VMXm will perform atomic structure determination for studies where large crystals are difficult to produce or suffer from weak diffraction. This is a common challenge for protein complexes and other flexible biological macromolecules. The smallest X-ray beam size on VMXm will be 0.5 µm and will uniquely combine scanning electron microscopy with X-ray diffraction, to allow the smallest protein crystals to be aligned into the X-ray beam and small wedges of rotation data to be recorded. VMXm can be thought of as a hybrid of X-ray and cryo-electron microscopy techniques, making use of methods for sample preparation from cryo-electron-microscopy, imaging from scanning electron microscopy and diffraction data collection methods from X-ray crystallography. In 2017, the X-ray optics were installed and successfully commissioned. Currently, the end-station is being installed and the first users are expected in summer 2018.

DIAD: Dual Imaging and Diffraction

DIAD is based on an innovative X-ray optical concept to allow the study of *in situ* processes with both imaging and diffraction simultaneously, enabling the user to take measurements of a live process as it evolves. Obtaining microscopic resolution, the instrument will provide the spatial and time-evolution of the structural properties of samples that undergo a range of treatments including mechanical, chemical or thermal. As a result of the unique dual beam design, DIAD is able to simultaneously obtain information from the 3D microstructure, phase composition and stress state of the material. This means that a whole range of research can be carried out within a vast variety of fields including bio-medical, material science, chemistry, geological science, biology and energy. DIAD is in the final construction stages.

Machine Operation and Development

Richard Walker, Technical Director

In 2017/18, our 11th year of operations, a total of 213 days (5112 hours) were scheduled for beamline operations, 198 days of User Mode, and 5 beamline start-up days. The majority of the beam delivery was in standard multibunch mode (900 bunch train) or 'hybrid' mode (686 bunch train + a single bunch) with total current of 300 mA. In addition there were two days in May 2017 of 156 bunch operation and two days of 'low-alpha' mode in March 2018, to produce short bunches (3.5 ps rms). All beamline operations were carried out in top-up mode.

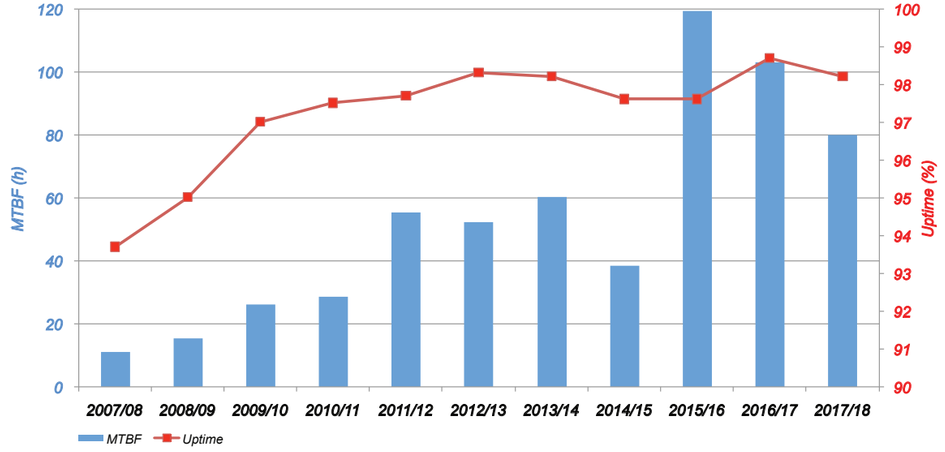

Figure 1: Mean Time Between Failures (MTBF) and Uptime by operating year.

The annual operating statistics are shown in Figure 1. The Mean Time Between Failures (MTBF) for the year was 79.9 hours, a little disappointing when compared with the previous two years but nevertheless still exceeding the target minimum of 72 hours. The reduction in MTBF this year is mainly attributed to an elevated number of trips due to power outages, BPM (Beam Position Monitor) electronics faults and front-end vacuum interlocks. The latter two are problems that have been known for some time, and for which solutions have been devised and are in the process of being implemented. Despite these issues the overall uptime (beam delivered as a percentage of scheduled hours) remained high at 98.2%.

Normal conducting cavities

In response to the risk of extended downtime in the event of further superconducting radiofrequency (RF) cavity failures, it was decided some time ago to augment the existing superconducting RF system with two normal conducting cavities, of the Higher-Order Mode (HOM) damped cavity design currently in use at ALBA and BESSY. The two cavities were delivered in February and March 2017 and after testing and conditioning in the RF Test Facility were installed in the ring in August and November 2017. The cavities are installed in straights 16 and 18, on either side of straight 17 which hosts the two superconducting cavities, and in each case upstream of insertion devices (Fig. 2).

Figure 2: The cavities are installed in straights 16 and 18, on either side of straight 17 which hosts the two superconducting cavities.

The first normal conducting cavity has been successfully conditioned in the ring and was operated for the first time in user mode during the two day low-alpha period in March 2018 without a trip, with an accelerating voltage of 400 kV. The additional voltage provided by the cavity allowed the voltage on the superconducting cavities to be reduced, which gave a significant improvement in the trip rate compared to previous low-alpha periods. The second cavity will be brought into operation in the summer of 2018 following delivery and installation of its transmission line and circulator.

Digital low-level RF systems

A digital low-level RF system (for stabilisation of cavity RF voltage and phase) is being developed in collaboration with ALBA. The first system is in operation on the first normal conducting cavity and has already demonstrated superior stability compared to the analogue system currently in use on the superconducting cavities. Further systems are in construction and will be deployed on the second normal conducting cavity and later also on the two superconducting cavities.

Longitudinal Multi-Bunch Feedback system

A Longitudinal Multi-Bunch Feedback (LMBF) system has recently been implemented, in order to combat potential longitudinal instabilities of the electron bunches due to higher order modes in the normal conducting cavities, as well as to provide valuable additional diagnostic features.

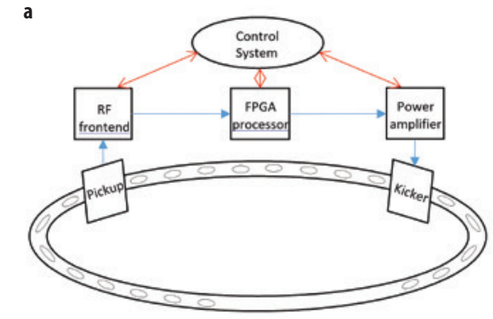

Figure 3: Schematic showing the operation of the longitudinal multi-bunch feedback (LMBF) system (a) and a view of the kicker cavity installed in the storage ring (b).

The LMBF system provides monitoring and correction of the precise relative timing of the individual bunches in the storage ring. All bunches should ideally arrive at a fixed phase relative to the driving field in the accelerating cavities. However, there was a risk when installing the normal conducting cavities that interactions with the beam could lead to 'coupled bunch instabilities' which could limit the beam current. Having detected the start of an instability in the beam the LMBF is capable of suppressing it by acting on the beam with a suitable correction signal.

Conceptually, the system is similar to the Transverse Multi Bunch Feedback (TMBF) already in use since 2008 (Fig. 3a). A pickup registers the arrival time of each bunch, which is then processed in a digital feedback controller. This feedback controller is continuously calculating 500 million control values per second, which it sends through an amplifier to a kicker to influence each bunch. The whole feedback process takes only a few microseconds and relies on the predictability of the motion of a bunch over such short periods.

To implement the LMBF a new kicker cavity needed to be designed, manufactured and installed. The fabricated structure was installed in April 2017 in straight 22 just upstream of the insertion device and is only recognisable by the eight feedthroughs connecting power from the amplifier to the complex structure on the inside (Fig. 3b).

The feedback processor is based on commercial MicroTCA hardware, while FPGA and EPICS components were developed in-house. During this project the opportunity was taken to update the TMBF to the new hardware, which now allows synchronised measurements of the horizontal, transverse and longitudinal position of each individual bunch, a formidable new diagnostic tool.

'Missing sextupole' scheme

The Dual Imaging and Diffraction (DIAD) beamline (K11) is the last new beamline to be funded and is currently under construction. Originally envisaged to be installed on a 'Superbend' (a bending magnet with higher magnetic field than the standard bending magnets in the ring) it was later proposed to be installed on an insertion device, using a second Double-Double Bend Achromat (DDBA) cell (as described in last year's Annual Review). Calculations however indicated that a second DDBA cell posed a significant risk to the operation of the ring, and so another scheme was investigated, the 'missing sextupole' scheme (Fig. 4). This involves removing a sextupole magnet from one of the achromats and using the space created to install a short 10-pole wiggler magnet as the source for the DIAD beamline. Having confirmed its feasibility in simulations, this mode of operation has now been thoroughly tested during machine development periods by switching off the relevant magnet and retuning the machine. Meanwhile the new vacuum vessels have been designed and constructed, and the modified girders are being prepared (Fig. 5). These are due to be installed in the June 2018 shutdown.

Figure 5: Replacement girder under construction; the arrow indicates the position of the 'missing sextupole' and the new narrow gap vacuum vessel where the DIAD mini-wiggler will be installed.

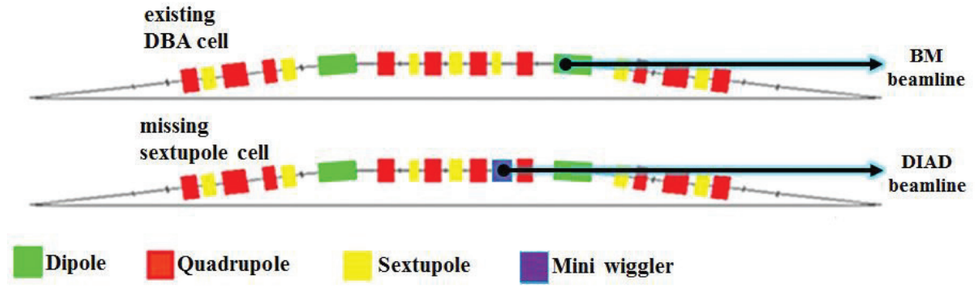

Figure 4: The 'missing sextupole' scheme consists of removing a sextupole magnet from the standard double-bend achromat (DBA) cell, and in its place installing a mini-wiggler magnet as a source for the new DIAD beamline.

Optics and Metrology Group

Kawal Sawhney, Optics and Metrology Group Leader

As Phase III comes to an end, the Optics and Metrology Group continue to provide expert support in the design, testing, and optimisation of X-ray optics for new and upgraded beamlines. Looking to the future, the Optics and Metrology Group is also heavily involved in planning for Diamond-II. Ray-tracing and wavefront propagation simulations are being used to predict the likely performance of current beamlines, and how they might be upgraded to optimally use the proposed brighter X-ray source.

Ultra-high accuracy characterisation of state-of-the-art X-ray optics continues to be an essential procedure, both for quality control and the development of novel optics. Continuous improvement of metrology instrumentation and techniques has led to ever more accurate at-wavelength (using X-rays) and *ex situ* (using visible light) characterisation of X-ray optics. We have also increased the technical capabilities of many existing and future beamlines by pursuing a broad range of optical research projects[1-6].

With our strong reputation for optical metrology expertise, we have also begun offering a paid commercial service to manufacturers to characterise and optimise beamline optical systems of other synchrotrons. Diamond's enhanced metrology capabilities provide manufactures with a two-fold advantage: helping to improve the quality of their products, and to provide an independent verification of high quality.

Rapidly varying the size and shape of X-ray beams using high speed, bimorph deformable mirrors

Piezo-electric, deformable 'bimorph' mirrors are used to focus X-rays on many beamlines at Diamond and at other facilities around the world. The tangential curvature of bimorph mirrors is typically only changed every few hours or days. This operation can take tens of minutes and often requires expert guidance. Following a large change in curvature, bimorph mirrors are known to take more than 15 minutes to stabilise on the nanometre scale. Historically, the dynamic performance of active X-ray optics has therefore not been exploited at synchrotrons. This is in stark contrast to ultra-fast adjustments made to adaptive optics in other scientific fields such as Astronomy. However, many synchrotron beamlines, especially those dedicated to macromolecular crystallography, now analyse hundreds of samples per day. Such beamlines would greatly benefit from the ability to rapidly modify the X-ray beam profile in only a few seconds to match to the size of small samples, or to vary the illuminated region of larger samples. The time-dependent behaviour of a series of micro-focus, bimorph mirrors was investigated using Fizeau interferometry in the Optical Metrology Lab. A novel 'speedy' bimorph (Fig. 1) was developed by making several hardware and software improvements. Utilising a new high-voltage power supply, the magnitude of the mirror's curvature drift after applying a large voltage shift to the piezo actuators was significantly reduced (Fig. 2a). The residual drift, attributed to piezo creep, was shown to be repeatable and could readily be compensated. Once installed on the Microfocus Macromolecular Crystallography beamline (I24) at Diamond, the Kirkpatrick-Baez (KB) pair of bimorphs focused the X-ray beam in less than

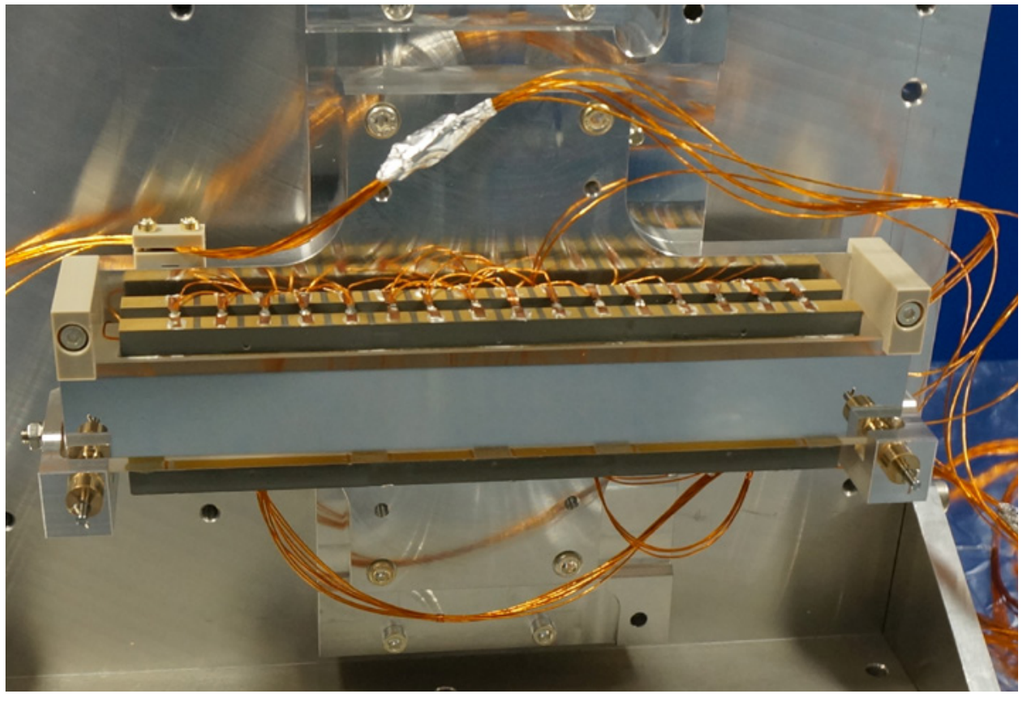

Figure 1: Photograph of I24's horizontal micro-focussing 'speedy' bimorph mirror.

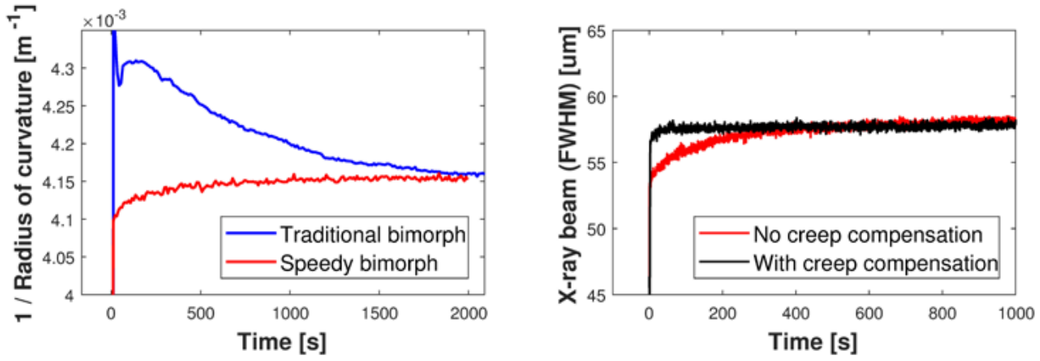

Figure 2: (a) Improved curvature drift of a 'speedy' bimorph mirror compared to a traditional model; (b) Further stability improvement to the size of the X-ray beam using creep compensation for the speedy bimorph.

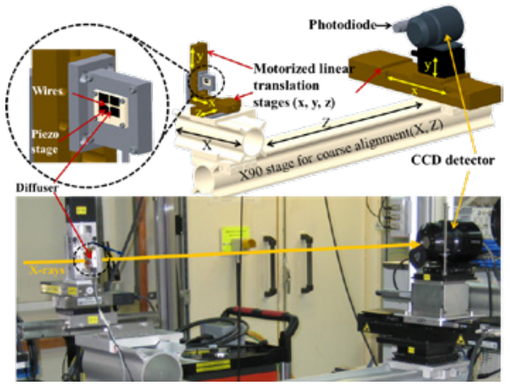

Figure 3: (Top) Schematic of the portable device for in situ characterisation of X-ray optics. The diffuser, wires, CCD detector, and photo-diode can be translated into the X-ray beam using motorized linear stages. (Bottom) Photograph of the portable metrology device installed on the B16 beamline to characterise X-ray mirrors.

10 seconds. Of equal importance, compensating piezo creep ensured that the size of the X-ray beam remained stable for more than one hour after making a major change (Fig. 2b). This enables continuous 'adaptive' shaping of the X-ray beam in almost real time. Such innovations could lead to significant scientific improvements in how active X-ray optics are utilised at synchrotron and free-electron laser (FEL) sources.

A portable device for *in situ* characterisation of X-ray mirrors

The push towards imaging samples with higher spatial resolution requires diffraction-limited and coherence-preserved X-ray beams. This demands accurate metrology of X-ray mirrors, ideally under working conditions. The Optics and Metrology Group have developed a portable device for *in situ* characterisation and optimisation of X-ray mirrors using a X-ray speckle-based technique. A schematic of the mechanical layout and a photograph of the device are shown in Figure 3. The entire setup has been purposefully designed for ease of portability. The diffuser is mounted on a piezo stage for precision scanning, and a pair of crossed gold wires is also attached to the piezo stage to permit measurement of the X-ray beam-size. Further downstream, a CCD detector and a photodiode detector are used to record the speckle pattern and perform knife edge scans. The device is capable of measuring either horizontal or vertical reflection X-ray mirrors, which is especially useful if there is a need to characterise composite optics, such as Kirkpatrick-Baez (KB) mirror systems. Trial experiments were conducted at the Test beamline (B16) and Hard X-ray Nanoprobe beamline (I14). Ultra-high angular sensitivity is achieved by scanning the speckle generator in the X-ray beam. In addition to the compact setup and ease of implementation, a user-friendly graphical user interface has been developed to ensure that characterisation and alignment of X-ray mirrors is simple and fast. This fast, compact and accurate X-ray speckle-based device can be easily implemented on a variety of beamlines and is expected to find wide application for *in situ* characterisation or optimisation of X-ray mirrors at Diamond and other synchrotron radiation facilities.

Publications:

1. Hand M, Wang H, Maccherozzi F, Apollonio M, Zhu J, Dhesi SS, *et al*. Quantitative investigation of linear arbitrary polarization in an APPLE-II undulator. *J Synchrotron Rad.*, **25**, 378-384 (2018).
2. Sutter JP, Alianelli L. Aberration-free aspherical lens shape for shortening the focal distance of an already convergent beam. *J Synchrotron Rad.*, **24**, 1120-1136 (2017).
3. Nistea IT, Alcock SG, Kristiansen P, Young A. Long, elliptically bent, active X-ray mirrors with slope errors <200 nrad. *J Synchrotron Rad*., **24**, 615-621 (2017).
4. Laundy D, Sawhney K, Dhamgaye V. Using refractive optics to broaden the focus of an X-ray mirror. *J Synchrotron Rad.*, **24**, 744-749 (2017).
5. Roth T, Alianelli L, Lengeler D, Snigirev A, Seiboth F. Materials for X-ray refractive lenses minimizing wavefront distortions. *MRS Bulletin,* **42**, 430 – 436 (2017).
6. Yavas H, Sutter JP, Gog T, Wille H, Baron A. New materials for high-energy-resolution X-ray optics. *MRS Bulletin,* **42**, 424 – 429 (2017).
7. Yang X, Wang H, Hand M, Sawhney K, Kaulich B, Kozhevnikov IV, *et al*. Design of a multilayer-based collimated plane-grating monochromator for tender X-ray range. *J Synchrotron Rad.*, **24**, 168-174 (2017).
8. Yang X, Kozhevnikov IV, Huang Q, Wang H, Hand M, Sawhney K, *et al*. Analytic theory of alternate multilayer gratings operating in single-order regime. *Opt Express*, **25**, 15987-16001 (2017).

Detector Group

Nicola Tartoni, Detector Group Leader

During the past 12 months the Detector Group at Diamond has been working on two major development projects. The first project is the completion of the Xpress4 digital pulse processor, and the second the development of the large area detector for time resolved experiments, now called Tristan. The latter is still ongoing but has made substantial progress towards the delivery of the first prototype.

In January 2018 the Detector Group successfully completed the final installation and commissioning of the Xspress4 digital pulse processor (DPP) on a branchline of the Versatile X-ray Spectroscopy beamline, I20-Scanning (Fig. 1). Xspress4 is Diamond's new spectroscopy DPP and has been designed to significantly improve the spectral and rate performance that can be measured using the existing 64-element monolithic hyper-pure germanium (HPGe) detector – the workhorse for fluorescence mode X-ray Absorption Spectroscopy on I20-Scanning.

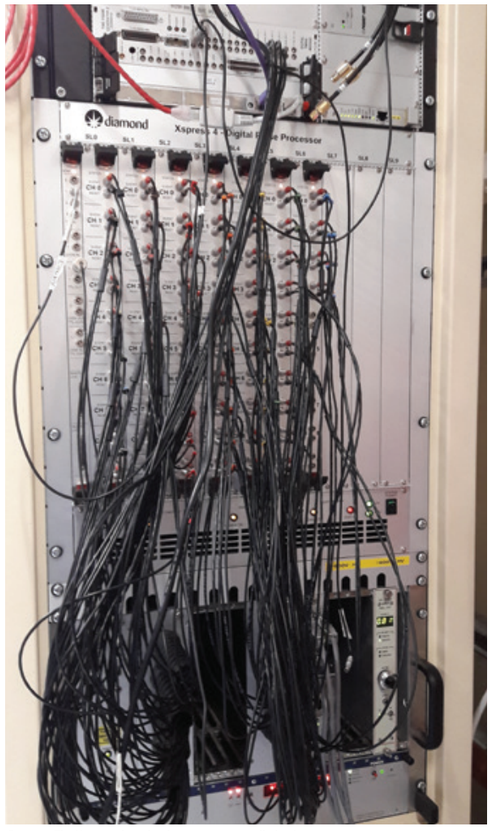

Figure 1: The Xpress4 digital pulse processor installed in I20.

Analysis of the HPGe detector signals had shown that a major barrier to high rate, high resolution performance was the presence of element to element crosstalk within the HPGe detector. A digital domain based signal processing algorithm was developed (and patented) to effectively remove crosstalk, allowing further downstream processing to more accurately measure fluorescence X-rays. Xspresss4 is the physical and firmware realisation of this algorithm. It is a channel count scalable, custom designed, rack mounted hardware architecture whose salient features include a new high performance front-end digitiser, the latest high capacity high performance digital processing FPGA hardware and high speed serial links to cross-connect all channels in the digital domain. New firmware implements the crosstalk correction algorithm, enhances X-ray energy measurement precision, and reliably manages the inherently high data flows within the system in real time.

The Xpress4 DPP manages to considerably enhance the energy resolution of spectra at high counting rates (Fig. 2). For a molybdenum sample (K-alpha fluorescence at 17.47 keV) the maximum input count rate (ICRmax) increases six-fold from 210 kcps per pixel to 1.25 Mcps per pixel for the same usable FWHM resolution (e.g. < 600 eV on all pixels). At lower energies where crosstalk has less impact, ICRmax increase four-fold e.g. manganese K-alpha (5.9 keV) ICRmax increases from 200 kcps to 800 kcps for a usable FWHM resolution < 300 eV.

With challenging user samples it is sometimes not be possible to operate at very high count rates simply due to the diluteness of the sample under study. In such cases, using Xspress4 still improves measurement accuracy by enhancing the resolution of the small fluorescence peak of interest while supressing the impact of the inevitably large close-by elastic peak in an XAS scan. Comparative tests with ultra-dilute nickel nitrate solutions shows a two-fold improvement in dilution for a given performance using Xspress4 compared with previous results. Finally the characteristics of the spectra delivered by Xpress4 do not depend as heavily as before on the counting rate, which helps in improving the data quality of absorption spectroscopy beam lines when the beam intensity changes during a scan.

In parallel to the development of the Xpress4 DPP some work has been carried out to characterise a demonstrator of a 19-channel monolithic segmented HPGe detector with a pad size smaller than the pad size currently in use at Diamond. The pads of the demonstrator have hexagonal shape with 1 mm apothem as opposed to the current ones that have square shape with 5 mm side. The demonstrator has been equipped with Cube preamplifiers[1] and it was tested twice at Diamond's Test beamline (B16). The results of the first beam test has been published at the IEEE 2017 Nuclear Science Symposium[2]. During the second beam test the demonstrator was read-out with Xpress4, a very preliminary analysis shows that the detector can operate at about 1 million counts per second per channel with a count loss less than 13% that is still in the usable range of X-ray Absorption Fine Structure (XAFS) experiments. The energy resolution is still sub-optimal because in order to keep the cost within the budget the optimisation of all the parts was not pursued; however the tests done give a clear indication that this is a possible path to enhance the throughput of the fluorescence systems for XAFS by increasing the segmentation of the detector and by enhancing the counting rate of the individual channels.

The Tristan project aims at building a detector for time resolved experiments based on the Timepix3 chip[3]. Sixteen Timepix3 chips are bonded to a monolithic pixelated silicon sensor with more than a million pixels. The Tristan project is being carried out in two phases: the first phase is the development of a prototype with a single sensor (Tristan 1M), which serves as pilot detector and the second phase delivers a detector with ten sensors (Tristan 10M), which will then be installed on the Small-Molecule Single-Crystal Diffraction beamline (I19).

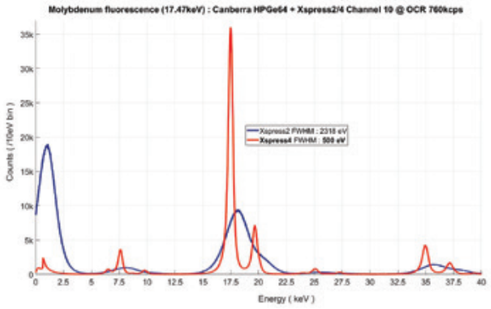

Figure 2: Molybdenum fluorescence spectrum acquired from channel 10 at 760 kilocounts per second by using algorithms with no cross talk correction (blue line) and with cross talk correction (red line). The energy resolution is greatly enhanced as it goes from 2318 eV FWHM down to 500 eV FWHM.

Most of the parts of Tristan 1M have been developed and assembled. The detector is undergoing tests with a single chip connected to the rest of the electronics through an adapter board (Fig. 3). The front end printed circuit board to which the Timepix3 chips are wire bonded and routes the signals to the back end electronics is currently under manufacturing. When this printed circuit board is delivered the Tristan 1M will be able to be tested in full. In parallel the mechanics of the Tristan 10M has been designed and the parts are currently being manufactured. The timescale for the completion of the project is to deliver a working Tristan 1M during the summer 2018 and then to assemble the Tristan 10M in autumn 2018 with the target to install it on the I19 during the winter of 2018/19.

References

1. XG LAB, www.xglab.it/low-noise-preamplifier.shtml, (2018).
2. Tartoni, N. *et al.* High channel density germanium detector demonstrator for high throughput X-ray spectroscopy. *IEEE-NSS Conference Proceedings* (2017).
3. Poikela, T. *et al.* Timepix3: a 65K channel hybrid pixel readout chip with simultaneous ToA/ToT and sparse readout. *Journal of Instrumentation* **9**, 5, (2014).

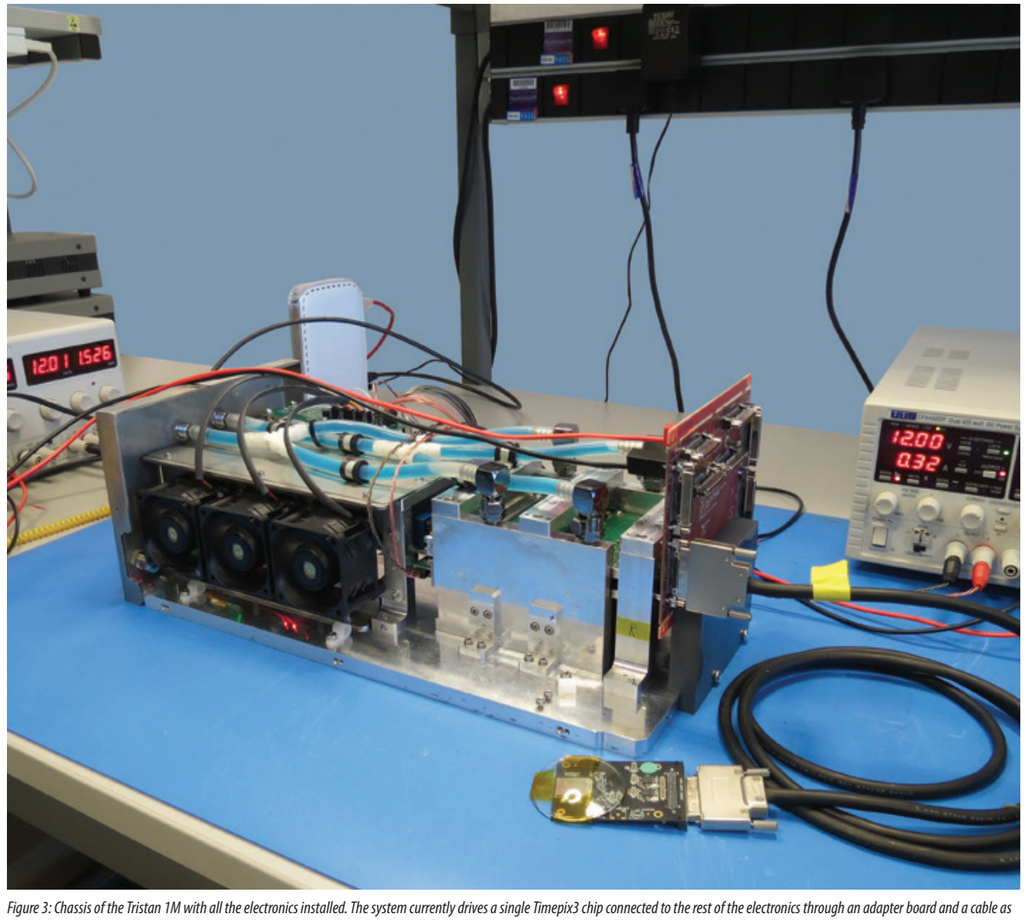

Figure 3: Chassis of the Tristan 1M with all the electronics installed. The system currently drives a single Timepix3 chip connected to the rest of the electronics through an adapter board and a cable as shown in the picture.

Data Analysis and Scientific Software Group

Alun Ashton, Data Analysis and Scientific Software Group Leader

DAWN *Steering Committee and Data Visualisation*

This year saw the formation of the DAWN Steering Committee; a collection of Diamond scientists selected to help guide the fundamental data visualisation features and general usability of the DAWN package. Under the supervision of the committee, a completely new 3D visualisation library has been integrated, greatly adding to DAWN's existing tools.

The DataVis perspective developed in collaboration with the committee also integrates with the latest version of GDA, and is being used for live visualisation of raw and processed data on the XPDF beamline (I15-1).

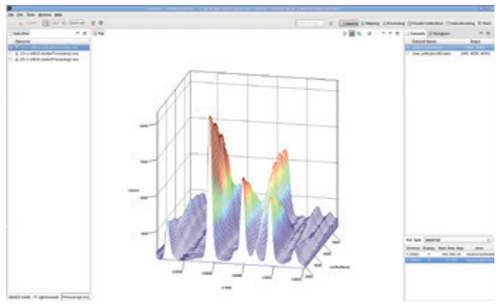

Figure 1: DAWN's new DataVis perspective showing processed data from I15-1 displayed as a waterfall plot (available in DAWN 2.8 released March 2018).

Small Angle Scattering

Building on one of last year's key successes whereby DAWN gained the functionality to automatically process data following data acquisition; this year's focus has moved to harnessing this capability, extending the functionality available within DAWN to provide bespoke, *in situ*, data analysis for users during experiments.

This effort has given rise to a number of processing steps designed to analyse a multitude of data types, providing results or parameters of interest to the user. In particular, for small angle scattering users, this has led to the development of a number of analysis routines for orientational, structural and kinetic characterisations of a sample.

These advances have been underpinned by a rigorous set of data corrections, as described in our recent *J. Appl. Cryst.* publication (B. R. Pauw, *et al*. 2017). This has facilitated progress in developing rigorous background subtraction routines, which can also be run autonomously, alongside the development of a methodology for the removal of a detector grid to provide one continuous, uniform, dataset.

Eclipse Science and IoT

This year at Diamond, we hosted one of the Eclipse Science group and Internet of Things (IoT) workshops, which involved several invited talks and an IoT playground. Participants from Diamond, around the Harwell campus and the wider business community all enjoyed the excellent presentations and demos which showcased the state of the art in software for science.

Savu

2017 saw the release of Savu version 2.0, which features an improved user interface and significant performance increases. The roll-out of Savu onto Diamond's mapping tomography beamlines has reduced multi-modal processing from eight hours to ten minutes, and Savu is now able to replicate the standard full-field tomography processing of its predecessor in less computational time.

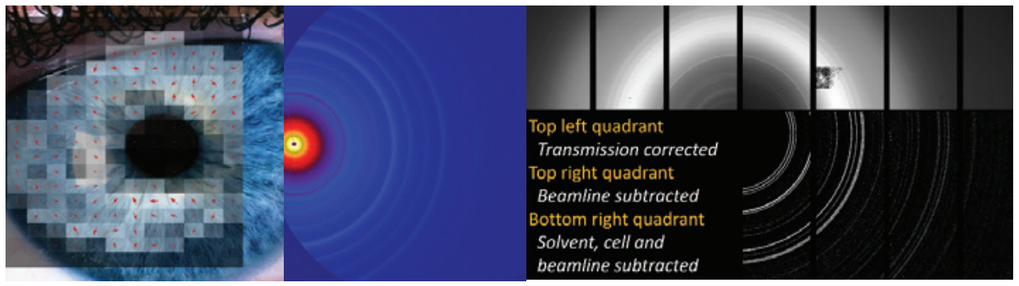

Figure 2: Mapped scan showing the orientation of collagen in a sample overlaid on an image of a human eye (L. Paletto, Albon Group, Cardiff University, UK, Collected October 2017) (left). A gridless Pilatus 2M image gathered from 3 detector frames at differing positions (Y. Zhang and S. Prabakar, New Zealand Leather and Shoe Research Institute, Collected August 2017) (middle). A wide angle X-ray scattering (WAXS) scan highlighting various levels of background subtraction, made possible by applying data corrections before subtraction (Stawski Group, GFZ Centre for Geosciences, Germany, Collected July 2017) (right).

Figure 5: ISPyB/MXCuBE meeting in January 2018.

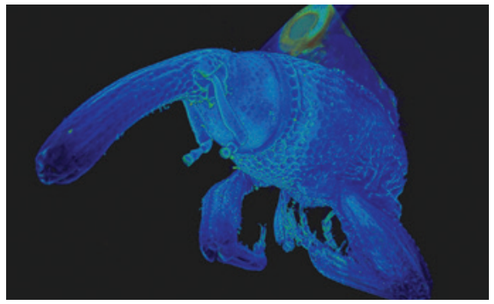

Figure 3: A rendering of an insect collected on I13 reconstructed using Savu.

Now routinely used on Diamond beamlines, Savu provides a larger array of processing methods and more flexible processing than previously available to Diamond's tomography community. It also provides a platform for beamline staff to contribute their own methods in the form of Savu plugins, which has led to a rise in the sharing of methods and collaboration between beamlines.

After recent integration of Savu with GDA data acquisition software, the Joint Engineering, Environmental and Processing beamline (I12) and X-ray Imaging and Coherence beamline (I13) now perform auto-processing on tomography data as soon as data collection is complete. This allows beamline scientists to immediately identify if there are any problems with the current experimental setup.

Zooniverse

Building on last year's success with the SuRVoS software for analysing data from the Full Field Cryo-Transmission X-ray Microscope beamline (B24), SuRVoS has gone on to analyse biological data from other imaging beamlines as well, such as the Imaging branchline (I13-2). In addition to this, the scope has been extended further by making use of the Zooniverse platform (www.zoonoverse.org) to host some work on protein misfolding disorders, specifically Huntington's disease initially, but with the aim to extend to other problems where humans are better than machines at identifying information in complex image data.

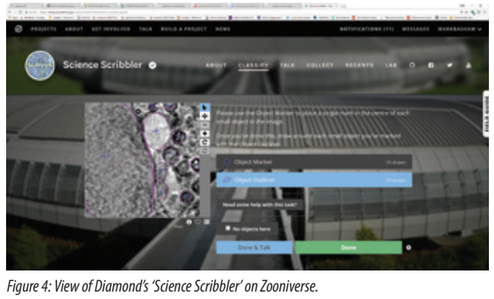

Figure 4: View of Diamond's 'Science Scribbler' on Zooniverse.

ISPyB

The ISPyB database and SynchWeb software services store and present experimental meta-data, generate beamline performance statistics and provide remote access to users and beamline scientists. To reflect its growing importance, the team supporting the ISPyB and SynchWeb software services is increasing. A full time project lead was appointed in September 2017 and will be followed by a full time SynchWeb developer joining the team in early 2018. Additional support has also been contracted to re-establish support for mobile devices.

New features added to SynchWeb in the past year have included the integration of automated sample shipping to the facility. This includes support for users across the EU. Work has also been underway to add support to new and emerging techniques including XPDF beamline (I15-1) and continued refinement of the *in situ* beamline VMXi.

Diamond and the Scientific Software team continue to support the international ISPyB collaboration through developer, scientific and steering committees. Diamond co-hosted the most recent joint ISPyB/MXCuBE meeting in January 2018. One of the key areas for discussion in the collaboration is the growing field of cryo-electron microscopy. The team at Diamond established the integration of electron microscopy experimental data with ISPyB through the development of Scipion workflows. The development activities continue to enhance ISPyB as it evolves from a bespoke solution for a single technique to a general purpose Laboratory Information Management System (LIMS) for Diamond.

Acknowledgements: We wish to thank all our collaborators, Diamond beamline staff and users for their continued support and input.

Data Acquisition Group

Keith Ralphs, Interim Data Acquisition Group Leader

In recent years Diamond has invested a lot of software engineering effort across the Data Acquisition, Data Analysis and Beamline Controls groups in an attempt to standardise and advance the frameworks that support the science carried out here. Under the auspices of the Mapping Project, this has delivered a platform, initially proven on a few beamlines, which can now start to be rolled out across the organisation as a whole to deliver enhanced capabilities in terms of the definition, orchestration and visualisation of experimental scans. Building on this, during the last year we have begun to see these benefits feeding into areas of usability and beamline development as well as facilitating the development of more advanced approaches such as ptychography. Going forward, this should allow us to better support the needs of Diamond's scientists and users as these new tools are adopted across the organisation.

The Data Acquisition Group develops, supports and maintains the software that controls experiments carried out on the majority of beamlines at Diamond. All aspects of the experimental process are covered, but initial setup of the sample environment is always crucially important in obtaining accurate and meaningful results further down the line. It is here that software usability can be very significant in enabling quick, easy, repeatable initialisation of the experimental environment to guarantee consistency between groups of measurements.

Focus on Usability

Focus scans, which are made to ensure the hardware holding an experimental sample is correctly positioned with respect to the incoming beam, are a particular example where usability becomes a key factor in making progress, as the ability to re-establish the best focus point with a few clicks of the mouse can save a lot of time. Automating the data gathering part of this operation as much as possible, leaving the user to just select the focus point itself, can become especially important during long, perhaps overnight experimental sessions when the risk of human error in manually filling in such data can increase. This is one of the areas where the advances delivered as part of the Mapping Project by the Data Acquisition, Data Analysis and Beamline Controls groups have allowed us to substantially improve usability by implementing such an automated solution, removing sources of potential error from the process. On the Scanning X-ray Microscopy beamline (I08) this new Focus Scan wizard has been very well received by beamline staff and users allowing them to get on quickly to the actual business of their experiment and removing the potentially costly risk of misconfiguration. Making use of the new hardware triggered scanning infrastructure implemented by the Beamline Controls group, the data acquisition software is quickly able to produce a single image on screen from which the user can easily interpret the best point of focus and then click it to prompt the experimental hardware to move to the corresponding position. This wizard is now a standard tool on the Mapping User Interface and is thus available to other mapping enabled beamlines, some of whom have begun to adopt it in the last few weeks. By harnessing the new techniques available in our software platforms in this way, we can now start to effectively target our efforts towards improving and simplifying the process of carrying out experiments at Diamond. This in turn should lead to more productive user sessions helping scientists get the most out of their time on the beamline.

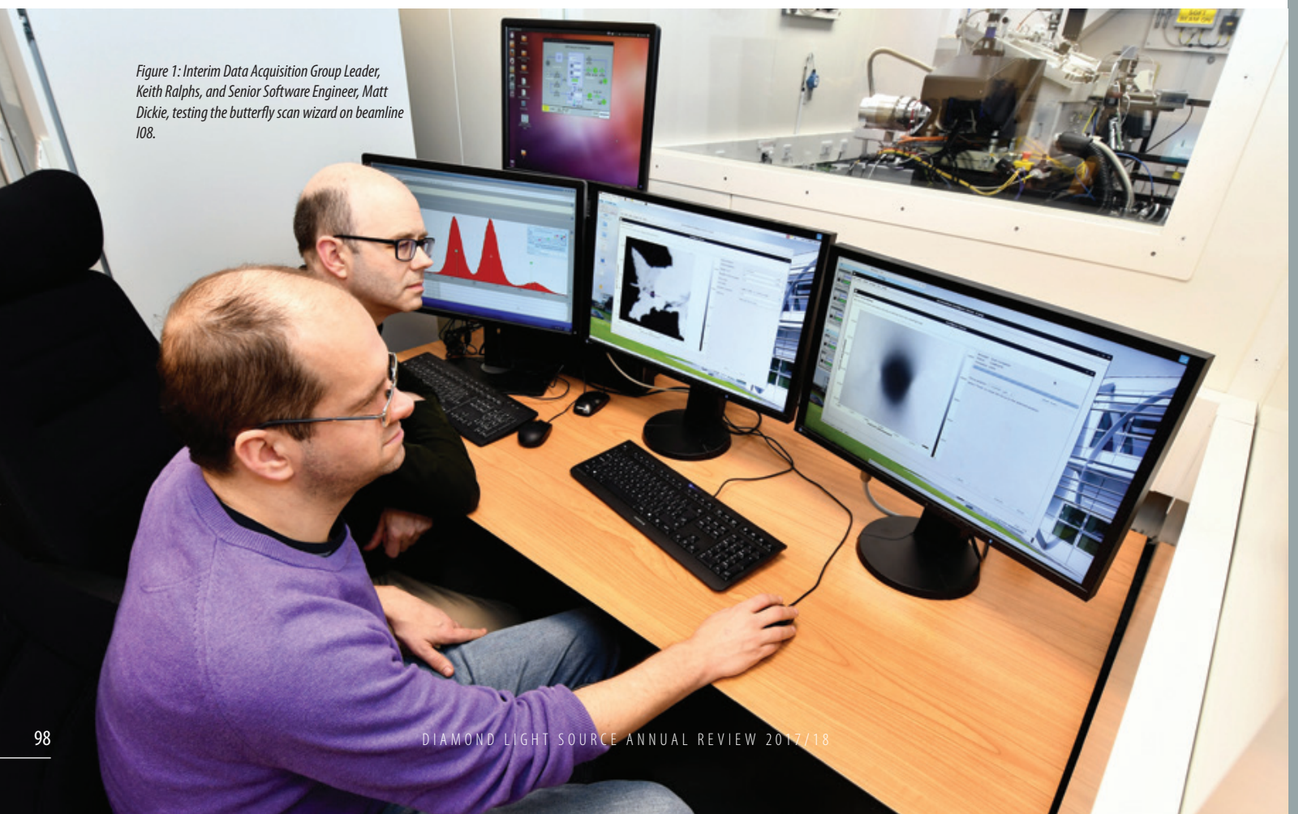

Figure 1: Interim Data Acquisition Group Leader, Keith Ralphs, and Senior Software Engineer, Matt Dickie, testing the butterfly scan wizard on beamline I08.

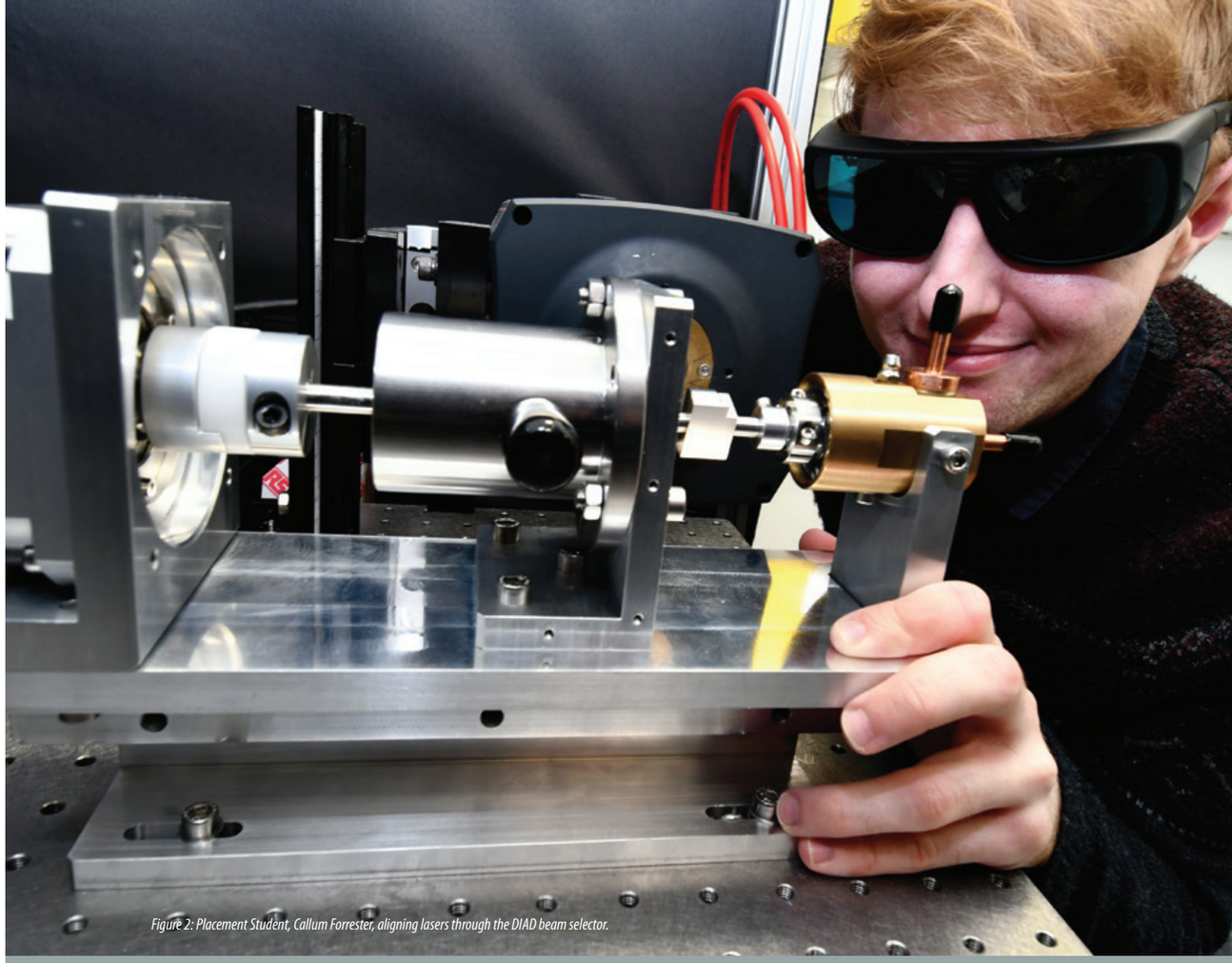

Figure 2: Placement Student, Callum Forrester, aligning lasers through the DIAD beam selector.

Try before you buy

In producing Data Acquisition support software for new and upgraded beamlines, the ability to prototype, evaluate and hone the tools we develop as early as possible in the beamline build and commissioning process is key to ensuring successful delivery of new experimental capabilities at Diamond. It allows us to debug and address problems up front and to work closely with beamline scientists to collaboratively design the user experience that will eventually be delivered, long before the finished beamline exists. During the last year, the opportunity to do this has been improved substantially by the installation of the P99 test beamline as part of the ongoing ptychography Data Analysis project being carried out by the data analysis group. Use of this small scale laser based analogue of a full beamline setup enables Data Acquisition engineers to exercise the software tools and processes they are developing, whilst connected to actual representative hardware of the sort that will eventually be used on the real installation. This approach has come to the fore in recent months on the project to develop Data Acquisition support of the new DIAD (Dual Imaging And Diffraction) beamline, currently under construction next to I12. DIAD will produce two separate beams to enable the use of two different X-ray measurement techniques; diffraction and imaging. To allow each technique to capture the desired results a Novel Beam Selector device (a prototype of which exists) is placed in the path of the main beam at the end of the optics hutch. This selector will need to be controlled by our data acquisition software via the hardware triggering layer developed by the Controls Group to ensure the high speed switching required for the planned experiments. The availability of the P99 test beamline has allowed both our teams to start actively developing the processes that will drive this selector on the real beamline by temporarily installing the prototype on P99 and working together to design and debug scans on a setup that closely resembles the real installation. Working in this way ensures that we maximise the chance of discovering and addressing any issues that arise long before the functionality is needed and also allows us to engage DIAD's beamline scientists in this process to get their feedback and ensure that our approaches are valid.

The way forward

In the coming years the upgraded Data Acquisition and Controls platform now available to us will allow us to start to roll out similar targeted functionality across all of Diamond's beamlines using this collaborative approach. This should allow us to deliver functionality that enables new techniques and optimises existing ones, allowing our scientists and users to concentrate on the specifics of their experiments and the insights they yield. In addition, the hardware level control now supported will help develop other recent automated beamline installations such as VMXi allowing them to optimise the control of their experiments to maximise their efficiency.

Key Facts and Figures

Facility usage

In our eleventh year of operations (1st April 2017 to 31st March 2018), we received 1,515 proposals for experiments on our instruments via peer reviewed access routes, requesting a total of 19,507 shifts. After peer review 1,095 proposals were awarded beamtime. This resulted in 11,667 experimental shifts being awarded across 28 operational beamlines, one commissioning beamline and eight electron microscopes. We welcomed 5,668 onsite user visits from academia across all instruments, with an additional 3,656 remote user visits.

In the last 12 months Diamond started to review its reporting method on facility usage. A new reporting tool is currently being developed and allows us to report more precisely and more consistently. As a result, some of the reporting criteria in this review have evolved compared to previous years. Further efforts on reporting are being carried out and should continue in the next 12 months.

User shifts requested, awarded and delivered by group, beamline and electron microscope 2017/18

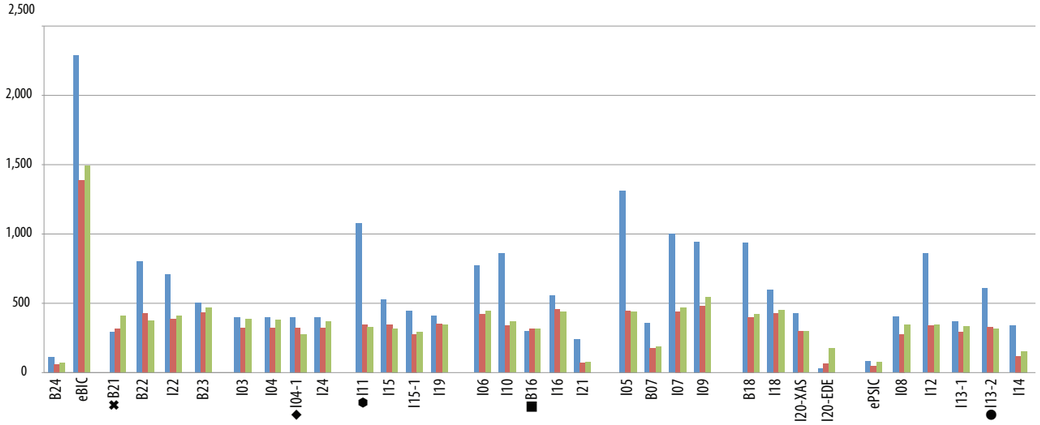

✖ B21: Until April 2018, some B21 shifts are requested as part of MX BAG proposals. These shifts are not included as requested shifts in the graph above.
◆ I04-1: some delivered shifts are delivered as part of XChem campaigns which are not included in this report
⬢ For I11, LDE experiments are not included in this section.
● I13-2 Provides 35% of the available shifts to the Diamond Manchester Collaboration: these shifts are not included in this section.
■ B16 is an optical testing beamline with only 50% of beamtime for users

Total user shifts requested, awarded and delivered

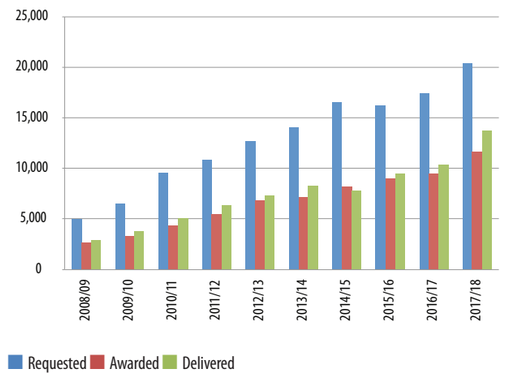

Total numbers of proposals and users per year

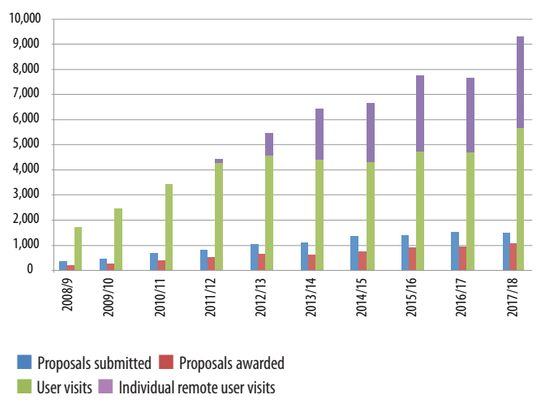

Proposals by discipline and research theme

Experimental shifts scheduled by Diamond by main subject area for 2017/18

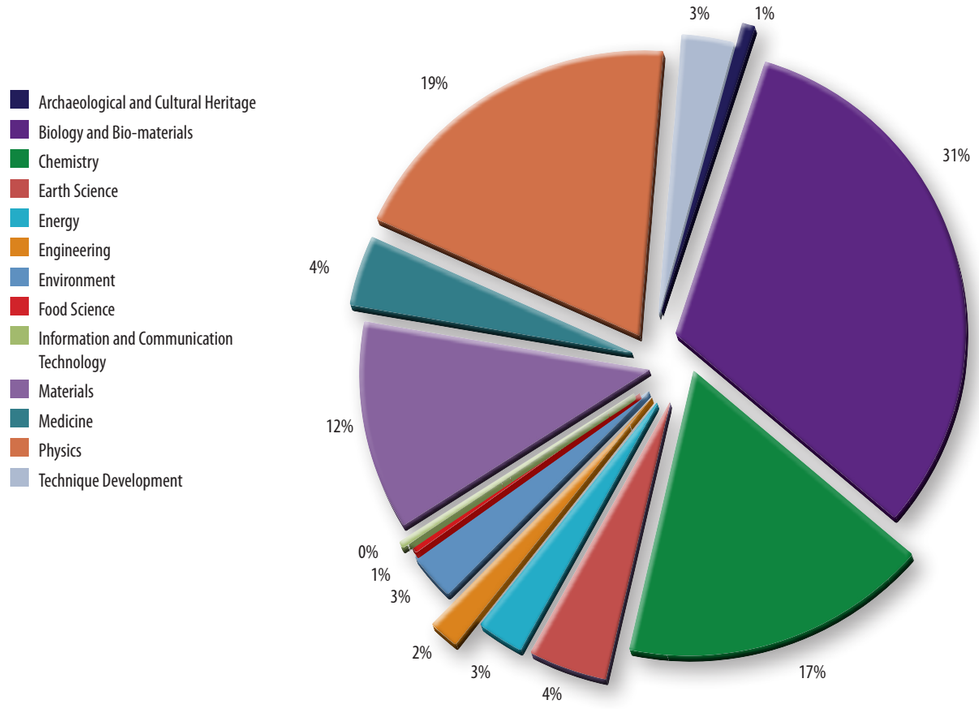

Cumulative number of items in Diamond Publications Database by our scientists and users and cumulative number of protein structures solved

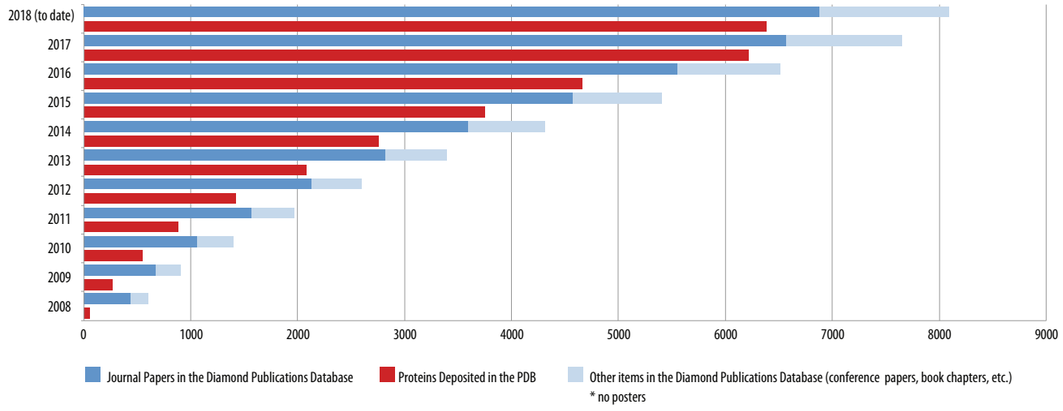

Machine performance

	2008/9	2009/10	2010/11	2011/12	2012/13	2013/14	2014/15	2015/16	2016/17	2017/18
Total no. operational beamlines by end FY	13	17	19	20	22	24	25	26	28	28
Scheduled hours of machine operation	5640	5712	5808	6000	5832	5976	5808	5928	5688	6072
Scheduled hours of user operation	4305	4728	4728	5064	4872	5088	4944	5040	4584	5160
Machine uptime %	95.0	97.0	97.5	97.7	98.3	98.2	97.6	97.6	98.7	98.2
Mean time between failures (hours)	15.3	26.2	28.5	55.4	52.4	60.3	38.6	119.4	103.1	79.9

Collaborations

Diamond Manchester Collaboration

The collaboration between the University of Manchester and Diamond Light Source was established to construct and operate an imaging facility at Diamond's X-ray Imaging and Coherence beamline (I13). Complementary to the Coherence branchline (I13-1), the Diamond Manchester Imaging branchline (I13-2) performs real space imaging and tomography on a length or timescale not achievable in home laboratories. Thanks to the high flux from Diamond, images of high signal-to-noise ratios can be recorded very quickly on I13-2. This enables the study of dynamic processes such as electrochemical deposition for explaining battery failure, bubble dynamics in molten metals for understanding how metals solidify and therefore fail, and the dynamics of the closed cochlea, the part of the ear that converts sound waves to electrical signals.

Manchester assisted financially to the building of the I13-2 branchline and continues to contribute to its beamline staff, operations and development. Diamond owns and has overall responsibility for the branchline, and provides all other funding necessary to ensure I13 conducts world-leading science. I13 has its own beamline team which is led by Principal Beamline Scientist Professor Christoph Rau and director of the collaboration is Professor Neil Bourne.

In return for its investment, Manchester has guaranteed access to beamtime at Diamond. The majority of this is carried out on I13-2, but substantial amounts of beamtime are available on other beamlines as well. Manchester uses I13-2 for research that spans materials science, biomedicine, geology and engineering, as well as methods to develop the fields of X-ray imaging and tomography. To complement the work undertaken at Diamond, Manchester has set up a chapter of the Manchester X-ray Imaging Facility at the Research Complex at Harwell (RCaH) situated next to Diamond. To date the collaboration has produced 78 publications.

The partnership formally began in May 2010 and will continue until at least 2020. Both partners view the collaboration as a long-term, ongoing relationship, working together as key national players in X-ray imaging and tomography as well as providing access to the forefront of new technology. With this vision in mind there are significant plans on the horizon for the partnership. These plans include technical and instrument upgrades as well as increasing the extent of the collaboration to involve many stakeholders. Incorporated in the project is brand new technology, some of which has not yet been accomplished.

The Diamond Manchester collaboration has been involved in many other partnerships including US National Labs, Advanced Light Source, ESRF, CLF and the nuclear industry.

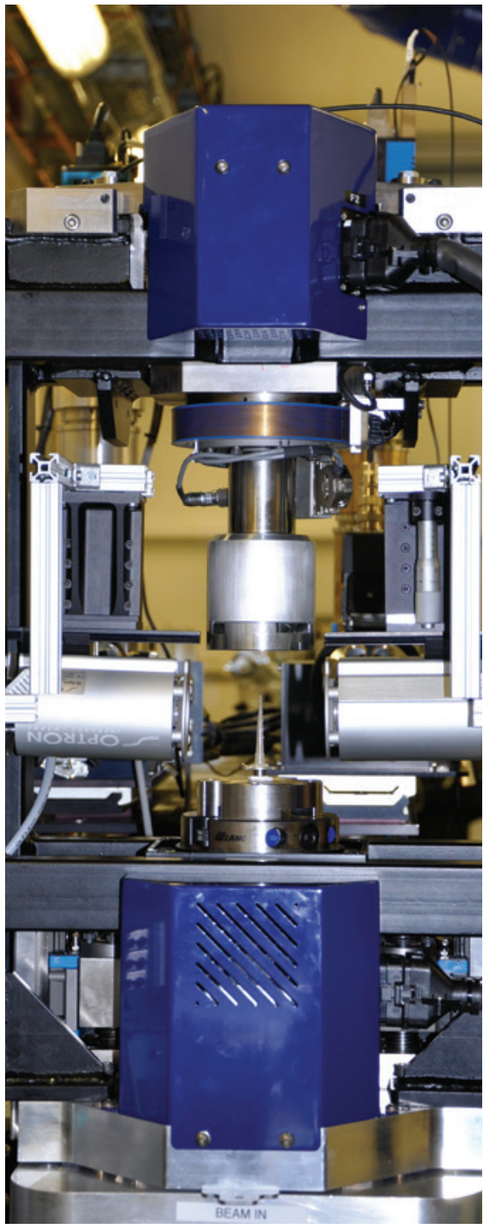

Figure 1: Investigating granite for nuclear storage on the Diamond Manchester branchline.

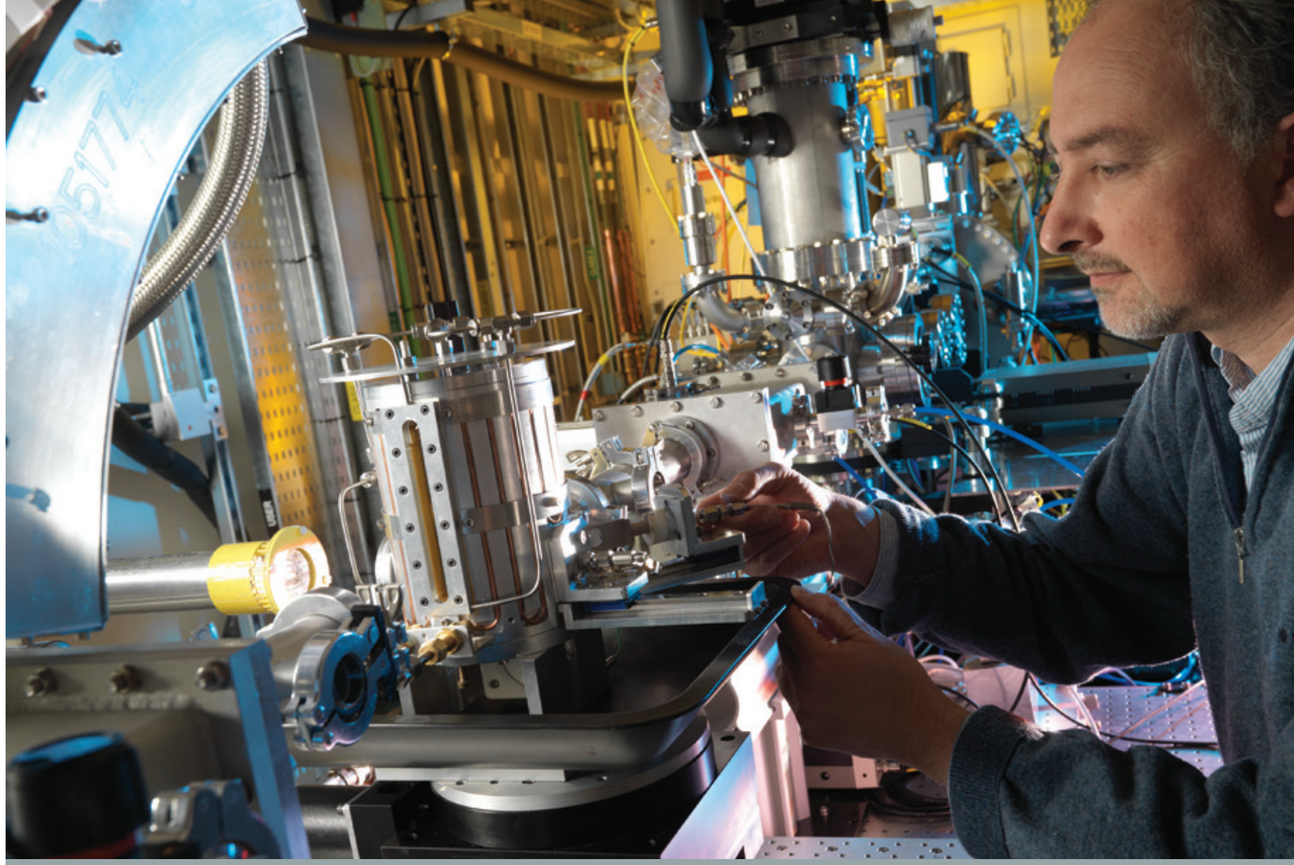

Figure 2: Principal Beamline Scientist, Giannantonio Cibin, in the experimental hutch of B18.

The UK Catalysis Hub

Catalysis is a core area of contemporary science, engineering and technology that has substantial economic and societal impact. Although rooted in chemistry and chemical engineering, catalytic science is now largely multidisciplinary, drawing strongly from materials and bio-sciences.

The Hub is a national network with over 35 collaborating universities. It was established in 2013 with funding from EPSRC to coordinate, promote and advance the UK catalysis research portfolio. Its physical centre is located next door to Diamond at the Research Complex at Harwell (RCaH). The project has five themes each directed by a lead investigator from five partner universities:

- Catalyst Design:
  Led by Prof Richard Catlow, UCL and based in the RCaH
- Catalysis for Energy:
  Led by Prof Christopher Hardacre, Queen's University Belfast
- Catalysis for Chemical Transformations:
  Led by Prof Matthew Davidson, Bath
- Environmental Catalysis:
  Led by Prof Graham Hutchings, Cardiff
- Bio Catalysis and BioTransformations :
  Led by Prof Nick Turner, Manchester

The Hub provides a platform for researchers to work collectively and gain frequent access to the Diamond synchrotron, as well as other facilities at Harwell. A whole system approach to the study of catalysis combined with high throughput allows optimal experiments to be carried out which shorten the path to development of commercially useful products, and promote the UK catalysis effort and expertise on a global stage. The Hub has strong links with industry which are coordinated by an Industrial Advisory Panel comprising of several UK and international industrial members.

One of the main benefits of the Catalysis Hub is sustained access to a synchrotron radiation source. Members of the Hub may apply for access to Diamond through a Beamtime Access Group (BAG), which provides the team with access to the Core EXAFS beamline (B18) per allocation period. This access route increases the efficiency of data acquisition by coordinating projects to reduce the dead time of experimental setup, and by allocating small amounts of time for proof of concept investigations before a full study starts. Applications are judged by a panel of expert academics and beamline scientists, who consider (i) the quality of the underpinning science, (ii) the likely success of the experiments, (iii) bringing in new users of synchrotron radiation, and (iv) coordinating time effectively to maximise efficiency.

This opportunity is open to every academic working in catalysis in the UK. The model of access brings together complementary expertise to ensure that experimental time is maximised, and presents opportunities for researchers that have not used a synchrotron before. The Catalysis Hub team have worked with a variety of catalysis samples, and the B18 beamline team know exactly how to get the best out of the samples they are working on.

The UK catalysis Hub also presents a training experience; a number of PhD students have been placed at the RCaH working on catalysis projects with the Hub. This initiative forms part of the Hub's aim to develop the next generation of catalytic scientists, through courses, conferences, PhD programmes, summer schools and outreach activities.

Industrial Liaison at Diamond

Elizabeth Shotton, Head of Industrial Liaison

The past year has once again been a year of growth for the industrial user programme at Diamond. From across the globe 50 companies are making regular use of the beamlines, and increasingly the cryo-electron microscopy (cryo-EM) facilities. The Industrial Liaison team are supporting around 250 different experimental sessions with industrial users each year, with the majority of users coming from the life science sector.

The growth in industrial usage by life science companies has been supported by the expansion of Diamond's capabilities in this area and we are now able to offer a wider range of structural biology services than ever before. Recent developments in detectors and the latest generation of microscopes has meant that previously unattainable resolutions are now routinely possible through cryo-EM at Diamond's Electron Bio-Imaging Centre (eBIC). This has resulted in an increased demand for the technology across both academia and industry. To support this growth, Jason Van Rooyen joined the team in May 2017 from the University of Cape Town as the Industrial Liaison Scientist for cryo-EM.

The XChem facility for X-ray structure-accelerated, synthesis-aligned fragment medicinal chemistry which has been established at Diamond in partnership with the Structural Genomics Consortium is also proving an attractive service for our industrial users. Several campaigns have been conducted through the service; with demand outstripping supply, a parallel facility has been funded for industrial users. This will allow us to provide more timely access to our clients to allow for quicker feedback into their drug discovery programmes.

We are working to enable industrial access to the full wealth of technology and knowledge available at Diamond by extending our services to the technical expertise of our Optics and Metrology Group in addition to our beamlines and microscopes.

At synchrotron radiation sources and free-electron lasers (FELs), the quality of X-ray optics is often a major limitation to beamline performance. Recent advances in deterministic polishing techniques have greatly improved the quality of optical surfaces but have revealed a new challenge for X-ray optics; minimising additional slope errors introduced by mounting the substrate into its holder, adding cooling manifolds, and bending it.

High quality metrology instruments and ultra-stable environments are essential to aid optimisation of clamping and bending to guarantee the best possible X-ray performance for beamline optics. *Ex situ* optimisation and fault-finding investigations of such systems prior to beamline installation have saved significant amounts of valuable X-ray commissioning time, and it is here where the testing capabilities of the Optics and Metrology Group at Diamond come into play (Fig. 3). Commercial suppliers of synchrotron optical systems have been able to benefit from Diamond's state-of-the-art metrology instruments and facilities that enable testing to unprecedented levels.

A successful industrial consultancy between Diamond and FMB Oxford Ltd, an established leader in the supply of beamlines and beamline components, has developed mechanical systems that can accurately bend long X-ray mirrors to a range of useful ellipses. On several occasions, FMB Oxford have successfully exploited this metrology service, including the recent tests of their newly developed two-moment actuator systems for elliptical bending of long X-ray mirrors which have been published in Journal of Synchrotron Radiation.

In an effort to reduce barriers to innovation, the Industrial Liaison team have been working with colleagues across STFC in two funding schemes which aim to help companies overcome intractable product, manufacturing or process performance problems through advanced measurement and analytical technologies.

The first scheme was funded through Innovate UK and STFC plus other external partners such as the National Physical Laboratory. Analysis for Innovators (A4I) opened to applications in January 2017, allowing companies to apply for a share of £6.5 million to work with facilities such as Diamond on solutions for analysis and measurement problems. Two projects were funded to use Diamond, including one with a micro-SME, Lewtas Science & Technologies, studying "phase change control by very low power ultrasound".

Low power ($< 10\ W\ m^{-2}$) ultrasound spectroscopy has been used for many years for the characterisation of materials, particularly in the food industry, with respect to particle size distribution, adiabatic compressibility, particle solvation and dissolution, crystal nucleation and solid content. High power ($> 1\ kW\ m^{-2}$) ultrasound methods are applied for material modification and processing, ultimately speeding up processing times, improving product quality and reducing costs. However, high power ultrasound methods are well-known to impact on crystallisation and structuring which can have many drawbacks. In the case of food production, they can cause off-flavours through product oxidation. Furthermore, the success of process development with power ultrasound is hit and miss, mainly due to the complex and poorly understood detailed physics involved, but also issues such as the generation of free radicals (which can promote oxidation of fats) and shock-wave related wear of the sonotrode and processing equipment, ultimately leading to contamination of the product.

Recent experiments have shown that well-controlled crystal nucleation can be obtained using low power ultrasound but fundamental studies in this area are lacking and this is where the project aimed to gain deeper understanding (Fig. 2). In order to measure and understand the nature of this effect the team used simultaneous Small Angle and Wide Angle X-ray Scattering (SAXS and WAXS) on the Small Angle Scattering and Diffraction beamline (I22) to test many different types of candidate molecules such as waxes, fats, fuels and oils, model pharmaceutical and agrochemical molecules in a specially created acoustic cell. Schemes such as A4I are invaluable to micro-SMEs such as Lewtas Science & Technologies as they give small companies the opportunity to better protect their IP and get to the market much quicker.

Figure 1: Participants in the Newton Fund workshop held in Bangkok in December 2017.

Figure 2: Two identical cooled, stirred wax solutions. The cell on the right is sonicated with specific low power ultrasound while the one on the left is not. The sample on the left crystallises as normal whereas nucleation is completely suppressed in the sonicated sample.

Building on the success of A4I, Diamond has joined STFC to further support UK business productivity and growth as part of the government funded Bridging for Innovators (B4I) programme. The four-year programme run by STFC will provide access to the world leading large-scale science facilities at Harwell, Daresbury and the Royal Observatory in Edinburgh covering a wide range of analytical techniques and exploiting their expertise and capabilities. The aim is to increase growth and productivity throughout the UK by helping organisations overcome product, manufacturing or process performance challenges. The Industrial Liaison team has participated in a number of briefing sessions across the country to enable organisations to explore the potential of the programme and discuss their requirements. We look forward to welcoming participants of the programme in the coming months.

As well as growing the industrial programme here at Diamond, the Industrial Liaison team has been active in a number of international collaborations. Within the EU, the team participates in CALIPSOplus, a project funded through the European Union's Horizon 2020 Research and Innovation programme. The grant provides funding for marketing activities where the light sources can join forces to have a greater impact on the European industrial science community and also for SME access to the facilities.

Further afield, the team have been awarded funding via the Newton Fund. The Newton Fund's aim is to develop science and innovation partnerships that promote the economic development and welfare of collaborating countries. The grants awarded to the Industrial Liaison team are for projects in Thailand and Indonesia. For the Thailand project, the aim is to support the Thai synchrotron facility, SLRI, in the development of their industrial user engagement through a four year programme. In December 2017, the first activity under this grant took place in Thailand where a three-day workshop was held to demonstrate the importance of large-scale scientific facilities to business (Fig. 1). We were supported in this workshop by the British Embassy in Bangkok and by the participation of Peter Dowding from Infineum and Paul Collier from Johnson Matthey who both spoke about the importance of Diamond and access to large science facilities to their research.

As the facilities and knowledge available at Diamond continue to expand and develop, the industrial programme continues to flourish. Our range of services has now extended to include a broader range of instrumentation and expertise and the demand from our clients has enabled us in turn to add capacity to some of Diamond's facilities. Through participation in a range of funding schemes, we have additional resources to help us spread the message of the great value of synchrotron science to both the UK industry base and the European industrial science community as well as to support regional development with our global synchrotron partners. We look forward to sharing the results of our new initiatives in due course. If you would like to learn more about any of these recent developments, please do contact us on industry@diamond.ac.uk.

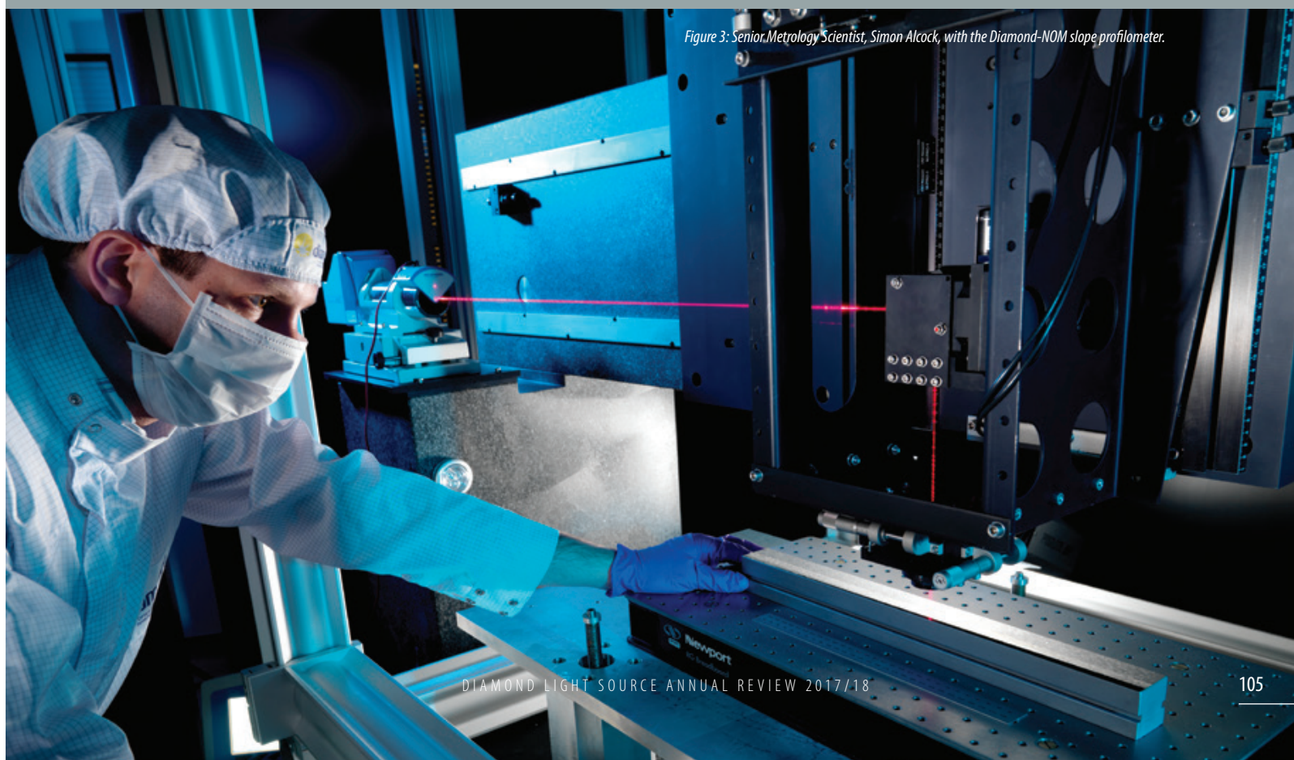

Figure 3: Senior Metrology Scientist, Simon Alcock, with the Diamond-NOM slope profilometer.

Engaging with Diamond Light Source

Communications and Engagement Team

Diamond has continued to commit to its engagement programme throughout 2017-18, linking the facilities world leading science and engineering professionals with a diverse range of audiences. The year has seen us deliver a wide range events and engagement opportunities, reflecting the needs of our staff and users as well as the interest of a range of communities in the general public.

In total our events welcomed 5,635 visitors to the facility, comprising; 1,413 for scientific and technical events, 668 undergraduate and postgraduate visitors, 3,121 school students and members of the general public, and 433 VIPs and stakeholders.

The majority of our visitors come for Diamond's core program of events, including our regular Inside Diamond open day, which continues to be extremely popular and gives members of the public a chance to visit the facility in small groups, to see inside the synchrotron and visit a beamline.

"From start to finish the atmosphere was great with many people on hand to chat . . .The tour around the facilities was also most informative with some aspects and numbers producing jaw dropping reactions from members of the group."

- visitor to an Inside Diamond open day, 2018

In July we hosted a new family focused event 'Meet the Scientist', where over 20 Diamond staff and members of our user groups came with a raft of interactive exhibits to showcase their work to a younger audience. Over 600 visitors attended over the day to participate in activities that included levitating trains, lifting weights with vacuums and building viruses as well as taking tours inside the synchrotron building.

"A good way of engaging children and adults in science. My children loved it."

"Enthusiastic and passionate staff were great at engaging with children and gave a real positive impression about working in a science, in a way my daughters perhaps don't see anywhere else."

- visitors to Diamond's 'Meet the Scientist' event, July 2017

We have offered regular schools open days, giving A-level students a general overview of the facility and highlighting career opportunities available to them. There are also dedicated activities for students to experience specialist areas within the facility including biology, computing, engineering and science applications. The Diamond schools work experience program continues to develop taking its third cohort in 2017, offering 28 students an immersive week of project based work in areas across the organisation.

Away from site, Diamond has also been active promoting our work. In September we partnered with Harwell Campus and the Medical Research Council to host a stand at the New Scientist Exhibition at the ExCel Centre in in London, with over 30,000 people attending the four day event. The Bluedot music festival at Jodrell Bank Observatory, where music is combined with a programme of live science and expert talks, provided the opportunity to engage with a different audience. Thousands of festival goers were able to visit our exhibition stand and talk to some of Diamond's summer placement students.

Diamond continues to work closely with the engagement team at STFC, jointly delivering a series of activities, including the school's Particle Physics Masterclasses and public Stargazing events which between them welcome over 1,200 visitors to site every year.

Over the past 15 years of operation, Diamond's staff numbers have continued to grow and so the past year has seen a targeted increase in internal engagement activities. As well as talks and training, an internal science open day took place in November, where 20 beamlines opened their doors and welcomed 160 staff from across the facility to learn more about the operations and science delivered within.

Figure 1: Learning about static electricity at the new 'Meet the Scientist' event.

Figure 2: The 2017 student placement cohort with the Student Engagement Officer.

"It was so good, I wondered why we had not done it before. Thanks to everyone involved."

"Seeing Principal Beamline Scientists interact with staff they wouldn't normally even see was very rewarding."

-Diamond staff attending the internal open day, November 2018

Engaging with Higher Education

Our work placement schemes for undergraduates continued to provide students with in-depth research projects whilst also developing life-long skills in communication, engagement and project management. In June 2017, six Year in Industry and 14 summer placement students arrived at Diamond to begin their projects. Whilst based at Diamond, the students also had opportunities to visit other research teams and facilities on-site and to present their research to the wider Diamond organisation.

Diamond welcomed 25 new PhD students in 2017, bringing the total number of co-funded PhD studentships to over 90 active students. We proudly collaborate with research organisations around the UK and beyond, hosting co-funded PhD students and training the synchrotron scientists of the future. Continuing from the successful introduction of a centralised call for collaborative PhD proposals in 2016, the 2017 scheme received 59 proposals. Following an internal review process, 16 studentships were funded and we look forward to welcoming our new students starting in October 2018.

The demand for visits from the university student community continues to increase and Diamond met this by hosting 26 postgraduate and undergraduate groups from across the country in 2017.

Scientific Workshops and Conferences

Diamond hosted a range targeted events to meet the interests and development needs of our staff and user community. A summary of these events is outlined herein, which includes workshops, conferences and training schools relating to specialist fields, techniques and software that can further research and discoveries in Synchrotron Science.

During the summer months, Diamond hosted three international conferences, each from an established conference series. The 20th International Magnetic Measurement Workshop (IMMW20) was held onsite in June 2017 with a whole week of presentations and open discussions on the equipment and techniques used to measure and characterise magnetic fields on accelerator magnets and insertion devices. In August, we welcomed experts in the field of X-ray Absorption Spectroscopy to discuss aspects of the technique that affect data quality in XAFS experiments at Q2XAFS, a satellite workshop the IUCr Congress meeting. We ended the summer with the ninth International Workshop on Infrared Microscopy and Spectroscopy with Accelerator Based Sources (WIRMS 2017) at Worcester College in Oxford, a key meeting for staff and users of IR/THz beamlines at Synchrotrons (SR), Energy Recovery Linac (ERL) and Free Electron Laser (FEL) facilities around the globe.

Date	Event	Participants
4 April 2017	Advanced Characterisation for Functional Materials	50
12 April 2017	Actinide XAS conference, Poster session and Tours	70
24 - 26 April 2017	eBIC Opening and CCP-EM Spring Symposium	120
1 - 2 June 2017	Dawn Training for Small Angle Scattering Workshop	30
4 - 9 June 2017	20th International Magnetic Measurement Workshop (IMMW20)	70
6 June 2017	Microfluidics Focus Group Meeting	30
13 June 2017	Advances in X-ray Imaging: Expanding the Frontiers of Knowledge	70
23 June 2017	Microscopy, Tomography, Ptychography Data Analysis at Diamond: Future Planning Workshop	50
4 July 2017	SOS Minerals school organised by NHM as lead in COG-3 consortium	24
5 - 6 July 2017	MX Bag Training Workshop	30
18 - 19 July 2017	Electronic Structure of 2D Materials: theory meets experiment	50
14 – 15 August 2017	International Workshop on Improving Data Quality in XAFS Spectroscopy (Q2XAFS)	60
1 September 2017	Early Career Scientist Symposium	62
25 - 28 September 2017	9th International Workshop on Infrared Microscopy and Spectroscopy with Accelerator Based Sources (WIRMS 2017)	120
2 - 4 October 2017	Cyro-EM Sample Preparation Workshop	22
24 – 26 October 2017	NeXus International Advisory Committee Annual Code Camp	14
30 - 31 October 2017	Dawn Training for Small Angle Scattering Workshop	30
17 November 2017	Microscopy of Catalysts Workshop	38
29 November - 7 December 2017	Diamond-CCP4 Data Collection and Analysis Workshop	22
8 - 9 January 2018	XFEL @ Diamond Meeting	40
31 – 2 January 2018	Joint ISPyB and MXCube Collaboration Meetings	40
5 - 9 February 2018	eBIC User Training Workshop	5
6 February 2018	ePSIC Science User Meeting	35
21 - 22 February 2018	MX Bag Training Workshop	40
23 February 2018	Eclipse Science and IOT Meeting	40
19 - 21 March 2018	X-ray Absorption Spectroscopy Training Workshop	30
26 - 27 March 2018	ePSIC Hyperspy Training Workshop	30
	Total	**1,222**

Governance and Management

Diamond Light Source Ltd was established in 2002 as a joint venture limited company funded by the UK Government via the Science and Technology Facilities Council (STFC) and by the Wellcome Trust, owning 86% and 14% of the shares respectively. Diamond now employs over 630 scientists, engineers, technicians and support staff from over 40 countries worldwide. The Chief Executive and Directors are advised by committees representing key stakeholder groups, including the Science Advisory Committee (SAC), Diamond User Committee (DUC), and Diamond Industrial Science Committee (DISCo).

Diamond is free at the point of access for researchers accessing Diamond via peer review, and provided the results are published in the public domain for everyone's benefit. Allocation of beam time is via a peer-review process to select proposals on the basis of scientific merit and technical feasibility. Eight peer-review panels meet twice a year to assess the proposals submitted for each six-month allocation period. Diamond also welcomes industrial researchers through a range of access modes including proprietary research.

Board of Directors

Prof Sir Adrian Smith (Chairman)
Vice-Chancellor, University of London

Prof Andrew Harrison
Chief Executive Officer, Diamond Light Source

Marshall Davies
Business Advisor, Science and Technology Facilities Council

Prof Mark Thomson
Executive Chair, Science and Technology Facilities Council

Prof Michael Fitzpatrick
Pro-Vice-Chancellor, Coventry University

Tim Livett
Chief Financial Officer, The Wellcome Trust

Jane Tirard
Director of Finance & Corporate Services, Diamond Light Source

Company Secretary
Andrew Richards, Diamond Light Source

As at April 2018

Executive

Prof Andrew Harrison took the helm as CEO of Diamond Light Source in January 2014. He was previously Director General of the Institut Laue-Langevin neutron source in Grenoble, France, where he had worked since 2006. With a background as an inorganic chemist and Professor of Solid State Chemistry at the University of Edinburgh, Prof Harrison brings a wealth of experience of scientific leadership to the organisation.

Prof Laurent Chapon joined Diamond as Director of Physical Sciences in 2016 from the Institut Laue-Langevin in Grenoble, France. Whilst there, Prof Chapon was Senior Fellow and Leader of the Diffraction Group for over five years. He is an expert in materials science as well as X-ray and neutron diffraction techniques. His principal interests include transmission metal oxides, frustrated oxides, and multiferroics.

Prof David Stuart is MRC Professor of Structural Biology at the University of Oxford, and Head of the Division of Structural Biology at the Department of Clinical Medicine. He was appointed Director of Life Sciences at Diamond in 2008. His principal research interests include the structure of viruses and viral proteins as well as cellular proteins, especially those that interact with viruses.

Prof Richard Walker joined Diamond Light Source as Technical Director in January 2002. He was previously Director of the Light Sources Division at Sincrotrone Trieste in Italy, and prior to that he was a key member of the Daresbury Laboratory SRS team. He is a visiting Professor of Physics at the University of Oxford.

Jane Tirard joined Diamond as Director of Finance and Corporate Services in 2015. With over 30 years of regional and global experience in business and financial management, she was most recently Finance Director at Queen Mary University of London, and previously held the post of Executive Director of Finance at STFC. Prior to joining the public sector, Jane held several positions at Pfizer.

Staffing and Financial Information

Outline Organisational Chart

Chief Executive's Office

Communications
Safety, Health & Environment
Industrial Liaison

Science Division

Instrument Groups:
Biological Cryo-Imaging
Crystallography
Imaging and Microscopy
Macromolecular Crystallography
Magnetic Materials
Soft Condensed Matter
Spectroscopy
Structures and Surfaces

Data Acquisition Group
Data Analysis Group
Detector Group
Experimental Hall Labs Services
Optics & Metrology
Planning & Projects Office
User Office

Technical Division

Accelerator Physics
Controls
Diagnostics
Engineering
Operations
Insertion Devices
Installation & Facility Mgt
Power Supplies
Radiofrequency Systems
Vacuum

Finance and Corporate Services

Soft Facilities
Finance
Human Resources
IT Systems
Procurement

Summary of Financial Data

	2008/09	2009/10	2010/11	2011/12	2012/13	2013/14	2014/15	2015/16	2016/17	2017/18
Operating Costs £m	28.4	30.5	33.5	36.5	39.9	42.5	44.5	54.6	56.9	62.8
Total Staff (Year End)	369	401	419	438	481	507	534	582	609	639
Capital Expenditure – Operations £m	4.5	5.7	8.6	5.1	8.0	7.5	6.2	8.0	10.5	12.8
Phase II £m	25.5	22.0	16.2	9.9	2.8	0.8	0.2	0.0	0.0	0.0
Phase III £m	0.1	0.3	3.0	10.3	14.2	17.2	23.7	20.6	11.5	3.7
Other capital projects £m							4.8	5.6	7.3	4.3

Figures up to and including 2014/15 exclude VAT, thereafter figures include VAT.

Committee Membership

The Scientific Advisory Committee (SAC) advises the CEO and the Science Directors on the scientific and technical questions impacting the specification, design, commissioning and operation of the facility; experimental and user support facilities, and opportunities for scientific exploitation.

Dr Andrew Thompson (Chair)
SOLEIL (France)

Dr Tom Hase (Vice-Chair)
University of Warwick (UK)

Dr John Barker
Evotec (DISCo Representative)

Dr Bridget Carragher
New York Center for Structural Biology (USA)

Dr Nick Brooks
Imperial College (UK) – (Chair of the DUC)

Prof John SO Evans
University of Durham (UK)

Dr Paul Fuoss
SLAC (USA)

Prof Philip Hofmann
Aarhus University (Denmark)

Prof Peter Hatton
University of Durham (UK)

Prof Tim Lodge
University of Minnesota (USA)

Dr Lisa Miller
Brookhaven National Lab/NSLS-II

Prof Arwen Pearson
The Hamburg Centre of Ultrafast Imaging (Germany)

Dr Ilme Schlichting
Max Planck Institute for Medical Research (Germany)

Prof Christian Schroer
DESY (Germany)

Prof Sam Shaw
University of Manchester (UK)

Prof Moniek Tromp
University of Amsterdam (Netherlands)

The Diamond Industrial Science Committee (DISCo) advises the CEO and Directors on opportunities for industry to be engaged in research at Diamond, industrial research priorities that will help shape operational strategy, including the best way to exploit the current suite of beamlines and to develop the case for investment in future beamlines, and to develop best practice for industrial engagement.

Dr Malcolm Skingle (Chair)
GlaxoSmithKline

Dr John Barker
Evotec

Dr Andrew Barrow
Rolls-Royce

Prof. David Brown
Charles River Laboratories

Dr Paul Collier
Johnson Matthey

Dr Rob Cooke
Heptares Therapeutics

Dr Cheryl Doherty
Pfizer

Prof. Peter Dowding
Infineum

Prof. Jonathan Hyde
NNL

Prof. Ken Lewtas
Lewtas Science & Technologies

Dr Jonathan Mitchener
Innovate UK

Dr John Pollard
Vertex Pharmaceuticals (Europe) Ltd

Dr Richard Storey
AstraZeneca

Dr Ian Tucker
Unilever

The Diamond User Committee (DUC) has been set as a platform for discussion between Diamond and the user community of matters relating to the operation and strategy of Diamond.

Dr Nick Brooks (Chair)
Imperial College London

Dr Arnaud Basle
University of Newcastle

Dr Yvonne Grunder
University of Liverpool

Dr Tim Knowles
University of Birmingham

Dr Gareth Law
University of Manchester

Dr Ed Lowe
University of Oxford

Prof Colin Pulham
University of Edinburgh

Dr Neil Telling
Keele University

Dr Andrew Thomas
The University of Manchester

Dr Amber Thompson
University of Oxford

Dr Laura Spagnolo
University of Glasgow

Membership as at April 2018

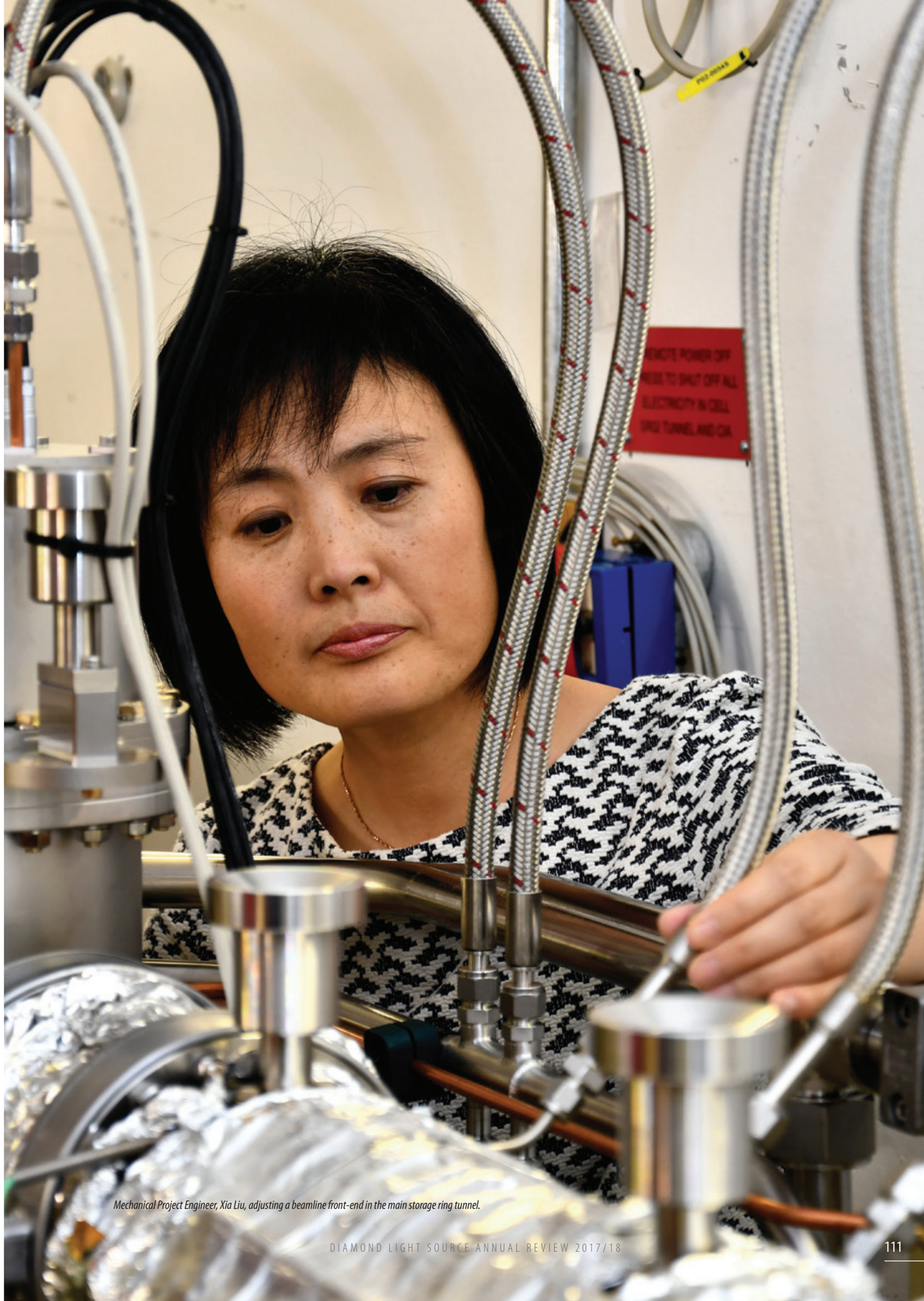

Mechanical Project Engineer, Xia Liu, adjusting a beamline front-end in the main storage ring tunnel.

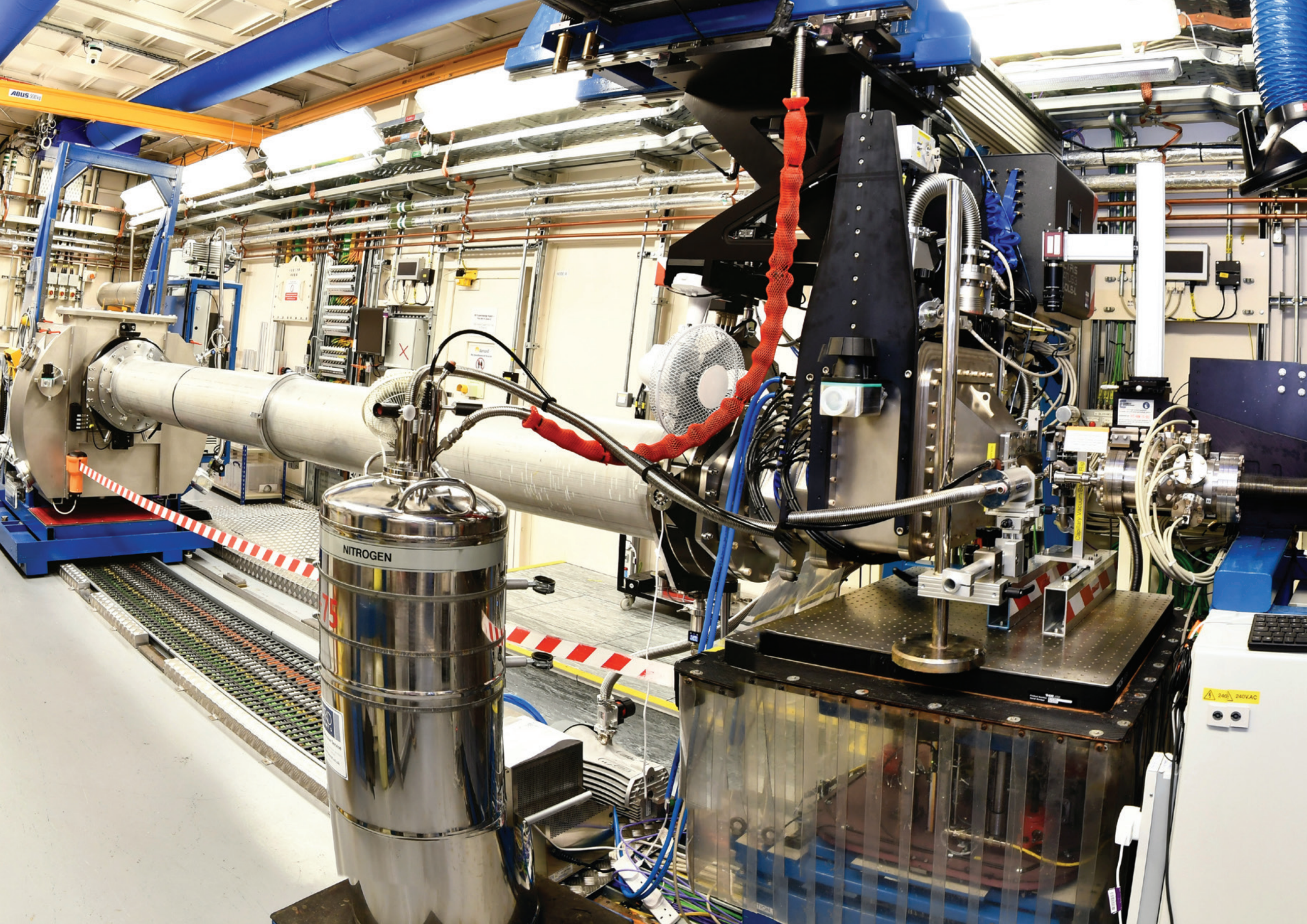
ABUS SEW
NITROGEN
240 240V.AC

Diamond Light Source Ltd
Harwell Science & Innovation Campus
Didcot, Oxfordshire OX11 0DE
Tel: +44 (0)1235 778 639
Fax: +44 (0)1235 778 499
www.diamond.ac.uk

Acknowledgement:
We would like to thank the authors and all
colleagues who contributed to this publication.

Printed on Forest Stewardship
Council (FSC) accredited paper stock.

Published May 2017